



UNIVERSITY
OF
JOHANNESBURG

COPYRIGHT AND CITATION CONSIDERATIONS FOR THIS THESIS/ DISSERTATION



- Attribution — You must give appropriate credit, provide a link to the license, and indicate if changes were made. You may do so in any reasonable manner, but not in any way that suggests the licensor endorses you or your use.
- NonCommercial — You may not use the material for commercial purposes.
- ShareAlike — If you remix, transform, or build upon the material, you must distribute your contributions under the same license as the original.

How to cite this thesis

Surname, Initial(s). (2012). Title of the thesis or dissertation (Doctoral Thesis / Master's Dissertation). Johannesburg: University of Johannesburg. Available from: <http://hdl.handle.net/102000/0002> (Accessed: 22 August 2017).



Gold, Palladium and Mesoporous Oxide-based Nanocatalysts for Redox Processes and Sustainable Catalysis: Synthesis and Catalytic Evaluation.

By:

Oluwatayo Racheal Onisuru

(218097842)

Thesis

Submitted to the Department of Chemical Sciences, Faculty of Science,
in fulfillment of the requirements for the degree

**UNIVERSITY
OF
JOHANNESBURG
PHILOSOPHIAE DOCTOR**

in **Chemistry**

at the

University of Johannesburg

Supervisor: Prof. Reinout Meijboom

May 2022

Acknowledgments

Firstly, with gladness and gratitude of heart, I expressed my appreciation to the most high God, my salvation, and only hope for the possibility of this achievement.

My sincere appreciation goes to my supervisor, Prof Reinout Meijboom, for financial support, guidance, care, patience, and motivational drive. Your liberality and drive are exceptional. Thank you, sir.

I wish to express my profound gratitude to my husband; I am indeed blessed and fortunate to have you as my husband. Your support and care are transcendently genuine; your input and involvement in this work are overwhelmingly significant. You have demonstrated and established in me that I can make it with God on my side, and your prayers and encouragement kept me going. Your love remains ever in my heart. To my gracious children, Anthony and Glory of God, I thank God for his grace upon you both for holding forth for me during this period. I love you both.

This achievement would not have been easy without the input of my mother, Deaconess Agnes Funke Owolabi, Mr and Mrs Onisuru (my father and my mother-in-law), Mr and Mrs Ahmed, Dr and Mrs Adeyemi, Mr and Mrs Onisuru (my brother-in-law's family), Dr and Mrs Saliu, Pharm and Mrs Akiniyi. You are all appreciated for your support and care for my children while I was away. Special thanks to my siblings; Mr Oluwadamilare Victor Owolabi, Mrs Olaitan Ruth Awolola, Olaniyi Ojo Owolabi, and Monisola Olorunfemi Owolabi. Pastor and Mrs Adebisi, I am deeply grateful for your involvement in my path in life since my undergraduate days.

To all members of the teaching staff of the Department of Chemical Sciences (Dr N.S. Bingwa in particular), I am grateful for your support. I also expressed my appreciation for the non-teaching staff, especially Mrs Eureka (the secretary), Mrs Nelmarie Muller, Dr. Batsile Mogudi, and Siyasanga Mpelane (Instrument Scientist).

My unreserved appreciation goes to all members of the metacatalysis group for providing an enabling environment, support, and assistance. Especially Dr. Mulisa Nemanashi, Dr. Mrs Chistianah Akinnawo, Dr. Oyekunle A Alimi, Dr. Kariska, Dr Joe Ndolomingo, Dr Ali K

Illunga, Charles Oseghale, and Dele Peter Fopujuwo, to mention a few. Your suggestions were helpful.

Special thanks, Dr. Emmanuel Folorunso Olasehinde, who contributed immensely to the achievement of my MTech as a supervisor and ensured I qualified for this PhD. As well as my brothers and sisters of the household of faith, I am indeed very grateful. Thank you all.



Declaration

I hereby declare that all data acquired and reported in this thesis were carried out and written by me. The publications and the manuscripts to be submitted were all written by me, and my supervisor was responsible for proofreading and editing. I confirmed that the project had not been submitted for qualification in another University.



Abstract

Transition metals' exceptional ability and properties at the nanoscale level transcend their corresponding bulk metals in chemical transformation both in the laboratories and the industries. However, the nanoparticles are prone to particle growth and agglomeration at this nanoscale state, inhibiting their excellent performance and compromising their uniqueness. Hence, the stability of the particles presents a significant factor in governing their innovative attributes. Therefore, organic polymers, such as polyvinylpyrrolidone (PVP) and dendrimer, were considerably employed as soft templates to ensure stability and prevent the agglomeration of these nanoparticles in a homogeneous phase. These synthesized nanoparticles include AuPVP, PdPVP, AuPdPVP nanoparticles, and CuDENs.

Although conventional homogeneous catalysts possess a vast tendency to enhance high conversion and product selectivity in chemical reactions, nevertheless, they present limiting phenomenon of recoverability, recyclability, and deactivation at high temperatures. Therefore, to circumvent these limitations, we fabricated metal nanoparticles through the dispersion of metals onto an insoluble and solid mesoporous silica and metal oxide support by adapting a dual templating approach, followed by a galvanic replacement protocol. In addition, inverse micelle, sol-gel, and wet impregnation methods were also employed to design ideal heterogeneous catalysts such as $\text{Cu}_n@SiO_2$, $\text{Au}@SiO_2$, $\text{Pd}@SiO_2$, CoMMO, and MnMMO, which are capable of high operating procedures, easy recoverability, and reusability for oxidation and reduction reactions.

Different analytical techniques were used to characterize and obtain the properties of these catalysts. These techniques include nitrogen sorption with Brunauer-Emmett-Teller (BET) and Barret-Joyner-Halenda (BJH) to examine the surface area, pore size, and pore volume distribution, high-resolution transmission electron microscopy (H-TEM) for internal morphologies, powder X-ray diffraction (p-XRD), for the diffraction patterns of the materials. While thermogravimetric analysis (TG) was performed to determine the sample's thermal stability, Fourier transform infrared spectroscopy (FT-IR) identified the specific functional groups present. Scanning electron microscopy (SEM) with energy-dispersive X-ray spectroscopy (EDX) obtained the surface morphologies and identification of metal composition. In addition, hydrogen-temperature programmed reduction (H_2 -TPR) was used to examine the reducibility of the catalyst. Another characterization technique used was

ultraviolet-visible (UV-vis) spectroscopy to know the absorbance of the heterogeneous catalyst.

The technique showed that the catalysts possess the characteristic properties exhibited by a mesoporous material with good surface area, reducibility profile, and corresponding crystallinity according to the JSCD number. The spherical structure of the mesoporous silica support was preserved even after a galvanic displacement reaction on $\text{Cu}_n@SiO_2$ to fabricate $\text{Au}_n@SiO_2$, and the internal morphology revealed that the materials were supporting the nanoparticles with good stability after chemical evaluation.

The activity and effectiveness of the catalysts were initially demonstrated in traditional batch operating procedures and then in continuous flow protocol. Compared with the conventional batch reaction, continuous flow reaction is considered a better option in the catalytic investigation. This is because it exhibits superb catalytic performance, which is cost-effective with minimal chemical consumption and shorter reaction time. It has been confirmed over time as sustainable and suitable for chemical processes. The catalytic evaluation began with model reactions such as reducing orange II acid (OII), 4-nitrophenol, and oxidation of rhodamine B. Also, oxidation of styrene and hydrogenation of acetophenone were investigated, while the efficiency of the continuous flow set-up was observed in the reduction of hexacyanoferrate.

The model reaction of OII computed after the Langmuir-Hinshelwood (Langmuir-Hinshelwood) approach revealed that the reaction follows the Langmuir-Hinshelwood model. Other model reactions also follow a *pseudo*-first-order reaction. The catalytic results in the batch procedure presented excellent activities with both high selectivity and quantitative product yield. While a shorter reaction time was noticed for the continuous flow reaction, we obtained a higher rate constant, lower activation energy, and higher turnover frequency (TOF) value than the traditional batch method, both in this work and in other published reports.

Keywords

Silica sphere; $\text{Cu}_n@SiO_2$ NPs; *In-situ* replacement; galvanic exchange; oxidation-reduction; poly(vinylpyrrolidone) nanoparticles; orange II acid; reaction kinetics; Langmuir-Hinshelwood; 3D-Printing; continuous flow reaction; microfluidic reactor; mesoporous metal oxide; hexacyanoferrate; $\text{Pd}@SiO_2$ particles; Hydroxypropyl methylcellulose (HPMC); water; acetophenone reduction; 1-phenyl ethanol.

Publications

- 1. Oluwatayo Racheal Onisuru**, Charles O. Oseghale, and Reinout Meijboom, *In-situ* replacement of CU-DEN: an approach for a more noble metal nanocatalyst for catalytic use *New J. Chem.*, 2020, 44, 20322 (Published).
- 2. Oluwatayo Racheal Onisuru**, Oyekunle Azeez Alimi, Kariska Potgieter, and Reinout Meijboom, Continuous Flow Catalytic Degradation of Hexacyanoferrate Ion through electron transfer induction in a 3D-Printed Flow Reactor. *Journal of Materials Engineering and Performance*, 2021, 30, 4891-4901 (Published).
- 3. Oluwatayo Racheal Onisuru**, Kariska Potgieter, Ali K. Illunga, Charles O. Oseghale, and Reinout Meijboom, Kinetic degradation modeling of Orange II Acid dye: A decolorization abatement within a Microplate reader system. (Manuscript to be submitted).
- 4. Oluwatayo Racheal Onisuru**, Dele Peter Fapojuwo, Charles Oseghale, Oyekunle Azeez Alimi, and Reinout Meijboom, Chemoselectivity Hydrogenation of ketone; An *In-situ* and Eco-friendly Reduction for Nature compatibility and Greener Chemistry Reaction. (Manuscript to be submitted).



Conferences and Award

Conferences

Synthesis by Galvanic Replacement: A One-step Approach towards Nano-catalyst Fabrication, **Oluwatayo Racheal Onisuru**, and Reinout Meijboom. Oral presentation, South African Young Spectroscopist / Mass Spectroscopist 2019 Annual symposium.

Continuous Flow Catalytic Degradation of Hexacyanoferrate Ion through electron transfer induction in a 3D-Printed Flow Reactor, **Oluwatayo Racheal Onisuru**, Oyekunle Azeez Alimi, Kariska Potgieter, and Reinout Meijboom, SACI/RSC National Young Chemist's Symposium 2021.

Award

Best presented slide, 2019 South Africa Spectroscopic Society together with South African Association for Mass Spectrometry Certificate of Achievement.



List of Abbreviations

AM	Additive manufacturing
Au _n @SiO ₂ NPs	Silica-supported gold nanoparticles
AuNPs	Gold nanoparticles
AuPdNPs	GoldPalladium nanoparticles
BET	Brunauer-emmett-teller
BJH	Barrett-Joyner-Halenda
CAD	Computer-aided design
CuDENs	Dendrimer encapsulated copper nanoparticles
Cu _n @SiO ₂ NPs	Silica-supported copper nanoparticles
CTAB	Cetyltrimethylammonium bromide
DEN	Dendrimer encapsulated nanoparticle
E _a	Activation energy
E°	Standard electrode potential
EDS	Electron dispersion spectroscopy
Eq	Equation
Fig	Figure
FR	Flow rate
FTIR	Transform infrared spectroscopy
GC-FID	Gas chromatography flame ionization detector
h	Hour
H-TEM	High-resolution Transmission Electron Microscope
HPMC	Hydroxypropyl methylcellulose
ICP-OES	Inductively coupled plasma-optical emission spectroscopy
k _{obs}	Observed rate constant
kV	Kilovolt
M	Molarity
mg	Milligram
min	Minute
mL	Millilitre
mM	Milli molarity
MMO	Mesoporous metal oxide
nm	Nanometer

NP	Nanoparticle
NPs	Nanoparticles
OII	Orange II
pH	Potential hydrogen
p-XRD	Powder X-ray diffraction
PAMAM	Polyamidoamine
PAMAM (G4 PAMAM-NH ₂)	Generation 4 amine-terminated PAMAM dendrimers
PdNPs	Palladium nanoparticles
PLA	Polylactic acid
PVP	Polyvinylpyrrolidone
R	Universal gas constant
RhB	Rhodamine B
RT	Residence time
S	Supplementary
SEM	Scanning electron microscope
SD	Secure digital
STL	Stereolithographic
T	Temperature
TBHP	Tertiarybutyl hydrogen peroxide
TEOS	Tetraethyl orthosilicate
TGA	Thermogravimetry analysis
TOF	Turn over frequency
TPR	Temperature programmed reduction
UV-Vis	Ultra-violet visible
λ	Wavelength
°C	Degree Celsius
μ L	Microlitre
μ mol	Micro mole
3D	Three dimensional
4-nitrophenol	4- Nitrophenol

Table of Contents

Dedication	i
Acknowledgments	ii
Declaration	iv
Abstract	Error! Bookmark not defined.
Keywords	v
Publications	vii
Conferences and Award	viii
List of Abbreviations	ix
Table of Contents	xi
List of Figures	xvi
List of Tables	xix
List of Schemes	xxi
Chapter 1: Encapsulation Approaches: Synopsizing viable Strategies for Nanocomposite Stability in Catalysis	1
1.1 Introduction	1
1.1.2 Catalysts and catalysis.....	2
1.2 Literature review	4
1.2.1 Nanoparticles and nanocomposites.....	4
1.2.2 Nanoparticles as nanocatalysts.....	6
1.2.3 Nanoparticle’s synthesis and limitation	7
1.3 Nanoparticle’s encapsulation approach as an overcoming measure	8
1.3.1 Encapsulation using dendrimers	9
1.3.2 Encapsulation using graphene.....	13
1.3.3 Encapsulation using carbon	14
1.3.4 Encapsulation using polyvinylpyrrolidone (PVP)	14
1.3.5 Encapsulation using mesoporous zeolites.....	15
1.3.6 Encapsulation in silica nanosphere/aluminosilicates	15
1.4 Characterization approach.....	16
1.5 Encapsulated nanoparticle: advantages, uses, and application	17
1.6 Encapsulation in reduction reactions.....	17
1.6.1 Reduction of nitroaromatics.....	18
1.2.2 Reduction of azo dyes	18

1.7	Mesoporous metal oxides in catalysis.....	19
1.8	Catalytic transformation: from batch to continuous flow state.....	20
1.9	Aims and objectives of the thesis.....	20
1.10	Outline of the thesis.....	21
1.11	References.....	23
CHAPTER 2.....		377
Kinetic Degradation Modeling of Orange II Acid Dye: A Decolorization Abatement within a Microplate Reader System.....		377
Graphical abstract.....		377
Abstract.....		388
2.1	Introduction.....	399
2.2	Experimental section.....	411
2.2.1	Materials and reagents.....	411
2.2.2	Synthesis of PVP stabilized nanoparticles.....	411
2.3	Characterization.....	422
2.4	Catalytic evaluation.....	422
2.4.1	Reaction conditions used for kinetic studies.....	422
2.5	Result and discussion.....	433
2.5.1	Synthesis of Pd, Au, and bimetallic AuPd-PVP NPs.....	433
2.5.2	Characterization of Pd, Au, and bimetallic AuPd-PVP NPs.....	433
2.5.3	Orange II acid catalytic activity and kinetic evaluation.....	455
2.5.4	Orange II acid catalytic activity dependence on temperature.....	544
2.5.5	Catalytic comparison of OII acid degradation with other catalytic systems.....	566
2.6	Conclusion.....	588
2.7	References.....	59
Chapter 3.....		64
<i>In-situ</i> Replacement of Cu-DEN: An Approach for Preparing a More Noble Metal Nanocatalyst for Catalytic Use.....		64
Graphical abstract.....		65
Abstract.....		66
3.1	Introduction.....	67
3.2	Experimental Section.....	70

3.2.1	Chemicals and materials	70
3.2.2	Synthesis of SiO ₂ spheres	70
3.2.3	Synthesis of Cu _n @SiO ₂ NPs with G4-PAMAM-NH ₂ dendrimer as a stabilizer	70
3.2.4	Preparation of Au _n @SiO ₂ NPs by in-situ replacement.....	71
3.2.5	Characterization of the catalyst.....	71
3.2.6	Catalytic reactions.....	72
3.3	Result and discussion	72
3.3.1	TEM Characterization of silica spheres, Cu _n @SiO ₂ NPs and Au _n @SiO ₂ NPs ...	74
3.3.2	FTIR measurement of silica sphere before and after calcination	74
3.3.3	p-XRD Characterization	74
3.3.4	Brunauer-Emmett-Teller nitrogen sorption analysis	75
3.3.5	Thermogravimetric Analysis (TGA).....	77
3.3.6	Catalytic evaluation of the synthesized Cu _n @SiO ₂ and Au _n @SiO ₂ on 4-nitrophenol reduction.....	79
3.3.7	Catalytic investigation on oxidation of RhB.....	80
3.3.8	Catalytic evaluation of Au _n @SiO ₂ in the oxidation of styrene to benzaldehyde and phenylacetaldehyde.....	82
3.4	Conclusion.....	86
3.5	References	87
Chapter 4	93
Hydrogenation of ketone; An <i>In-situ</i> Approach towards an Eco-friendly Reduction....	93
Graphical abstract	93
Abstract.....	94
4.1	Introduction	95
4.2	Experimental section	97
4.2.1	Chemicals and Materials.....	97
4.2.2	Synthesis of silica support for the Pd Particle and Loading of Pd onto the silica support	98
4.2.3	Catalyst's characterization	98
4.2.4	Hydrogenation of Ketone in HPMC solution	99
4.3	Result and discussion	100
4.3.1	Characterization	100
4.3.2	Hydrogenation of ketone in HPMC solution	103
4.3.3	Comparison test of HPMC solution with water.....	105
4.3.4	Effect of catalyst amount	106

4.3.5	Effect of substrate amount	109
4.3.6	Effect of borohydride amount.....	109
4.3.7	Effect of temperature	110
4.3.8	Turnover frequency of Pd@SiO ₂ Catalyst.....	111
4.3.9	Stability and recyclability	112
4.3.10	Hydrogenation with other ketone.....	113
4.3.11	Comparative study of Pd@SiO ₂ with other Pd based Catalyst.....	114
4.4	Conclusion.....	116
4.5	References	117
Chapter 5	122
Continuous Flow Catalytic Degradation of Hexacyanoferrate Ion through electron transfer induction in a 3D-Printed Flow Reactor.....	122
Graphical abstract	123	
Abstract.....	124	
5.1	Introduction	125
5.2	Experimental section	126
5.2.1	Materials	126
5.2.2	Design of the reactor and experimental setup.....	127
5.2.3	Mesoporous manganese metal oxide fabrication (MnMMO).....	128
5.2.4	Mesoporous cobalt metal oxide fabrication (CoMMO).....	128
5.2.5	Characterization of catalysts.....	129
5.2.6	Fabrication of microfluidic systems.....	129
5.2.7	Hexacyanoferrate ion catalytic redox transformation in a 3D-printed U-shaped flow reactor.....	131
5.3	Result and discussion	132
5.3.1	Characterization Techniques.....	132
5.3.2	Catalytic transformation in the microfluidic reactor.....	135
5.3.3	Catalyst turn over frequency	141
5.3.4	Stability and recyclability of catalysts	142
5.3.5	Comparative analysis	144
5.4	Conclusion.....	146
5.5	References	147
Chapter 6	153

Conclusions and recommendations	153
6.1 Conclusions	153
6.1.1 Catalytic activities	153
6.2 Recommendations	154
Appendix.....	156
Supplementary information.....	156
Chapter 2.....	156
Chapter 3.....	160
Chapter4.....	162
Chapter 5.....	177
5. S2 References	185



List of Figures

Chapter I

Figure 1.1: Combined advantages of homogeneous and heterogeneous catalyst possessed by nanocatalyst.....	3
Figure 1.2: Advantages of nanocatalysis	7
Figure 1.3: Schematic illustration of some encapsulation approaches.	9
Figure 1.4: NP's synthesis approaches	12
Figure 1.5: Synthesis of bimetallic DENs catalysts via (a) Co-complexation, (b) Sequential loading (or reduction), and (c) Partial displacement (or galvanic displacement).....	13

Chapter 2

Figure 2.1: H-TEM images of (a) Au-PVP NPs, (b) Pd-PVP NPs, and (c) AuPd-PVP bimetallic NPs.....	44
Figure 2.2: The FT-IR absorption Spectra of Au-PVP, Pd-PVP NPs, and AuPd-PVP bimetallic NPs.....	45
Figure 2.3: OII (a) reduction spectra of the absorbance versus time (b) non-linear regression profile.....	47
Figure 2.4: (a-c) Plot of the surface area of the different catalysts versus the observed rate constant.	47
Figure 2.5: The Plot of observed rate constant dependence on the OII concentration while maintaining a constant $[\text{NaBH}_4]$ (in a, and b respectively), and on NaBH_4 concentration, while keeping $[\text{OII}]$ (in c, and d respectively) constant using Langmuir-Hinshelwood approach for Au-PVP catalyzed reaction.....	51
Figure 2.6: The Plot of observed rate constant dependence on the OII concentration while maintaining a constant $[\text{NaBH}_4]$ (in a, and b respectively), and on NaBH_4 concentration, while keeping $[\text{OII}]$ (in c, and d respectively) constant using Langmuir-Hinshelwood approach for AuPd-PVP catalyzed reaction.....	52
Figure 2.7: The Plot of observed rate constant dependence on the OII concentration while maintaining a constant $[\text{NaBH}_4]$ (in a, and b respectively), and on NaBH_4 concentration, while keeping $[\text{OII}]$ (in c, and d respectively) constant using the Langmuir-Hinshelwood approach for Pd PVP catalyzed reaction.....	53
Figure 2.8: The Plot of (a) Arrhenius and (b) Eyring obtained for the thee different catalysts.....	56

Chapter 3

- Figure 3.1:** The TEM images of (a) G4-PAMAM-NH₂ templated silica sphere (G4-PAMAM-NH₂-SiO₂) (b) Cu_n@SiO₂NPs and (c) Au_n@SiO₂NPs. 73
- Figure 3.2:** FTIR analysis of dendrimer and silica sphere interaction..... 75
- Figure 3.3:** p-XRD pattern of (a) Cu_n@SiO₂ and Au_n@SiO₂ (b) calcined and uncalcined silica sphere. 75
- Figure 3.4:** N₂ adsorption-desorption isotherm of (a) silica sphere before and after calcination, (b) Cu_n@SiO₂ before and after calcination, and Au_n@SiO₂. Pore distribution patterns of (c) silica sphere before and after calcination, (d) Cu_n@SiO₂ before and after calcination, and Au_n@SiO₂. 77
- Figure 3.5:** Thermogravimetric analysis of (a) silica sphere, (b) Cu_n@SiO₂, and (c) Au_n@SiO₂. 78
- Figure 3.6:** UV-vis spectra showing the degradation of 4-nitrophenol using (a) Cu_n@SiO₂ and (b) Au_n@SiO₂, non-linear regression against time with (c) Cu_n@SiO₂ and (d) Au_n@SiO₂.... 80
- Figure 3.7:** (a) UV-vis spectrum of RhB oxidation using Au_n@SiO₂, (b) non-linear fits data. 81
- Figure 3.8:** Concentration variation of (a) RhB (b) H₂O₂..... 82
- Figure 3.9:** (a) Plot revealing conversion and selectivity of Au_n@SiO₂ at 80 °C: 0.1 g catalyst, 0.59 wt% metal loading, 214 μL (2 mmol) styrene, 415.2 μL (3 mmol) TBHP, 6 h and (b) Catalyst recyclability. 83

Chapter 4

- Figure 4.1:** (a) N₂ adsorption-desorption isotherm, (b) powder-XRD pattern of Pd@SiO₂.. 101
- Figure 4.2:** Thermogravimetric analysis of Pd@SiO₂ (a) Percentage weight loss, (b) Differential weight. 101
- Figure 4.3:** (a) TEM image obtained for Pd@SiO₂ and (b) is the EDS showing the composition of the Pd@SiO₂..... 102
- Figure 4.4:** (a) H₂-Temperature program reduction analysis (b) FTIR profile of Pd@SiO₂... 103
- Figure 4.5:** UV-Vis spectra of (a) acetophenone substrate before catalysis, (b) 1-phenyl ethanol after the product is formed..... 105
- Figure 4.6:** Percentage conversion comparison of HPMC modified water and unmodified water..... 106
- Figure 4.7:** Different plots revealing the variations at 80 °C of (a) catalyst amount variation, (b) substrate variation, (c) Borohydride variation obtained..... 108

Figure 4.8: (a) Percentage conversion of acetophenone at different temperatures used, (b) The Arrhenius plot of $\ln k_{obs}$ against $1/T$ at various temperatures. 111

Figure 4.9. Recyclability plot of acetophenone conversion to 1-Phenyl ethanol (at 80 °C, 0.22 g catalyst, 21.60 mmol of acetophenone). 112

Chapter 5

Figure 5.1: (a) Three-dimensional printing of a transparent U-shaped reactor using a thermoplastic polylactic acid filament. 128

Figure 5.2: (a) Measurement of N₂ adsorption-desorption for MnMMO and CoMMO. (b) Pore volume pattern for MnMMO and CoMMO. 133

Figure 5.3: (a) H₂-TPR profiles of MnMMO and CoMMO (b) p-XRD analysis graphs of MnMMO and CoMMO..... 134

Figure 5.4: Transmission Electron Micrograph of (a) MnMMO and (b) CoMMO. 135

Figure 5.5: Thermal analysis of (a) MnMMO and (b) CoMMO 135

Figure 5.6: (a) Shows flow rate absorption spectrum as a function of ferrocyanide reduction. (b) Comparison of MnMMO and CoMMO conversion (percentage) (c) percentage conversion of ferrocyanide at various catalyst concentrations..... 138

Figure 5.7: (a) Percentage conversion of ferrocyanide at various temperatures, (b) plot demonstrating the rate constant's temperature dependence, and (c) thermodynamic plot of $\ln k$ versus $1/T$ at various temperatures. 141

Figure 5.8: (a) The plot of relative absorbance against residence time (b) Catalyst recycling bar graph. 143

List of Tables

Chapter 2

Table 2.1:	54
Summary of the kinetic rate constant and the adsorption constant parameters obtained for Au-PVP, Pd-PVP, and AuPd-PVP catalysts from the experimental data following the Langmuir-Hinshelwood approach.....	54
Table 2.2:	56
Activation and thermodynamic parameters for the reduction of OII.....	56
Table 2.3:	57
Data showing thermodynamic parameters in comparison with other systems.	57

Chapter 3

Table 3.1:	76
Surface area data and pore structure parameters of silica sphere, $Cu_n@SiO_2$ before calcination, after calcination, and $Au_n@SiO_2$	76
Table 3.2:	83
Oxidation comparison with other previous reports on Au-based catalysts.....	85

Chapter 4

Table 4.1:	109
Data obtained for the conversion of acetophenone at different catalyst amount.	109
Table 4.2:	112
Data showing the increasing order of the TOF obtained at different temperatures.	112
Table 4.3:	112
Reduction of other ketone substrates by $Pd@SiO_2$	113
Table 4.4:	115
Comparison of $Pd@SiO_2$ catalysts activity with Pd-based catalysts previous reports towards hydrogenation of ketone.	115

Chapter 5

Table 5.1:	137
Data showing the impact of flow rate at 45 °C on the reaction and the conversion obtained using 3 mg of MnMMO.....	137

Table 5.2:	139
Data showing the conversion of $[\text{Fe}(\text{CN})_6]^{3-}$ obtained at different temperatures, minimum flow rate, and maximum flow rate using 3 mg of MnMMO.....	139
Table 5.3:	142
Data showing the increasing order of the TOF obtained at different temperatures.	142
Table 5.4:	145
Comparison of $\text{Fe}(\text{CN})_6^{3-}$ reduction by other catalysts under batch system reported with this work (TW), continuous flow system.	145



List of Schemes

Chapter 2

Scheme 2.1: Schematic illustration of OII reduction by borohydride interaction driven by a catalyst.40

Chapter 3

Scheme 3.1: Schematic illustration of CuDENS immobilization on silica and subsequent *in-situ* replacement.68

Scheme 3.2: Representative illustration of styrene oxidation showing the products formed. 70

Chapter 4

Scheme 4.1: Schematic representation of 1-phenyl ethanol formation.....97

Chapter 5

Scheme 5.1: The schematic depiction of the technique for 3D printing as described by Rossi *et al.*.....130



Chapter 1:

Encapsulation Approaches: Synopsizing viable Strategies for Nanocomposite Stability in Catalysis

1.1 Introduction

Encapsulation is an area of research that has over the years gained tremendous recognition, getting scientists not only in academia but also in the industrial research arena to be interested. This approach is with the view of stabilizing and controlling nano-sized particles [1]. A giant leap has also been made in catalysis to determine the structural detail of catalysts, including magnitude, form, and surface properties. This effort has led to recognizing designed nanostructures of transition metal origin as promising catalysts with improved selectivity [2]. Nevertheless, metal nanoparticles' high energy makes them agglomerate and sinter into larger particles which change their shapes, sizes, and surface properties before and during catalytic reactions. Agglomeration and sintering result in a significant decrease in their activity, selectivity, and practical applications. Hence, it becomes pertinent to use approaches aimed at preventing such agglomeration or sintering.

This is obtainable though encapsulating the dispersed nanoparticles within permeable materials or stabilizing agents [2–4]. Stabilizing or capping agents are added to metal nanoparticles (MNPs) to disallow their interactiveness through adsorption of organic compounds or covalent attachment [5]. The addition of these stabilizing agents to MNPs bring about controlling of their growths and circumventing agglomeration [6]. The stabilization of MNPs can either be sterically, electrostatically or electrosterically (the combination of the two) [5,6]. The last decades have witnessed considerable attention placed on catalysts encapsulation into molecular sieves. This process is motivated to prepare intercrossed materials that project the advantages of catalysts with mixed supports.

The advantages include recoverability and better handling [2]. Significant work and progress have been made to develop various shell materials for the encapsulation process. Some examples of these shell materials used for encapsulation process are polymers [7], carbons [8,9], mesoporous silica (mSiO₂) [10,11], and metal oxides. Others include core-shell, yolk-shell, core-tube, or ship-in-a-bottle techniques [12]. In encapsulation framing, the

homogeneous catalyst is enclosed within the support channels to prevent percolation. This method is particularly applicable in a liquid-phase catalytic reaction [12]. Encapsulation stabilizes NPs within templating agents for them not to agglomerate, as unprotected nanoparticles are unstable and coagulate during catalytic transformation. This is as templating agents' function is in controlling the particles' activity and selectivity [13].

This review gives an insight into both the meaning and some concepts of encapsulation with nanoparticles as nano-catalysts. Their advantages over homogeneous and heterogeneous catalysts, alongside their applications in different fields, are also discussed. We reviewed essentially some of the different strategies employed for encapsulation of nanoparticles to achieve stabilization and prevent agglomeration. Also, some of the various methods of nanoparticles characterization will be mentioned as well.

1.1.2 Catalysts and catalysis

Catalysts are materials that speed up chemical reactions rate and enhance selectivity without getting consumed themselves [14]. Significant conversion and quantitative yield of many chemical processes are by a catalyst and through catalysis. This is supported by the involvement of nothing less than at least 85% of catalyst in industrial chemical processes, leading to the formation of synthetic materials and commodity production. A variety of products in medical sciences (medicines), fine chemicals (chemistry), polymers, fibers, fuels, paints, lubricants, among others, that the whole of humanity benefits from today would not have been possible without the existence of catalysts [15].

There are two types of catalysts, and they include:

Homogeneous catalysts are catalysts in the same phase or medium with the reactants and products. Homogeneous catalysts dissolve in solution in the course of the catalytic reaction. This homogeneous form of catalysts has been applied to catalytic reactions, such as catalytic hydrogenation reactions [16,17] and oxidation reactions [18]. Homogeneous catalyst industrialization is frequently restrained on the economic front due to their limitation of recovery and reusability. They are different from heterogeneous catalysts, which are linked to framework support during their synthetic procedure.

A heterogeneous catalyst means that catalysts are in a different phase from the reactants. The heterogeneous catalysts may exist as a solid or are immobilized on a solid inert matrix. The use of solid precursors as the support in the bid to provide complimentary options and benefits in catalyst separation and recovery [19–22]. Heterogeneous catalysts overcome the problems associated with homogeneous catalysts and improve the stability of the catalyst. Research geared towards heterogeneous catalyst development in catalysis has been receiving continuous attention by replacing homogeneous catalysts with heterogeneous catalysts. This development will enhance the catalytic system's sustainability, yielding a highly recyclable, scalable, and competent system [23]. Both homogeneous and heterogeneous catalysts have merits and demerits, while nanocatalysts combined the advantages of both catalytic systems as described in **Figure 1.1**. [24].

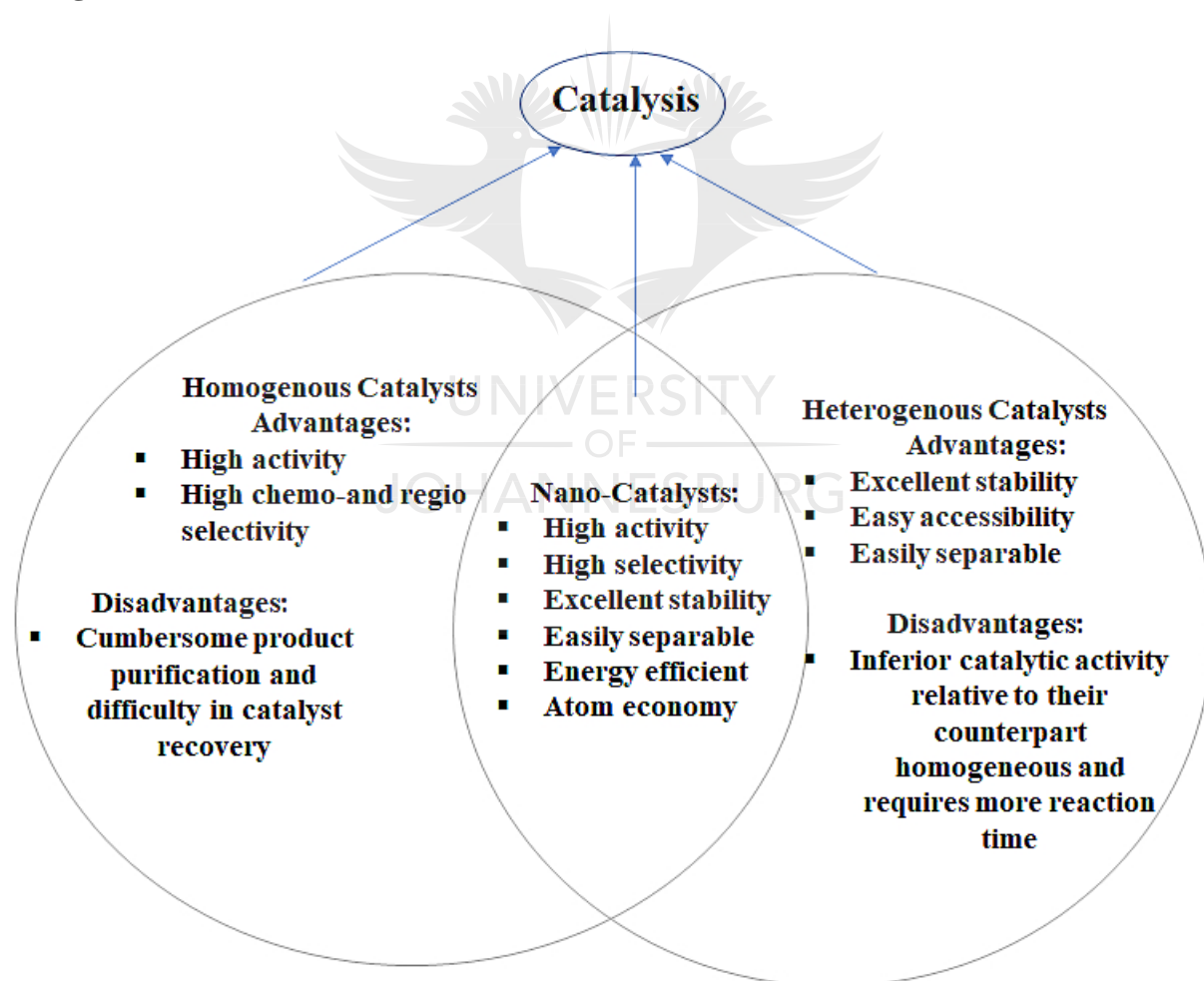


Figure 1.1: Combined advantages of homogeneous and heterogeneous catalyst possessed by nanocatalyst [24].

These advantages are made possible by allowing rapid, chemical transformations' selectivity with excellent product yield in addition to the ease at which the catalyst can be separated and recovered after use [25–27]. At a molecular level, homogeneous catalysts have the advantage of being soluble in the reaction medium and are well defined. However, the need to have the catalyst removed from the reaction mixture constitutes a significant challenge.

The chemical industries' most important goal has been the development of a stabilized and more expeditious catalysts. This development is because they make up a significant portion of catalysts used for many commercial catalytic processes. Catalysts are so crucial in many synthetic procedures [28] that their absence can stall multiple end-products or productions [24]. Catalysts helps enhance the reaction selectivity toward target products that are potentially devoid of any undesirable products and side effects, thus leading to green technology. However, as excellent in properties as these catalysts are, they are not without limitations of particle agglomeration and sintering either under high or low-temperature reactions, leading to loss of catalytic activities. This situation leads scientists to find processes that prevent such sintering and agglomeration during synthesis [29,30]. Hence encapsulation of noble metal particles becomes imperative [31].

1.2 Literature review

1.2.1 Nanoparticle and nanocomposites

There has been appreciation in using the prefix word "nano" in recent years, and this is because the development of nanoscience and nanotechnologies has created a whole new "nanoworld." This prefix term "nano" has its origin from both the greek word "Nanos" and the Latin word "Nanus," which means "dwarf," and it refers to things that are one-billionth in size [32]. These "nano" words have been severally used interchangeably. They include nanomaterials, nanoclusters, nanocrystals, nanostructures, nanocomposites, nanoscience, nanorods, nanotubes, nanowires, and nanotechnology. Scientific and technological research spotlighting nanoparticles have escalated over the last decades. These have been seen in all development stages, from synthesis to characterization, while performance and applications are not left out [33–35].

Nanoparticles (NP) are simply 1-100 nm sized particles with unique properties and applications. They possess a wide surface area per unit volume which are not found in their bulk form. Theoretically, it has been used interchangeably with other *nano* words like nanomaterials (less than micrometer-scale dimensional particles) and nanoclusters. Frequently, nanoparticles are regarded as nanoclusters or, in simple terms, “clusters,” meaning an aggregation of several multi-layered atoms [32]. Nanomaterials have varying forms, such as nanorods, nanofibers, and nanolayers [6].

On the other hand, a nanocomposite is a mixture of more than one material to produce a nano range dimensional new material with an average property of the constituting materials. This mixture thereby exhibits enhanced catalytic, thermal, adsorption properties, and stability. Nanotechnology is an interdisciplinary and cutting-edge science that applies knowledge and matter control of particles with dimensions of 1-100 nm [32,36]. Nanomaterials, when compared with their bulk counterpart possess unique physicochemical properties due to a quantum effect, thereby bringing an entirely new feature for better application of them [37,38]. These properties is an attribute that the size and shape of nanoparticle plays a significant role in all nanotechnology applications [39].

Nanoparticles can be classified into either magnetic or non-magnetic. This classification include metallic or transition metal NPs, depending on the constituted metal atom, which invariably determines their properties. Metallic NPs are either monometallic, bimetallic, trimetallic NPs, and so on. This is dependent on the number of metals fused into making the metallic NPs [32]. Magnetic NPs are magnetic elements which are influenceable under magnetic fields. Examples of magnetic NPs include the following magnetic elements; cobalt (Co), iron (Fe), nickel (Ni), and their respective oxides [40,41]. In addition, there are also metal oxide nanoparticles. They have high chemical activity and are interaction-specific while also possessing a large surface-to-volume ratio as other nanoparticles. These metal oxide NPs, in particular, the transition metal oxide NPs, possess magnetic, optical, electrical, and catalytic properties. Hence, making them potentially useful in many fields, and these properties are worthy of note scientifically and technologically [42,43].

Though there are monometallic and bimetallic metal NPs, bimetallic nanoparticles are of greater interest from both scientific and technological points of view. This is because interest drawn towards them is across a variety of fields like plasmonics [44,45], sensing [46,47], electrocatalysis [48,49], and notably in heterogeneous catalysis [50,51]. The preparation of bimetallic nanoparticles is generally through simultaneous reduction involving two metallic ions. This approach uses appropriate and efficient stabilization strategies like steric hindrance alongside static-electronic repulsive force [32]. Various bimetallic nanoparticles synthesized by researchers have been to get specific properties. The following includes a few of the bimetallic nanoparticles that have been synthesized;

- (i) Platinum (Pt) based bimetallic nanoparticles e.g: Pt-Cu, Pt-Au, Pt-Ag [52,53].
- (ii) Nickel (Ni) based bimetallic nanoparticles, e.g: Cu-Ni, Ni-Sn [54,55].
- (iii) Iron (Fe) based bimetallic nanoparticles, e.g: Fe-Cu, Pd-Fe [56].
- (iv) Palladium (Pd) based bimetallic nanoparticles e.g: Pd-Au, Pd-Ag [53,57].
- (v) Gold (Au) based bimetallic nanoparticles e.g: Au-Pd, Au-Ag [17,58].

1.2.2 Nanoparticles as nanocatalysts:

The use of metal nanoparticles as catalysts for diverse organic and inorganic reactions stems from the limitation transition-metal-based homogeneous catalysts are known to have. Although a homogeneous transition-metal-based catalyst is a well-defined, highly active, and selective catalyst [61], they are however limited in their usefulness. The limitation is in the difficulty and cost implication of separating these homogeneous catalysts from the reaction medium, thereby hindering their commercial application [59]. One advantage of catalytic processes involving MNPs over stoichiometric reagents that uses transition-metal-based homogeneous catalysts is that very little waste is generated [60]. This advantage of MNPs among others are highlighted in **Figure 1.2**. Furthermore, in addition to metal-based nanocatalysts, there also exist other forms of nanocatalyst which are core-shell, silica, mesoporous silica, and nanocarbon-based, and nano quantum or quantum dots [62]. They are however beyond the scope of this literature review.

The greatest threat or drawback to the nanoparticles' catalytic development is preparing nanomaterials known to be highly active, selective, stable, solid, and cheap [63]. The stabilization of metal nanoparticles can be pretty challenging. This challenge is due to their

high active surface atom/energy, making them thermodynamically unstable and deactivated. These factors cause irreversible aggregation while also reducing the surface energy of the entire system. These factors pose a severe challenge to the practical application and activity of metal nanoparticles [64,65]. Nanocatalyst has significantly influenced reaction rate though contact made in the homogeneous and heterogeneous system with reduced sintering, better reaction yield, and labourless catalyst separation [62].

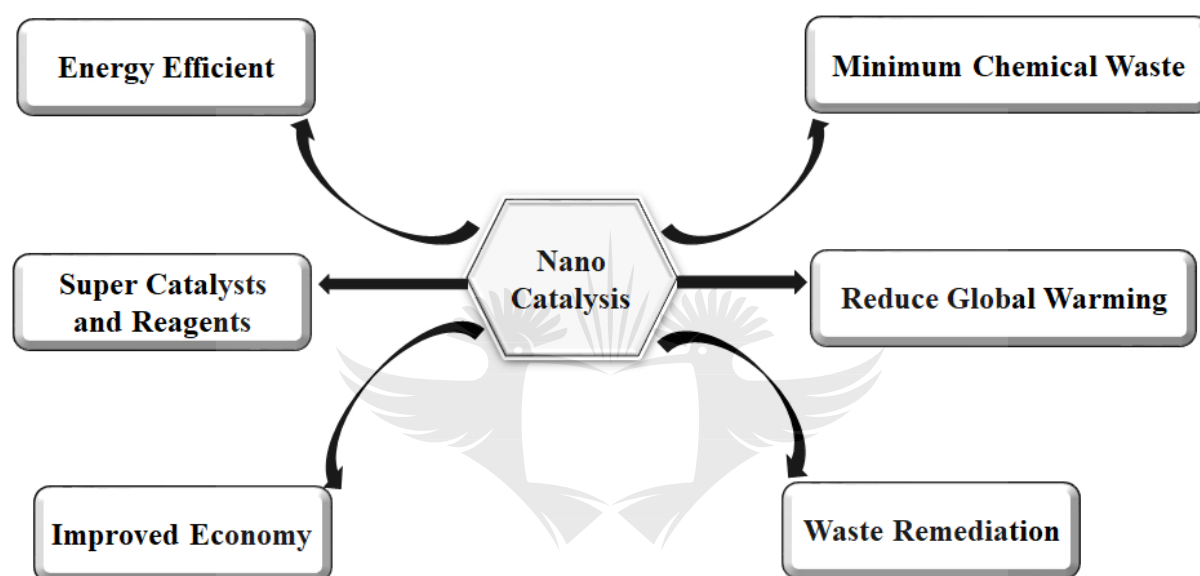


Figure 1.2: Advantages of nanocatalysis [24].

1.2.3 Nanoparticle's synthesis and limitation

Generally, encapsulation strategy is used in NPs synthesis to improve efficiency, enhance stability and compatibility of active ingredients, increase safety, ensure target delivery, and of course, to bring about a novel and enhanced performance [1]. Metallic and metal oxide nanoparticles synthesis can be carried out using different physicochemical means [62]. However, it is essential to note that these syntheses processes impact the morphological structure and size, stability, physical and chemical properties. Hence, it is imperative to put into consideration the choice of the synthetic method [66,67]. Synthesis of a nanoparticle can generally be through methods such as the following (i). Thermal and Photochemical decomposition, (ii). Electrochemical reduction, (iii). Chemical reduction, (iv). Sputtering method, (v). Sol-gel method, (vi), Chemical precipitation method, (vii). Micro-emulsion, (viii). Hydrothermal method, (ix) Templating method [68,69].

The fact that metal NPs have an immense surface area to volume ratio brings about a corresponding high surface energy with higher aggregation propensity. Hence, this leads to an accelerated diminishment of their catalytic action or properties in the course of catalytic reactions [70]. It, therefore, becomes imperative to use any possible approach to prevent such agglomeration [71]. Besides, nanoparticles' high surface energies and large surface areas have made them to be considered unstable thermodynamically. Therefore, the use of protecting capping agents for stabilizing them in a nano region during synthesis is imperative [72]. Metal nanoparticle stabilization can be through alloying, metal-support interface, or nanostructure support modification [73]. The stabilization of metal nanoparticles is challenging due to their highly active surface atoms, which causes their aggregation and deactivation [64].

1.3 Nanoparticle's encapsulation approach as an overcoming measure

Nanoparticles, which are essentially the building blocks for different nanotechnology applications, are the pillar of nearly all nanoscience and engineering aspects [74]. The most important industrial catalysts are nanoparticles, which are also known to have more comprehensive applications in manufacturing chemicals, energy conversion, and storage [24]. Properties such as the high surface area to volume ratio, in addition to the reduced melting point of metallic nanoparticles, size, and shape, are what essentially justify their use in catalytic applications [75]. NP's intrinsic attribute of agglomeration or sintering inevitably brings about their minimized surface energies, especially for high-temperature reactions. These lead to their well-reported missing stability, which is highly needed for their practical and industrial use as nanocatalysts [73].

In an encapsulation approach, catalysts are anchored and stabilized through different means, as shown in **Figure 1.3**. Dendrimers (polymers), graphene, carbon, polyvinylpyrrolidone (PVP), mesoporous zeolites, and silica nanospheres are a few examples of templating agents in use. These approaches aim to achieve the singular purpose of preventing agglomeration and bringing about the nanoparticle's stability. It is known that the most direct method of stabilizing MNPs is through encapsulation [73]. The different approaches of encapsulation are hence discussed;

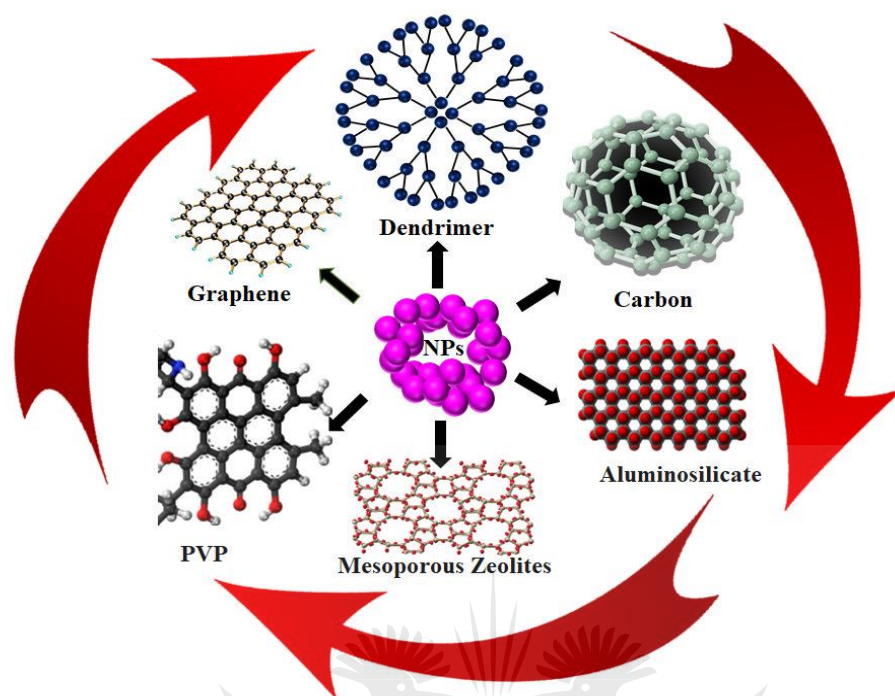


Figure 1.3: Schematic illustration of some encapsulation approaches.

1.3.1 Encapsulation using dendrimers

Dendrimers, otherwise known as discrete, well-defined polymers, are an essential templating agent for controlling nanoparticles' size, stability, and solubility. Encapsulation of nanoparticles using dendrimers, otherwise called Dendrimer Encapsulated Nanoparticles (DENs), became significantly crucial because of its ability to control nanoparticles of uniquely small sizes. This process projects the physicochemical attributes of the encapsulated nanoparticles whose solubility is tunable at the dendrimer's reactive template surface. The fact that dendrimers have a globular uniform composition and asymmetric structure as templating agents, makes the yield of well-defined NPs replica possible. Furthermore, this makes the prevention of agglomeration of encapsulated NPs using dendrimer to be conveniently achieved [76,77].

Dendrimers: uses and application in encapsulation:

Descriptively, dendrimers can be a repetitive spherical shape with a sterical microenvironment into which metal nanoparticles can be encapsulated. Dendrimers terminal group enables it to be used in various solvents while also controlling the substrate diffusion [78]. Dendrimers can also be described as a particular class of hyper-branched polymers emanating from a central core with repetitive branching units having a particular molecular structure and controllable size. Dendrimers have a distinct 3-dimensional composition with variable surface functionality making it suitable to synthesize well-defined nanoparticles. The synthesized DENs possess high stability and a narrow size distribution with active sites which are highly reactive [59]. Dendrimers have practical application in catalysis and this is because they possess distinct characteristics. These characteristics include persistent and controllable nanoscale dimension, a chemically reactive surface, and an exemplary configuration with all active sites exposed towards the reaction mixture. It is this characteristic nanoscale dimension that makes them accessible to reactants and most importantly recoverable by filtration after reaction [79,80].

Doubtless, to say, heterometallic nanocomposites rely on nanoparticle morphology, size, and distribution which can be altered in the event of supported nanoparticles. To get past this drawback, dendrimers (while with the advantage of combining homogeneous or heterogeneous catalysis) give room to synthesize well-defined metallic NPs [77]. Researchers' increased attention and interest in dendrimer use result from their physicochemical properties, structure, and accessibility [61,75,81]. Dendrimer's involvement in encapsulation is known to control the nanoparticle size and to prevent agglomeration. The merits of the use of dendrimer encapsulated metal nanoparticles (DENs) are related to several factors. Its use as micro dispersed templates allows for kinetic control of the particle size and prevents aggregation of the NPs without passivating active sites on the surface [75,82].

The use of dendrimers as templates for the synthesis of both monometallic and bimetallic nanoparticles is what has given birth to the following terms, namely:

- (a) Monometallic dendrimer encapsulated nanoparticles (MDENs)
- (b) Bimetallic dendrimer encapsulated nanoparticles (BDENs)

Monometallic DENs are nanoparticles formed only by adding a specific metal salt to the dendrimer and reducing with sodium borohydride to form NPs. Many studies have been carried

out using this method and are catalytically active for many hydrogenation reactions [83]. While MDENs are composed of one type of metal element, bimetallic DENs are important NPs composed of two different metal salts. They have been known to demonstrate significant performance in many systems when used as catalysts compared to the monometallic DENs. The unique characteristics that make bimetallic DENs different from monometallic DENs include the additional degrees of frequency, composition, and flexible structure leading to their enhanced catalytic behavior [84].

More attention has been drawn to bimetallic nanoparticles in recent times owing to the advantages of combining more than one metal in the same heterocomposite (nanocomposite) structure. This feature has gained widespread application in different fields, including biomedical, electronic, and, significantly, catalysis. Bimetallic nanoparticles are of greater importance and relevance than monometallic NPs in catalysis. This is because bimetalization will improve catalytic activity while creating a new property, which monometallic catalysts may not achieve. Bimetallic particles of tiny particle sizes are the primary option in heterogeneous catalysis due to their geometrically and electronically synergistic effects. This effect is not without considerable physical and chemical behavior, making the bimetallic nanoparticles different from the mere two metal constituents [79,80,85].

Synthesis of monometallic and bimetallic DENs

Catalytic metal NPs are usually synthesized using two approaches: (a) The Top-Down Approach (b) The Bottom-Up approach, as shown in **Figure 1.4**.

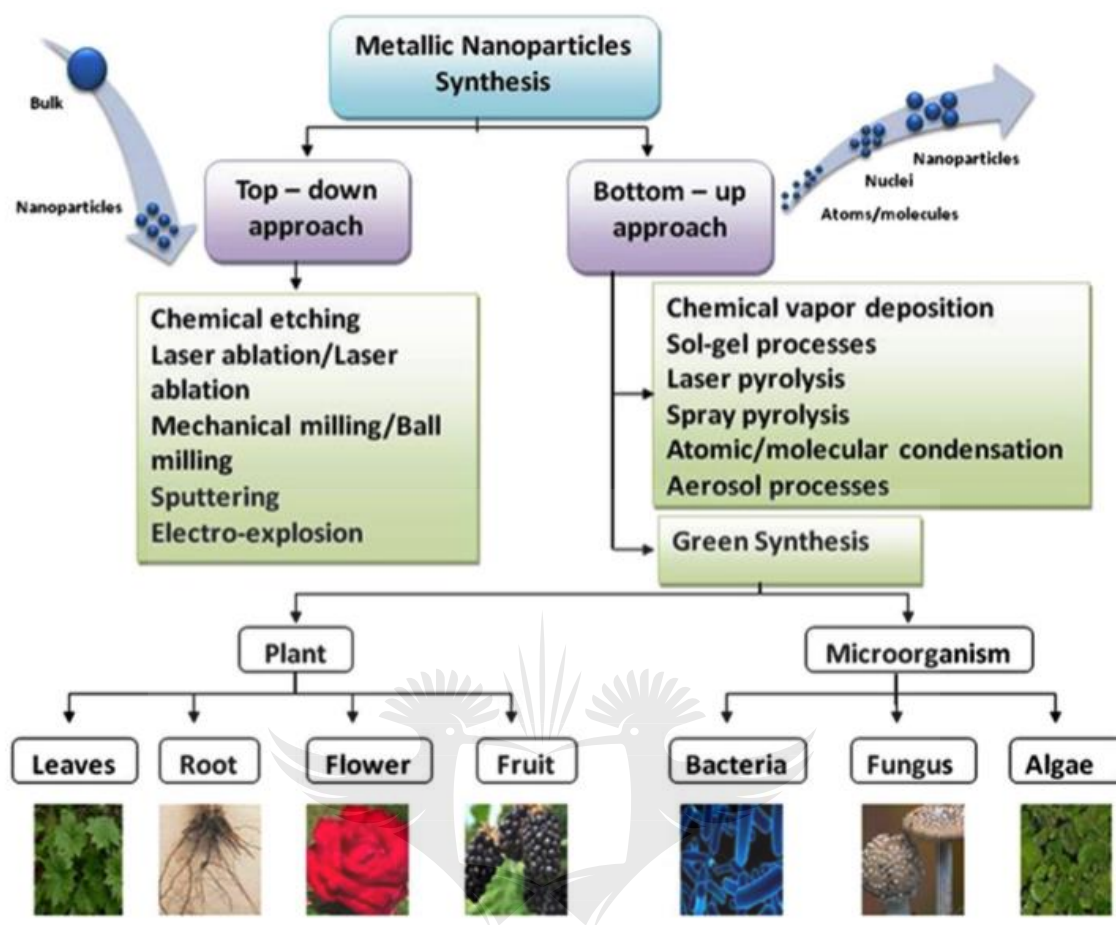


Figure 1.4: NP's synthesis approaches [86].

The top-down approach entails the formation of metal NPs by mechanical breakdown. The bottom-up approach involves synthesizing metal NPs starting with the metal complex precursor reduced using a reducing agent and subsequently stabilized by various chemical stabilizers. The standard approach for the synthesis of NPs is the bottom-up approach, as it gives better control of particle size compared to the top-down approach [32,72].

Bimetallic dendrimers encapsulated NPs (BDENs) are synthesized in either of the following as presented in **Figure 1.5a – 1.5c** [87].

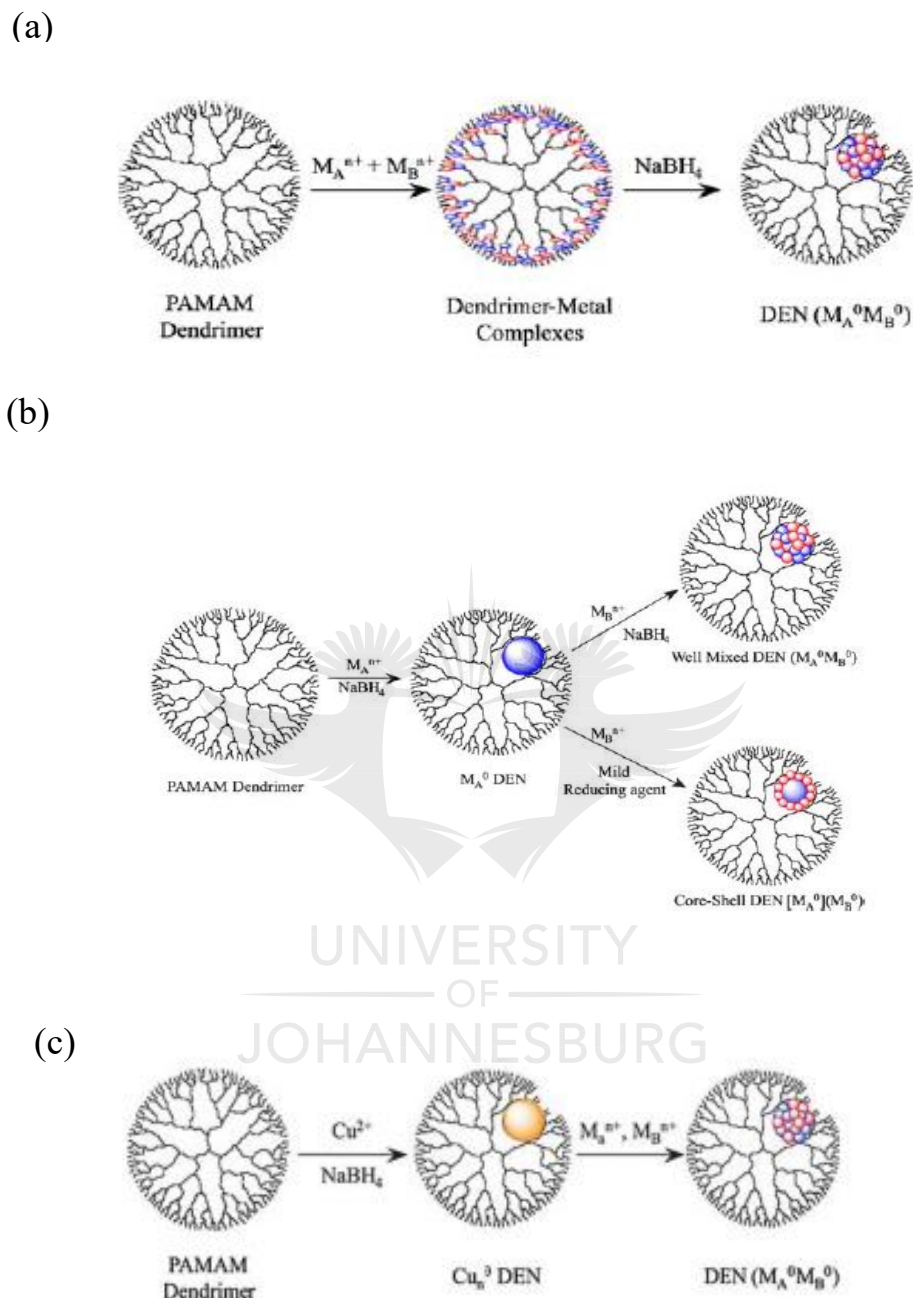


Figure 1.5: Synthesis of bimetallic DENs catalysts via (a) Co-complexation, (b) Sequential loading (or reduction), and (c) Partial displacement (or galvanic displacement) [87].

1.3.2 Encapsulation using graphene

The use of graphene nanoshell is an emerging encapsulation (of Au in particular) method. It has shown significant possibility as providing carbon chemistry and potential surface functionalities for its use in many catalysis systems, chemical sensors, and bio-compatible

devices. Graphene's extraordinary electronic, thermal, and mechanical properties made it of significant interest in material science and hence in the encapsulation of NPs [88]. Graphene, which is composed of thick sheets, comprises sp^2 bonded carbon atoms organized in a distinctly two-dimensional (2D) honeycomb structure. This structure thereby makes them possess distinct structural, optical, and electronic characteristics [89]. In graphene encapsulated nanoparticles, the nanoparticles' surface is draped or glassed with graphene, preventing sintering or agglomeration during chemical reactions.

1.3.3 Encapsulation using carbon

It has been established that undraped metal NPs are quickly oxidized and agglomerate, a condition that readily restricts their potential usefulness. Another form of encapsulation is composite carbon material, which has a core-and-shell composition of a nanoscale dimension. Carbon is an ideal inert material that can encapsulate MNPs, thereby preventing oxidation in the air [90], dissolution in acid, and effortless agglomeration [91]. The outer carbon shell protects the metallic core (nanoparticle) from oxidization and agglomeration in the real sense. This feature thereby makes Carbon Encapsulated Metal Nanoparticles (CEMNs) have present and prospective usefulness not only in catalysis but in magnetic data storage and resonance imaging. The application of CEMNs extends to the biomedical arena and in optical limiting devices [92,93].

1.3.4 Encapsulation using polyvinylpyrrolidone (PVP)

Polyvinylpyrrolidone is a non-toxic, non-ionic polymer widely used in the synthesis of NPs. PVP has been found to function as a surface stabilizer, growth moderator, preventer of nanoparticle clumping, and reducing agent. These characteristics, however, depend mainly on the particular synthetic conditions and material systems. It is used to fabricate well-dispersed metal NPs of relatively small nano range and size controlling agent [94]. In addition, PVP prevents metallic nanoparticles agglomeration using the repulsive forces arising from its hydrophobic carbon chains [95,96]. PVP has been well used as NPs anti-agglomerate and as an agent to obtain narrowly distributed NPs [96–101].

1.3.5 Encapsulation using mesoporous zeolites

Zeolites are example of an encapsulating agent which possesses a well-structured 3D framework which are made of synthesizable crystalline inorganic material. These make them possess even cavities with broad architectures and composition [102–104]. Several reasons may be attributed as to why encapsulating metal nanoparticles using zeolites is feasible. They include the zeolite framework's ability to control the nanoparticle size, resulting in a high metal dispersion. This ability invariably protects them against agglomeration caused by migration and coalescence [16,30,105]. The zeolite encapsulated metal nanoparticles have advantages conferred on them due to the distinctive metal support interface close to the framework's active sites [106]. Encapsulating NPs using zeolites provide an additional advantage to the NPs aside from circumventing sintering under harsh condition. They also protect NPs from the unfriendly environment in catalytic reactions [103]. However, it is worthy of note that encapsulation of metal nanoparticles in zeolites is still not fully established despite the tremendous technological, environmental, and economic interest involved [16].

1.3.6 Encapsulation in silica nanosphere/aluminosilicates

One approach of nanoparticle preparation and encapsulation that is also feasible involves using mesoporous silica nanospheres (MSNs). This method is made possible because of their distinctive properties like controllable particle and pore sizes, robust morphology, large surface area, ease of surface modification, and low toxicity [107–109]. This encapsulation method also protect NPs from making contact with impurities and simultaneously making the silica nanosphere inert [110]. Zeolites are crystalline microporous aluminosilicate networks primarily made up of TO_4 tetrahedra as fundamental building blocks with the T in TO_4 either made up of aluminium or silica [104,111]. Zeolite materials have also been considered an emerging encapsulation strategy to protect nanoparticle agglomeration and poisoning by confining active metal particles in protective shell space or matrix [112]. Zeolite materials possess properties like multi-porosities, manageable synthesis processes, and large surface areas, making them ideal for nanoparticle encapsulation [104].

There are other means of encapsulation that are not explained above, but they include encapsulation of metal nanoparticles within porous liquids [113], encapsulation of nanoparticles by colloidal dimers [114], and microencapsulation using microfluidics [115].

1.4 Characterization approach

Characterization of nanoscale materials like metallic nanoparticles becomes an extensively studied aspect of nanocatalysis. The reason for this is due to nanoparticles' mechanical, optical, electronic, and chemical properties which make them different from their bulk counterparts due to their increased activity occasioned by high surface-to-volume ratio [116]. Various instrumental techniques have been used in the characterization of NPs. This characterization is with different approaches to accomplish the following: finding out their actual magnitude, configuration, surface structurality, valency, chemical constituent, electron bandgap, binding arena, emission of light, and adsorption, scattering, and diffraction properties. To fully characterize NPs, the following technique, among others, have been used, and they include;

Ultra-violet and Visible Spectroscopy (UV-Vis)

Transmission Electron Microscopy (TEM)

Scanning Tunneling Microscopy (STM)

Scanning Electron Microscopy (SEM)

Temperature programmed reduction (TPR)

Infrared spectroscopy (IR)

Energy Dispersive X-ray Spectrometer (EDS)

X-ray Diffraction (XRD)

X-ray Photoelectron Spectroscopy (XPS)

Brunauer-Emmett-Teller (BET)

Nanoparticles' characterization related to their size and shape is usually obtained through the means of Transmission Electron Microscopy (TEM) and High-Resolution Transmission Electron Microscopy (HTEM). In addition to characterizing the size and shape of NPs, HTEM is also found to provide veritable information related to the crystal structure and chemical composition of single NPs when in association with Electron Diffraction Analysis and Energy Dispersive X-ray Spectroscopy (EDS), respectively. In another perspective, Scanning Electron Microscopy (SEM) is employed to examine large micrometer-scale assemblies of nanoparticles, but TEM (with superior resolution) is used to analyze individual nanoparticles and smaller assemblies. Moreover, HTEM, X-Ray Diffraction (XRD) can also be used to determine the crystal structure of nanomaterials and NP size. Other methods employed for surface characterization of bulk materials include X-Ray Photoelectron Spectroscopy (XPS)

and Rutherford Back-scattering Spectroscopy (RBS) as they provide helpful information about the whole NP in terms of its elemental composition but with a limitation of not being able to distinguish between surface and interior atoms [117–120].

1.5 Encapsulated nanoparticle: advantages, uses, and application

Nanoparticles research has made a significant leap into materials manufacturing, nanoelectronics, healthcare, medicine, energy, biotechnology, and safety [133] and pharmaceuticals, electronics, magnetics, optoelectronics, energy, catalytic and environmental detection and monitoring [121]. These applications of NPs are unarguably on the increase in many fields like molecular biology, organic and inorganic chemistry, physics, material science, and medicine. These applications are as contemporary researchers have been paying close attention to metal nanoparticle synthesis owing to the unique properties that made them very useful in catalysis, preparation of composite-like polymer, diagnosis and treatment of diseases, sensor technology, and optoelectronic recorded media [122–124]. Nanoparticles are also anticipated to have broad application in biomedical, radiotherapy, controlled drug delivery systems, HIV vaccine, photo-and-radio-therapy sensitizers [121,125]. Nanoparticles have a unique and distinct surface area to volume ratio which are 35-40% times high when put in comparison with large particle atom which in turn give them size-dependent surface reactivity and thus making them have multifunctional attributes with increased use and applications in diverse fields like energy, medicine, and nutrition [3].

1.6 Encapsulation in reduction reactions

Reduction reactions are usually carried out either as a model reaction or as a transformational process whereby environmentally or toxic industrial materials are transformed into more minor toxic derivatives. Encapsulated metal nanoparticles have been reportedly used for various reduction reactions to form derivatives or intermediates with practical applications in diverse fields. Hence, it can suffice to say that the encapsulation process is essential in chemical reduction reactions. Several toxic organic or inorganic compounds have been catalytically reduced using the encapsulation process to prevent the sintering of the metal nanoparticles used as a catalyst.

1.6.1 Reduction of nitroaromatics

Nitroaromatic organic compounds are aromatics and aliphatic nitro compounds such as 4-nitrophenol (4-nitrophenol), 4-chloronitrobenzene (4-CNB), and 4-nitroaniline (4-NA). They are toxic materials of industrial origin [126,127]. However, nitroaromatic compounds are comparatively infrequent but usually find their way into the environment through diverse human activities, thereby becoming environmentally unfriendly [128]. Nitroaromatics are very dangerous to human health, with their being carcinogenic and mutagenic having been reported. Hence, the United States Environmental Protection Agency has designated nitroaromatics (especially 4-nitrophenols) as a primary contaminant [129,130]. The chemical transformation involving encapsulated metal nanoparticles for catalytic reduction of these nitro compounds has quality significance in organic synthesis, producing intermediates that are of industrial relevance. The intermediate formed from the catalytic reduction of these nitro compounds are employed to prepare dyes, antioxidants, pharmaceuticals, and agrochemicals [126,128,131,132]. Owing to the importance of these intermediate products from reducing nitroaromatics, it is not surprising that a variety of encapsulated metal nanoparticle enhanced catalytic reduction reactions has been carried out in nitroaromatics. These reactions are to ensure a more efficient, cheaper, and faster production of these intermediates. Some of the examples of reported metal nanoparticle enhanced catalytic reduction reactions are; 4-nitrobenzene [127], 4-nitrophenol, methyl orange [133], and methylene blue reduction [134].

1.6.2 Reduction of azo dyes

Azo dyes constitute a significant and most recognized dye in wastewater pollution with a complex structure, toxic, various metabolic intermediates, and non-degradable [135,136]. Examples of azo dyes include orange II acid dye, methyl orange, alizarin yellow, among others. These azo dyes also find their way into the environment as effluent in fabrics, paper, latex, medicines, plastics, leather, cosmetics, and the food manufacturing sector [137]. Azo dyes' effect as environmental pollutant has mutagenic effect in humans. This mutagenic effect of azo dyes is as a result of their bioaccumulation and resistance to sunlight and oxygen due to their complex nitrogen-nitrogen double bond (N=N) [138]. Azo dyes possess a high chemical, microbial, and photolytic stability due to their sulphonate group and azo bonds, thus making them recalcitrant to biological and photolytic degradation [139,140]. Catalytic reduction of azo dyes through metal nanoparticles that have been effectively encapsulated is considered the best

approach to degrade them as they overcome the drawbacks and challenges associated with the biological and photocatalysis method [133,134,137,138].

1.7 Mesoporous metal oxides in catalysis

Mesoporous metal oxides are materials having ordered and tunable pore sizes with easy functionalization. They are of great interest due to their unique redox, electronic and magnetic properties [141]. Mesoporous metal oxides possess high surface area and excellent thermal/chemical stability, making them have multiple potential applications in industrial use and catalysis [142]. The synthetic methods for the fabrication of mesoporous metal oxides include; hard templating, soft templating, colloidal templating, and superlattice approaches [141–143]. However, the templating approach will be our focus.

The hard templating method, otherwise called nanocasting, is one of the accessible methods for synthesizing mesoporous materials, which employs rigid molds having a well-defined porous structure that can readily accommodate the precursor. The initial molds can therefore be removed following the fabrication of the material. The synthetic strategy involves three steps which include; (i) the fabrication of the mold (e.g., aluminates, carbons, and silica), (ii) filling of the mold with the precursors and thermal decomposition for good crystallinity of the material, and finally, (iii) is the hard template removal through calcination for pores formation.

On the other hand, the soft templating approach is a valuable method of synthesizing a well-ordered material through the self-assembly of surfactant molecules [144]. It makes use of unrigid nanostructures formed as a templating agent through intermolecular interaction. Mesostructures have well-ordered and defined pore structures and sizes formed through interaction after adding the inorganic species into the inner or surface part of the soft templating agent.

Significant activity has been demonstrated by mesoporous metal oxides in catalysis [142,145]. This excellent performance can be ascribed to metal oxide's tendency to harbor and generate oxygen for related oxidation and reduction reactions. Some examples include mesoporous cerium oxide/cobalt oxide for complete oxidation of methane [146], mesoporous Mn metal oxide, and cobalt oxide for effective reduction of hexacyanoferrate [147].

1.8 Catalytic transformation: from batch to continuous flow state

The catalytic transformation from batch to continuous flow state evades the necessity of catalyst separation from the reaction [23]. Continuous flow reactions provide considerably more advantages of reaction mixing, thermal control, scalability, efficient energy, waste generation, safety, and platform to all-encompassing reaction conditions and unique possibilities in heterogeneous catalysis, multi-dimensional synthesis, among others [23,148,149]. Batch (multi-step) reactions such as distillation, crystallization, filtration, pH control, evaporation, among others, are usually laborious and time-consuming. This reaction type inadvertently leads to the challenge of waste, excessive solvent usage, and inadequate energy management [149]. On the other hand, flow chemistry comes in handy in heterogeneous catalysis and mainly in bulk and chemical synthesis. In addition to the benefits mentioned above, the continuous flow reaction system provides a veritable tool for determining kinetic parameters like the catalytic reactions' activation energy [23].

1.9 Aims and objectives of the thesis

This research aims to fabricate a range of metal NPs in homogeneous form and then in heterogeneous form using a more noble and active metal through a single route via galvanic replacement beginning from the homogeneous phase. This is owing to the combined advantages of homogeneous catalysts that are possessed by heterogeneous catalysts. Also, another range of mesoporous and non-mesoporous materials, including manganese, cobalt, and palladium, will be fabricated using the developed synthetic protocol of inverse micelles, sol-gel, and wet impregnation methods.

The ranges of catalysts will be evaluated regarding the chemical transformation of toxic compounds to less toxic derivatives or chemical intermediates for industrial use, thus promoting the greener aspect of chemistry. The catalytic investigation will be obtained regarding the reaction rate through temperature variation, catalysts dosage amount, substrate variation, and oxidant/reductant variation.

The following are the objectives considered;

1. Synthesis and characterization of monometallic and bimetallic PVP NPs;

2. Synthesis and characterization of dendrimer encapsulated CuNPs;
3. Synthesis and characterization of Silica supported porous Cu@SiO₂;
4. Synthesis and characterization of Au@SiO₂ from Cu@SiO₂ through a galvanic replacement route and its characterization;
5. Synthesis and characterization of MnMMO, COMMO, and silica-supported Pd@SiO₂;
6. Catalytic evaluation of these synthesized catalysts in various oxidation, reduction, and hydrogenation reactions.

1.10 Outline of the thesis

Chapter 1 entails introduction to the basic concept and background to the research carried out in this thesis, the synthetic and characterization approach employed, some catalytic reactions to further explain the overall thesis scope, the descriptions about the research terminologies, in a review format, and the chapter concludes with the study's aims and objectives.

Chapter 2 contains the synthesis of homogeneous monometallic Au, Pd, and bimetallic AuPd-PVP NPs and their characterization. The catalysts' activity was evaluated in redox degradation of orange II acid by monitoring the decrease in absorbance at λ 480 nm. Comparison of their activities was modeled after the Langmuir-Hinshelwood mechanism and was found conformed to the model.

Chapter 3 addressed the synthesis of a homogeneous catalyst, its transition from this phase to the heterogeneous phase through a dual templating approach, and subsequent fabrication of more noble metal heterogeneous NPs through a galvanic displacement method. The benefit of this single-route synthetic procedure was reported. The catalytic activity of the heterogeneous catalysts was initially demonstrated in model reactions before the oxidative investigation of styrene. The activity of the galvanic synthesized catalyst was still maintained after three cycles of reaction. The chapter has been published as; **Oluwatayo Racheal Onisuru**, Charles O. Oseghale, and Reinout Meijboom, *New J. Chem.*, 2020, 44, 20322.

Chapter 4, in this chapter, the descriptive fabrication of Pd@SiO₂ catalyst, the characterization techniques performed, and its activity in chemoselective hydrogenation of ketone were

documented. The hydrogenation carried out in HPMC demonstrated the activeness of the silica-supported Pd catalyst as a highly effective and efficient catalyst.

Chapter 5, this chapter presents the synthesis and characterization of Mn and Co mesoporous metal oxides. Their catalytic evaluation was investigated in the degradation of hexacyanoferrate Ion through electron transfer induction under a continuous flow procedure. It focuses on the benefits connected to catalysis carried out using this recent flow procedure. The chapter has been published as **Oluwatayo Racheal Onisuru, Oyekunle Azeez Alimi, Kariska Potgieter, and Reinout Meijboom**, *Journal of Materials Engineering and Performance*, 2021, 30, 4891-4901.

Chapter 6 summarizes the results contained in chapter II to chapter V and the recommendations.

Appendix: Supplementary information	155
Chapter 2.....	155
Chapter 3.....	159
Chapter 4.....	161
Chapter 5.....	176
References	184

1.11 References

- [1] B. Andrade, Z. Song, J. Li, S.C. Zimmerman, J. Cheng, S. Moore, K. Harris, and J.S. Katz, New Frontiers for Encapsulation in the Chemical Industry, ACS Appl. Mater. Interfaces. 2015, 7 (12) 6359–6368.
- [2] Z. Zhang, S. Wang, Catalysts Encapsulated in Nanostructured Carbon Systems, In Encapsulated catalysts. Academic Press, (2017) 71-122.
- [3] P. Govindrao, N.W. Ghule, A. Haque, M.G. Kalaskar, Journal of Drug Delivery Science and Technology Metal nanoparticles synthesis : An overview on methods of preparation, advantages, and disadvantages, and applications, J. Drug Deliv. Sci. Technol. 2019, 53, 101174.
- [4] Y. Lei, J. Lu, X. Luo, T. Wu, P. Du, X. Zhang, Y. Ren, J. Wen, D.J. Miller, J.T. Miller, Y.-K. Sun, J.W. Elam, K. Amine, Synthesis of Porous Carbon Supported Palladium Nanoparticle Catalysts by Atomic Layer Deposition: Application for Rechargeable Lithium–O₂ Battery, Nano Lett. 2013, 13 (9) 4182–4189.
- [5] I. De Leersnyder, L. De Gelder, I. Van Driessche, P. Vermeir, Revealing the importance of aging, environment, size and stabilization mechanisms on the stability of metal nanoparticles: A case study for silver nanoparticles in a minimally defined and complex undefined bacterial growth medium, Nanomaterials. 9(12), 1684.
- [6] M. Hecold, R. Buczkowska, A. Mucha, J. Grzesiak, O. Rac-Rumijowska, H. Teterycz, K. Marycz, The Effect of PEI and PVP-Stabilized Gold Nanoparticles on Equine Platelets Activation: Potential Application in Equine Regenerative Medicine, J. Nanomater. 2017, 4–8.
- [7] Z. Zhai, Q. Wu, J. Li, B. Zhou, J. Shen, Z.H. Farooqi, W. Wu, Enhanced catalysis of gold nanoparticles in microgels upon on site altering the gold – polymer interface interaction, J. Catal. 369 (2019) 462–468.
- [8] P. Zhang, C. Shao, X. Li, M. Zhang, X. Zhang, Y. Sun, Y. Liu, *In-situ* assembly of well-dispersed Au nanoparticles on TiO₂ / ZnO nanofibers : A three-way synergistic heterostructure with enhanced photocatalytic activity, J. Hazard. Mater. 237–238 (2012) 331–338.
- [9] G. Lai, H. Zhang, A. Yu, H. Ju, Biosensors and Bioelectronics *In-situ* deposition of Prussian blue on mesoporous carbon nanosphere for sensitive electrochemical immunoassay, Biosens. Bioelectron. 74 (2015) 660–665.

- [10] J. Martins, N. Batail, S. Silva, A. Chaumonnot, D. Uzio, T.S. Nguyen, L. Piccolo, *Applied Catalysis A : General*, "Applied Catal. A, Gen. (2014) 1–5.
- [11] K. Nam, J. Wolfenstine, H. Choi, R. Garcia-mendez, J. Sakamoto, Study on the mechanical properties of porous tin oxide, 43 (2017) 10913–10918.
- [12] S.K. Sharma, R. V. Jasra, *Encapsulated Catalysts for Synthesis of Bulk and Fine Chemicals*, Encapsulated Catalysts., 2017, 477-504.
- [13] M. Hasanzadeh, N. Shadjou, M. Eskandani, J. Soleymani, F. Jafari, Trends in Analytical Chemistry Dendrimer-encapsulated and cored metal nanoparticles for electrochemical nanobiosensing, *Trends Anal. Chem.* 53 (2014) 137–149.
- [14] A. Chaudhary, A. Singh, *Nano Catalysts : A New fangled Gem in the Catalytic World*, Recent Advances in Petrochemical Science, 3 (2017) 3–6.
- [15] Y. Niu, R.M. Crooks, Dendrimer-encapsulated metal nanoparticles and their applications to catalysis, *Comptes Rendus Chim.* 6 (2003) 1049–1059.
- [16] K.H. Rasmussen, F. Goodarzi, D.B. Chistensen, J. Mielby, S. Kegnæs, Stabilization of Metal Nanoparticle Catalysts via Encapsulation in Mesoporous Zeolites by Steam-Assisted Recrystallization, *ACS Appl. Nano Mater.* 2 (2019) 8083–8091.
- [17] P. Venkatesan, J. Santhanalakshmi, Core-Shell Bimetallic Au-Pd Nanoparticles: Synthesis, Structure, Optical and Catalytic Properties, *Nanosci. Nanotechnol.* 1 (2012) 43–47.
- [18] S. Jagtap, Heck reaction—State of the art, *Catalysts.* 7 (2017) 267.
- [19] L.M. Bronstein, Z.B. Shifrina, Nanoparticles in Dendrimers : From Synthesis to Application, *Nanotechnologies in Russia*, 4 (2009) 576–608.
- [20] X. Peng, Q. Pan, G.L. Rempel, Bimetallic dendrimer-encapsulated nanoparticles as catalysts: a review of the research advances, *Chem. Soc. Rev.* 37 (2008) 1619.
- [21] W. Soutter, *Nanocatalysis : New Dimensions in Catalysis*, *Azo Nano*, 3079 (2012) 1–5.
- [22] B. Ding, H. Wang, S. Tao, Y. Wang, J. Qiu, RSC Advances Preparing electrochemical active hierarchically porous carbons for detecting nitrite in drinkable, *RSC Advance* 6 (2016) 7302–7309.
- [23] E. Gross, F. Dean Toste, G.A. Somorjai, Polymer-Encapsulated Metallic Nanoparticles as a Bridge Between Homogeneous and Heterogeneous Catalysis, *Catal. Letters.* 145 (2015) 126–138.

- [24] S.B. Singh, P.K. Tandon, Catalysis : A Brief Review on Nano-Catalyst, *J. Energy Chem. Eng.* 2 (2014) 106–115.
- [25] S.G.B.R. Karvembu, Copper Based Nanoparticles-Catalyzed Organic Transformations, *Catalysis Surveys from Asia*, 17 (2013) 156–176.
- [26] K. Yan, G. Wu, T. La, C. Jarvis, Production, properties and catalytic hydrogenation of furfural to fuel additives and value-added chemicals, *Renewable and sustainable energy reviews*, 38 (2014) 663–676.
- [27] S. Feo, O.D. Membrane, H. Luo, H. Jiang, T. Klande, Z. Cao, F. Liang, H. Wang, J. Caro, Novel Cobalt-Free, Noble Metal-Free Oxygen-Permeable, *Chemistry of Materials*, 24 (2012) 2148-2154.
- [28] M.E. Ali, M.M. Rahman, S.M. Sarkar, S.B.A. Hamid, Heterogeneous metal catalysts for oxidation reactions, *J. Nanomater.* 2014 (2014) 209.
- [29] L.H. Gong, Y.Y. Cai, X.H. Li, Y.N. Zhang, J. Su, J.S. Chen, Room-temperature transfer hydrogenation and fast separation of unsaturated compounds over heterogeneous catalysts in an aqueous solution of formic acid, *Green Chem.* 16 (2014) 3746–3751.
- [30] T.L. Cui, W.Y. Ke, W.B. Zhang, H.H. Wang, X.H. Li, J.S. Chen, Encapsulating Palladium Nanoparticles Inside Mesoporous MFI Zeolite Nanocrystals for Shape-Selective Catalysis, *Angew. Chemie - Int. Ed.* 55 (2016) 9178–9182.
- [31] J. Wang, A.H. Lu, M. Li, W. Zhang, Y.S. Chen, D.X. Tian, W.C. Li, Thin porous alumina sheets as supports for stabilizing gold nanoparticles, *ACS Nano.* 7 (2013) 4902–4910.
- [32] G. Sharma, A. Kumar, S. Sharma, M. Naushad, R. Prakash, Z.A. Allothman, G. Tessema, *Journal of King Saud University – Science* Novel development of nanoparticles to bimetallic nanoparticles and their composites : A review, *J. King Saud Univ. - Sci.* 31 (2019) 257–269.
- [33] L.C. Varanda, C.G.S. Souza, D.A. Moraes, H.R. Neves, J.B. Souza Junior, M.F. Silva, R.A. Bini, R.F. Albers, T.L. Silva, W. Beck, Size and shape-controlled nanomaterials based on modified polyol and thermal decomposition approaches. A brief review, *Anais da Academia Brasileira de Ciências*, 91 (2019).
- [34] M.A. Boles, M. Engel, D. V. Talapin, Self-assembly of colloidal nanocrystals: From intricate structures to functional materials, *Chem. Rev.* 116 (2016) 11220–11289.
- [35] M. V Kovalenko, L. Manna, A. Cabot, Z. Hens, D. V Talapin, C.R. Kagan, X.V.I.

- Klimov, A.L. Rogach, P. Reiss, D.J. Milliron, P. Guyot-sionnest, G. Konstantatos, W.J. Parak, T. Hyeon, B.A. Korgel, C.B. Murray, W. Heiss, Prospects of Nanoscience with, nanocrystals, *ACS nano*. 9 (2015) 1012–1057.
- [36] E. Palou, Metallic Nanoparticles: Development, Applications, and Future Trends for Alcoholic and Nonalcoholic Beverages, In *Nanoengineering in the Beverage Industry*, (2020) 263-300.
- [37] J. Li, T. Shi, C. Feng, Q. Liang, X. Yu, J. Fan, S. Cheng, G. Liao, Z. Tang, The novel Cu nanoaggregates formed by 5 nm Cu nanoparticles with high sintering performance at low temperature, *Mater. Lett.* 216 (2018) 20–23.
- [38] J. Li, Q. Liang, T. Shi, J. Fan, B. Gong, C. Feng, J. Fan, G. Liao, Z. Tang, Design of Cu nanoaggregates composed of ultra-small Cu nanoparticles for Cu-Cu thermocompression bonding, *J. Alloys Compd.* 772 (2019) 793–800.
- [39] P. Slepíčka, N. Slepíčková Kasálková, J. Siegel, Z. Kolská, V. Švorčík, Methods of Gold and Silver Nanoparticles Preparation, *Materials (Basel)*. 13 (2019) 1.
- [40] S. Shylesh, V. Schünemann, W.R. Thiel, Magnetically separable nanocatalysts: Bridges between homogeneous and heterogeneous catalysis, *Angew. Chemie - Int. Ed.* 49 (2010) 3428–3459.
- [41] N. Sharma, H. Ojha, A. Bharadwaj, D.P. Pathak, R.K. Sharma, Preparation and catalytic applications of nanomaterials: a review, *RSC Adv.* 5 (2015) 53381–53403.
- [42] A. Akbari, M. Amini, A. Tarassoli, B. Eftekhari-Sis, N. Ghasemian, E. Jabbari, Transition metal oxide nanoparticles as efficient catalysts in oxidation reactions, *Nano-Structures and Nano-Objects*. 14 (2018) 19–48.
- [43] J.A. Vara, P.N. Dave, Metal oxide nanoparticles as catalyst for thermal behavior of AN based composite solid propellant, *Chem. Phys. Lett.* 730 (2019) 600–607.
- [44] C.Y. Chiu, M.Y. Yang, F.C. Lin, J.S. Huang, M.H. Huang, Facile synthesis of Au-Pd core-shell nanocrystals with systematic shape evolution and tunable size for plasmonic property examination, *Nanoscale*. 6 (2014) 7656–7665.
- [45] Y. Tsao, S. Rej, C. Chiu, M.H. Huang, Aqueous Phase Synthesis of Au–Ag Core–Shell Nanocrystals with tunable shapes and their optical and catalytic properties, *Journal of the American Chemical Society*, 136 (2013) 396-404.
- [46] M. Janyasupab, C.W. Liu, Y. Zhang, K.W. Wang, C.C. Liu, Bimetallic Pt-M (M = Cu, Ni, Pd, and Rh) nanoporous for H₂O₂ based amperometric biosensors, *Sensors and*

- Actuators, B: Chem. 179 (2013) 209–214.
- [47] C. Chen, Q. Xie, D. Yang, H. Xiao, Y. Fu, Y. Tan, S. Yao, Recent advances in electrochemical glucose biosensors: A review, RSC Adv. 3 (2013) 4473–4491.
- [48] B.A. Kakade, H. Wang, T. Tamaki, H. Ohashi, T. Yamaguchi, Enhanced oxygen reduction reaction by bimetallic CoPt and PdPt nanocrystals, RSC Adv. 3 (2013) 10487–10496.
- [49] D. Wang, H.L. Xin, R. Hovden, H. Wang, Y. Yu, D.A. Muller, F.J. Disalvo, H.D. Abruña, Structurally ordered intermetallic platinum-cobalt core-shell nanoparticles with enhanced activity and stability as oxygen reduction electrocatalysts, Nat. Mater. 12 (2013) 81–87.
- [50] W. Ye, S. Kou, X. Guo, F. Xie, H. Sun, H. Lu, J. Yang, Controlled synthesis of bimetallic Pd-Rh nanoframes and nanoboxes with high catalytic performances, Nanoscale. 7 (2015) 9558–9562.
- [51] S. Iihama, S. Furukawa, T. Komatsu, Efficient Catalytic System for Chemoselective Hydrogenation of Halonitrobenzene to Haloaniline Using PtZn Intermetallic Compound, ACS Catal. 6 (2016) 742–746.
- [52] B. Karthikeyan, M. Murugavelu, Sensors and Actuators B : Chemical Nano bimetallic Ag / Pt system as efficient opto and electrochemical sensing platform towards adenine, Sensors and Actuators B: Chem. 163 (2012) 216–223.
- [53] M. Murugavelu, B. Karthikeyan, Study of Ag-Pd bimetallic nanoparticles modified glassy carbon electrode for detection of L-cysteine, Superlattices Microstruct. 75 (2014) 916–926.
- [54] M. Shah, Q. Guo, Y. Fu, The colloidal synthesis of unsupported nickel-tin bimetallic nanoparticles with tunable composition that have high activity for the reduction of nitroarenes, CatCom. 65 (2015) 85-90.
- [55] B.K. Ghosh, S. Hazra, B. Naik, N.N. Ghosh, Preparation of Cu nanoparticle loaded SBA-15 and their excellent catalytic activity in reduction of variety of dyes, Powder Technol. 269 (2015) 371–378.
- [56] A. Kumar, C. Guo, G. Sharma, D. Pathania, M. Naushad, S. Kalia, P. Dhiman, Magnetically recoverable ZrO₂/Fe₃O₄/chitosan nanomaterials for enhanced sunlight driven photoreduction of carcinogenic Cr(VI) and dechlorination & mineralization of 4-chlorophenol from simulated waste water, RSC Adv. 6 (2016) 13251–13263.

- [57] M. Nasrollahzadeh, A. Azarian, M. Maham, A. Ehsani, Synthesis of Au/Pd bimetallic nanoparticles and their application in the Suzuki coupling reaction, *J. Ind. Eng. Chem.* 21 (2015) 746–748.
- [58] H. Yu, Y. He, Seed-assisted synthesis of dendritic Au-Ag bimetallic nanoparticles with chemiluminescence activity and their application in glucose detection, *Sensors and Actuators B: Chem.* 209 (2015) 877–882.
- [59] M. Nemanashi-Maumela, I. Nongwe, R.C. Motene, B.L. Davids, R. Meijboom, Au and Ag nanoparticles encapsulated within silica nanospheres using dendrimers as dual templating agent and their catalytic activity, *Mol. Catal.* 438 (2017) 184–196.
- [60] S.H.A.M. Leenders, R. Gramage-Doria, B. De Bruin, J.N.H. Reek, Transition metal catalysis in confined spaces, *Chem. Soc. Rev.* 44 (2015) 433–448.
- [61] A.K. Ilunga, R. Meijboom, Journal of Molecular Catalysis A : Chemical Catalytic oxidation of methylene blue by dendrimer encapsulated silver and gold nanoparticles, *Journal of Molecular Catalysis A: Chemical*, 411 (2016) 48–60.
- [62] R. Bhadouria, D. Misha, V.K. Singh, P. Singh, P. Srivastava, S. Tripathi, R. Singh, Nanocatalyst types and their potential impacts in agroecosystems: An overview, *Materials as Photocatalysts for Degradation of Environmental Pollutants*, (2020) 323-344.
- [63] M. Ali, B. Aissa, A. Andrieux-ledier, E. Maisonhaute, and A. Courty, Copper nanoparticles of well-controlled size and shape: a new advance in synthesis and self-organization. *Nanoscale*, 7 (2015) 3189–3195.
- [64] D. Xu, H. Lv, B. Liu, Encapsulation of metal nanoparticle catalysts within mesoporous zeolites and their enhanced catalytic performances: A review, *Front. Chem.* 6 (2018) 550.
- [65] M. Duan, L. Jiang, G. Zeng, D. Wang, W. Tang, J. Liang, H. Wang, D. He, Z. Liu, L. Tang, Bimetallic nanoparticles/metal-organic frameworks: Synthesis, applications and challenges, *Appl. Mater. Today.* 19 (2020)100564.
- [66] R. Geethalakshmi, D.V.L. Sarada, Gold and silver nanoparticles from *Trianthema decandra*: Synthesis, characterization, and antimicrobial properties, *Int. J. Nanomedicine.* 7 (2012) 5375–5384.
- [67] M. Vijayakumar, K. Priya, F.T. Nancy, A. Noorlidah, A.B.A. Ahmed, Biosynthesis, characterisation and anti-bacterial effect of plant-mediated silver nanoparticles using

- Artemisia nilagirica, *Ind. Crops Prod.* 41 (2013) 235–240.
- [68] R. Katwal, H. Kaur, G. Sharma, M. Naushad, D. Pathania, Electrochemical synthesized copper oxide nanoparticles for enhanced photocatalytic and antimicrobial activity, *J. Ind. Eng. Chem.* 31 (2015) 173–184.
- [69] G. Sharma, V.K. Gupta, S. Agarwal, A. Kumar, S. Thakur, D. Pathania, Fabrication and characterization of Fe@MoPO nanoparticles: Ion exchange behavior and photocatalytic activity against malachite green, *J. Mol. Liq.* 219 (2016) 1137–1143.
- [70] S. Das, T. Asefa, Core-Shell – Shell Microsphere Catalysts Containing Au Nanoparticles for Styrene Epoxidation, *Topics in catalysis*, 55 (2012) 587–594.
- [71] B. Wu, Y. Kuang, X. Zhang, J. Chen, Noble metal nanoparticles/carbon nanotubes nanohybrids : Synthesis and applications, *Nano Today*, 6 (2011) 75-90.
- [72] L. Gan, C. Cui, S. Rudi, P. Strasser, Core-Shell and Nanoporous Particle Architectures and Their Effect on the Activity and Stability of Pt ORR Electrocatalysts, *Topics in Catalysis*, 57 (2014) 236–244.
- [73] A. Cao, R. Lu, G. Veser, Stabilizing metal nanoparticles for heterogeneous catalysis, *Phys. Chem. Chem. Phys.* 12 (2010) 13499–13510.
- [74] R. Purbia, S. Paria, Yolk/shell nanoparticles: Classifications, synthesis, properties, and applications, *Nanoscale*. 7 (2015) 19789–19873.
- [75] A.K. Ilunga, R. Meijboom, *Applied Catalysis A: General Synthesis of narrowly dispersed silver and gold nanoparticles and their catalytic evaluation for morin oxidation*, *Applied Catalysis A: General*, 509 (2016) 17–29.
- [76] R.W.J. Scott, O.M. Wilson, R.M. Crooks, Synthesis, characterization, and applications of dendrimer-encapsulated nanoparticles, *J. Phys. Chem. B.* 109 (2005) 692–704.
- [77] V.S. Myers, M.G. Weir, E. V. Carino, D.F. Yancey, S. Pande, R.M. Crooks, Dendrimer-encapsulated nanoparticles: New synthetic and characterization methods and catalytic applications, *Chem. Sci.* 2 (2011) 1632.
- [78] B.A. Howell, D. Fan, L. Rakesh, Thermal decomposition of a generation 4.5 pamam dendrimer platinum drug conjugate, *Journal of thermal analysis and calorimetry*, 85 (2006) 17–20.
- [79] Y. Chung, H. Rhee, Synthesis and catalytic applications of dendrimer-templated bimetallic nanoparticles, *Catalysis surveys from Asia*, 8 (2004) 211–223.
- [80] Y. Chung, H. Rhee, Internal / External Use of Dendrimer in Catalysis, Y. Chung, H.

- Rhee, Internal/External Use of Dendrimer in Catalysis, Korean Journal of Chemical Engineering, 21 (2004) 81–97.
- [81] A.K. Ilunga, R. Meijboom, Applied Catalysis B : Environmental Catalytic and kinetic investigation of the encapsulated random alloy (Pd n -Au 110-n) nanoparticles, "Applied Catal. B, Environ. 189 (2016) 86–98.
- [82] M. Nemanashi, R. Meijboom, “ Cat in a bag ” recycling of dendrimer encapsulated Au nanoparticles by use of dialysis membrane bag in the reduction of 4-nitrophenol : proof of heterogeneous catalysis, Cat. Com. 83 (2016) 53–57.
- [83] A. Berger, R.J.M. Klein Gebbink, G. van Koten, Transition metal dendrimer catalysts, In Dendrimer catalysis. Top. Organomet. Chem. 20 (2006) 1–38.
- [84] P. Ncube, N. Bingwa, H. Baloyi, R. Meijboom, Catalytic activity of palladium and gold dendrimer-encapsulated nanoparticles for methylene blue reduction: A kinetic analysis, Appl. Catal. A Gen. 495 (2015) 63–71.
- [85] Y. Chung, H. Rhee, Pt – Pd bimetallic nanoparticles encapsulated in dendrimer nanoreactor, Catalysis letters, 85 (2003) 159–164.
- [86] J. Singh, T. Dutta, K.H. Kim, M. Rawat, P. Samddar, P. Kumar, “Green” synthesis of metals and their oxide nanoparticles: Applications for environmental remediation, J. Nanobiotechnology. 16 (2018) 1–24.
- [87] B.D. Chandler, J.D. Gilbertson, Dendrimer-encapsulated bimetallic nanoparticles: synthesis, characterization, and applications to homogeneous and heterogeneous catalysis. In *Dendrimer catalysis*. Springer, Berlin, Heidelberg (2006) 97-120.
- [88] H. Wang, H. Liu, S. Wang, L. Li, X. Liu, In fl uence of tunable pore size on photocatalytic and photoelectrochemical performances of hierarchical porous TiO₂ / C nanocomposites synthesized via dual-Templating, Applied Catalysis B : Environmental, 224 (2018) 341–349.
- [89] P.T. Yin, S. Shah, M. Chhowalla, K. Lee, Design, Synthesis, and Characterization of Graphene – Nanoparticle Hybrid Materials for Bioapplications, Chemical review 115 (2015) 2483-2531.
- [90] N. Luo, X.J. Li, X.H. Wang, F. Mo, H.T. Wang, Synthesis of carbon-encapsulated metal nanoparticles by a detonation method, Combust. Explos. Shock Waves. 46 (2010) 609–613.
- [91] C. Ma, B. Luo, H.H. Song, L.J. Zhi, Preparation of carbon-encapsulated metal magnetic

- nanoparticles by an instant pyrolysis method, *Xinxing Tan Cailiao/New Carbon Mater.* 25 (2010) 199–204.
- [92] X. Cai, R.Y. Hong, L.S. Wang, X.Y. Wang, H.Z. Li, Y. Zheng, D.G. Wei, Synthesis of silica powders by pressured carbonation, *Chemical Engineering Journal*, 151 (2009) 380–386.
- [93] Y. Jiao, S.W. Cho, S. Lee, S.H. Kim, S. Jeon, K. Hur, S.M. Yoon, M. Moon, A. Wang, A Hierarchically Porous Carbon Fabric for Highly Sensitive Electrochemical Sensors, *Advanced Engineering Materials*, 20 (2018) 1–7.
- [94] P. Abdulkin, T.L. Precht, B.R. Knappett, H.E. Skelton, D.A. Jefferson, A.E.H. Wheatley, Systematic Control of Size and Morphology in the Synthesis of Gold Nanoparticles, *Particle & Particle Systems Characterization*, 31 (2014) 571–579.
- [95] Y. Li, E. Boone, M.A. El-sayed, Size Effects of PVP - Pd Nanoparticles on the Catalytic Suzuki Reactions in Aqueous Solution, *Langmuir*, 18 (2002) 4921–4925.
- [96] K.M. Koczkur, S. Mourdikoudis, L. Polavarapu, S.E. Skrabalak, K.M. Koczkur, S. Mourdikoudis, L. Polavarapu, S.E. Skrabalak, Polyvinylpyrrolidone (PVP) in nanoparticle synthesis, *Dalton Transactions*, 44 (2015) 17883–17905.
- [97] N.V. Long, M. Ohtaki, M. Yuasa, S. Yoshida, T. Kuragaki, C.M. Thi, M. Nogami, Synthesis and Self-Assembly of Gold Nanoparticles by Chemically Modified Polyol Methods under Experimental Control, *Journal of Nanomaterials*, 2013 (2013).
- [98] T. Gutul, E. Rusu, N. Condur, V. Ursaki, E. Goncarenco, P. Vlazan, Preparation of poly(N-vinylpyrrolidone)-stabilized ZnO colloid nanoparticles, *Beilstein J. Nanotechnol.* 5 (2014) 402–406.
- [99] G. Bandekar, N.S. Rajurkar, I.S. Mulla, U.P. Mulik, D.P. Amalnerkar, P. V Adhyapak, Synthesis, characterization and photocatalytic activity of PVP stabilized ZnO and modified ZnO nanostructures, *Applied Nanoscience*, 4 (2014) 199–208.
- [100] A. Guzman, J. Arroyo, L. Verde, J. Rengifo, Synthesis and characterization of copper nanoparticles / polyvinyl chloride (Cu NPs / PVC) nanocomposites, *Procedia Mater. Sci.* 9 (2015) 298–304.
- [101] A.R. Prasad, A. Joseph, Synthesis, characterization and investigation of methyl orange dye removal from aqueous solutions using waterborne poly vinyl pyrrolidone (PVP) stabilized poly aniline (PANI) core-shell nanoparticles, *RSC Adv.* 7 (2017) 20960–20968.

- [102] N. Zhang, Y. Zhou, Y. Zhang, W. Jiang, T. Wang, J. Fu, Dual-templating synthesis of compressible and superhydrophobic spongy polystyrene for oil capture, *Chem. Eng. J.* 354 (2018) 245–253.
- [103] D. Farrusseng, A. Tuel, Perspectives on zeolite-encapsulated metal nanoparticles and their applications in catalysis, *New J. Chem.* 40 (2016) 3933–3949.
- [104] C. Pagis, A.R. Morgado Prates, D. Farrusseng, N. Bats, A. Tuel, Hollow Zeolite Structures: An Overview of Synthesis Methods, *Chem. Mater.* 28 (2016) 5205–5223.
- [105] S. Li, A. Tuel, D. Laprune, F. Meunier, D. Farrusseng, Transition-metal nanoparticles in hollow zeolite single crystals as bifunctional and size-selective hydrogenation catalysts, *Chem. Mater.* 27 (2015) 276–282.
- [106] F. Goodarzi, L. Kang, F.R. Wang, F. Joensen, S. Kegnæs, J. Mielby, Methanation of Carbon Dioxide over Zeolite-Encapsulated Nickel Nanoparticles, *ChemCatChem.* 10 (2018) 1566–1570.
- [107] M. Huang, L. Liu, S. Wang, H. Zhu, D. Wu, Z. Yu, S. Zhou, Dendritic Mesoporous Silica Nanospheres Synthesized by a Novel Dual-Templating Micelle System for the Preparation of Functional Nanomaterials, *Langmuir*, 33 (2017) 519-526.
- [108] D. Tarn, C.E. Ashley, M.I.N. Xue, E.C. Carnes, J.I. Zink, C.J. Brinker, Mesoporous Silica Nanoparticle Nanocarriers: Biofunctionality and Biocompatibility, *Accounts of chemical research*, 46 (2012) 792-801.
- [109] R. Atwi, A. Tuel, M. Maffre, L. Burel, J. Rousset, F. Meunier, Applied Catalysis A, General Highly dispersed Au, Ag and Au-Ag alloy nanoparticles encapsulated in single crystal multi-hollow silicalite-1, *Appl. Catal. A, Gen.* 569 (2019) 86–92.
- [110] S. Goel, Z. Wu, S.I. Zones, E. Iglesia, Synthesis and Catalytic Properties of Metal Clusters Encapsulated, *J. Am. Chem. Soc.* 134 (2012) 17688–17965.
- [111] M. Dusselier, M.E. Davis, Small-Pore Zeolites: Synthesis and Catalysis, *Chem. Rev.* 118 (2018) 5265–5329.
- [112] B. Zhang, Y. Tian, D. Chen, L. Li, G. Li, L. Wang, X. Zhang, G. Liu, Selective steam reforming of n-dodecane over stable subnanometric NiPt clusters encapsulated in Silicalite-1 zeolite, *AIChE J.* 66 (2020) 16917.
- [113] E.B. Hemming, A.F. Masters, T. Maschmeyer, The encapsulation of metal nanoparticles within porous liquids, *Chem. Commun.* 55 (2019) 11179–11182.
- [114] G. Munaò, D. Costa, S. Prestipino, C. Caccamo, Encapsulation of spherical

- nanoparticles by colloidal dimers, *Phys. Chem. Chem. Phys.* 18 (2016) 24922–24930.
- [115] U. De Bordeaux, S. Ingmar, I. Polenz, J. Baret, As featured in : Soft Matter Monitoring reactive microencapsulation dynamics using microfluidics, *Soft matter.* 11 (2015) 2916-2923.
- [116] S. Mourdikoudis, R.M. Pallares, Characterization techniques for nanoparticles : comparison and complementarity upon studying, *Nanoscale*,10 (2018) 12871–12934.
- [117] J. Noh, R. Patala, R. Meijboom, Applied Catalysis A : General Catalytic evaluation of dendrimer and reverse microemulsion template Pd and Pt nanoparticles for the selective oxidation of styrene using TBHP, "Applied Catal. A, Gen. 514 (2016) 253–266.
- [118] M. Nemanashi, R. Meijboom, Synthesis and characterization of Cu, Ag and Au dendrimer-encapsulated nanoparticles and their application in the reduction of 4-nitrophenol to 4-aminophenol, *J. Colloid Interface Sci.* 389 (2013) 260–267.
- [119] F.A. Al-Marhaby, R. Seoudi, Preparation and Characterization of Silver Nanoparticles and Their Use in Catalytic Reduction of 4-Nitrophenol, *World J. Nano Sci. Eng.* 6 (2016) 29–37.
- [120] A. Nadeem, S. Naz, J. Sarfraz, A. Mannan, M. Zia, Synthesis, characterization and biological activities of monometallic and bimetallic nanoparticles using *Mirabilis jalapa* leaf extract, *Biotechnol. Reports.* 24 (2019) e00338.
- [121] K. Čubová, V. Čuba, Synthesis of inorganic nanoparticles by ionizing radiation – a review, *Radiat. Phys. Chem.* 158 (2019) 153–164.
- [122] D. Moura, M.T. Souza, L. Liverani, G. Rella, G.M. Luz, J.F. Mano, A.R. Boccaccini, Development of a bioactive glass-polymer composite for wound healing applications, *Mater. Sci. Eng. C.* 76 (2017) 224–232.
- [123] K. Banerjee, S. Das, P. Choudhury, S. Ghosh, R. Baral, S.K. Choudhuri, A Novel Approach of Synthesizing and Evaluating the Anticancer Potential of Silver Oxide Nanoparticles in vitro, *Chemotherapy.* 62 (2017) 279–289.
- [124] S.F. Shaikh, R.S. Mane, B.K. Min, Y.J. Hwang, O.S. Joo, D-sorbitol-induced phase control of TiO₂ nanoparticles and its application for dye-sensitized solar cells, *Sci. Rep.* 6 (2016) 1–10.
- [125] E.R. Evans, P. Bugga, V. Asthana, R. Drezek, Metallic nanoparticles for cancer immunotherapy, *Mater. Today.* 21 (2018) 673–685.
- [126] S. Keshipour, A. Kamran, Reduction of nitroaromatics to amines with cellulose

- supported bimetallic Pd/Co nanoparticles, Iran. J. Chem. Chem. Eng. 37 (2018) 23–31.
- [127] Y. Xu, W. Shan, X. Liang, X. Gao, W. Li, H. Li, X. Qiu, Cobalt Nanoparticles Encapsulated in Nitrogen-Doped Carbon Shells: Efficient and Stable Catalyst for Nitrobenzene Reduction, Ind. Eng. Chem. Res. 59 (2020) 4367–4376.
- [128] P. Viswanathan, T.S. Bhuvaneswari, R. Ramaraj, Investigation on the catalytic activity of aminosilane stabilized gold nanocatalysts towards the reduction of nitroaromatics, Colloids Surfaces A Physicochem. Eng. Asp. 528 (2017) 48–56.
- [129] H. Veisi, S. Kazemi, P. Mohammadi, P. Safarimeh, S. Hemmati, Catalytic reduction of 4-nitrophenol over Ag nanoparticles immobilized on Stachys lavandulifolia extract-modified multi walled carbon nanotubes, Polyhedron. 157 (2019) 232–240.
- [130] M. Ismail, M.I. Khan, S.B. Khan, K. Akhtar, M.A. Khan, A.M. Asiri, Catalytic reduction of picric acid, nitrophenols and organic azo dyes via green synthesized plant supported Ag nanoparticles, J. Mol. Liq. 268 (2018) 87–101.
- [131] S. Keshipour, S.S. Mirmasoudi, Chitosan supported bimetallic Pd/Co nanoparticles as a heterogeneous catalyst for the reduction of nitroaromatics to amines, Adv. Environ. Technol. 3 (2017) 59–65.
- [132] R. Rajesh, R. Venkatesan, Encapsulation of silver nanoparticles into graphite grafted with hyperbranched poly(amidoamine) dendrimer and their catalytic activity towards reduction of nitro aromatics, J. Mol. Catal. A Chem. 359 (2012) 88–96.
- [133] M.A. Ahsan, V. Jabbari, A.A. El-Gendy, M.L. Curry, J.C. Noveron, Ultrafast catalytic reduction of environmental pollutants in water via MOF-derived magnetic Ni and Cu nanoparticles encapsulated in porous carbon, Appl. Surf. Sci. 497 (2019) 143608.
- [134] M.A. Ahsan, E. Deemer, O. Fernandez-Delgado, H. Wang, M.L. Curry, A.A. El-Gendy, J.C. Noveron, Fe nanoparticles encapsulated in MOF-derived carbon for the reduction of 4-nitrophenol and methyl orange in water, Catal. Commun. 130 (2019) 105753.
- [135] B. Shi, S. Gao, H. Yu, L. Zhang, C. Song, K. Huang, Fe₀ nanoparticles encapsulated in hollow porous nanosphere frameworks for efficient degradation of methyl orange, React. Funct. Polym. 153 (2020) 104614.
- [136] B. Shi, Y. Xu, T. Wang, S. Gao, G. Meng, K. Huang, Applied Catalysis A, General Ag nanoparticles encapsulated in carboxyl-functionalized hollow microporous organic nanospheres for highly efficient catalysis applications, Appl. Catal. A, Gen. 588 (2019)

- 117276.
- [137] A. Aziz, N. Ali, A. Khan, M. Bilal, S. Malik, N. Ali, H. Khan, Chitosan-zinc sulfide nanoparticles, characterization and their photocatalytic degradation efficiency for azo dyes, *Int. J. Biol. Macromol.* 153 (2020) 502–512.
- [138] S. Iqbal, C. Zahoor, S. Musaddiq, M. Hussain, R. Begum, A. Irfan, M. Azam, Z.H. Farooqi, Silver nanoparticles stabilized in polymer hydrogels for catalytic degradation of azo dyes, *Ecotoxicol. Environ. Saf.* 202 (2020) 110924.
- [139] A. Bafana, S.S. Devi, T. Chakrabarti, Azo dyes: Past, present and the future, *Environ. Rev.* 19 (2011) 350–370.
- [140] K. Naseem, R. Begum, W. Wu, A. Irfan, A.G. Al-Sehemi, Z.H. Farooqi, Catalytic reduction of toxic dyes in the presence of silver nanoparticles impregnated core-shell composite microgels, *J. Clean. Prod.* 211 (2019) 855–864.
- [141] L. Zhang, L. Jin, B. Liu, J. He, Templated growth of crystalline mesoporous materials: from soft/hard templates to colloidal templates, *Front. Chem.* 7 (2019) 22.
- [142] X. Deng, K. Chen, H. Tüysüz, Protocol for the nanocasting method: Preparation of ordered mesoporous metal oxides, *Chem. Mater.* 29 (2017) 40–52.
- [143] Y. Kuroda, Y. Shimbo, Y. Sakamoto, H. Wada, K. Kuroda, A Mesoporous Superlattice Consisting of Alternately Stacking Interstitial Nanospace within Binary Silica Colloidal Crystals, *Angew. Chemie Int. Ed.* 55 (2016) 10702–10706.
- [144] D. Shen, J. Yang, X. Li, L. Zhou, R. Zhang, W. Li, L. Chen, R. Wang, F. Zhang, D. Zhao, Biphasic Stratification Approach to Three-Dimensional Dendritic Biodegradable Mesoporous Silica Nanospheres, *Nano letters*, 14 (2014) 923-932.
- [145] C.-H. Kuo, I.M. Mosa, A.S. Poyraz, S. Biswas, A.M. El-Sawy, W. Song, Z. Luo, S.-Y. Chen, J.F. Rusling, J. He, Robust mesoporous manganese oxide catalysts for water oxidation, *ACS Catal.* 5 (2015) 1693–1699.
- [146] S.M. Vickers, R. Gholami, K.J. Smith, M.J. MacLachlan, Mesoporous Mn-and La-doped cerium oxide/cobalt oxide mixed metal catalysts for methane oxidation, *ACS Appl. Mater. Interfaces.* 7 (2015) 11460–11466.
- [147] O.R. Onisuru, O.A. Alimi, K. Potgieter, R. Meijboom, Continuous-Flow Catalytic Degradation of Hexacyanoferrate Ion through Electron Transfer Induction in a 3D-Printed Flow Reactor, *J. Mater. Eng. Perform.* 30 (2021) 4891-4901.
- [148] C. Wiles, P. Watts, Continuous flow reactors: A perspective, *Green Chem.* 14 (2012)

38–54.

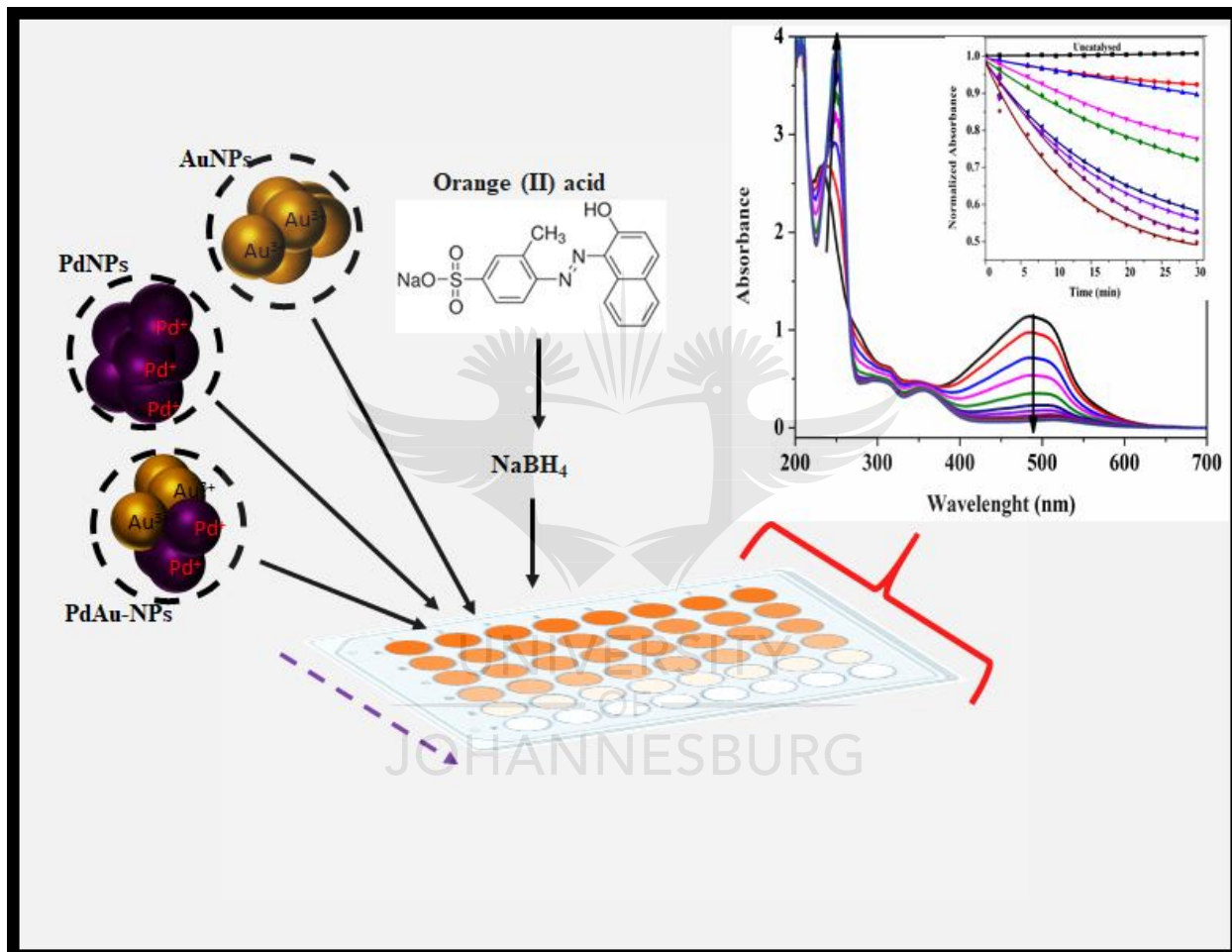
[149] S. V. Ley, On being green: Can flow chemistry help?, *Chem. Rec.* 12 (2012) 378–390.



CHAPTER 2

Kinetic Modeling of Orange II Acid Dye Degradation: A Decolorization Abatement within a Microplate Reader System

Graphical abstract



Abstract

A kinetic study of how orange II acid (OII) dye is catalytically degraded using an individually stabilized Pd, Au nanoparticles (NPs), and bimetallic AuPd NPs synthesized by polyvinylpyrrolidone (PVP) stabilizing method is investigated in the presence of sodium borohydride (BH_4^-). The stabilized and dispersed mono and bimetallic PVP NPs were qualitatively characterized by UV-visible (UV-vis) spectrophotometry and High-Resolution Transmission Electron Microscopy (H-TEM). The TEM images revealed the various distributions of the nanoparticles, while the UV-vis revealed the absorbance of each nanoparticle. The kinetic data was acquired by monitoring the absorbance at the wavelength of 487 nm using a microplate reader. The degradation process followed a *pseudo-first-order* condition, and it was also found conformed with the Langmuir-Hinshelwood model. The adsorption of OII (K_{OII}) and BH_4^- ($K_{\text{BH}_4^-}$) onto the catalyst surfaces were demonstrated. AuPd NPs demonstrated the highest activity. The reaction was endothermic and spontaneously driven.

Keywords: Poly(vinylpyrrolidone) nanoparticles; Orange II acid; Reaction kinetics; Langmuir-Hinshelwood.



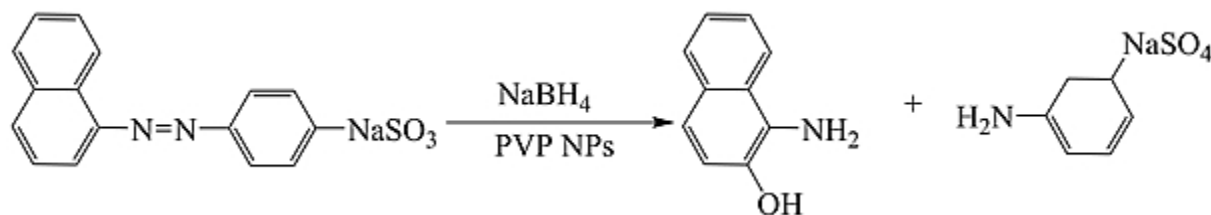
2.1 Introduction

Orange II acid (OII) is an example of azo dyes widely used in diverse products like textiles, leather, plastics, hair dye, paper, food products, and the wood industry. It has posed a dangerous risk to the environment and ecosystem [1]. This risk is mainly seen in the effluents generated by the textile industry. It has resistance to degradation by light, oxygen, acid, or base attacks, hence making the process of removing it from effluents tedious and challenging [2,3]. This degradation resistance is because textile wastewaters are rich in bio-persistent, non-biodegradable, toxic, and carcinogenic dyes, making them environmentally and humanly hazardous [4].

Dyes are typical examples of pollutants rich in color intensity, toxicity, and synthetic in origin while also possessing complex molecular structures. These structures make them challenging to be degraded biologically [5]. Precisely, it has been estimated that the dyeing process in the textile industry constitutes up to 65% effluents of textile wastewaters out of the total colored contaminants in wastewaters [1]. Dye's presence in water, even at a trace amount, has unhealthy and undesirable consequences. They possess characteristics that make them toxic, mutagenic, and carcinogenic, making them harmful to the environment, aquatic life, and, most importantly, humans [6,7]. The over 60-70% of all organic dyes produced worldwide are azo dyes [1]. About 280,000 tons of these dyes are released as effluents from the textile industry [8], and nothing less than 15% of these dyes find their way into the environment as effluents and wastewaters [9,10]. They consequently cause non-friendly environmental problems and issues of public health [11]. These ecological problems being posed by azo dyes are further compounded as they are generally resistant to biodegradation owing to their complex structures [12].

Globally, azo dyes such as orange II acid dyes are emptied into water bodies in large quantities as colored effluents without efficient treatment methods. These methods include biodegradation and physicochemical treatments like coagulation, flocculation, adsorption, and membrane separation [13]. The reducibility of OII to the formation of small organic molecules and non-toxic compounds is possible with reductants such as NaBH_4 . Although the rate of reduction of the dye is extremely slow, the acceleration in reaction rate is achievable. This acceleration can be achieved using a metal nanoparticle of high reactivity and specific surface area, which sufficiently speeds up the reducing effect of NaBH_4 upon the dye [14].

The progressive reduction occurs through hydrogenation, propelled by the catalysts to indicate an interaction between the catalyst surface and the substrates at the reaction interface [15]. This resulted in $-N=N-$ bond-breaking (**Scheme 2.1**) as previously reported [14].



Scheme 2.1: Schematic illustration of OII reduction by borohydride interaction driven by a catalyst.

An aspect of research that has gained intense attention is transition metal nanoparticles application in catalysis [16]. This is because noble metal NPs have displayed distinct characteristics not seen with their bulk counterparts [17]. Metal nanoparticles made by alloying two metals into a catalyst, known as bimetallic NPs, bring about new catalytic and chemical properties [18,19]. Thereby showing an improved and remarkable property when compared to the individually unalloyed metals [18]. Gold (Au) has been studied for its properties regarding size-dependent catalytic reactions [20–23], while palladium (Pd) is also known to possess excellent catalytic activity [24].

Generally, transition metal NPs are only stable kinetically upon being stabilized with support as they naturally will disperse freely in solution. Hence, the need to be stabilized with the aid of stabilizers, such as PVP NPs in preventing agglomeration is crucial [25]. Stabilizers such as poly(vinylpyrrolidone) (PVP) are known to play a significant supportive role in metal nanoparticles preparation as it relates to controlling their formation and stability in reactions [17]. An intermediate organic compound of aromatic amine origin is formed upon complete reduction. The intermediate produced is significantly used in dye manufacturing, chemical fiber, medicine, pesticide, and rubber additives [26]. In this work, synthesized PVP stabilized monometallic Pd, Au, and bimetallic AuPd NPs were used to degrade OII acid catalytically, and the kinetics of degradation were discussed.

Langmuir-Hinshelwood has been widely used to mechanically describe the reactants' adsorption onto the catalyst's surface before the reaction [21–23,27,28]. The approach was used to ascertain that initial adsorption of both the OII and sodium borohydride is taking place on the catalyst's surface before the transfer of electrons from BH_4^- leading to the reduction of OII. This model is completed by fitting the experimental data with the theoretical equations to confirm if the reaction mechanism aligns with the proposed mechanism.

2.2 Experimental section

2.2.1 Materials and reagents

Poly (vinylpyrrolidone) (PVP = 10,000 g/mol), ethylene glycol (99.8%), potassium tetrachloropalladate (II), (K_2PdCl_4 99.99%), hydrogen tetrachloroaurate (III) hydrate (HAuCl_4 99.99%), sodium borohydride (NaBH_4), orange II sodium salt $\geq 85\%$, sodium hydroxide pellets ($\text{NaOH} \geq 99.86\%$) were all obtained from Sigma-Aldrich. Sodium hydrogen carbonate (NaHCO_3 , $\geq 99.86\%$) and sodium (Na_2CO_3 , $\geq 99.5\%$) were purchased from Merck Laboratories. Micropipettes acquired from Accumax PRO and DLAB Scientific were used to take all aliquots into the polystyrene multi-well plate obtained from Becton Dickinson Labware. A microplate reader (BioTek Power wave XS2) was used to monitor the reduction progression. All the materials were used as purchased, and analyses conducted were performed with Milli-Q water ($18.2 \text{ M}\Omega \cdot \text{cm}$).

2.2.2 Synthesis of PVP stabilized nanoparticles NPs

Synthesis Pd-PVP NPs

Ethylene glycol was used to prepare PVP NPs by the polyol method. The method proceeded by weighing out the appropriate amount of K_2PdCl_4 (0.9790 g) to make a total concentration of 0.05 M solution. This solution was added to 10 mL ethylene glycol, followed by the addition of PVP (0.2775 g, average MW= 10 000). The mixing was done at 120°C using 45 rpm on a carousel TM multi-reactor connected to a reflux condenser (Radley Discovery Technologies). Finally, as the mixing continues, the ethylene glycol reduces from Pd^{2+} to Pd^0 , and no further purification was done before using the particles for the reaction.

Synthesis of Au-PVP NPs

A polyol method using ethylene glycol was also used for the synthesis of Au-PVP NPs. Simply, PVP (0.5095 g, average MW= 10 000) was dissolved in 5 mL ethylene glycol to form a solution. After stirring for 2 h in a multi-reactor carousel fitted with a reflux condenser (Radley Discovery Technologies), at 180 °C, to dissolve all the PVP, aqueous solution of AuCl₃ was added from a stock solution of AuCl₃ (0.1558 g) prepared in (2.5 mL) Milli-Q water. The mixture was stirred for approximately 15 min, the solution's pH was adjusted to 9 with 1 M NaOH, and the mixture was heated at 100 °C.

Synthesis of AuPd-PVP Bimetallic NPs

Equally, the polyol method was adapted for the synthesis of bimetallic AuPd-PVP NPs composition. Typically, in a 50 mL ethylene glycol under vigorous stirring with a reflux condenser, a PVP sample (0.4 g) was dissolved. After the entire dissolution of the PVP in ethylene glycol at a working temperature between 100 to 190 °C, 2 mL of 0.05 M aqueous solution of PdCl₂ was added, followed by the subsequent addition of 1 mL aqueous solution of HAuCl₄ (0.1 M). The mixture was left to stir for 3 h at a constant temperature.

2.3 Characterization

Characterization of the catalysts was performed before the kinetic evaluation of these catalysts. UV-vis (Shidmazu UV-1800 Spectrophotometer) was used to observe the Pd, Au, and AuPd-PVP NPs spectra. The catalysts' high-resolution image (H-TEM) was captured with the JOEL JEM-2100F electron microscope of 200 kV accelerating voltage. This image was obtained using copper grids by placing a few drops of the catalyst solution on the carbon-coated grids after dispersing the catalyst ultrasonically. The catalyst solution was allowed to dry in the air on the carbon-coated grids, inserted into the machine, and images were captured. FTIR analysis of the PVP NPs was carried out on a Shimadzu IRAffinity-1 spectroscopy.

2.4 Catalytic evaluation

2.4.1 Reaction conditions used for kinetic studies

Typically, the catalytic experiments were performed within the catalyst dynamic range by using the following conditions; Pd-PVP NPs (50 μL, 2×10⁻⁴ M), NaBH₄ (200 μL, 1.6×10⁻³ M), and

OIIA (200 μL , 8×10^{-5} M). The ratio of catalyst to the substrate was 1:4, and all reagents were measured inside a 24-well polystyrene plate and made to reach the appropriate concentration with milli-Q water. The plate reader monitored the change that accompanied the absorbance of OII with time at $\lambda = 480$ nm. This wavelength was used to obtain all kinetic studies regarding dye, NaBH_4 (reducing agent), and catalyst variations at different temperatures of 25, 35, and 45 $^\circ\text{C}$. The same method and condition were used for Au-PVP NPs, and AuPd alloyed NPs.

2.5 Result and discussion

2.5.1 Synthesis of Pd, Au, and bimetallic AuPd-PVP NPs

The synthetic procedure of Pd, Au, and bimetallic AuPd-PVP NPs was accompanied by a color change to confirm the successful reduction of each NPs. A proof of Pd reduction is the emergence of a brown solution from dark orange, while the subsequent transition in color from dark brown to a wine-red color was evidence of the Au-PVP NPs formation. The synthesis of AuPd-PVP NPs was indicated by a color change from yellow to a dark brown solution.

2.5.2 Characterization of Pd, Au, and bimetallic AuPd-PVP NPs

The UV-vis spectra obtained for Pd, Au, and bimetallic AuPd-PVP NPs are shown in the appendix (**Appx. 2. 1**). The different absorbance obtained for both Au-PVP NPs, and bimetallic AuPd-PVP NPs showed a peak at exactly $\lambda = 519$ nm, while the absorbance obtained for Pd-PVP NPs showed no peak. Notably, a reduction in absorbance is seen in AuPd-PVP NPs due to the interaction between Pd and Au-PVP NPs. Analysis of the particles' internal structures obtained from H-TEM revealed the shape, size, and morphology of the synthesized Pd, Au, and bimetallic AuPd-PVP NPs. The particles are well dispersed, and their shapes, both rhombus and spherical, are similar to the previous report [29]. The different shapes they exhibited are due to the amount of PVP used in the synthesis. PVP has been used as a stabilizing precursor to circumvent agglomeration and control the nanomaterials' shapes [30]. The TEM images obtained are displayed in **Figure 2.1a**, **2.1b**, and **2.1c** Au, and bimetallic AuPd-PVP NPs, respectively. Their corresponding size distribution is represented in **Figure 2.1d**, **2.1e**, and **2.1f** for Pd, Au, and bimetallic AuPd- PVP NPs, respectively.

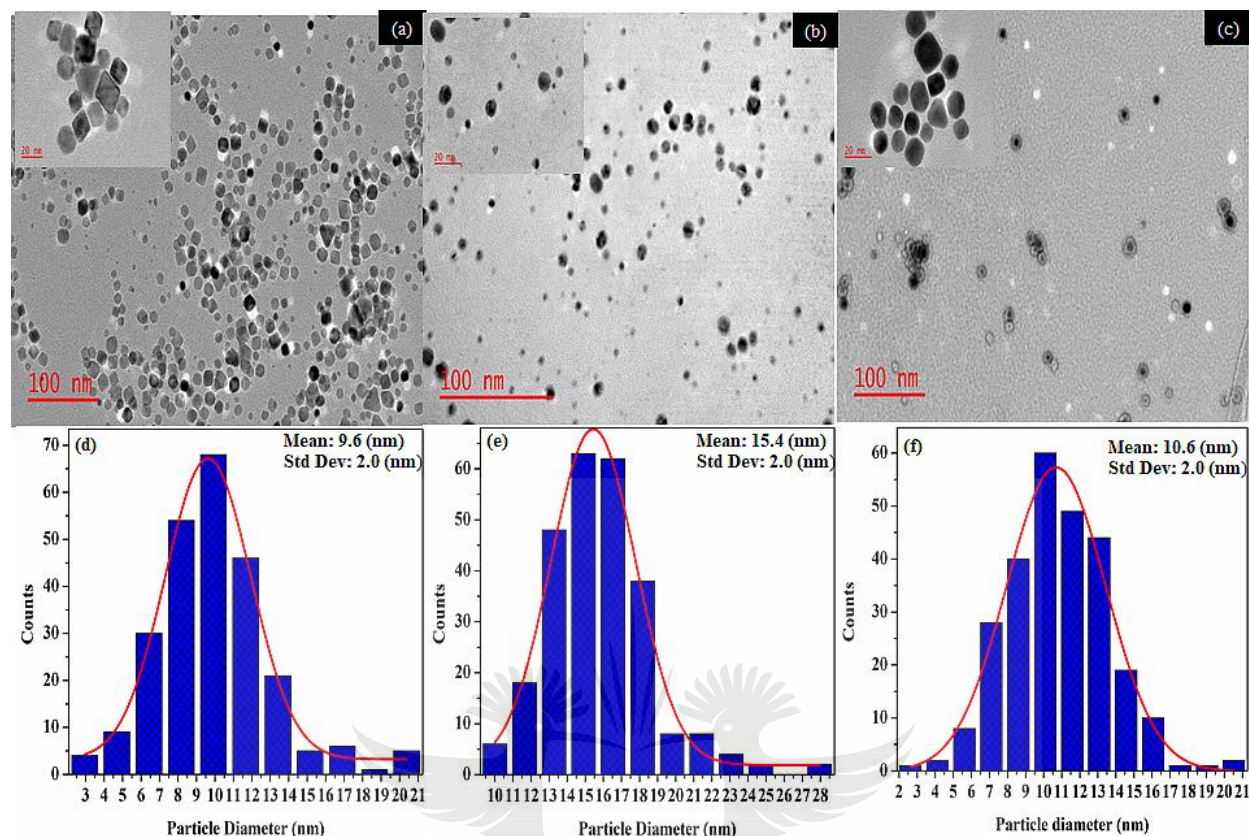


Figure 2.1: H-TEM images of (a) Au-PVP NPs, (b) Pd-PVP NPs, and (c) AuPd-PVP bimetallic NPs.

In light of the infrared spectra shown in **Figure 2.2**, it is noteworthy that the metal nanoparticles were stabilized by the coordination of the PVP with the metal nanoparticles through electrostatic attraction. This stability results from the lone pair of electrons' contribution from the nitrogen or carbonyl oxygen of the PVP repeating unit onto the hybrid orbitals of Au and Pd ions [29]. The absorption peak at ν 1642 cm^{-1} is deduced to be a C=O double bond of the carbonyl group present in pyrrolidone groups [31]. The peaks at ν 1453 cm^{-1} can be ascribed to C-N stretching vibration due to the presence of the CH₂ group of the pyrrole ring present in PVP [32]. The comparison of the three spectra also showed similar peaks at ν 1025 and ν 1086 cm^{-1} , while the broad bands between ν 3600-2400 cm^{-1} correspond to the hydroxyl group [33], also seen in all the spectra.

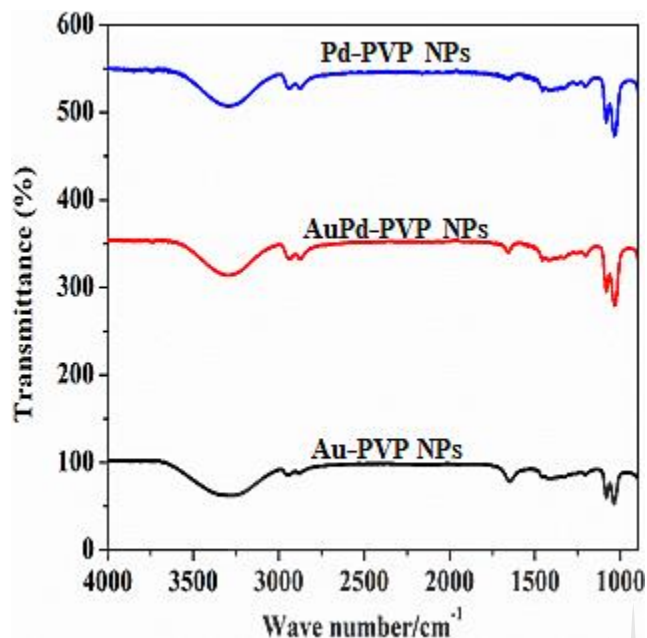


Figure 2.2: The FT-IR absorption Spectra of Au-PVP, Pd-PVP NPs, and AuPd-PVP bimetallic NPs.

2.5.3 Orange II acid catalytic activity and kinetic evaluation

The degradation of OII monitored by microplate reader following the maximum peak at $\lambda = 480$ nm was obtained in batch experiments. First, the catalyst concentration was varied from 4 - 32 μM while keeping borohydride (BH_4^-) and OII concentrations constant. Another data set collected by varying the [OII] was between 40 and 180 μM while the catalysts amount and BH_4^- concentration remained unchanged. We obtained the third set of data by varying the BH_4^- concentration was from 800 - 3600 μM , and other reactants stayed unaltered. Finally, these sets of experiments were performed at different temperatures ranging from 25 - 45 $^\circ\text{C}$.

The catalytic reduction displayed a decrease in absorbance with time, as shown in **Figure 2.3a**. Generally, through the coherent electron oscillations, metallic nanoparticles are known to possess localized surface plasmon resonance (LSPR) which is induced by the photon incidence [34]. This property lead to the strong light absorption in AuNPs and the combination of Au and Pd bimetallic further enhanced the LSPR property due to their dual-functionality. High availability of binding sites on the catalysts surface results in increased surface resonance response, therefore, as the adsorption and desorption takes place, the number of available sites decreases which leads to

decrease in binding rate. At a certain point, when the number of binding and unbinding molecules becomes equal this reduces the surface resonance response. The absorbance peaks observed at $\lambda = 250$ nm and the minor peak at $\lambda = 312$ nm can be ascribed to $\pi - \pi^*$ transition state concerning the aromatic rings [35]. The absorption seen at 489 nm can be attributed to the $n - \pi^*$ transformation in azo bond ($-N=N-$) [35,36], and the absorbance continue to gradually decline until complete disappearance. It was accompanied by new peaks at $\lambda = 246$ nm, which correspond to the amino groups ($-NH_2$) [37]. This new absorbance is a confirmation of efficiency in dye reduction due to the isosbestic point it possesses. **Figure 2.3b** revealed a time-dependent exponential increase in the catalytic degradation of OII in the presence of Au-PVP NPs in different amounts. The reduction process was found in conformity to the *pseudo*-first-order condition (**Eqn. 2.1a**) [38,39] since the concentration of BH_4^- was considerably high compared to the concentration of OII. The resulting catalytic parameters were fitted into **Eqn. 2.1b** to compute the observed rate constant (k_{obs}) [40]. **Appx. II.2a** shows the non-linear regression graph obtained.

$$-\frac{d[Fe(CN)_6^{3-}]}{dt} = k_{obs} \cdot [Fe(CN)_6^{3-}]^n \quad (2.1a)$$

$$X_{(absorbance)} = A \cdot e^{-k_{obs} \cdot t} + C \quad (2.1b)$$

However, the catalytic role was accounted for though the uncatalyzed reduction process in **Figure 2.3b**, and the absorbance displayed a non-progressive degradation with time at $\lambda = 480$ nm throughout. This points out that the catalysts were responsible for the efficient and fast reduction of OII because the reaction did not proceed in the absence of catalysts. This reduction typically depicts that the reaction was catalytically driven. Moreover, while every other reactant remains unchanged, the catalysts' reduction abilities were investigated using a more considerable amount of BH_4^- compared to the substrate. **Figure 2.4a-II.4c** shows a linear increase in the k_{obs} versus catalysts surface area plot. This pattern can be ascribed to the fact that the reaction proceeds on the catalysts' surface and is catalytically dependent. However, Pd-PVP NPs in 4b revealed some points where the k_{obs} did not increase linearly compared to the catalyst's surface area. This indication could be that adsorption of the OII is rapidly occurring on the surface of the catalysts before their interaction.

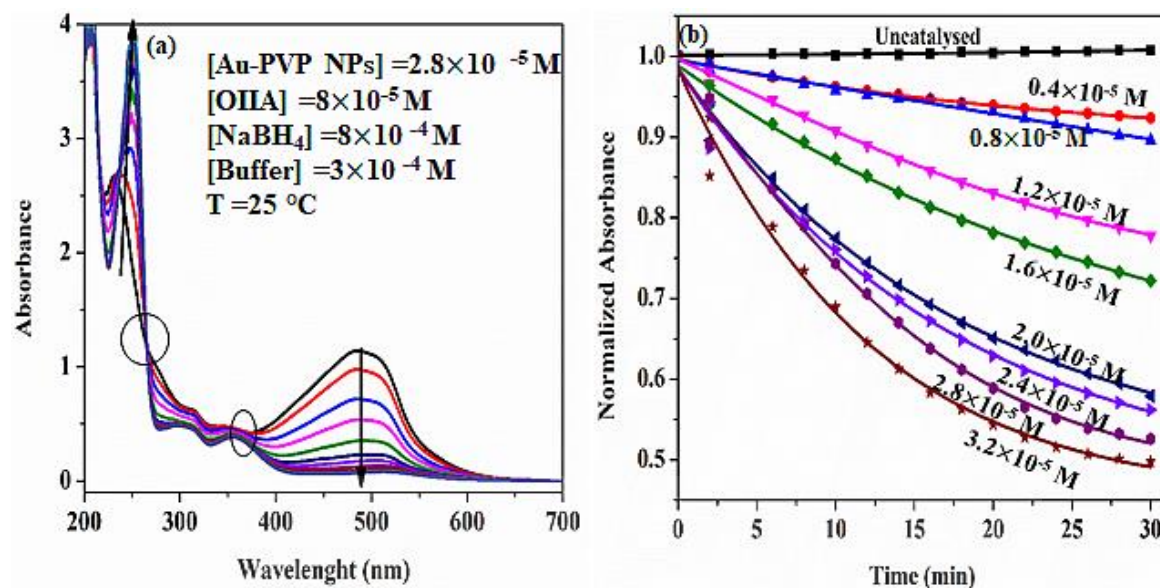


Figure 2.3: OII (a) reduction spectra of the absorbance versus time (b) non-linear regression profile.

A comparison of the catalytic activity was performed by obtaining a histogram plot of all the catalysts' observed rate constant, **Appx. 2. 2b**. It was revealed that the AuPd catalyst has the highest performing activity of all the catalysts. Both Au and Pd possess high electron affinity and hence, the higher performance of bimetallic AuPd catalysts compare to monometallic AuNPs and PdNPs may be as a result their synergistic effect.

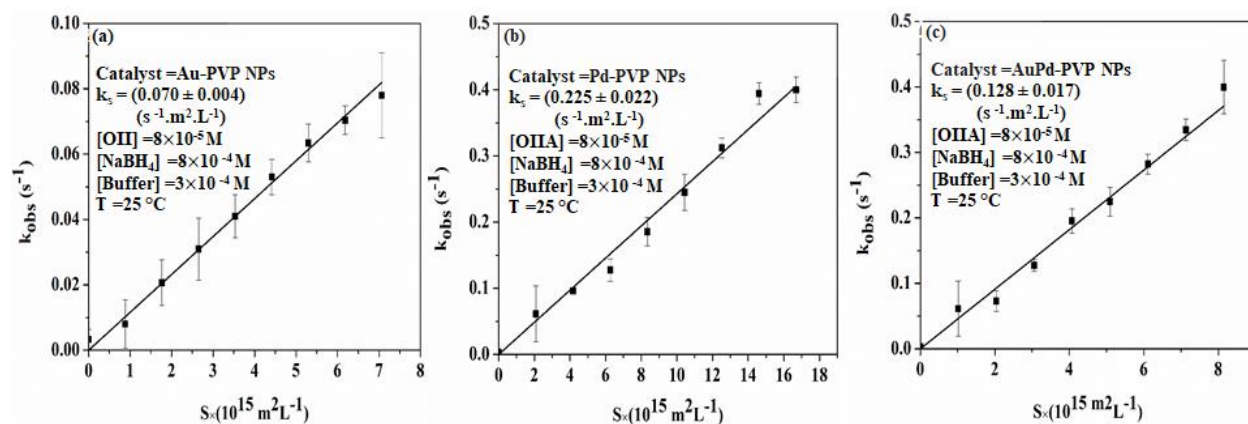


Figure 2.4: (a-c) plot of the surface area of the different catalysts versus the observed rate constant.

The degradation efficiency is characterized by the reactant adsorption on the catalyst's surface, in which k_{obs} directly relate to both the catalyst concentration and the total surface area of the metal nanoparticle. Therefore, the exponential increase in the rate constant as the catalyst increases shows the linear relationship between the observed rate constant and the catalyst's concentration using **Eqn. (2.2)**.

$$-\frac{d[\text{OII}]}{dt} = k_{obs} \cdot [\text{OII}]^n = k_S \cdot S \cdot [\text{OII}]^n \quad (2.2)$$

Where $[\text{OII}]$ is the concentration of OII at time t , S represents the surface area, while k_S refers to the apparent rate constant with respect to the metal nanoparticle's surface area per unit volume.

In the analysis of Langmuir-Hinshelwood, the mechanism assumes that the reaction between the species reacting takes place on the catalyst surface. In our case, both OII and BH_4^- diffuse to the nanoparticles' surface. Electrons generated from borohydride are released to the catalyst's available active site. These subsequently migrate to the OII molecules, which are adsorbed onto the metal nanoparticle's surface. Such interaction resulted in a product's formation as the decolorized OII dissociates from the catalyst's active site [40]. Fresh OII afterward occupied the nanoparticle's active sites. The diffusion of BH_4^- to the catalyst surface and the simultaneous adsorption of OII on the surface took place very fast, serving as the rate-determining step [41]. Therefore, due to the reaction on the catalyst surface and the reaction rate's dependence on the surface coverage of both reacting species, the reaction kinetics can be described with **Eqn. (2.3) - (2.5)**. These resulted in the Langmuir-Hinshelwood **Eqn (2.6)** [42].

$$-\frac{d[\text{OII}]}{dt} = k \cdot S \cdot \theta_{\text{OII}} \cdot \theta_{\text{BH}_4^-} \quad (2.3)$$

Where k is the rate constant kinetics of the surface reaction, while θ_{OII} and $\theta_{\text{BH}_4^-}$ indicate surface coverage of OII and BH_4^- respectively upon the nanoparticle's surface, the surface coverage values are expressed as:

$$\theta_{\text{OII}} = \frac{(K_{\text{OII}} \cdot [\text{OII}])^n}{1 + (K_{\text{OII}} \cdot [\text{OII}])^n + (K_{\text{BH}_4^-} \cdot [\text{BH}_4^-])^m} \quad (2.4)$$

$$\theta_{\text{BH}_4^-} = \frac{(K_{\text{BH}_4^-} \cdot [\text{BH}_4^-])^m}{1 + (K_{\text{OII}} \cdot [\text{OII}])^n + (K_{\text{BH}_4^-} \cdot [\text{BH}_4^-])^m} \quad (2.5)$$

In **Eqn. (2.4)** and **(2.5)**, K_{OII} and $K_{\text{BH}_4^-}$ are the adsorption constants of OII and BH_4^- , $[\text{OII}]$, and $[\text{BH}_4^-]$ refers to the concentration of OII and BH_4^- respectively. At the same time, n and m , which represent Freundlich exponents, describe the heterogeneity of the nanoparticle's surface and not of the reaction orders.

Substitution of Eqn. **Eqn. (2.3) – (2.5)** into the expressed rate in **Eqn. (2.2)** will generate the kinetic data for OII reduction modeled on the Langmuir-Hinshelwood mechanism, as shown in **Eqn. (2.6)**.

$$k_{\text{obs}} = k \cdot S \cdot [\text{OII}]^{n-1} \cdot \frac{(K_{\text{OII}})^n \cdot (K_{\text{BH}_4^-} \cdot [\text{BH}_4^-])^m}{\{1 + (K_{\text{OII}} \cdot [\text{OII}])^n + (K_{\text{BH}_4^-} \cdot [\text{BH}_4^-])^m\}^2} \quad (2.6)$$

Where the surface rate constant is represented by k , S indicates the total catalyst surface area in the reactor.

The Langmuir-Hinshelwood model in **Eqn. (2.6)** is demonstrated through the fittings of the different catalysts. These are shown in **Figure 2.5, 2.6, and 2.7. Figure 2.5a and 2.b, Figure 2.6a and 2.b**, including **Figure 2.7a and 2.b**. They all displayed a corresponding decrease in the observed rate constant as the $[\text{OII}]$ increased at constant $[\text{BH}_4^-]$. In contrast, while maintaining a constant $[\text{OII}]$, in **Figure 2.5c and 2.5d, Figure 2.6c and 2.6d**. Also, in **Figure 2.7c and 2.7d**, an increase in the $[\text{BH}_4^-]$ increased the k_{obs} .

The decrease in the observed rate constant is due to the increased concentration of OII, which occurred from substrate saturation upon the surfaces of the catalyst. Therefore, BH_4^- reaction with the catalyst surface significantly decreased by limiting the interaction of the nucleophile that is

being generated from BH_4^- . On the other hand, the non-linear reaction pattern obtained at high $[\text{BH}_4^-]$ leading to an increase in k_{obs} is a clear indication of the adsorption competition between the substrate molecule and the redox agent upon the catalyst. This is demonstrated though the adsorption constants (K_{OII} and $K_{\text{BH}_4^-}$). Initially, the addition of BH_4^- at constant $[\text{OII}]$ means higher adsorption or interaction of BH_4^- onto the catalyst's active sites. However, a maximum saturation is reached at some point whereby the additional supply of electrons from BH_4^- produces a leveling off. This pattern of increase in k_{obs} as $[\text{OII}]$ increases and non-linear increase in BH_4^- while keeping one constant is also observed in the other kinetic data fits presented in **Appx. 2.3**, **Appx. 2.4**, and **Appx.2.5**.

The parameters obtained from the experimental fits are all listed in **Table 2.1**. The table depicted a quantitative analysis of the reaction pattern of the observed rate constant with the competitive changes that accompanied $[\text{BH}_4^-]$ and $[\text{OII}]$. The trends obtained in these experiments showed consistency with the previously reported result [43].



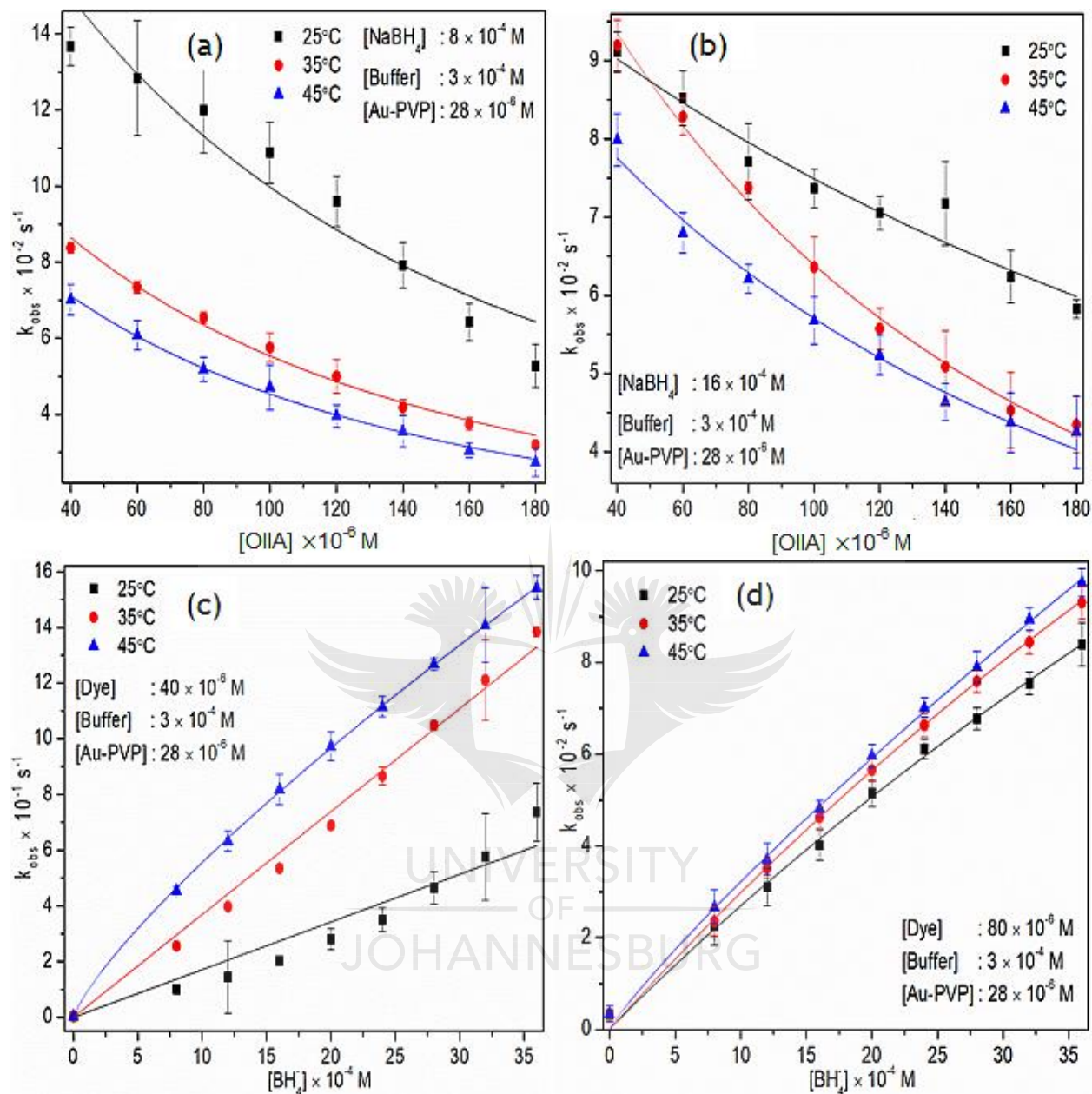


Figure 2.5: The plot of observed rate constant dependence on the OII concentration while maintaining a constant $[NaBH_4]$ (in a, and b respectively), and on $NaBH_4$ concentration, while keeping $[OII]$ (in c, and d respectively) constant using Langmuir-Hinshelwood approach for Au-PVP catalyzed reaction.

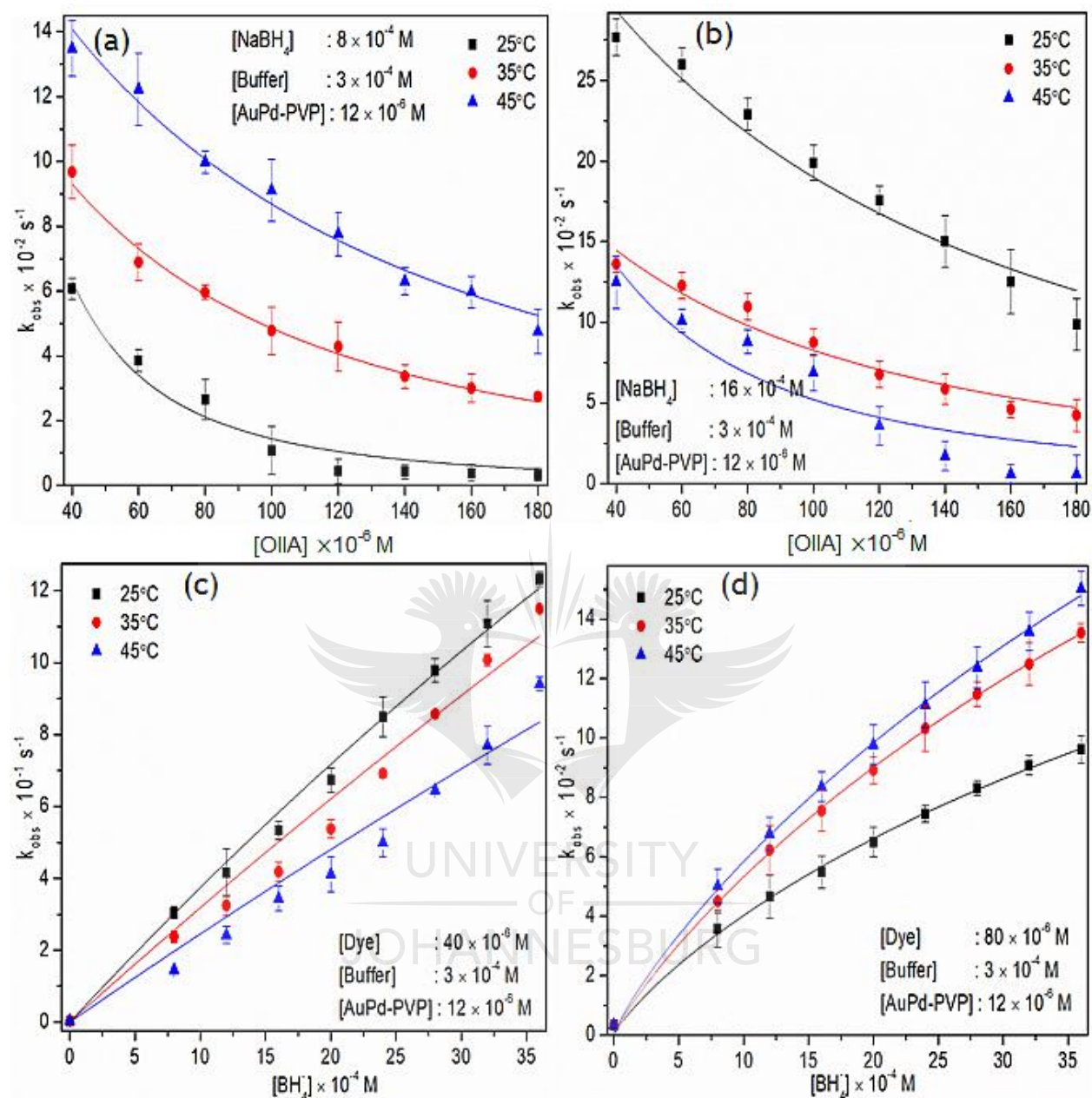


Figure 2.6: The plot of observed rate constant dependence on the OII concentration while maintaining a constant $[NaBH_4]$ (in a, and b respectively), and on $NaBH_4$ concentration, while keeping $[OII]$ (in c, and d, respectively) constant using Langmuir-Hinshelwood approach for AuPd-PVP catalyzed reaction.

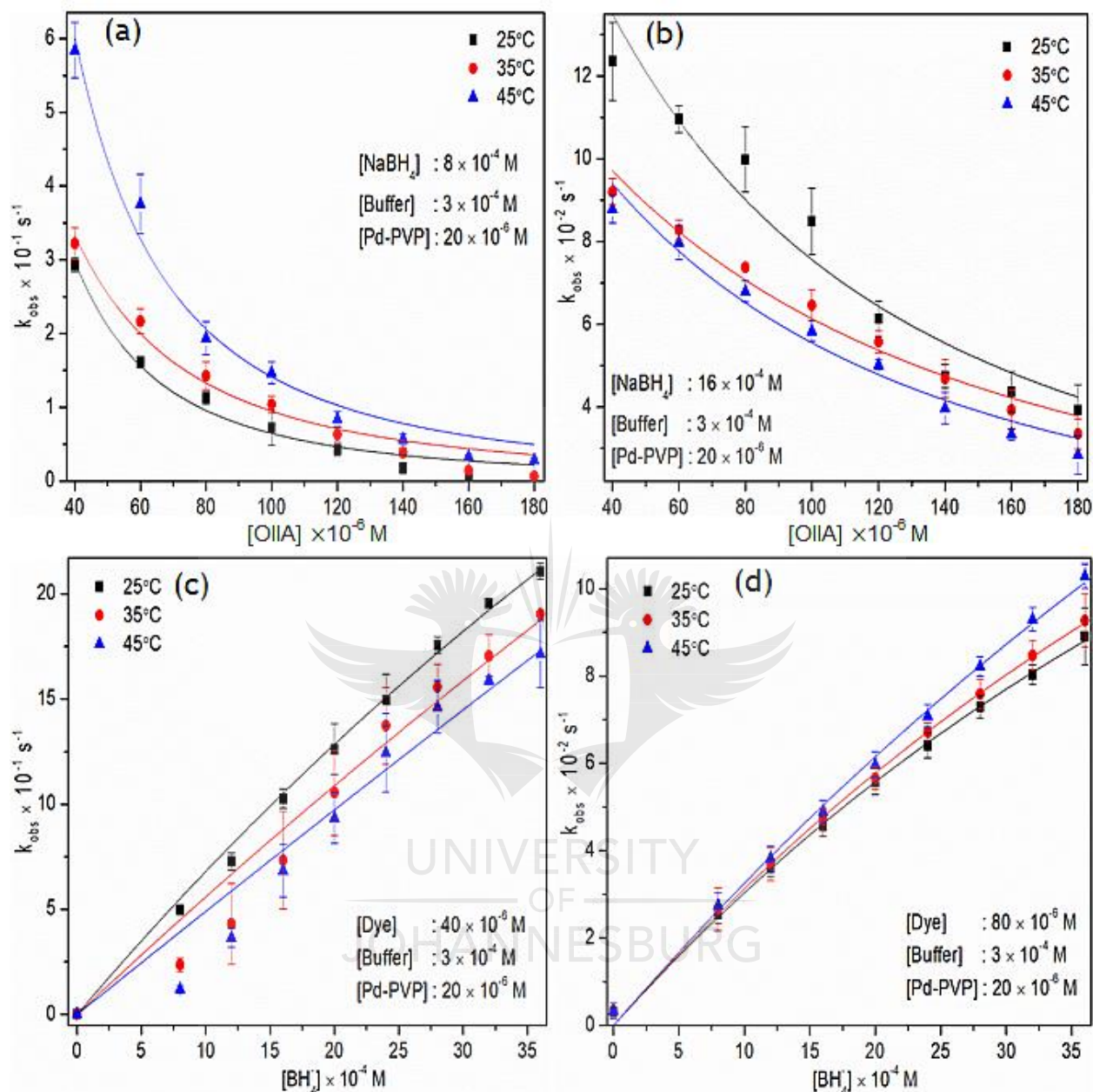


Figure 2.7: The plot of observed rate constant dependence on the OII concentration while maintaining a constant $[\text{NaBH}_4]$ (in a, and b respectively), and on NaBH_4 concentration, while keeping $[\text{OII}]$ (in c, and d, respectively) constant using the Langmuir-Hinshelwood approach for Pd-PVP catalyzed reaction.

Table 2.1:

Summary of the kinetic rate constant and the adsorption constant parameters obtained for Au-PVP, Pd-PVP, and AuPd-PVP catalysts from the experimental data following the Langmuir-Hinshelwood approach.

Catalyst	T (°C)	$k \cdot S$ (mol·m ² ·L ⁻¹ ·s ⁻¹)	K_{OII} (L·mol ⁻¹)	K_{BH_4} (L·mol ⁻¹)	n	m
Au-PVP	25	68.79 ± 7.08	7.22 ± 1.39	753.62 ± 86.23	0.90 ± 0.17	0.87 ± 0.18
	35	65.03 ± 7.12	6.07 ± 1.04	430.67 ± 60.48	0.90 ± 0.16	0.84 ± 0.22
	45	63.51 ± 7.29	5.35 ± 0.91	472.63 ± 62.10	0.90 ± 0.16	0.83 ± 0.22
AuPd-PVP	25	59.58 ± 6.81	10.89 ± 2.58	237.02 ± 35.97	1.00 ± 0.01	0.93 ± 0.08
	35	54.94 ± 5.81	16.58 ± 4.99	478.79 ± 105.60	1.00 ± 0.00	0.97 ± 0.04
	45	49.59 ± 4.99	21.04 ± 4.99	479.37 ± 120.86	1.00 ± 0.00	0.93 ± 0.09
Pd-PVP	25	90.14 ± 10.69	2.01 ± 0.27	138.79 ± 14.62	1.00 ± 0.00	0.94 ± 0.09
	35	111.72 ± 12.88	3.27 ± 0.51	163.24 ± 17.35	1.00 ± 0.00	0.90 ± 0.13
	45	151.24 ± 18.62	4.39 ± 0.70	235.84 ± 28.69	1.00 ± 0.00	0.95 ± 0.09

2.5.4 Orange II acid catalytic activity dependence on temperature

Catalyst's activity over the reduction of OII was investigated using three different temperatures at 25, 35, and 45 °C to get the activation energy. This parameter dependence on temperature was calculated through the observed rate constant obtained using the Arrhenius **Eqn. (2.7)** [44].

$$\ln k_{\text{obs}} = \ln A - \frac{E_a}{RT} \quad (2.7)$$

A defines the pre-exponential factor, R represents the universal gas constant, and T indicates the absolute temperature in Kelvin.

Also, the Eyring **Eqn. (2.8)** [45,46] was used to determine the thermodynamic parameters, which expressed the process of adsorption upon the catalyst's surface and the reduction process of the catalyst.

$$\ln \left(\frac{k_{\text{obs}}}{T} \right) = \frac{\Delta H^\ddagger}{RT} + \ln \left(\frac{k_B}{h} \right) + \frac{\Delta S^\ddagger}{R} \quad (2.8)$$

Where h expressed the Planck's constant, k_B is the Boltzmann constant, ΔH^\ddagger indicates enthalpy of activation, and entropy of activation is represented by ΔS^\ddagger . The Gibbs free energy (ΔG^\ddagger) is obtained from the values of ΔH^\ddagger and ΔS^\ddagger .

The plot of $\ln(k_{\text{obs}})$ against temperature reciprocal through which the activation energy was obtained is displayed in **Figure 2.8a**, while the Eyring graph constructed to evaluate both the enthalpy and entropy of activation is shown in **Figure 2.8b**. **Table 2.2** presents the summary of the values obtained for the activation and the thermodynamic parameters. The activation energy calculated for AuPd-PVP NPs was the lowest parameter compared to the Pd-PVP and Au-PVP NPs. This also accounts for the highest performing activity of AuPd-PVP, as earlier mentioned. The synergy effect contributed by both Pd and Au made up the catalyst. The reduction process of OII is seen to follow an endothermic process which validated the reaction is favoured with an increase in temperature [43]. Also, the computation of entropy of activation having positive parameters is an indication of a highly disordered system that produces a spontaneity effect. The IIO reduction upon the PVP-NPs interface was determined to be a spontaneous process from the negative values obtained for ΔG^\ddagger at 298.15 K also in **Table 2.2**.

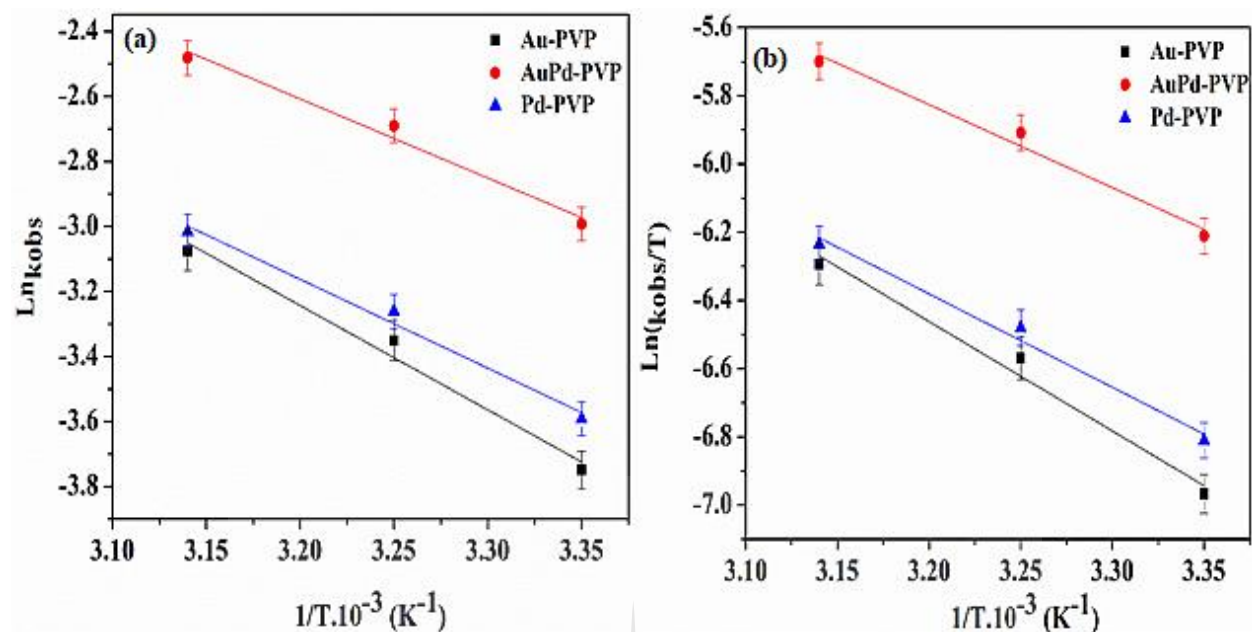


Figure 2.8: The plot of (a) Arrhenius and (b) Eyring obtained for the three different catalysts.

Table 2.2:

Activation and thermodynamic parameters for the reduction of OII

Catalyst	E_A (kJ.mol ⁻¹)	ΔH^\ddagger (kJ.mol ⁻¹)	ΔS^\ddagger (J.mol ⁻¹)	ΔG^\ddagger (kJ.mol ⁻¹) ^a
Au-PVP	8.19	26.66	136.62	-14.07
AuPd-PVP	5.38	20.22	134.77	-19.51
Pd-PVP	7.23	22.76	135.20	-17.55

^a 8×10^{-4} of M OII, and 16×10^{-4} M of NaBH₄ at 293.15 K

2.5.5 Catalytic comparison of OII acid degradation with other catalytic systems

Comparative analysis is a means of evaluating the effectiveness of a system. In order to establish the effectiveness of the PVP NPs activeness in degradation of OII within the microplate reader, a comparative thermodynamic analysis of the system was made with other catalytic processes in OII and MO (methyl orange). The comparison is summarized in **Table 2.3**. From the ranges of data obtained, it is evident that OII degradation has thermodynamic parameters relevant within the anticipated values when compared with other systems. The $+\Delta S^\ddagger$ peculiar to all the dye indicates the catalysts have affinity for dyes, while the $+\Delta H^\ddagger$ obtained in all shows that all dyes adsorption followed an endothermic process, and hence reactions are favored at high temperatures.

Table 2.3:

Data showing thermodynamic parameters comparison with other systems.

Catalysts	Dye	E_A (kJ.mol ⁻¹)	ΔH^\ddagger (kJ.mol ⁻¹)	ΔS^\ddagger (J.mol ⁻¹)	ΔG^\ddagger (kJ.mol ⁻¹) ^a	Ref
MnO ₂ /MCM-41	OII	-	26.34	114.29	-8.94	[42]
Zero-valent iron	OII	27.90	-	-	-	[47]
Pd ₁₁₀ /Dens-OH	MO	31.76	31.49	94.52	93.11	[15]
PVP-Pd	MO	89.27	95.06	101.12	64.93	[39]
PVP-Pt	MO	65.70	68.16	16.37	63.28	[39]
Au-PVP	OII	8.19	26.66	136.62	-14.07	TW
AuPd-PVP	OII	5.38	20.22	134.77	-19.51	TW
Pd-PVP	OII	7.23	22.76	135.20	-17.55	TW

Ref = Reference, MO = Methyl Orange, TW = This work.

2.6 Conclusion

Polyvinylpyrrolidone was used as stabilizing precursor for the synthesis of Au, Pd, and AuPd NPs to prevent agglomeration. The three different PVP NPs formed were applied for the catalytic reduction of OII to access their activity and examine the reaction mechanism if the Langmuir-Hinshelwood approach can be followed. The reaction depicted a *pseudo-first-order* reaction, and it conformed well with the Langmuir-Hinshelwood model, which provided clarity of the OII and BH_4^- adsorption process on the surface of PVP-NPs. The energy of activation determined revealed AuPd-PVP NPs as the most active NPs. Also, the reaction was found to be endothermically driven, and it was spontaneous for the three different catalysts.



2.7 References

- [1] C. Cabrera, A. Cornaglia, A. Córdoba, I. Magario, M. Lujan, Kinetic modelling of the hematin catalysed decolourization of Orange II solutions, *Chem. Eng. Sci.* 161 (2017) 127–137.
- [2] M.E. Ali, M.M. Rahman, S.M. Sarkar, S.B.A. Hamid, Heterogeneous metal catalysts for oxidation reactions, *J. Nanomater.* 2014 (2014).
- [3] E.C. Paz, V.S. Pinheiro, J. Frank, S. Joca, R. Augusto, S. De Souza, T.C. Gentil, M.R. V Lanza, D. Oliveira, A. Maria, P. Neto, I. Gaubeur, H. Paulo, Chemosphere Removal of Orange II (OII) dye by simulated solar photoelectro-Fenton and stability of WO₂ / Vulcan XC72 gas diffusion electrode, 239 (2020).
- [4] M. Hasan, K. Neon, S. Islam, Environmental Nanotechnology, Monitoring & Management MoO₃ and Ag co-synthesized TiO₂ as a novel heterogeneous photocatalyst with enhanced visible-light-driven photocatalytic activity for methyl orange dye degradation, *Environ. Nanotechnology, Monit. Manag.* 12 (2019) 100244.
- [5] A. Nasar, Application of polyaniline-based adsorbents for dye removal from water and wastewater — a review, *Environ. Sci. Pollut. Res.* (6) (2019) 5333-5356.
- [6] A.R. Prasad, A. Joseph, RSC Advances using waterborne poly vinyl pyrrolidone (PVP), *RSC Adv.* 7 (2017) 20960–20968.
- [7] H.B.M. Emrooz, M. Maleki, M. Shokouhimeh, Excellent adsorption of orange acid II on a water fern-derived micro-and mesoporous carbon, *J. Taiwan Inst. Chem. Eng.* 102 (2019) 99–109.
- [8] H., Chen, J., Motuzas, W., Martens, J.C.D., da Costa, Degradation of azo dye Orange II under dark ambient conditions by calcium strontium copper perovskite. *Applied Catalysis B: Environmental*, 221, (2018) 691-700.
- [9] X. Qin, Z. Li, Z. Zhu, H. Fu, H. Li, A. Wang, H. Zhang, H. Zhang, Journal of Materials Science & Technology Mechanism and kinetics of treatment of acid orange II by aged Fe-Si-B metallic glass powders, *J. Manuf. Syst.* 33 (2017) 1147–1152.
- [10] S. Batool, S. Akib, M. Ahmad, K.S. Balkhair, M.A. Ashaf, Study of Modern Nano Enhanced Techniques for Removal of Dyes and Metals, 2014 (2014).
- [11] He, Liang-Nian, R. D. Rogers, D. Su, P. Tundo, and Z. C. Zhang. "Green chemistry and sustainable technology." (2016).
- [12] T. Ohashi, A.M.T. Jara, A.C.L. Batista, L.O. Franco, M.A.B. Lima, M. Benachour,

- C.A. Alves, G.M. Campos-takaki, An Improved Method for Removal of Azo Dye Orange II from Textile Effluent Using Albumin as Sorbent, (2012).
- [13] E.C. Paz, L.R. Aveiro, V.S. Pinheiro, F.M. Souza, V.B. Lima, F.L. Silva, P. Hammer, M.R. V Lanza, M.C. Santos, Applied Catalysis B : Environmental Evaluation of H₂O₂ electrogeneration and decolorization of Orange II azo dye using tungsten oxide nanoparticle-modified carbon, Appl. Catal. B Environ. 232 (2018) 436–445.
- [14] G. Li, Y. Li, Z. Wang, H. Liu, Green synthesis of palladium nanoparticles with carboxymethyl cellulose for degradation of azo-dyes, Mater. Chem. Phys. 187 (2017) 133–140.
- [15] A.K. Ilunga, T. Khoza, E. Tjabadi, R. Meijboom, Effective Catalytic Reduction of Methyl Orange Catalyzed by the Encapsulated Random Alloy Palladium-Gold Nanoparticles Dendrimer, ChemistrySelect. 2 (2017) 9803–9809.
- [16] S. Wunder, F. Polzer, Y. Lu, Y. Mei, M. Ballauff, Kinetic Analysis of Catalytic Reduction of 4-Nitrophenol by Metallic Nanoparticles Immobilized in Spherical Polyelectrolyte Brushes, (2010) 8814–8820.
- [17] K. Hayakawa, T. Yoshimura, K. Esumi, Preparation of Gold - Dendrimer Nanocomposites by Laser Irradiation and Their Catalytic Reduction of 4-Nitrophenol, (2003) 5517–5521.
- [18] S. Cai, D. Wang, Z. Niu, Y. Li, Progress in organic reactions catalyzed by bimetallic nanomaterials, Chinese J. Catal. 34 (2013) 1964–1974.
- [19] K. An, and G.A.Somorjai, 2015. Nanocatalysis I: synthesis of metal and bimetallic nanoparticles and porous oxides and their catalytic reaction studies. Catalysis Letters, 145(1), pp.233-248.
- [20] N. Bingwa, R. Meijboom, Evaluation of catalytic activity of Ag and Au dendrimer-encapsulated nanoparticles in the reduction of 4-nitrophenol, J. Mol. Catal. A Chem. 396 (2015) 1–7.
- [21] A.K. Ilunga, R. Meijboom, Applied Catalysis A: General Synthesis of narrowly dispersed silver and gold nanoparticles and their catalytic evaluation for morin oxidation, 509 (2016) 17–29.
- [22] E. Blanco, P. Atienzar, P. Hernández, C. Quintana, The Langmuir-Hinshelwood approach for kinetic evaluation of cucurbit[7]uril-capped gold nanoparticles in the reduction of the antimicrobial nitrofurantoin, Phys. Chem. Chem. Phys. 19 (2017)

- 18913–18923.
- [23] S.R. Thawarkar, B. Thombare, B.S. Munde, N.D. Khupse, Kinetic investigation for the catalytic reduction of nitrophenol using ionic liquid stabilized gold nanoparticles, *RSC Adv.* 8 (2018) 38384–38390.
- [24] N. Yan, C. Xiao, Y. Kou, Transition metal nanoparticle catalysis in green solvents, *Coord. Chem. Rev.* 254 (2010) 1179–1218.
- [25] M.J. Ndolomingo, R. Meijboom, Kinetic analysis of catalytic oxidation of methylene blue over γ -Al₂O₃ supported copper nanoparticles, *Appl. Catal. A Gen.* 506 (2015) 33–43.
- [26] L. Guo, J. Bai, C. Li, Q. Meng, H. Liang, W. Sun, H. Li, H. Liu, Applied Surface Science A novel catalyst containing palladium nanoparticles supported on PVP composite nanofiber films : Synthesis, characterization and efficient catalysis, *Appl. Surf. Sci.* 283 (2013) 107–114.
- [27] M. Nemanashi, R. Meijboom, Catalytic Behavior of Different Sizes of Dendrimer-Encapsulated Au n Nanoparticles in the Oxidative Degradation of Morin with H₂O₂, (2015).
- [28] M.S. Xaba, R. Meijboom, Applied Surface Science Kinetic and catalytic analysis of mesoporous Co₃O₄ on the oxidation of morin, *Appl. Surf. Sci.* 423 (2017) 53–62.
- [29] K.M. Koczkur, S. Mourdikoudis, L. Polavarapu, S.E. Skrabalak, K.M. Koczkur, S. Mourdikoudis, L. Polavarapu, S.E. Skrabalak, P. Pvp, R.S. Chem-, Polyvinylpyrrolidone (PVP) in nanoparticle synthesis To cite this version : HAL Id : hal-01217114, *R. Soc. Chem.* 44 (2015) 17883–17905.
- [30] M.B. Gawande, A. Goswami, T. Asefa, X. Huang, R. Silva, X. Zou, R. Zboril, R.S. Varma, Cu and Cu-Based Nanoparticles : Synthesis and Applications in Catalysis, (2016).
- [31] A.R. Prasad, A. Joseph, Synthesis, characterization and investigation of methyl orange dye removal from aqueous solutions using waterborne poly vinyl pyrrolidone (PVP) stabilized poly aniline (PANI) core-shell nanoparticles, *RSC Adv.* 7 (2017) 20960–20968.
- [32] T. Gutul, E. Rusu, N. Condur, V. Ursaki, E. Goncarenco, P. Vlazan, Preparation of poly(N-vinylpyrrolidone)-stabilized ZnO colloid nanoparticles, *Beilstein J. Nanotechnol.* 5 (2014) 402–406.

- [33] I.A. Safo, M. Werheid, C. Dosche, M. Oezaslan, The role of polyvinylpyrrolidone (PVP) as a capping and structure-directing agent in the formation of Pt nanocubes, *Nanoscale Adv.* 1 (2019) 3095–3106.
- [34] S. Kunwar, P. Pandey, and J. Lee, Enhanced Localized Surface Plasmon Resonance of Fully Alloyed AgAuPdPt, AgAuPt, AuPt, AgPt, and Pt Nanocrystals: Systematical Investigation on the Morphological and LSPR Properties of Mono-, Bi-, Tri-, and Quad-Metallic Nanoparticles, *ACS Omega* 2019, 4, 17340-17351
- [35] X. Long, Z. Yang, H. Wang, M. Chen, K. Peng, Q. Zeng, A. Xu, Selective Degradation of Orange II with the Cobalt (II) – Bicarbonate – Hydrogen Peroxide System, (2012).
- [36] F.S. Freyria, B. Bonelli, R. Sethi, M. Armandi, E. Belluso, E. Garrone, Reactions of Acid Orange 7 with Iron Nanoparticles in Aqueous Solutions, (2011) 24143–24152.
- [37] X. Qin, Z. Li, Z. Zhu, H. Fu, H. Li, A. Wang, H. Zhang, H. Zhang, Mechanism and kinetics of treatment of acid orange II by aged Fe-Si-B metallic glass powders, *J. Mater. Sci. Technol.* 33 (2017) 1147–1152.
- [38] J. Fu, Z. Chen, M. Wang, S. Liu, J. Zhang, J. Zhang, R. Han, Q. Xu, Adsorption of methylene blue by a high-efficiency adsorbent (polydopamine microspheres): kinetics, isotherm, thermodynamics and mechanism analysis, *Chem. Eng. J.* 259 (2015) 53–61.
- [39] Y.C. Wong, Y.S. Szeto, W.H. Cheung, G. McKay, Pseudo-first-order kinetic studies of the sorption of acid dyes onto chitosan, *J. Appl. Polym. Sci.* 92 (2004) 1633–1645.
- [40] G. Lente, Facts and alternative facts in chemical kinetics: remarks about the kinetic use of activities, termolecular processes, and linearization techniques, *Curr. Opin. Chem. Eng.* 21 (2018) 76–83.
- [41] P. Ncube, N. Bingwa, H. Baloyi, R. Meijboom, Catalytic activity of palladium and gold dendrimer-encapsulated nanoparticles for methylene blue reduction: A kinetic analysis, *Appl. Catal. A Gen.* 495 (2015) 63–71.
- [42] N. Bingwa, S. Bewana, M. Haumann, R. Meijboom, Revisiting kinetics of morin oxidation: Surface kinetics analysis, *Appl. Surf. Sci.* 426 (2017) 497–503.
- [43] A.K. Ilunga, B.B. Mamba, T.T.I. Nkambule, Fabrication of palladium and platinum nanocatalysts stabilized by polyvinylpyrrolidone and their use in the hydrogenolysis of methyl orange, *React. Kinet. Mech. Catal.* (2020) 1–15.
- [44] C.C. Yang, Y.W. Mai, Thermodynamics at the nanoscale: A new approach to the investigation of unique physicochemical properties of nanomaterials, *Mater. Sci. Eng.*

- R Reports. 79 (2014) 1–40.
- [45] G. Lente, I. Fábián, A.J. Poë, A common misconception about the Eyring equation, *New J. Chem.* 29 (2005) 759–760.
- [46] S. Yang, Y. Wu, Y. Wu, L. Zhu, *Journal of the Taiwan Institute of Chemical Engineers* Optimizing decolorization of Acid Fuchsin and Acid Orange II solution by MnO₂ loaded MCM-41, *J. Taiwan Inst. Chem. Eng.* 50 (2015) 205–214.
- [47] C. Zhang, Z. Zhu, H. Zhang, Z. Hu, Rapid decolorization of Acid Orange II aqueous solution by amorphous zero-valent iron, *J. Environ. Sci.* 24 (2012) 1021–1026.



Chapter 3

In-situ Replacement of Cu-DEN: An Approach for Preparing a More Noble Metal Nanocatalyst for Catalytic Use.

NJC



PAPER

[View Article Online](#)
[View Journal](#) | [View Issue](#)



Cite this: *New J. Chem.*, 2020, 44, 20322

Received 1st September 2020,
Accepted 27th October 2020

DOI: 10.1039/d0nj04381h

rsc.li/njc

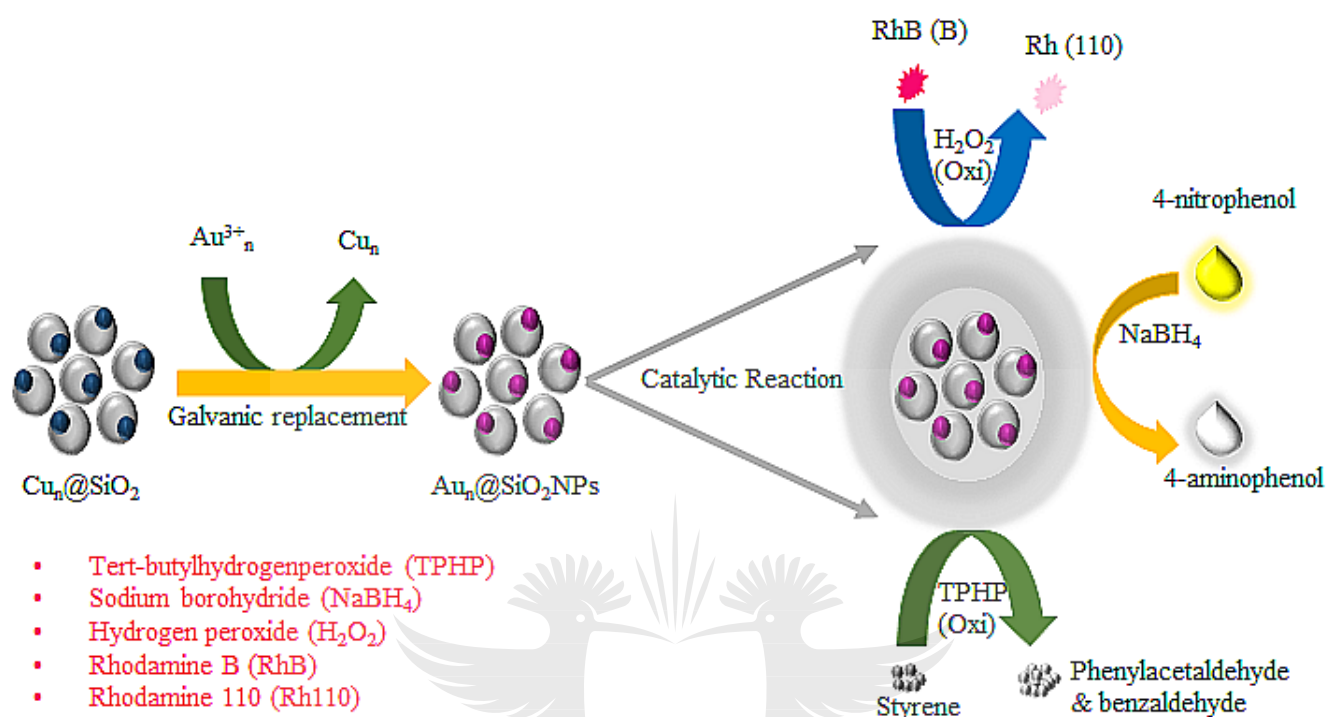
In situ replacement of Cu-DEN: an approach for preparing a more noble metal nanocatalyst for catalytic use†

Oluwatayo Racheal Onisuru, Charles O. Oseghale and Reinout Meijboom *

The advantage of dendritic monodisperse macromolecules' dual templating ability was useful in the formation of silica-supported copper nanoparticles $\text{Cu}_n@/\text{SiO}_2$ NPs. This was acquired by the initial synthesis of a silica framework (G4-PAMAM- NH_2 - SiO_2) as a mesoporous support using amine-terminated generation 4 PAMAM dendrimers (G4-PAMAM- NH_2). The encapsulated $\text{Cu}_n@/\text{SiO}_2$ NPs, calcined at 500 °C, were made to undergo a displacement reaction with Au^{3+} generated from the equivalent molar addition of HAuCl_4 . This resulted in the formation of $\text{Au}_n@/\text{SiO}_2$ NPs upon *in situ* replacement at a regulated pH. The synthesized nanoparticles were characterized and examined. The catalysts were shown to be catalytically active in the hydrogenation of 4-nitrophenol, and oxidation of rhodamine B as model reactions, before oxidation of styrene using TBHP. Also, the stability of the catalyst was evaluated, and the catalytic activity was retained after three consecutive cycles.

OF
JOHANNESBURG

Graphical abstract



UNIVERSITY
OF
JOHANNESBURG

Abstract

The dual templating ability of monodisperse dendritic macromolecules was used to produce silica-supported copper nanoparticles $\text{Cu}_n@ \text{SiO}_2 \text{NPs}$. This was accomplished by synthesizing a silica framework (G4-PAMAM- $\text{NH}_2\text{-SiO}_2$) as mesoporous support utilizing amine-terminated generation 4 PAMAM dendrimers (G4-PAMAM- NH_2). After calcining the encapsulated $\text{Cu}_n@ \text{SiO}_2$ NPs at 500 °C, the Au^{3+} produced by the equivalent molar addition of HAuCl_4 was used to initiate a displacement process. When $\text{Cu}_n@ \text{SiO}_2 \text{NPs}$ were replaced *in-situ* at a controlled pH of 3.2, this resulted in the production of $\text{Au}_n@ \text{SiO}_2 \text{NPs}$. The nanoparticles produced were described and analyzed. Catalytic activity was shown for the catalysts in the hydrogenation of 4-nitrophenol and the oxidation of rhodamine B as a model reaction prior to the oxidation of styrene with TBHP. Additionally, the catalysts' stability was determined, and catalytic activity was maintained after three consecutive cycles.

Keywords: Silica sphere; $\text{Cu}_n@ \text{SiO}_2 \text{NPs}$; *In-situ* replacement; Galvanic exchange; Oxidation-reduction.



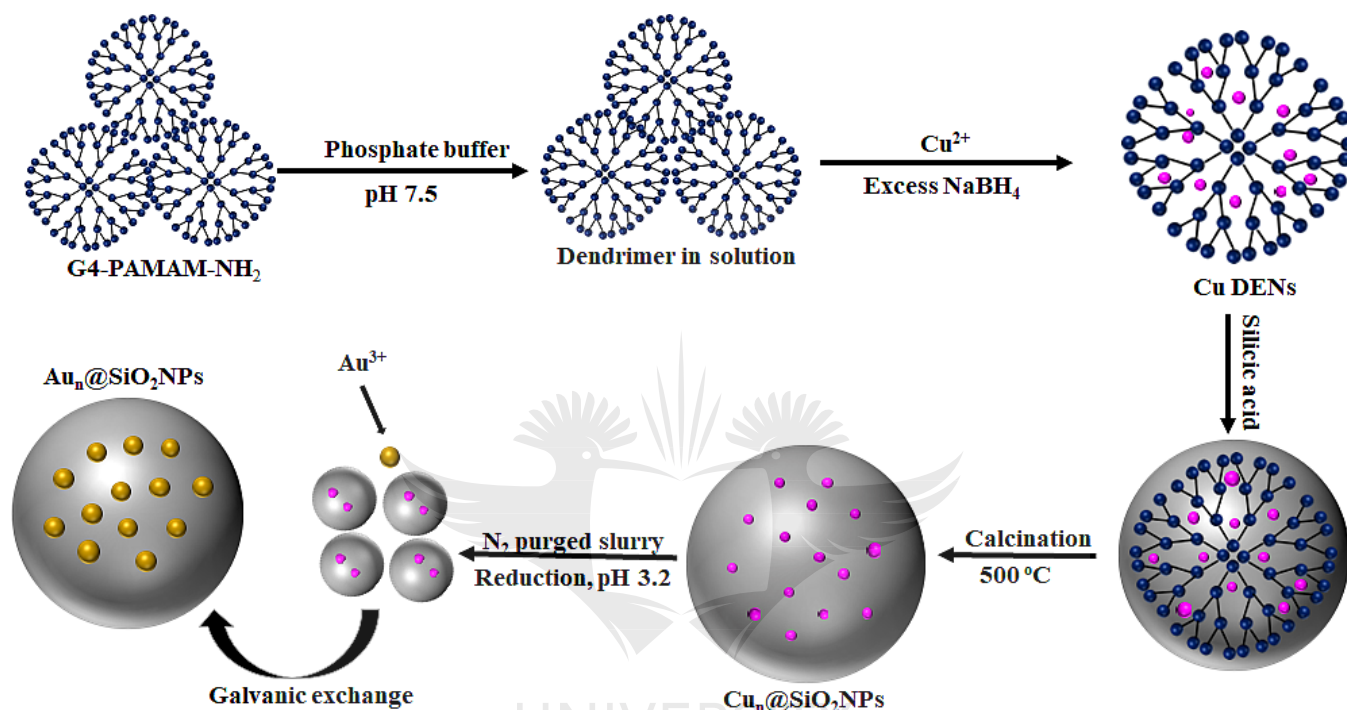
3.1 Introduction

The many uses of nanoparticles will continue to draw researchers' attention. This is owing to their unmatched ability to improve selectivity and productivity. Metal nanoparticles are paving the way for unprecedented advancements in the area of catalysis [1]. The critical property of metal nanoparticles, which is a high surface area to volume ratio, profoundly affects their performance. Generally, they are fabricated in the presence of stabilizers under normal circumstances to avoid agglomeration. This allows for precise control over the particle size that is produced [2]. The emphasis has long been on the use of dendrimers as stabilizers for metal nanoparticles, which has resulted in a considerable study on the production of dendrimer encapsulated nanoparticles throughout the years [1–11]. Dendrimers are three-dimensional macromolecules with a globular form that readily accept metal nanoparticles for application in catalysis [1]. However, the procedures for synthesizing some metal nanoparticles are not always as straightforward and rapid as expected. This is shown by dendrimer-encapsulated platinum nanoparticles (Pt-DENs), which need at least 72 h to accomplish full complexation of the metal ions with the dendrimer [12]. As a result, a more rapid alternate path is needed.

The purpose of this study was to synthesize dendrimer-encapsulated copper nanoparticles (CuDENs) stabilized using generation 4 amine-terminated PAMAM (G4 PAMAM-NH₂) dendrimers. Additionally, an attempt was made to immobilize colloidal CuDENs onto mesoporous silica support in order to create heterogeneous catalysts. Compared to homogeneous catalysts, heterogeneous catalysts possess the benefit of recoverability and separation from the reaction media [4]. Researchers have used silica as mesoporous support for metal nanoparticles [13–16]. Not only have mesoporous silica materials been shown to be great for chromatographic, cosmetic, and photographic applications, but they have also shown to be good for catalytic applications [17]. As a result, considerable attention has been directed towards its use. Yanqiu and colleagues [18] described the synthesis of hollow MCM-41 (Mobil Composition of Matter No. 41) microspheres using tetraethyl orthosilicate (TEOS) and a dual template. The dual template was produced by dissolving cetyltrimethylammonium bromide (CTAB) in soap-free latex poly(styrene-methyl methacrylate) microspheres and sequentially removing the polymer core with tetrahydrofuran [18].

In this work, we used TEOS and hydrochloric acid at room temperature to synthesize mesoporous silica spheres with a distinct phase for the immobilization of CuDENs. This is a convenient method for synthesizing silica-supported gold nanoparticles (Au_n@SiO₂) NPs through in-situ galvanic exchange with

gold after the initial synthesis of $\text{Cu}_n@/\text{SiO}_2$ NPs. This was followed by adding the Au^{3+} metal atom (Au) to the previously synthesized NPs, as shown in **Scheme 3.1**. Au is more noble, having a greater electrochemical potential and the ability to undergo simultaneous reduction and replacement [19]. This kind of catalyst is expected to have a significant effect on catalysis.



Scheme 3.1: Schematic illustration of CuDENS immobilization on silica and subsequent *in-situ* replacement.

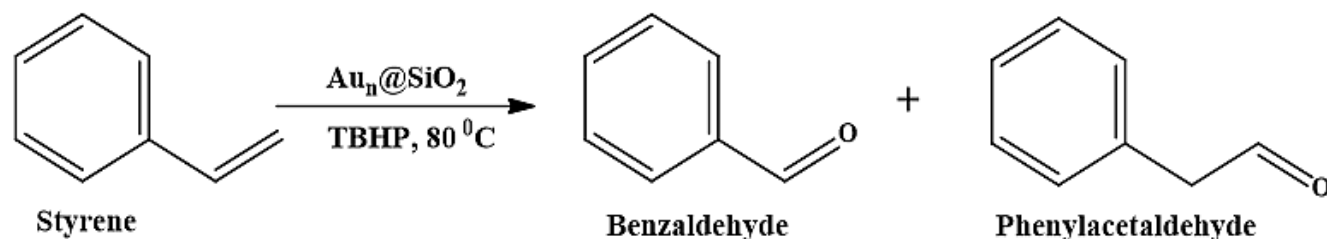
However, one disadvantage of Cu-based catalyst synthesis is that they are oxygen intolerant [20]. They oxidize rapidly when exposed to air. As a result, the synthesis was carried out in an inert environment prior to utilizing $\text{Cu}_n@/\text{SiO}_2$ NPs though a replacement reaction with Au to produce $\text{Au}_n@/\text{SiO}_2$ NPs. Meanwhile, this replacement was facilitated by lower standard electrode potential (+0.340 E^o) volts possessed by Cu^{2+} , enabling easy substitution with Au^{3+} possessing 1.50 E^o volts.

When a metal ion with a greater oxidative potential gets exchanged with another metal atom having a lower standard electrode potential, a replacement reaction occurs. This causes the surface metal atom to disintegrate though oxidation, resulting in the reduction of the metal ion with a greater oxidative potential [19]. Thus, galvanic replacement is the displacement that occurs when a zero-valent metal is replaced with

a more noble metal to form stable, well-distributed, and compositionally pure metal atom nanoparticles from a reduced precursor [21]. Galvanic exchange has been used successfully to manufacture metal nanoparticles in a homogeneous phase [12,21–23]. Hence we developed a heterogeneous catalyst in this study though a replacement reaction since in-situ replacement is a well-known technique for synthesizing NPs. Researchers may use it to generate completely reduced metal NPs with a particular atom at distinct periods while retaining the same amount of metal precursors [12,24].

One of the constraints on AuNPs is their mobility and sintering at elevated temperatures owing to thermal instability. Catalyst thermal stability is critical for many industrially produced high-temperature processes, including hydrocracking, partial oxidation, and total combustion [25]. As a result, a dual templating approach for metal nanoparticles was used first. To test this catalyst's activity in oxidation-reduction reaction, 4-nitrophenol reduction, rhodamine B (RhB) oxidation, and styrene oxidation were employed as model reactions. 4-nitrophenol and RhB are two of the most frequent pollutants produced by industrial processes such as textiles, medicines, cosmetics, dyeing, food additives, plastics, leather, and printing, among others [26,27]. The degradation of 4-nitrophenol and RhB was detected using time-resolved UV-vis spectroscopy at 400 and 554 nm, respectively [28].

Numerous investigations on the selective oxidation of styrene to styrene oxide, benzaldehyde, phenylacetaldehyde, acetophenone, and benzoic acid have been conducted through the years [29–31]. Due to their fragrance, phenylacetaldehyde and benzaldehyde are used as chemical intermediates in the synthesis of bulk chemicals, agriculture, fine chemical goods, and the production of fragrances, medicines, and dyes [30,32]. According to several reports, the reaction circumstances and catalyst type are significant determinants of product production [33]. As a result, early studies used standard reaction parameters such as reaction temperature [31], solvent type [30], oxidant [34], and catalyst concentration [30]. As a consequence of the results obtained, the selectivity of our catalysts was limited to benzaldehyde and phenylacetaldehyde, as shown in **Scheme 3.2**. without producing any undesirable product.



Scheme 3.2: Representative illustration of styrene oxidation showing the products formed.

3.2 Experimental Section

3.2.1 Chemicals and materials

Amine-terminated generation 4 PAMAM dendrimers (10 wt 5% in methanol), 2-phenylacetaldehyde ($\geq 98\%$), $[\text{HAuCl}_4] \cdot 3\text{H}_2\text{O}$ (99.9%), rhodamine B ($\geq 99.90\%$), styrene ($\geq 99\%$) TBHP (70% in water), styrene oxide ($\geq 97\%$), benzaldehyde ($\geq 99\%$), acetonitrile ($\geq 99.9\%$), 4-nitrophenol ($\geq 99.5\%$), dichloromethane (DCM) ($\geq 99.8\%$), tetraethyl orthosilicate (TEOS) (99%), phosphate buffer (pH ~ 7.87) with K_2HPO_4 (98%), HCl (32%), sodium carbonate (Na_2CO_3) (90%) hydrogen peroxide (H_2O_2) 30%, and $\text{CuSO}_4 \cdot 5\text{H}_2\text{O}$ were all acquired from Sigma-Aldrich. Promack Chemicals provided KMnO_4 (99.4%), NaOH (99.9%), and sodium bicarbonate (NaHCO_3) (99.60%). Fluka provided perchloric acid (HClO_4) (70.0%) and sodium borohydride ($\geq \text{NaBH}_4$ 98.0%). All materials were utilized as received. All experimental investigations were conducted using Milli-Q water $18.2 \text{ M}\Omega \cdot \text{cm}$.

3.2.2 Synthesis of SiO_2 spheres

The silica spheres were synthesized similarly to that described in a previous study with some modifications [4]. The synthesis started with the transfer of generation 4- NH_2 dendrimer (10 wt% in MeOH, 0.18 g, $1.28 \cdot 10^{-6} \text{ M}$) into a round-bottomed, two-necked flask for methanol removal *in vacuo*. To dissolve the dendrimer, 60 mM phosphate buffer was added and diluted with degassed Milli-Q water to produce a total volume of 8 mL and 0.16 mM. This was concluded by adding silicic acid (5 mL), which was generated by hydrolyzing TEOS in 1 mM HCl in a dropwise method and centrifuged the precipitate for 20 min at 3,500 rpm. Finally, it was washed with degassed Milli-Q water and dried *in vacuo* overnight at 70°C .

3.2.3 Synthesis of $\text{Cu}_n@SiO_2$ NPs with G4-PAMAM- NH_2 dendrimer as a stabilizer

A literature method was also used for the synthesis [4]. To summarize, an aqueous CuSO_4 solution prepared in a 16:1 ratio of G4-PAMAM- NH_2 dendrimer (40 μL , 0.1 M, 4.0 μmol) was pipetted into a

premade dendrimer in 60 mM phosphate buffer solution. This was followed by the addition of degassed Milli-Q deionized H₂O to a total volume of 8 mL. For 1 h in an inert environment, G4-PAMAM-NH₂/Cu²⁺ was agitated to achieve complete complexation at a fixed pH of 7.5. After this, a complete reduction of the Cu²⁺ ions in solution was achieved by adding tenfold excess of NaBH₄ (400 μL, 0.1 M, 0.5 μmol) to produce CuDENSs. Subsequently, preformed silicic acid was progressively added to the CuDENSs while constantly stirring under an inert environment for 15 min. This results in silica precipitation, which was collected after centrifuging and drying overnight at 70 °C. Finally, the template was removed by calcination for 3 h at 500 °C at a rate of 1°C/min.

3.2.4 Preparation of Au_n@SiO₂NPs by in-situ replacement

This was carried out using Zhao and Crooks' stepwise description [22]. First, a fine powder of Cu_n@SiO₂ produced via air calcination was suspended in Milli Q water and mixed to create a slurry. It was adequately reduced to avoid oxidation since calcination was carried out in air. Before adding H₂AuCl₄ (40 μL, 0.1 M, 4.0 μmol), the pH of the resulting slurry was controlled to 3.2 from 7.5 using 0.1 M HClO₄. The addition of H₂AuCl₄ changed the color from brownish to bright purple. However, it was allowed to stir for about 30 min at a temperature of 25 °C to allow for replacement. After centrifuging the slurry for 20 min at 3,500 rpm, the supernatant was collected and dried *in vacuo* at 70 °C to produce powdered Au_n@SiO₂NPs.

3.2.5 Characterization of the catalyst

All spectrophotometric studies used to measure the absorbance were performed in a 3 mL quartz cuvette using a Shimadzu UV-1800. The internal structure of the images acquired by high-resolution transmission electron microscopy (H-TEM) was performed using a JEOL JEM-2100F electron microscope equipped with a 200 kV voltage accelerator. This was accomplished by ultrasonically suspending the fine powders of Cu_n@SiO₂NPs and Au_n@SiO₂NPs in water. A few drops of Cu_n@SiO₂NPs and Au_n@SiO₂NPs were put on Ni and Cu grids, respectively, and the imaging system was set up. Micromeritics ASAP 2460 device was used for nitrogen sorption analyses of the materials. Before the analyses, the samples were degassed overnight at 90 °C under nitrogen gas, and the samples were allowed to cool under vacuum. The surface area of the samples was determined using the Brunauer-Emmett-Teller (BET) technique, and the pore size distributions were determined using the Barrett-Joyner-Halenda (BJH) method. The thermal stability of the samples was determined using the SDT Q600 thermogravimetric analyzer (TA Instrument) between 0 and 1000 °C at a heating rate of 10 °C/min. The FTIR analysis was performed using a Shimadzu

IRAffinity-1. Powder X-ray diffraction investigation was performed on a Rigaku SmartLab at two different angles ranging from 5° to 80° using Cu K radiation ($\lambda = 1.54056 \text{ \AA}$). Using an ORION model 520A pH meter equipped with a Schott 25 blue line pH electrode, all pH changes were made.

3.2.6 Catalytic reactions

The absorbance was monitored with a quartz cuvette (3 mL) in a Shimadzu UV-1800 spectrophotometer. At room temperature, the reduction of $\text{Cu}_n\text{@SiO}_2\text{NPs}$ and $\text{Au}_n\text{@SiO}_2\text{NPs}$ was monitored from $\lambda = 600$ to $\lambda = 200$ nm at 3 min and 1 min intervals, respectively. A stock solution of nitrophenol (4-nitrophenol; 0.2 μmol) in 0.1 M sodium hydroxide was prepared. A newly prepared NaBH_4 solution (0.1 M, 0.32 mM) was joined to the concentration of 4-nitrophenol in addition to aliquots of $\text{Cu}_n\text{@SiO}_2\text{NPs}$ and $\text{Au}_n\text{@SiO}_2\text{NPs}$. The UV-vis spectroscopy was continuously used to record the time-resolved absorbance at each degradation stage.

A UV-vis spectrophotometer was also used to examine the oxidation of RhB. We prepared an aqueous solution of RhB (0.1 M) and measured the oxidant's concentration by titrating against potassium permanganate. The reaction proceeded by varying $\text{Au}_n\text{@SiO}_2\text{NPs}$ catalyst from 0.3 mg and 0.7 mg while maintaining constant amounts of substrate and oxidant in the presence of a freshly prepared carbonate buffer. The process was repeated by changing the substrate and oxidant concentrations at various periods while keeping the other parameters constant. The substrate adsorption onto the catalyst's surface was examined at concentrations ranging from 0.012 mM to 0.020 mM, while the adsorption of oxidant at concentrations ranging from 24 mM to 32 mM. A constant buffer media (sodium carbonate and sodium hydrogen carbonate) with a pH of 7.5 was maintained throughout the investigation. [27] All validations were performed using a 3 mL quartz cuvette.

Styrene was catalytically oxidized using a carousel TM multi-reactor (Radley Discovery Technologies) connected to a reflux condenser. $\text{Au}_n\text{@SiO}_2\text{NPs}$ (0.1 g), 4.7 mmol (300 μL) decane was used as an internal standard, 2 mmol (214 μL) styrene, and 3 mmol (415.2 μL) TBHP were pipetted into a 50 mL vial containing 10 mL acetonitrile (solvent). At 450 rpm/80 °C, this was allowed to stir. For 6 h, samples were collected at 1h intervals. Shimadzu GC-2010 Plus equipped with a flame ionization detector (FID) and a Restek-800-356-1688 capillary column (30 m \times 0.25 mm \times 0.25 μmol of film thickness) were used to

analyze the goods. The injection port temperature was adjusted to 250 °C, while the FID stayed at 300 °C. The temperature of the column was maintained at 300 °C, and the carrier gas was nitrogen gas.

3.3 Result and discussion.

3.3.1 TEM Characterization of silica spheres, $\text{Cu}_n\text{@SiO}_2\text{NPs}$ and $\text{Au}_n\text{@SiO}_2\text{NPs}$

Figure 3.1a illustrates the morphological appearance of silica spheres produced in a 60 mM phosphate buffer solution. It has been observed that pH, temperature, and alkalinity significantly impact the materials' structure, such as silica [35]. Thus, the synthesis of silica spheres at room temperature and a pH of 7.87 results in the silica having a spherical shape. This facilitates the encapsulation of NPs. The particle size (283.3 nm) found is equivalent to that previously reported under comparable circumstances [4].

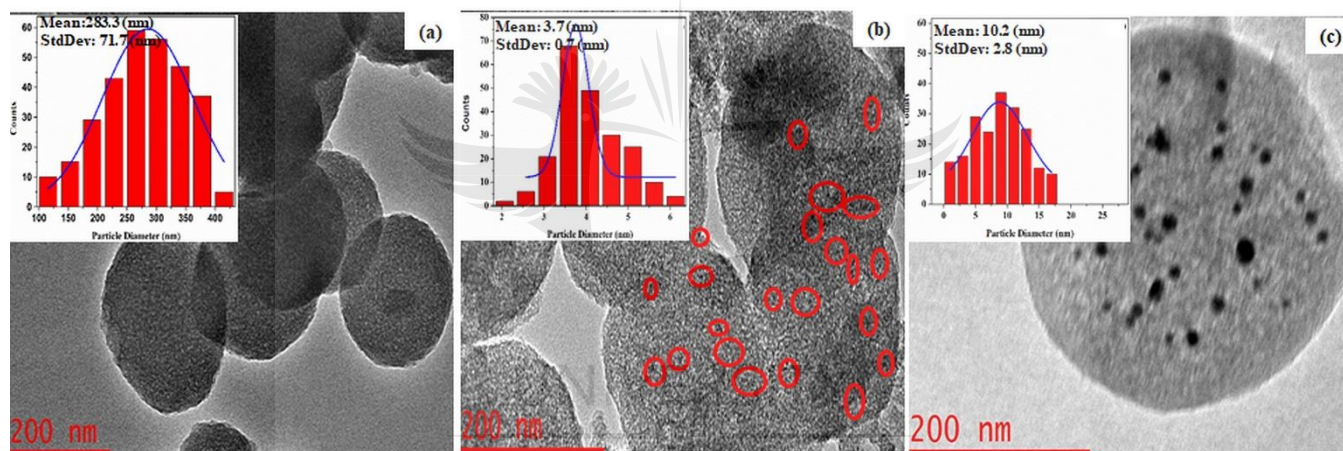


Figure 3.1: The TEM images of (a) G4-PAMAM-NH₂ templated silica sphere (G4-PAMAM-NH₂-SiO₂) (b) $\text{Cu}_n\text{@SiO}_2\text{NPs}$ and (c) $\text{Au}_n\text{@SiO}_2\text{NPs}$.

The TEM images as shown in **Figure 3.1b** and **3.1c** illustrate the interior morphology of $\text{Cu}_n\text{@SiO}_2\text{NPs}$ and $\text{Au}_n\text{@SiO}_2\text{NPs}$ produced using the templating and displacement methods, respectively. The histogram plotted for $\text{Cu}_n\text{@SiO}_2\text{NPs}$ showed that the particle size was 3.7 ± 0.7 nm, indicating that the NPs were sparsely distributed. The picture acquired for $\text{Au}_n\text{@SiO}_2\text{NPs}$ demonstrated that the silica framework with spherical shape was retained after replacement. This also demonstrates the effective encapsulation of the particles' increase in size distribution to 10.2 ± 3.7 nm. The significant increase may be the consequence of 3 h of calcination at 500 °C, and the breakdown of the organic dendrimer stabilizers present before calcination. Change in particle size has been documented as the implication of calcination

[25] due to the steady increase in the number of atoms [36]. However, it is worth noting that this increase in the particle size of $\text{Au}_n\text{@SiO}_2\text{NPs}$ had no impact on the catalyst's efficiency. The EDX result presented in (Supplementary Information) **Appx. 3.1.** demonstrates that $\text{Cu}_n\text{@SiO}_2\text{NPs}$ were successfully replaced with $\text{Au}_n\text{@SiO}_2\text{NPs}$.

3.3.2 FTIR measurement of silica sphere before and after calcination

To determine the connection between the organic dendrimer and the silica sphere, FTIR measurement was performed at a vibration frequency of $500\text{-}4000\text{ cm}^{-1}$. On the uncalcined silica sphere, we detected a mild C-N stretching/N-H bending vibration (**Figure 3.2**). This is attributable to the amide and amine groups located at $\nu\ 1641$ and 1551 cm^{-1} , respectively. Additionally, the interaction of the dendrimer with the silica sphere was verified [37]. This interaction was detected exclusively in the silica sphere prior to calcination because organic dendrimer breakdown has occurred after calcination at $500\text{ }^\circ\text{C}$. Bands at 1068 , 790 , and 452 cm^{-1} ν , on the other hand, may be attributed to the Si-O-Si stretching band [35]. The high absorption at 969 cm^{-1} shows the presence of Si-OH, indicating that the silica spheres have absorbed moisture [38].

3.3.3 p-XRD Characterization

Figure 3.3 illustrates the p-XRD patterns for the catalysts. $\text{Cu}_n\text{@SiO}_2\text{NPs}$ and $\text{Au}_n\text{@SiO}_2\text{NPs}$ peaks were indexed using the JCPDS numbers (89-2838) [39,40] and (04-0784), respectively, as shown in **Figure 3.3a** and **III.3b** [41]. Cu's diffractogram at $2\theta = 34.3^\circ$ has 110 phase. The additional peaks at 39.4° and 57.8° were caused by the oxidation of CuNPs [42–44] due to the sample exposure to air before analysis. These corresponded to JCPDS number 05-661. Additionally, four prominent distinctive peaks associated with Au at $2\theta = 38.1^\circ$, 44.4° , 64.5° , and 77.6° have been assigned to the (111), (200), (220), and (311) diffraction planes of face-centered cubic (fcc). These distinctive peaks associated with metallic Au have been previously described [41]. The diffraction peak at $2\theta = 23^\circ$, present in all of the data in **Figure 3.3a**, **3.3b**, and **3.3c**, is attributed to amorphous silica [45].

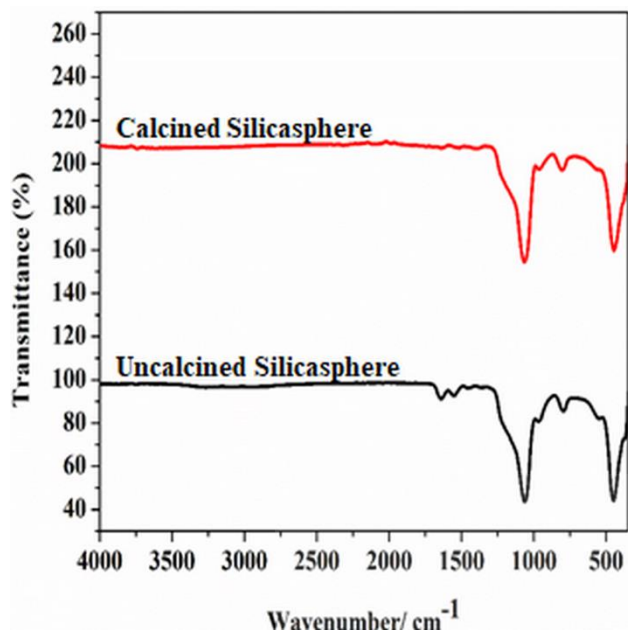


Figure 3.2: FTIR analysis of dendrimer and silica sphere interaction.

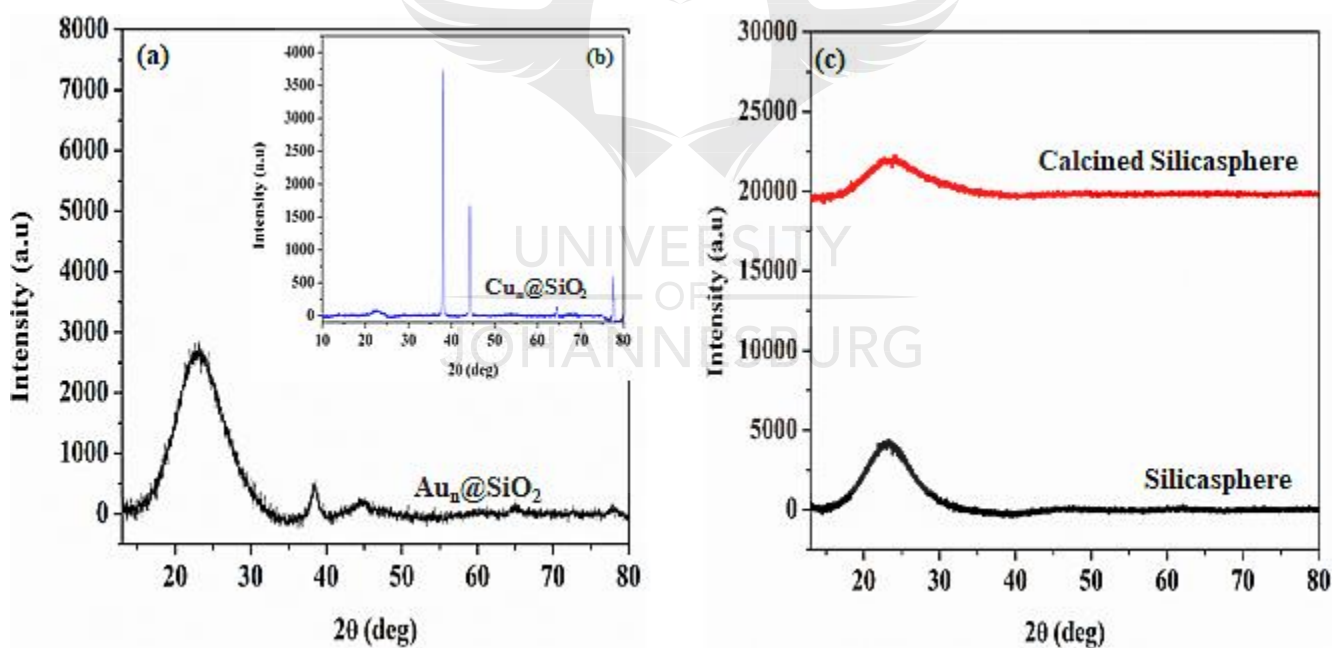


Figure 3.3: p-XRD pattern of (a) $\text{Cu}_n@SiO_2$ and $\text{Au}_n@SiO_2$ (b) calcined and uncalcined silica sphere.

3.3.4 Brunauer-Emmett-Teller nitrogen sorption analysis

The nitrogen adsorption-desorption isotherm capacity measurements of the samples' surface area and pore structure are shown in **Figure 3.4a–3.4d**. Except for $\text{Cu}_n@SiO_2$ prior to calcination, all hysteresis loops

had a surface area in the pressure range of 0.55-0.82 P/P_0 . The isotherm curves for this kind of hysteresis loop correspond to the type IV adsorption isotherm, which is a characteristic of uniform mesopore distribution [18,46]. $\text{Cu}_n@SiO_2$ prior to calcination, on the other hand, exhibits a type IV H3 hysteresis loop with no adsorption limit even at high P/P_0 values between 0.8 and 1.0, including the desorption closure [47]. Additionally, the existence of a tiny hysteresis loop indicates that the material has a high degree of porosity, with a surface area of $221.16 \text{ m}^2/\text{g}$. This surface area rose dramatically to $744.04 \text{ m}^2/\text{g}$ after calcination due to dendrimer elimination at $500 \text{ }^\circ\text{C}$ [45]. Additionally, the trend in pore volume increased from $0.02731 \text{ cm}^3/\text{g}$ to $0.07150 \text{ cm}^3/\text{g}$. While the surface area of the calcined $\text{Cu}_n@SiO_2$ is greater than that of the calcined silica sphere, we believe that this increased surface area is due to the increased number of adsorption sites on the surface of the calcined $\text{Cu}_n@SiO_2$ following the removal of the organic dendrimer during the calcination process. **Table 3.1** summarizes the surface area, pore-volume, and pore size distribution obtained.

Tableb 3.1:

Surface area data and pore structure parameters of silica sphere, $\text{Cu}_n@SiO_2$ before calcination, after calcination, and $\text{Au}_n@SiO_2$.

All samples	BET surface area (m^2/g)	BJH pore volume (cm^3/g)	BJH pore diameter(nm)
Silica sphere	136.69	0.40829	11.945
Calcined Silica sphere	632.55	0.07110	6.3257
$\text{Cu}_n@SiO_2$	221.16	0.02731	3.6261
Calcined $\text{Cu}_n@SiO_2$	744.04	0.07150	3.8441
$\text{Au}_n@SiO_2$	563.36	0.83954	5.9610

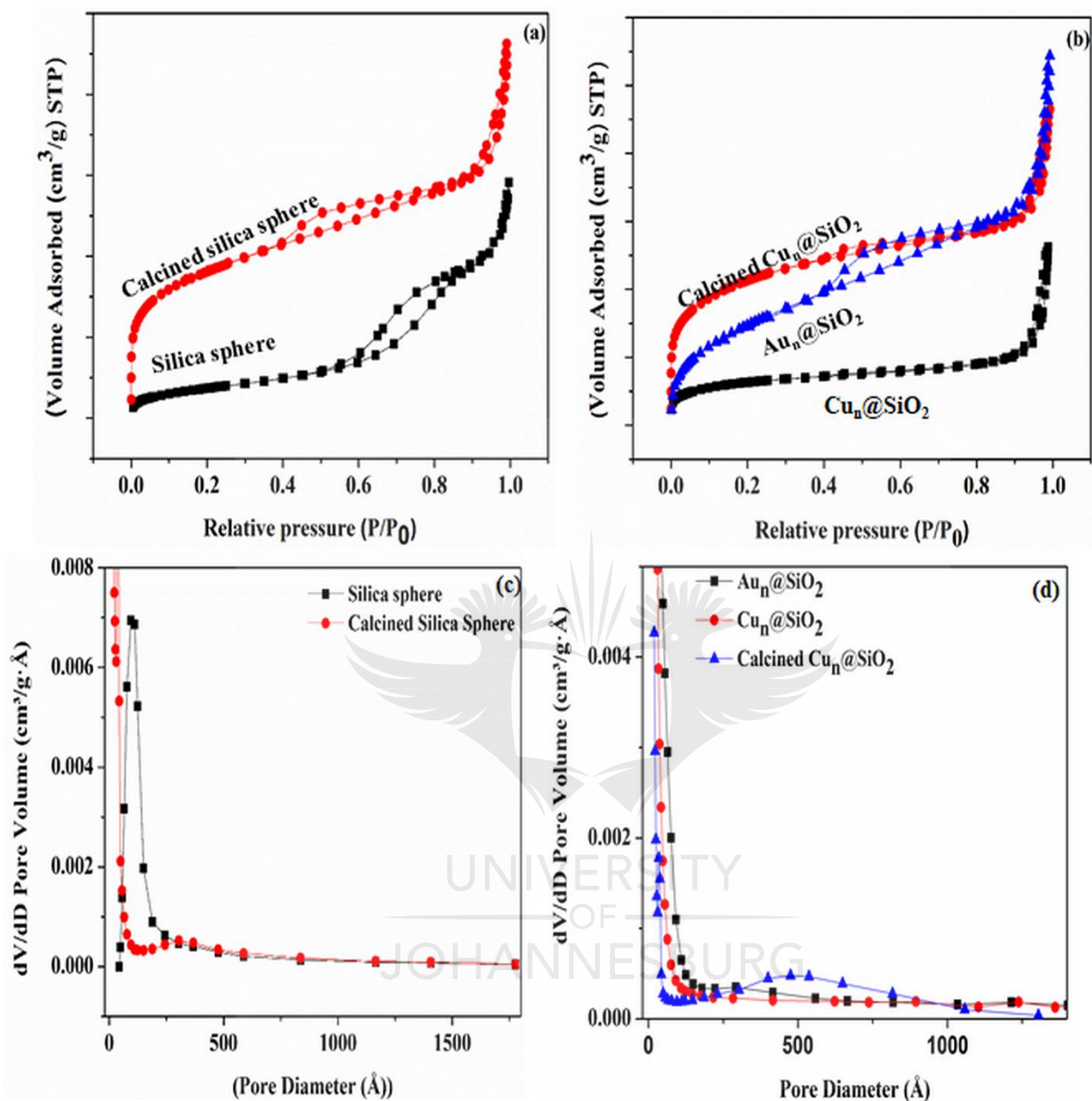


Figure 3.4: N_2 adsorption-desorption isotherm of (a) silica sphere before and after calcination, (b) $\text{Cu}_n@SiO_2$ before and after calcination, and $\text{Au}_n@SiO_2$. Pore distribution patterns of (c) silica sphere before and after calcination, (d) $\text{Cu}_n@SiO_2$ before and after calcination, and $\text{Au}_n@SiO_2$.

3.3.5 Thermogravimetric Analysis (TGA)

Figure 3.5 illustrates the thermal stability of the samples tested over time in terms of temperature change. The temperature profiles of the silica sphere and $\text{Cu}_n@SiO_2$ shown in **Figure 3.5a** and **3.5b**, respectively, demonstrate the distinct degradation pathways. The initial deterioration occurs below 170 $^\circ\text{C}$ owing to

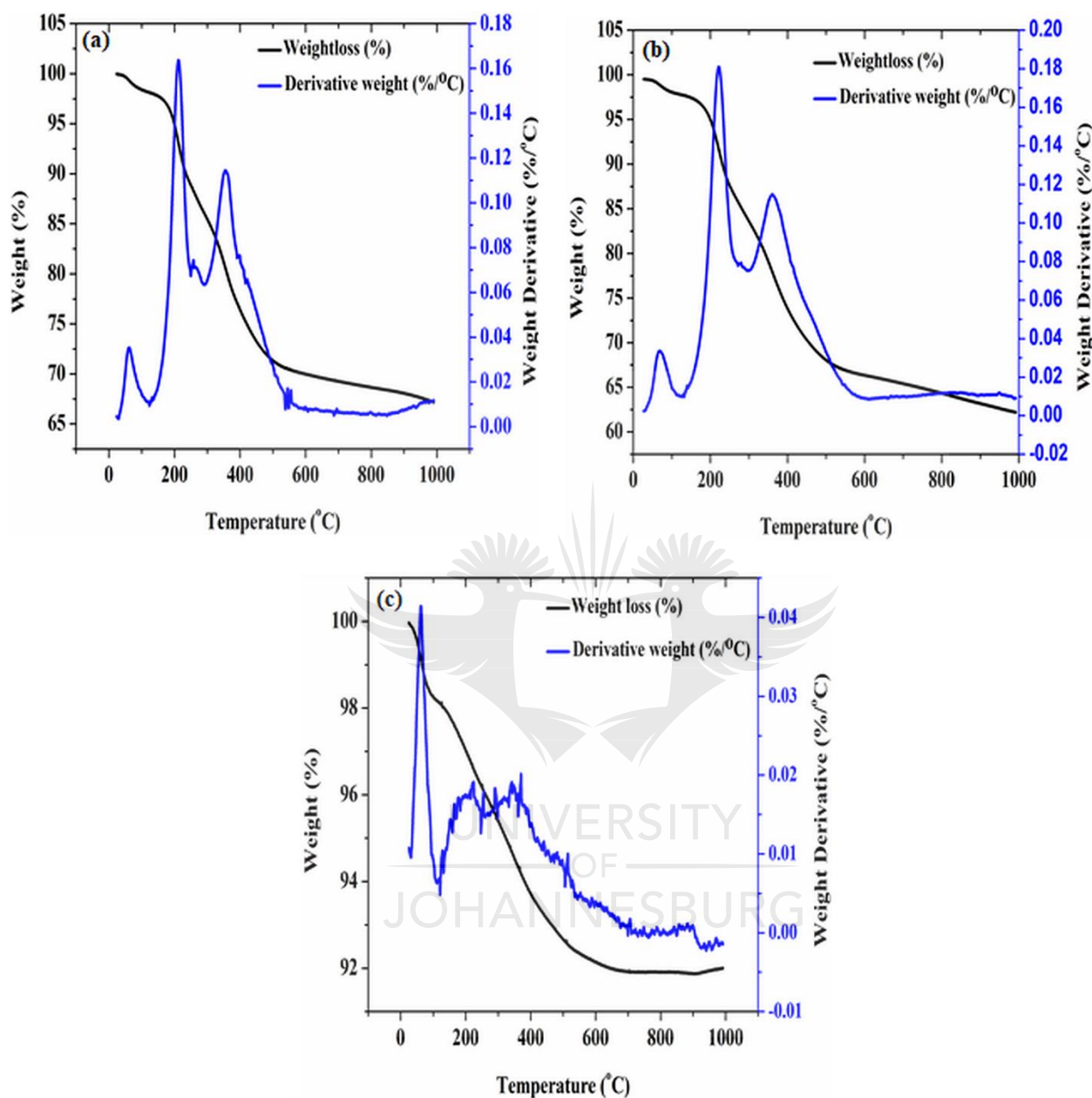


Figure 3.5: Thermogravimetric analysis of (a) silica sphere, (b) Cu_n@SiO₂, and (c) Au_n@SiO₂.

adsorbed moisture, while the second loss occurs above 495 °C due to the breakdown of organic dendrimer residues [48,49]. The last step over 495 °C is attributed to breakdown caused by silanol condensation, which resulted in the formation of oxides on the surfaces of the materials [50–52]. Hydrolysis of siloxane linkages ($\equiv \text{Si-O-Si} \equiv$) in amorphous silica may result in the formation of soluble silanols ($\equiv \text{Si-OH}$) [52]. This is shown in the FTIR spectrum given before. As demonstrated in **Figure 3.5c**, the Au_n@SiO₂ seemed

to undergo two breakdown stages between 120 and 620 °C before stabilizing. According to the thermogram, the first thermal event happened as a consequence of adsorbed moisture loss, and the second breakdown event occurred as a result of the formation of volatile 2SiO though the SiO₂ + Si reaction on the silica framework [53].

3.3.6 Catalytic evaluation of Cu_n@SiO₂ and Au_n@SiO₂ on 4-nitrophenol reduction

Reducing 4-nitrophenol with NaBH₄ is a typical reaction for studying catalytically active metal nanoparticles [54]. Cu_n@SiO₂ and Au_n@SiO₂ showed excellent catalytic activity in the reduction of 4-nitrophenol. 4-nitrophenol aqueous solution exhibited a maximum absorption peak at λ_{max} 400 nm. The addition of the catalyst and protonation of the reaction medium with NaBH₄ resulted in the transformation of the reaction medium from yellow to colorless. The simultaneous decrease occurred when a new absorbance intensity at λ = 300 nm was discovered with an isosbestic point. This is a sign that 4-nitrophenol has been reduced to 4-aminophenol [25]. The UV-vis absorption spectra for the catalytic reductions of Cu_n@SiO₂ and Au_n@SiO₂ are shown in **Figure 3.6a** and **3.6b**, respectively. The reaction with Au_n@SiO₂ was finished in ten minutes, while the reduction with Cu_n@SiO₂ lasted for thirty minutes. Considering the time required for the two catalysts to complete the reaction, it is clear that Au_n@SiO₂ is more effective. Fundamentally, Au possesses higher reduction potential and electron affinity compare to Cu. Hence, this property made it more reactive than Cu. The non-linear regression with respect to time seen in **Figure 3.6c** and **3.6d** corresponds to a *pseudo-first* order response. However, when the reduction process was carried out in the absence of both Cu_n@SiO₂ and Au_n@SiO₂ catalysts (results not shown), the peak intensity remained unchanged. This demonstrated that the reduction was catalyzed.

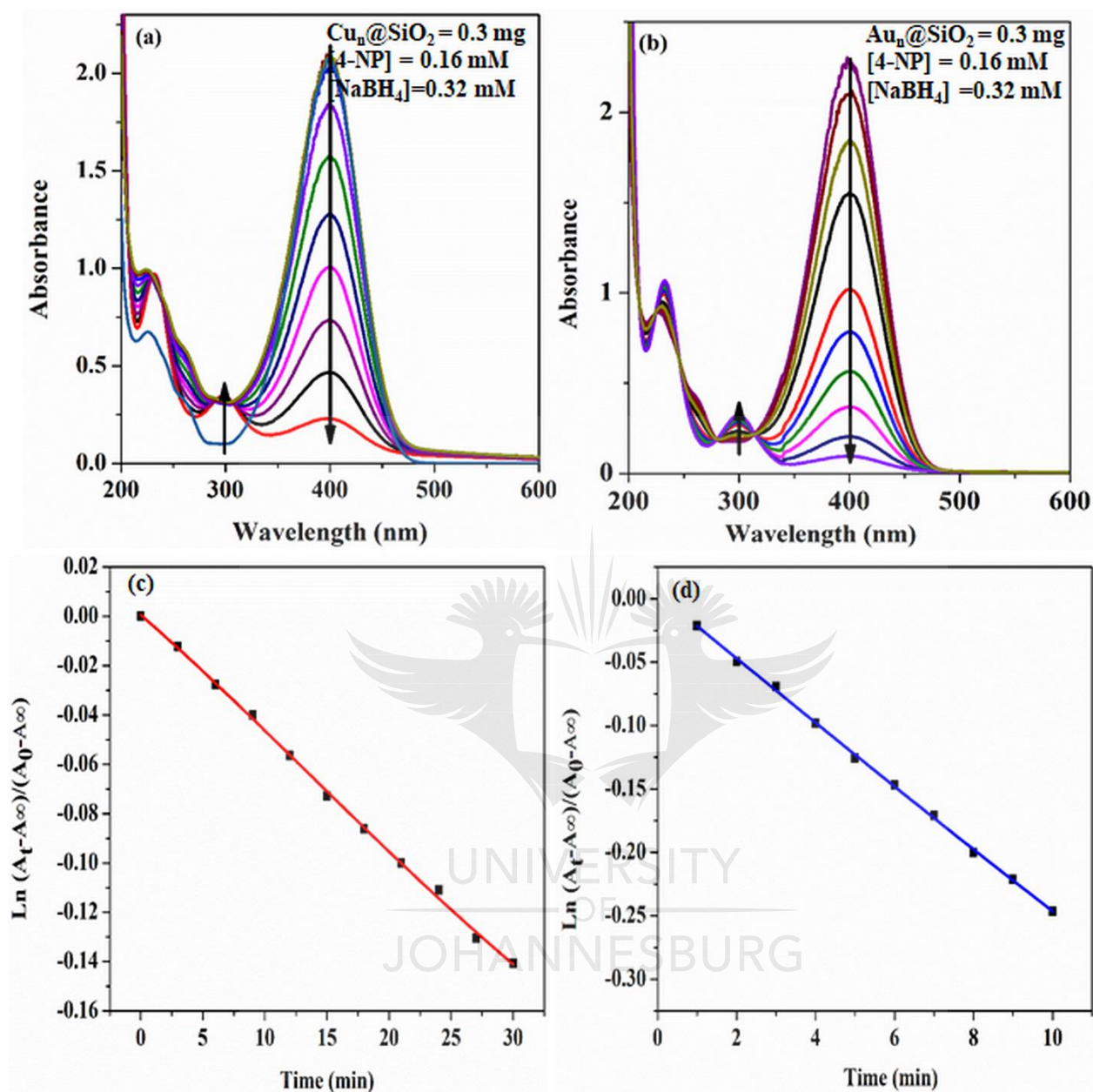


Figure 3.6: UV-vis spectra showing the degradation of 4-nitrophenol using (a) $\text{Cu}_n@SiO_2$ and (b) $\text{Au}_n@SiO_2$, non-linear regression against time with (c) $\text{Cu}_n@SiO_2$ and (d) $\text{Au}_n@SiO_2$.

3.3.7 Catalytic investigation on oxidation of RhB

The oxidation of RhB in the presence of H_2O_2 is also used as a model reaction to investigate the catalytic effect of metal nanoparticles [55]. After establishing $\text{Au}_n@SiO_2$ as an efficient catalyst for 4-nitrophenol reduction, the UV-vis spectrum of RhB oxidation produced at a 3-min interval for its degradation utilizing $\text{Au}_n@SiO_2$ is shown in **Figure 3.7a**. Within 30 min, the catalytic breakdown was seen for each degrading

step employing varying quantities of the catalyst, as illustrated in **Figure 3.7b**. This demonstrated that the increase in catalytic performance is directly proportional to the quantity of catalyst used. Using the mathematical formula for the kinetic *pseudo-first-order* in **Eqn. (3.1)**, [56]. A_0 and A_t denote the initial RhB concentration and the concentration at time t , respectively. A_{∞} is the final concentration of RhB, while k_{obs} is the measured rate constant.

$$-\ln \frac{A_t - A_{\infty}}{A_0 - A_{\infty}} = k_{obs} \times t \quad (3.1)$$

The catalytic reaction order was identical to that of a pseudo-first-order reaction. **Appx. 3.2** depicts the plot. Additionally, a carbonate buffer combination with a pH of 7.5 and Na_2CO_3 and NaHCO_3 supplied throughout the process guaranteed H_2O_2 stability and improved adsorption [33]. This occurred because the repulsive force between the catalyst and the dye was restricted [57]. In **Figure 3.8a**, the rate constant for RhB adsorption onto the catalyst's surface decreased as the substrate quantity increased due to dye saturation on the catalyst surface. This indicates that the reaction rate is dependent on the availability of the catalyst. In **Figure 3.8b**, the study of H_2O_2 adsorption reveals a concomitant rise in affinity for the oxidant owing to the increased supply of oxygen from H_2O_2 , hastening the substrate's breakdown.

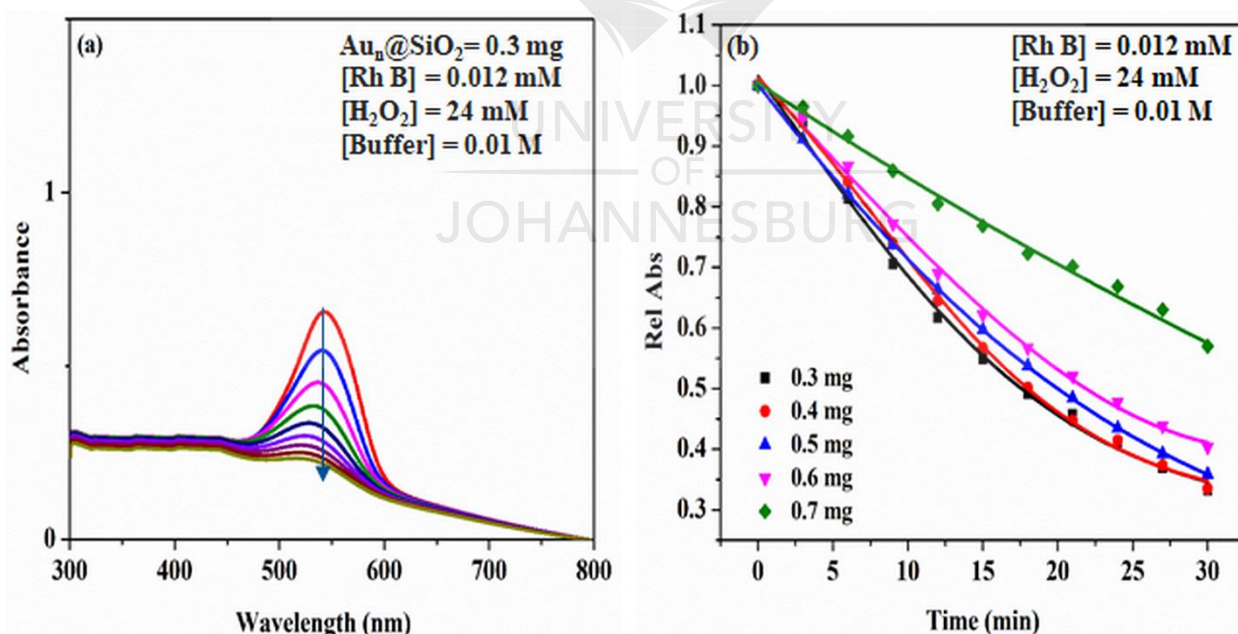


Figure 3.7: (a) UV-vis spectrum of RhB oxidation using $\text{Au}_n@SiO_2$, (b) non-linear fits data.

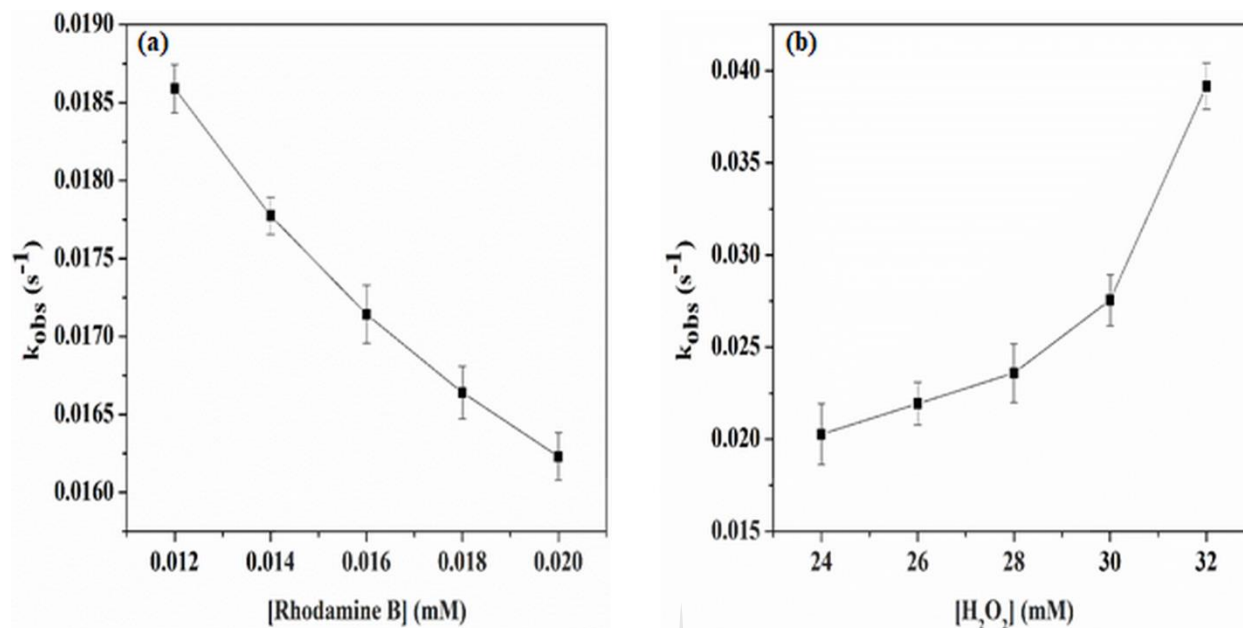


Figure 3.8: Concentration variation of (a) RhB (b) H₂O₂.

3.3.8 Catalytic evaluation of Au_n@SiO₂ in the oxidation of styrene to benzaldehyde and phenylacetaldehyde

The as-synthesized Au_n@SiO₂ catalyst was further evaluated catalytically for the oxidation of styrene in the liquid phase using TBHP as an oxidant. In the same vein, acetonitrile was used as a solvent at 80 °C. The heterogeneous catalytic oxidation of styrene produced primary products such as phenylacetaldehyde (PA) and benzaldehyde (BzA). **Figure 3.9a** illustrates the results obtained. A gradual response is seen with a proportionate rise in conversion as time passes, with a maximum styrene conversion of 54.3%. Styrene conversion is expressed as the ratio of styrene converted into a product to the amount of styrene present in the reaction mixture. The reaction, which was shown to be selective for both benzaldehyde and phenylacetaldehyde, showed more excellent selectivity for phenylacetaldehyde, 64.4% and 35.6% for benzaldehyde.

Additionally, the reaction mixture lacked the presence of additional products identified throughout the study, most notably acid production, due to the co-oxidation of benzaldehyde [58]. The surface electronic distribution, surface shape, and particle size of Au are all surmised to contribute to the catalyst's selectivity [36,59]. The electronic nature of the Au catalysts' site has been found to have a tuning impact on their catalytic activity and selectivity [60]. Thus, the structure of Au_n@SiO₂ enables the rearrangement of

hydrogen through ring-opening, resulting in the production of phenylacetaldehyde [30], while benzaldehyde is formed via oxidative cleavage [61].

Heterogeneity in catalysis' critical characteristic is the ease with which they may be recovered and recycled from the reaction media. Due to this economic advantage, they were preferred over homogeneous catalysts. After recovering $\text{Au}_n\text{@SiO}_2$ from the reaction media, its recyclability was determined, as shown in **Figure 3.9b**. The catalyst exhibited no significant degradation in activity over time, and it was shown to be constantly selective toward benzaldehyde and phenylacetaldehyde, with a steady preference for phenylacetaldehyde. Inductively coupled plasma-optical emission spectroscopy (ICP-OES) tests showed an Au loading of 0.59 wt% and the catalyst's potential leaching into the reaction solution. Additionally, it demonstrated that a small quantity of Au (0.03 mg/L) remained in the solution after the reaction. Together with the TOF of 306 h^{-1} , these findings indicate that the Au NPs are well immobilized and encapsulated on the silica sphere.

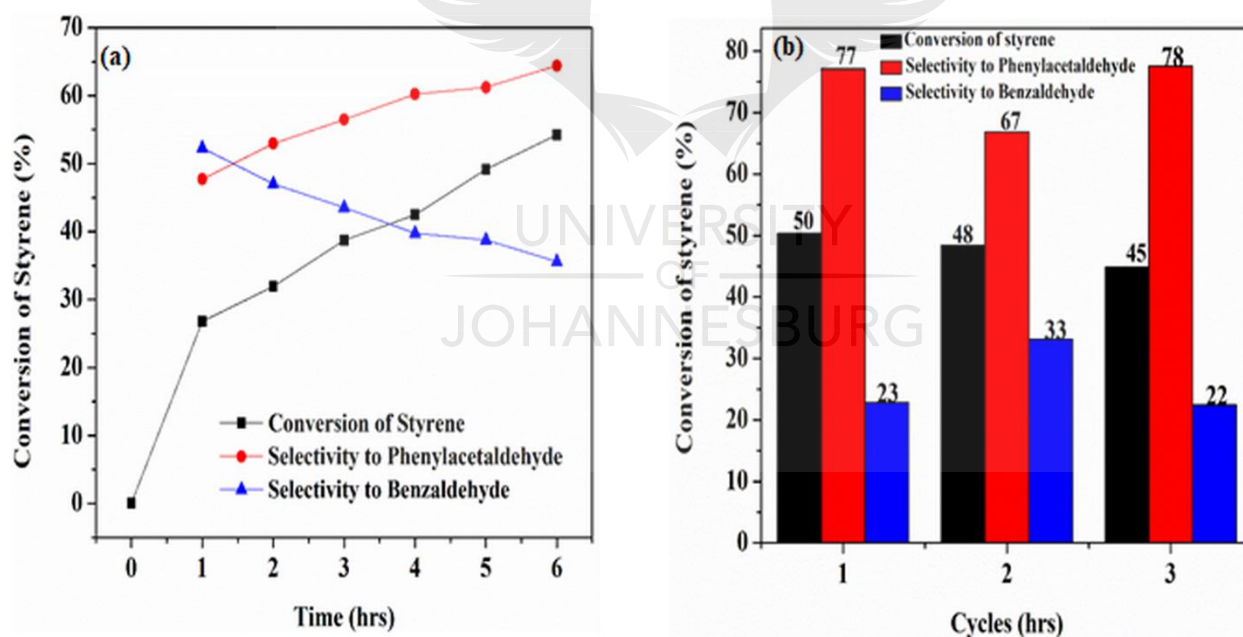


Figure 3.9: (a) Plot revealing conversion and selectivity of $\text{Au}_n\text{@SiO}_2$ at 80°C : 0.1 g catalyst, 0.59 wt% metal loading, 214 μL (2 mmol) styrene, 415.2 μL (3 mmol) TBHP, 6 h and (b) Catalyst recyclability.

Since the reaction was conducted in the open air, the impact of air on the mechanistic transition of styrene to phenylacetaldehyde and benzaldehyde was examined. Without the TBHP oxidant, less than 0.5%

conversion was seen (graph not shown). This finding indicates that oxygen had a negligible and minor impact on the reaction over the six-hour observation period. However, when the reaction was conducted using just the aqueous TBHP oxidant, we observed a conversion of just 8.2% (**Appx. III.3**). This established TBHP as the primary oxidant [62], creating a favorable oxidative environment for the process [63].

On styrene oxidation, the catalytic activity of $\text{Au}_n@SiO_2$ was compared to that of previously reported gold-based catalysts. As shown in **Table 3.2**, this catalyst is comparable in terms of TOF and conversion to other early reported gold-based catalysts due to the most outstanding TOF value and percentage (%) conversion obtained. The reaction time was much shorter, and the quantity of Au loaded was much less than any other catalyst. Although there was no selectivity for styrene oxide (SO) employing $\text{Au}_n@SiO_2$, this catalyst had an excellent selectivity for phenylacetaldehyde and benzaldehyde. This may have occurred as a result of Au being encapsulated in the silica sphere after direct replacement and a change in particle size, pore size, and surface area.



Table 3.2:

Oxidation comparison with other previous reports on Au-based catalysts

Catalysts	Au	Time	Temp.	Oxidant	TOF	Conv.		Selectivity (%)			Ref.
	(wt%)	(h)	°C		(h ⁻¹)	(%)	PA	BzA	SO	Others	
Ti-Au-s	1.3	15	70	TBHP	-	41.0	-	61.0	39.0	-	[62]
Ti-Au-w	1.8	15	70	TBHP	-	23.0	-	67.0	33.0	-	[62]
Au/SrO	0.6	24	80	TBHP	-	21.4	26.0	11.7	44.8	17.4	[64]
Au/MgO (HDP)	4.1	24	80	TBHP	-	44.6	16.8	10.8	54.3	18.1	[64]
1Au ₂₅ /AC	1.0	16	80	TBHP	-	35.3	-	-	4.3	-	[63]
1Au ₂₅ /PGO	1.0	16	80	TBHP	-	44.8	-	-	5.6	-	[63]
1Au ₂₅ /SiO ₂ -300	1.0	16	80	TBHP	-	46.9	-	-	14.7	-	[63]
Au/BaTNT	1.0	15	80	TBHP	182	46.8	4.8	18.9	70.9	5.4	[65]
Au/BaTNT	0.5	15	80	TBHP	273	31.0	3.4	14.0	75.8	6.8	[65]
Au ₂₅ /SiO ₂	2.0	24	82	TBHP	103 ± 10	15.1	-	6.6	93.4	-	[25]
Au _n @SiO ₂	0.59	6	80	TBHP	306	54.3	64.4	35.6	-	-	This work

Reaction condition: 0.1 g catalyst, 0.59 wt% metal loading, 214 μ L (2 mmol) styrene, 415.2 μ L (3 mmol) TBHP, Temperature 80 °C, 6 h, conversion = (converted styrene)/initial amount of styrene) \times 100.

3.4 Conclusion

The CuDENS templating approach's systematic procedure allowed the encapsulation of small-sized CuNPs in a silica sphere as $\text{Cu}_n@SiO_2$. The *in-situ* replacement via galvanic exchange was effectively accomplished using the difference in the electrode potential. Both $\text{Cu}_n@SiO_2$ and $\text{Au}_n@SiO_2$ preliminary catalytic activity on reducing 4-nitrophenol using NaBH_4 exhibited a unique pattern of a pseudo-first-order reaction. $\text{Au}_n@SiO_2$ demonstrated enhanced catalytic performance and also showed effective oxidation of RhB in the presence of H_2O_2 . Additionally, this corresponded to a pseudo-first-order reaction. Increases in the concentration of RhB resulted in decreased k_{obs} , followed by an increase in k_{obs} as the concentration of peroxide increased.

Additionally, in terms of reaction conditions, the catalyst promoted the oxidation of styrene with a conversion rate of 54.3%. This resulted in the selectivity of 35.6% and 64.4% for benzaldehyde and phenylacetaldehyde, respectively.



3.5 References

- [1] X. Peng, Q. Pan, G.L. Rempel, Bimetallic dendrimer-encapsulated nanoparticles as catalysts: a review of the research advances, *Chem. Soc. Rev.* 37 (2008) 1619.
- [2] P. Ncube, N. Bingwa, H. Baloyi, R. Meijboom, Catalytic activity of palladium and gold dendrimer-encapsulated nanoparticles for methylene blue reduction: A kinetic analysis, *Appl. Catal. A Gen.* 495 (2015) 63–71.
- [3] N. Bingwa, R. Meijboom, Kinetic evaluation of dendrimer-encapsulated palladium nanoparticles in the 4-nitrophenol reduction reaction, *J. Phys. Chem. C.* 118 (2014) 19849–19858.
- [4] M. Nemanashi-Maumela, I. Nongwe, R.C. Motene, B.L. Davids, R. Meijboom, Au and Ag nanoparticles encapsulated within silica nanospheres using dendrimers as dual templating agent and their catalytic activity, *Mol. Catal.* 438 (2017) 184–196.
- [5] M. Zhao, R.M. Crooks, Homogeneous hydrogenation catalysis with monodisperse, dendrimer-encapsulated Pd and Pt nanoparticles, *Angew. Chemie Int. Ed.* 38 (1999) 364–366.
- [6] R.M. Crooks, M. Zhao, L.I. Sun, V. Chechik, L.E.E.K. Yeung, Dendrimer-Encapsulated Metal Nanoparticles: Synthesis, Characterization, and Applications to Catalysis, 34 (2001) 181–190.
- [7] H. Lang, R. May, B. Iversen, B. Chandler, Dendrimer- Encapsulated Nanoparticle Precursors to Supported Platinum Catalysts, *J. Am. Chem. Soc.* 125 (2003) 14832–14836.
- [8] R.W.J. Scott, O.M. Wilson, R.M. Crooks, Synthesis, characterization, and applications of dendrimer-encapsulated nanoparticles, *J. Phys. Chem. B.* 109 (2005) 692–704.
- [9] Z.V. Feng, J.L. Lyon, J.S. Croley, R.M. Crooks, D.A. Vanden Bout, K.J. Stevenson, Synthesis and catalytic evaluation of dendrimer-encapsulated Cu nanoparticles. An undergraduate experiment catalytic nanomaterials, *J. Chem. Educ.* 86 (2009) 368–372.
- [10] V.S. Myers, M.G. Weir, E. V Carino, D.F. Yancey, S. Pande, R.M. Crooks, Dendrimer-encapsulated nanoparticles: new synthetic and characterization methods and catalytic applications, *Chem. Sci.* 2 (2011) 1632–1646.
- [11] M. Nemanashi, R. Meijboom, Journal of Colloid and Interface Science Synthesis and characterization of Cu, Ag and Au dendrimer-encapsulated nanoparticles and their application in the reduction of 4-nitrophenol to 4-aminophenol, *J. Colloid Interface Sci.*

- 389 (2013) 260–267.
- [12] T. Cho, C.W. Yoon, J. Kim, Repetitively Coupled Chemical Reduction and Galvanic Exchange as a Synthesis Strategy for Expanding Applicable Number of Pt Atoms in Dendrimer-Encapsulated Pt Nanoparticles, *Langmuir*. 34 (2018) 7436–7444.
- [13] G. Duan, A.C. Zhang, A. Li, A.X. Yang, A.L. Lu, A.X. Wang, Preparation and Characterization of Mesoporous Zirconia Made by Using a Poly (methyl methacrylate) Template, (2008) 118–122.
- [14] K. Nakanishi, M. Tomita, Y. Masuda, K. Kato, composites with enhanced antibody adsorption, (2015) 4070–4077.
- [15] M. Huang, L. Liu, S. Wang, H. Zhu, D. Wu, Z. Yu, S. Zhou, Dendritic Mesoporous Silica Nanospheres Synthesized by a Novel Dual-Templating Micelle System for the Preparation of Functional Nanomaterials, (2017).
- [16] N. Qiao, X. Zhang, C. He, Y. Li, Z. Zhang, J. Cheng, Z. Hao, Enhanced performances in catalytic oxidation of o -xylene over hierarchical macro- / mesoporous silica-supported palladium catalysts, 10 (2016) 458–466.
- [17] H. Zhang, J. Wu, L. Zhou, D. Zhang, L. Qi, Facile Synthesis of Monodisperse Microspheres and Gigantic Hollow Shells of Mesoporous Silica in Mixed Water - Ethanol Solvents, (2007) 1107–1113.
- [18] Y.Q. Jiang, Y.T. Pan, X.W. Li, W.J. Cheng, J.M. Sun K.F. Lin, and Z.C.Wang, Preparation and Characterization of Hollow Spheres with Cubic Mesoporous Shell. In *Advanced Materials Research* 785 (2013) 382-385.
- [19] J. Zhou, T. Yang, W. He, Z.Y. Pan, C.Z. Huang, A galvanic exchange process visualized on single silver nanoparticles via dark-field microscopy imaging. *Nanoscale*, 10 (2018) 12805–12812.
- [20] M.B. Gawande, A. Goswami, T. Asefa, X. Huang, R. Silva, X. Zou, R. Zboril, R.S. Varma, Cu and Cu-Based Nanoparticles : Synthesis and Applications in Catalysis, *Chemical reviews*, 116 (2016) 3722-3811.
- [21] S. Pande, M.G. Weir, B.A. Zacco, R.M. Crooks, Synthesis, characterization, and electrocatalysis using Pt and Pd dendrimer-encapsulated nanoparticles prepared by galvanic exchange, *New J. Chem*. 35 (2011) 2054.
- [22] M. Zhao, R.M. Crooks, Intradendrimer Exchange of Metal Nanoparticles Intradendrimer Exchange of Metal Nanoparticles, *Chem. Mater*. 11 (1999) 3379–3385.

- [23] R.M. Anderson, D.F. Yancey, J.A. Loussaert, R.M. Crooks, Multistep Galvanic Exchange Synthesis Yielding Fully Reduced Pt Dendrimer-Encapsulated Nanoparticles, *Langmuir*, 30 (2014) 15009-15015.
- [24] M.S. Xaba, J. Noh, R. Meijboom, Applied Surface Science Catalytic activity of different sizes of Pt n / Co 3 O 4 in the oxidative degradation of Methylene Blue with H 2 O 2, *Appl. Surf. Sci.* 467–468 (2019) 868–880.
- [25] V. Sudheeshkumar, A. Shivhare, R.W.J. Scott, Synthesis of sinter-resistant Au@ silica catalysts derived from Au 25 clusters. *Catalysis Science & Technology*, 7 (2017) 272–280.
- [26] J. Luo, Y. Gao, K. Tan, W. Wei, X. Liu, Preparation of a Magnetic Molecularly Imprinted Graphene Composite Highly Adsorbent for 4 - Nitrophenol in Aqueous Medium, *ACS Sustainable Chemistry & Engineering*, 4 (2016) 3316-3326.
- [27] M.S. Tehani, R. Zare-dorabei, Highly efficient simultaneous ultrasonic-assisted adsorption of methylene blue and rhodamine B onto metal organic framework MIL-68 (Al): central composite design optimization, *RSC Advances*, 6 (2016) 27416–27425
- [28] S. Wunder, F. Polzer, Y. Lu, Y. Mei, M. Ballauff, Kinetic Analysis of Catalytic Reduction of 4-Nitrophenol by Metallic Nanoparticles Immobilized in Spherical Polyelectrolyte Brushes, *The Journal of Physical Chemistry C*, 114 (2010) 8814–8820. Wunder, S., Polzer, F., Lu, Y., Mei, Y. and Ballauff, M., 2010.
- [29] J. Noh, R. Patala, R. Meijboom, Applied Catalysis A : General Catalytic evaluation of dendrimer and reverse microemulsion template Pd and Pt nanoparticles for the selective oxidation of styrene using TBHP, "Applied Catal. A, Gen. 514 (2016) 253–266.
- [30] N. Masunga, B.P. Doyle, E. Carleschi, R. Meijboom, Applied Catalysis A, General Excellent product selectivity towards 2-phenyl-acetaldehyde and styrene oxide using manganese oxide and cobalt oxide NPs for the selective oxidation of styrene, *Appl. Catal. A, Gen.* 559 (2018) 175–186.
- [31] T.A.G. Duarte, A.P. Carvalho, L.M.D.R.S. Martins, Styrene oxidation catalyzed by copper (II) C-scorpionates in homogeneous medium and immobilized on sucrose derived hydrochars, *Catal. Today.* (2019) 0–1.
- [32] C. Guo, Y. Zhang, L. Zhang, Y. Guo, N. Akram, J. Wang, 2-Methylimidazole-assisted synthesis of nanosized Cu₃ (BTC) 2 for controlling the selectivity of the catalytic oxidation of styrene, *ACS Appl. Nano Mater.* 1 (2018) 5289–5296.

- [33] M.S. Xaba, J. Noh, K. Mokgadi, R. Meijboom, Applied Surface Science Kinetic and catalytic analysis of mesoporous metal oxides on the oxidation of Rhodamine B, Appl. Surf. Sci. 440 (2018) 1130–1142.
- [34] V. Chaudhary, Chinese Journal of Chemical Engineering Synthesis and catalytic activity of SBA-15 supported catalysts for styrene oxidation, Chinese J. Chem. Eng. 26 (2018) 1300–1306.
- [35] N.H. Khadry, M.A. Ghanem, M.E. Abdesalam, M.M. Al-garadah, Sequestration of CO₂ using Cu nanoparticles supported on spherical and rod-shape mesoporous silica, J. Saudi Chem. Soc. 22 (2018) 343–351.
- [36] Y. Zheng, X. Zhang, Y. Yao, Ultra-small Au nanoparticles stabilized by silica hollow nanospheres for styrene oxidation with oxygen., RSC Advances 5 (2015) 105747–105752.
- [37] H. Kavas, Z. Durmus, E. Tanriverdi, M. Şenel, H. Sozeri, and A. Baykal, Fabrication and characterization of dendrimer-encapsulated monometallic Co nanoparticles, *Journal of alloys and compounds*, 509 (2011) 5341–5348.
- [38] Y.S. Chaudhary, J. Ghatak, M. Bhatta, D. Khushalani, One Step Method for the Self-Assembly of Metal Nanoparticles onto Facetted One-step method for the self-assembly of metal nanoparticles onto facetted hollow silica tubes, *Journal of Materials Chemistry*, 16 (2006) 3619-3623.
- [39] Z. Zhang, S.-S. Wang, R. Song, T. Cao, L. Luo, X. Chen, Y. Gao, J. Lu, W.-X. Li, W. Huang, The most active Cu facet for low-temperature water gas shift reaction, Nat. Commun. 8 (2017) 1–10.
- [40] M. Ahamed, H.A. Alhadlaq, M.A. Khan, P. Karuppiah, N.A. Al-Dhabi, Synthesis, characterization, and antimicrobial activity of copper oxide nanoparticles, J. Nanomater. 2014 (2014).
- [41] W. Shen, Y. Qu, X. Pei, S. Li, S. You, J. Wang, Z. Zhang, J. Zhou, Catalytic reduction of 4-nitrophenol using gold nanoparticles biosynthesized by cell-free extracts of *Aspergillus* sp. WL-Au, J. Hazard. Mater. 321 (2017) 299–306.
- [42] J. Li, T. Shi, C. Feng, Q. Liang, X. Yu, J. Fan, S. Cheng, G. Liao, Z. Tang, The novel Cu nanoaggregates formed by 5 nm Cu nanoparticles with high sintering performance at low temperature, Mater. Lett. 216 (2018) 20–23.
- [43] A. Kumar, A. Saxena, A. De, R. Shankar, S. Mozumdar, Facile synthesis of size-tunable

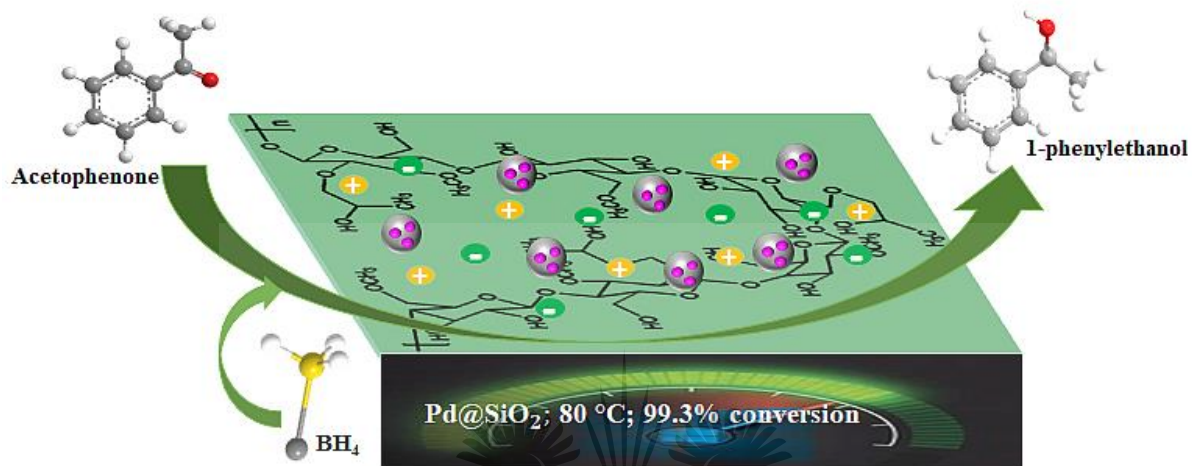
- copper and copper oxide nanoparticles using reverse microemulsions, *Rsc Adv.* 3 (2013) 5015–5021.
- [44] A.S. Lanje, S.J. Sharma, R.B. Pode, R.S. Ningthoujam, Synthesis and optical characterization of copper oxide nanoparticles, *Adv Appl Sci Res.* 1 (2010) 36–40.
- [45] Q. Yao, Z.H. Lu, Z. Zhang, X. Chen, Y. Lan, One-pot synthesis of core-shell Cu@SiO₂ nanospheres and their catalysis for hydrolytic dehydrogenation of ammonia borane and hydrazine boran *Scientific Reports.* 4 (2014) 1-8.
- [46] M. Thommes, K. Kaneko, A. V Neimark, J.P. Olivier, F. Rodriguez-reinoso, J. Rouquerol, K.S.W. Sing, Physisorption of gases, with special reference to the evaluation of surface area and pore size distribution (IUPAC Technical Report), 87 (2015) 1051–1069.
- [47] M. Thommes, Physical adsorption Characterization of Nanoporous Materials, *Chemie Ingenieur Technik*, 82 (2010) 1059-1073.
- [48] O. Ozturk, T.J. Black, K. Perrine, K. Pizzolato, C.T. Williams, F.W. Parsons, J.S. Ratliff, J. Gao, C.J. Murphy, H. Xie, H.J. Ploehn, D.A. Chen, Thermal Decomposition of Generation-4 Polyamidoamine Dendrimer Films : Decomposition Catalyzed by Dendrimer-Encapsulated Pt Particles, *Langmuir*, 21 (2005) 3998–4006.
- [49] B.A. Howell, D. Fan, L. Rakesh, Thermal Decomposition of a Generation 4 . 5 PAMAM Dendrimer Platinum Drug Conjugate, *Journal of thermal analysis and calorimetry*, 85 (2006) 17–20.
- [50] X. Guo, M. Lai, Y. Kong, W. Ding, Q. Yan, C.T.P. Au, Novel Coassembly Route to Cu - SiO₂ MCM-41-like Mesoporous Materials, *Langmuir*, 20 (2004) 2879–2882.
- [51] M.C. Rogers, B. Adisa, D.A. Bruce, Synthesis and characterization of dendrimer-templated mesoporous oxidation catalysts, *Catalysis letters*, 98 (2004) 29-36.
- [52] G.Z. Yang, D. Wibowo, J.H. Yun, L. Wang, A.P. Middelberg, C.X. Zhao, Biomimetic Silica Nanocapsules for Tunable Sustained Release and Cargo Protection, *Langmuir*, 33 (2017) 5777-5785.
- [53] I. Ilkiv, K. Kotlyar, D. Amel, S. Lebedev, G. Cirilin, Thermal Penetration of Gold Nanoparticles into Silicon Dioxide, 132 (2017) 366–368.
- [54] S.I. Park, H. Song, Synthesis of Prolate-Shaped Au Nanoparticles and Au Nanoprisms and Study of Catalytic Reduction Reactions of 4-Nitrophenol, *ACS Omega.* 4 (2019) 7874–7883.

- [55] H. Liang, S. Liu, H. Zhang, X. Wang, J. Wang, New insight into the selective photocatalytic oxidation of RhB through a strategy of modulating radical generation *RSC advances*, 8 (2018) 13625–13634.
- [56] A.K. Ilunga, T. Khoza, E. Tjabadi, R. Meijboom, Effective Catalytic Reduction of Methyl Orange Catalyzed by the Encapsulated Random Alloy Palladium-Gold Nanoparticles Dendrimer, *ChemistrySelect*. 2 (2017) 9803–9809.
- [57] A.K. Ilunga, R. Meijboom, Catalytic oxidation of methylene blue by dendrimer encapsulated silver and gold nanoparticles, *Journal of Molecular Catalysis A: Chemical* 411 (2016) 48–60.
- [58] T. Jiang, G. Gao, C. Yang, Y. Mao, M. Fang, Q. Zhao, Catalytic Activity of Ag-Co-MCM-41 for Liquid-Phase Selective Oxidation of Styrene to Benzaldehyde, *Journal of Nanoscience and Nanotechnology*, 20 (2020) 1670–1677.
- [59] R. Jain, C.S. Gopinath, Morphology-dependent, green, and selective catalytic styrene oxidation on Co₃O₄, *Dalton Transactions*, 48 (2019) 4574–4581.
- [60] B. Liu, P. Wang, A. Lopes, L. Jin, W. Zhong, Y. Pei, S.L. Suib, J. He, Au–carbon electronic interaction mediated selective oxidation of styrene, *ACS Catal.* 7 (2017) 3483–3488.
- [61] A. Blanckenberg, G. Kotze, A.J. Swarts, R. Malgas-Enus, Effect of nanoparticle metal composition: mono- and bimetallic gold/copper dendrimer stabilized nanoparticles as solvent-free styrene oxidation catalysts, *J. Nanoparticle Res.* 20 (2018) 1-15.
- [62] M. Nemanashi, R. Meijboom, Dendrimer derived titania-supported Au nanoparticles as potential catalysts in styrene oxidation, *Catal. Letters*. 143 (2013) 324–332.
- [63] J. Fang, J. Li, B. Zhang, X. Yuan, H. Asakura, T. Tanaka, K. Teramura, J. Xie, N. Yan, The support effect on the size and catalytic activity of thiolated Au 25 nanoclusters as, precatalysts. *Nanoscale*, 7 (2015) 6325–6333.
- [64] A.S. Sharma, D. Shah, H. Kaur, Gold nanoparticles supported on dendrimer@resin for the efficient oxidation of styrene using elemental oxygen, *RSC Adv.* 5 (2015) 42935–42941.
- [65] D. Nepak, D. Srinivas, Spectroscopy and catalytic activity study of gold supported on barium titanate nanotubes for styrene epoxidation, *Appl. Catal. A Gen.* 523 (2016) 61–72.

Chapter 4

Hydrogenation of ketone; An *In-situ* Approach toward an Eco-friendly Reduction

Graphical abstract



UNIVERSITY
OF
JOHANNESBURG

Abstract

The use of water as a solvent in chemical reactions has recently been brought to lime-light considering the exploration of eco-friendly procedures. It is readily available and abundantly accessible, non-toxic, non-costly, and non-flammable. As opposed to the previous limitation of reactant solubilities associated with aqueous media, a hydrogel such as a hydroxypropyl methylcellulose (HPMC) solution can significantly improve the reactant solubility. This investigation employed HPMC solution as the reaction solvent, and the reaction medium viscosity was impressively enhanced. Pd@SiO₂ particles were synthesized and effectively employed as a catalyst for reducing acetophenone in the presence of NaBH₄ as the hydrogen source. The conversion of acetophenone to 1-phenyl ethanol recorded remained at a very high value of > 99.34 % with 100 % selectivity towards 1-phenyl ethanol.

Keywords: Pd@SiO₂ catalyst; Hydroxypropylmethyl cellulose (HPMC); Water; Acetophenone hydrogenation; 1-phenyl ethanol.



4.1 Introduction

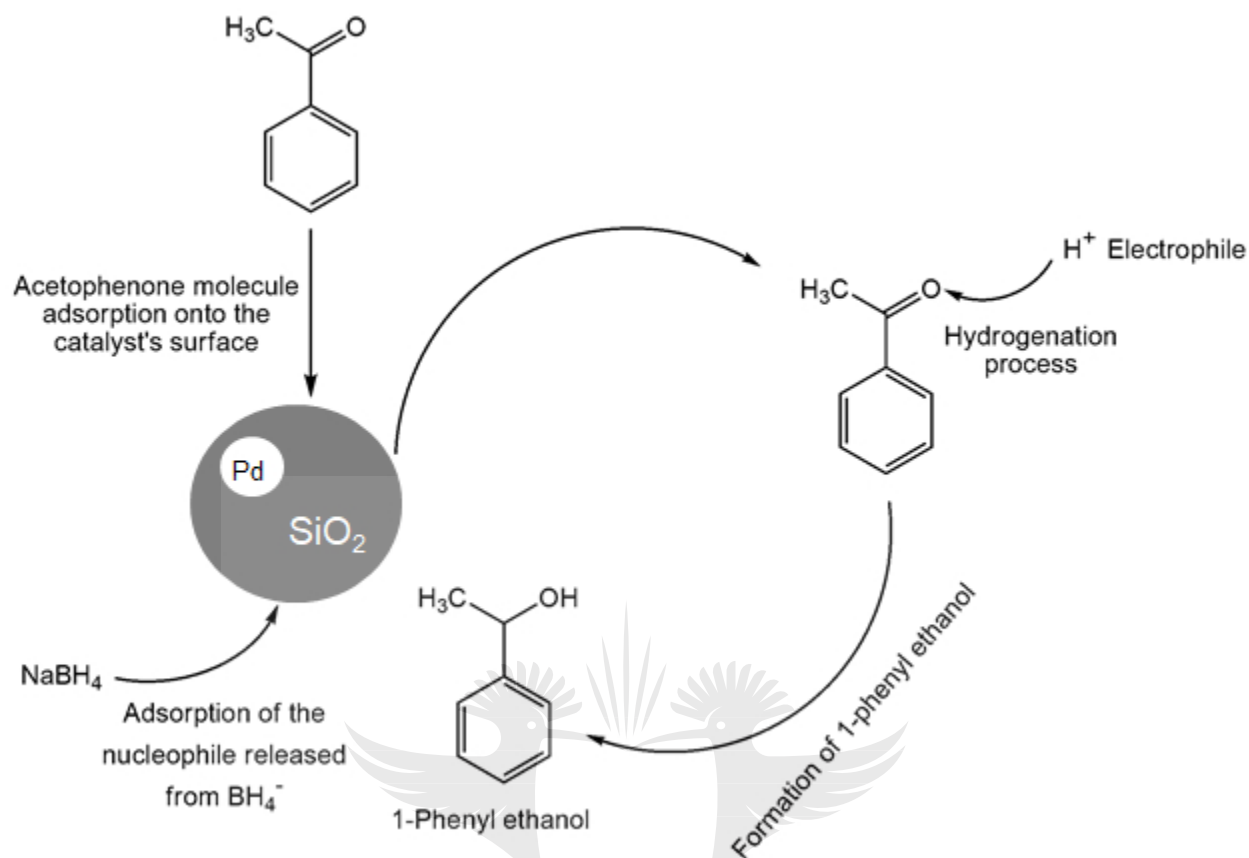
Water's versatility as a chemical system solvent is in its relatively high polarity and high specific heat. This versatility is in addition to water's high dielectric constant, surface tension, and significant energy density [1,2]. This is so as water molecule's charge is unevenly distributed, making different charged and polar molecules dissolvable in water [2]. Water's general availability, affordability, incombustibility, and inexplosive nature made it a perfect replacement for organic solvents in the development of practical reactions [1,3–5]. The hydrogen bonding permits the molecular groups to generate high heat of vaporization and polarizability of water. These are the characteristic features that bring about electron transfer as an essential process in water-mediated reactions. Also, these features are in addition to the viscousness, cohesive and adhesive nature of water that enables the product's facile extractive workup and purification [3,6]. These physical and chemical properties (ability to form hydrogen bonds and the amphoteric nature) of water help to theoretically enhance chemical reactions' reactivity and selectivity in water [1]. In recent years, water-tolerant catalysts and water-soluble ligands with excellent efficiency and stereoselectivity have been developed for organic reactions in water [7].

Hydroxypropyl methylcellulose (HPMC) is a group of cellulose ester that has substituted one or more of the hydroxyl groups occupying the cellulose ring with hydroxypropyl and methyl groups [8,9]. It is a water-soluble (hydrophilic), environmentally friendly, and biodegradable polymer. It has industrial applications ranging from pharmaceutical [10], agricultural to textiles (dye, paints), cosmetics [8], and to coating or adhesive [11]. Because of its edibility, its usefulness in food industries includes stabilization and emulsification. This is owing to its odorless, tasteless, non-toxic, and biocompatibility features [12,13].

Although hydroxypropyl methylcellulose is a temperature-sensitive biopolymer that forms a gel upon heating between 75 – 90 °C, it also has a dissolution tendency in cold organic solvents of polar nature. Hence, these properties make it relevant for use in both aqueous and non-aqueous solvents. Both hydroxypropyl (polar) and methyl (non-polar) groups enable interaction within the intermolecular, intramolecular, and hydrophobic environments [12].

Modern organic synthesis requires that attention be placed on selectivity related to the control of complete stereochemistry, reactivity, and productivity because these are key in ensuring efficiently catalyzed reactions [14]. Sustainability and green chemistry are two keywords or concepts which have put chemical synthesis and process chemistry into perspective. This is because of chemists' quest for environmental protection, safer design of molecules, materials, products, and processes increases [15]. The unrenewable source, cost ineffectiveness in production and disposal, environmental and human hazard of most organic solvents have put them on the spot, hence making the need to find a replacement for organic solvents more pressing [15]. One fundamental development in synthetic chemistry is the chemo-selective organic transformation through hydrogenation [3]. This process brings down the amount of materials consumed, leading to redundant trimming and reactions' step re-functionalization [3,16]. Hydrogenation is one of the most cardinal organic transformations, which entails the substitution of hydrogen with a molecule of non-H₂ possessing derivative [17]. There has not been a report on direct hydrogenation of acetophenone investigated using HPMC modified water (solution) to the best of our knowledge.

In recent years, the industrial application of ketone hydrogenation has been brought to the limelight as a diverse range of valuable alcohols, and chiral compounds are produced [18]. The great significance of acetophenone hydrogenation is in the synthetic relevance of the chemical intermediates it produces, including 1-phenyl ethanol, ethylbenzene, and cyclohexyl ethanol [19,20]. The chemo-selective hydrogenation of acetophenone being a model reaction is owing to acetophenone's hydrogenative groups, namely the phenyl group and the carbonyl group, which are reduced to their corresponding alcohol [21]. The carbonyl group's (C=O) double bond is hydrogenated to produce 1-phenyl ethanol, an essential chemical intermediate used in the fragrance, flavor, and pharmaceutical industry [22,23]. However, the phenyl group hydrogenation yields a cyclohexyl methyl ketone [24]. In this work, direct hydrogenation of acetophenone produced 1-phenyl ethanol as shown in the reaction pathway in Scheme 4.1 without side or unwanted products.



Scheme 4.1: Schematic representation of 1-phenyl ethanol formation.

There have been reports toward Pd-based materials' practical application as catalysts for ketone hydrogenation [25–27]. Pd/SiO₂-Al₂O₃ catalysts were successfully used to catalyze acetophenone, but the primary product generated was ethylbenzene with this material. Therefore, an effective catalyst that can potentially catalyze acetophenone to obtain the desired product is of crucial importance. Silica-supported Pd particles (Pd@SiO₂) been reported as a potentially efficient catalyst for hydrogenation [25].

4.2 Experimental section

4.2.1 Chemicals and Materials

The chemicals used were obtained from commercial suppliers of different companies and were of analytical grades. (Hydroxypropyl) methylcellulose (HPMC) average Mn ~10,000, ethanol (99.9%) was obtained from Monitoring Control Laboratories LTD, palladium (II) acetate (98%) (C₄H₆O₄Pd), tetraethyl orthosilicate (TEOS) (99%), and acetophenone (99%) (C₈H₈O) were

bought from Sigma-Aldrich. n-Decane, ($\text{CH}_3(\text{CH}_2)_8\text{CH}_3$) (99%) was purchased from Alfa Aesar, magnesium sulphate dried (MgSO_4) (52-70%) was obtained from Rochelle chemicals, sodium borohydride (NaBH_4) ($\geq 98.0\%$) was purchased from Sisco Research Laboratories (SRL) pvt. While ethyl acetate, sodium bicarbonate NaHCO_3 (99.50%), and NaOH (99.90%) were obtained from Promack chemicals. Milli-Q water of $18.2 \text{ M}\Omega\cdot\text{cm}$ was used to prepare all the solutions.

4.2.2 Synthesis of silica support for the Pd particle and impregnation of Pd onto the silica support

The silica support was synthesized following a literature procedure [28]. Typically, aqueous (11.20 mL) NH_4OH (27 wt%) was added to a mixture of ethanol (200 mL) and deionized water (50 mL) at room temperature and was allowed to stir for 30 min. After that, 8.93 mL of TEOS was added drop by drop to the mixture. It was further stirred for 12 h, and silica precipitation was observed. The formed silica precipitate was obtained through centrifugation, washed with deionized water, and centrifuged into pellets. The pellet was left to dry overnight in the oven at 70°C to obtain dry silica, which was later calcined at 500°C .

The silica support was dispersed in 8 mL of deionized water. A solution of Pd acetate containing 0.0212 g was added to the slurry, and it was left to stir for 4 h. Sodium borohydride (8 mL) was used to reduce the metal ion, and it was allowed to stir for another 4 h, and it was collected by centrifugation. The solid residue was dried overnight in the oven at 70°C and was calcined for 4 h at 150°C . After that, the dried product (Pd@SiO_2) obtained was ground, characterized, and catalytically tested. Inductively coupled plasma optical emission spectroscopy (ICP-OES) was used to determine the amount of Pd loaded on the silica (0.52 wt%).

4. 2.3 Catalyst characterization

The characterization techniques carried out include Brunauer-Emmett-Teller (BET) nitrogen sorption measurement to get the surface area, while the Barret-Joyner-Halenda (BJH) desorption isotherm was used to obtain the pore size and volume after degassing the sample at 100°C to constant weight. Powder X-ray diffraction (p-XRD) patterns were performed at room temperature using a Rigaku SmartLab at 2θ range from 5° to 80° angle with $\text{Cu K}\alpha$ radiation ($\lambda = 1.54056 \text{ \AA}$). High-resolution transmission electron microscopy (H-TEM) images were captured at 200 kV

accelerating voltage using a JEOL JEM-2100F electron microscope. A certain amount of the catalyst was suspended in methanol ultrasonically, and then a few drops were deposited on the carbon-coated grid and were allowed to dry before the analysis. Tescan Vega 3 LMH Scanning Electron Microscope (SEM) with a 20.0 kV electron scattering detector voltage was used to acquire the catalyst's morphology. Prior to the image capturing, the sample was carbon-coated using an Agar Turbo Carbon Coater. For the execution of catalyst's reducibility of the catalyst, hydrogen temperature-programmed reduction was performed using a Micromeritics Autochem II 2920, by probing with 10% H₂/Ar at a flow rate of 50 mL min⁻¹ within the range of 25 - 800 °C having 10 °C·min⁻¹ ramp rate. This was carried out after the catalyst's surface was purged by an argon flow at 200 °C for 1 h. Fourier transform infrared spectroscopy (FTIR) was conducted on Shimadzu IRAffinity-1 to identify the specific functional groups of the sample's chemical composition. Thermal analysis of the catalyst was done by subjecting a certain amount to a temperature range from 25 - 1000 °C with a heating ramp rate of 10 °C·min⁻¹ under a nitrogen flow of 100 mL·min⁻¹ flow rate, on a TGA Perkin-Elmer STA 6000.

4.2.4 Hydrogenation of ketone in HPMC solution

In a typical procedure, the reduction proceeded by pipetting 21.6 mmol acetophenone into a 50 mL carousel tube containing PdSiO₂ (0.22 g), 0.5 mmol of decane, a certain amount of NaBH₄, and 6 mL of water modified with Hydroxypropyl methylcellulose (HPMC) solution. The reaction was allowed to stir continuously at 600 rpm and 80 °C for a duration of 30 min, 1 h, and 2 h separately and repeatedly on a multi-reactor (Radley discovery Technologies) connected to a reflux condenser. Product extraction was done using ethyl acetate to separate the organic layer at the end of each catalytic run, and the extracts were passed through a column of MgSO₄. Spectrophotometric analysis of the substrate (acetophenone) and the product (1-phenyl ethanol) were monitored and obtained on a Shimadzu UV-1800 in 3 mL quartz cuvette. The absorbance was obtained from λ 700 to λ 250 nm. The product was analyzed using a Gas-chromatography GC-2010 plus (Shimadzu) connected with a flame ionization detector (FID) and a Restek-800-356-1688 capillary column of 30 m × 0.25 mm × 0.25 μ mol film thickness. While the injection port was fixed at 250 °C, the FID temperature was set at 300 °C. Besides, the carrier gas used was nitrogen gas, and the temperature of the column remained at 300 °C. Identification of the product

was acquired through a Shimadzu GC-MS QP2010, which uses a fused silica capillary column of 30 mm × 0.25 mm × 0.25 μmol film thickness.

4.3 Result and discussion

4.3.1 Characterization

The result N₂ adsorption-desorption curve obtained is shown in **Figure 4.1a**. The result reveals that an adsorption isotherm of a type I hysteresis loop is seen based on the IUPAC classification [29]. This is an indication of typical non-porous material [30]. The surface area obtained (13.14 m²g⁻¹) between the pressure range 0.91 and 1.00 P/P₀ is similar to the previously reported result [28]. Moreover, the surface area obtained for the silica support (44.91 m²g⁻¹) was obtained between the pressure range of 0.89 and 0.99 P/P₀. We observed that the surface area decreased after the impregnation of the Pd metal. We deduced that the surface area change is due to the surface coverage of the silica support after Pd impregnation.

The p-XRD pattern of the material is shown in **Figure 4.1b**. The diffraction peak centered at 2θ = 23° can be ascribed to amorphous silica [31]. The peaks observed at 2θ = 40.2° and 46.6° are exhibited by the Pd diffraction peak, and they correspond to the face-centered plane of (111) and (200), respectively [25,32]. In this case, the Pd peak obtained indicates well-dispersed homogenized particles on the support material.

The thermogravimetric analysis of Pd@SiO₂ and its differential profile (TG/DTG) measured as the temperature changes over time are shown in **Figure 4.2**. The thermogram profile in **Figure 4.2a**. demonstrated two different weight loss processes. The first degree of degradation between 0 and 109 °C is an indication of surface absorbed hydroxyl loss, of which its appearance is connected to moisture adsorption from exposure to the atmosphere before the analysis. Moreover, the second weightloss recorded is attributed to the decomposition of condensed silanol, which had aggregated into oxides on the silica surface [31]. Amorphous silica hydrolyzed by the disintegration of siloxane bond (≡ Si-O- Si ≡). Also, the differential curve in **Figure 4.2b**. shows the maximum weight loss, which was prominently displayed at the second degradation stage.

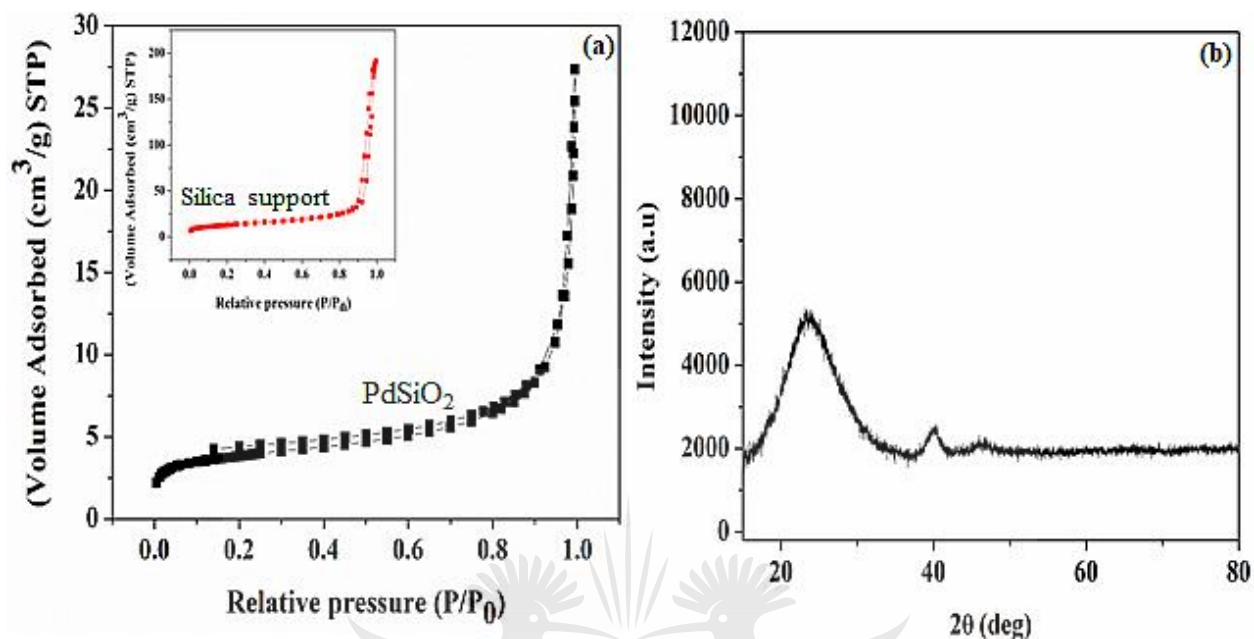


Figure 4.1: (a) N₂ adsorption-desorption isotherm, (b) powder-XRD pattern of Pd@SiO₂.

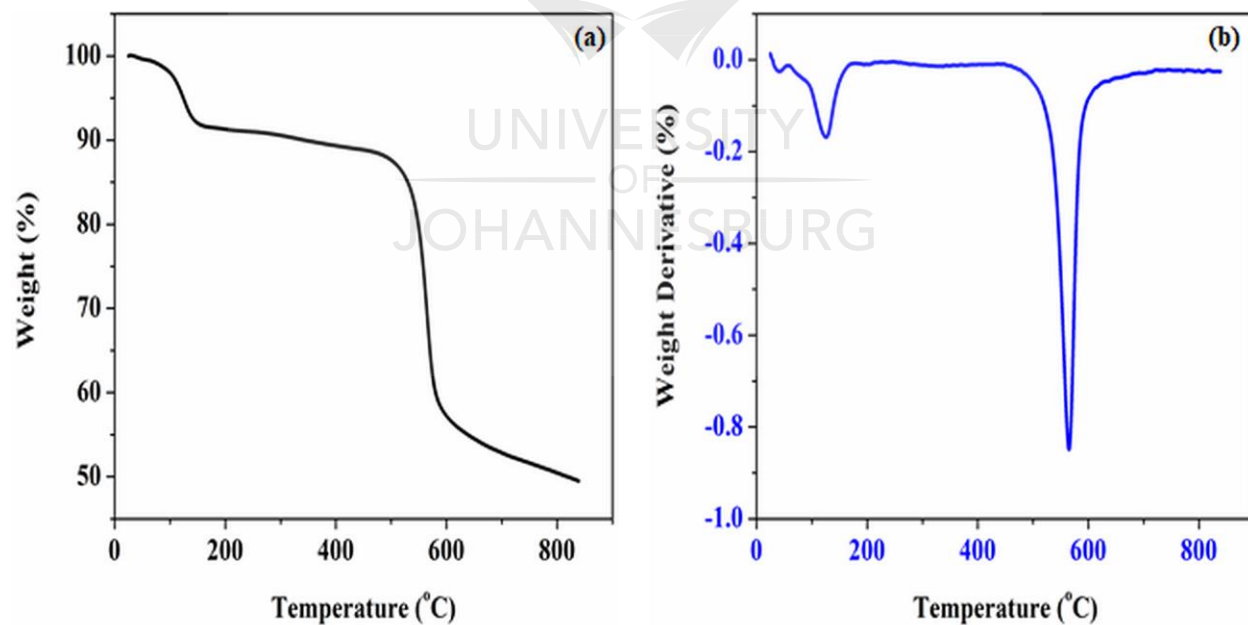


Figure 4.2: Thermogravimetric analysis of Pd@SiO₂ (a) Percentage weight loss, (b) Differential weight.

The TEM analysis that was performed to confirm the internal morphology of Pd@SiO₂ is presented in **Figure 4.3a**. The image revealed a well synthesized, transparent, and spherical structure of the silica framework with a surface that enhances the loading of the Pd particles. The metal particles are also shown to be loaded on the silica material. Hence, this conforms with the previously reported result [33]. The electron dispersion spectroscopy (EDS) analysis obtained from SEM/EDS is shown in **Figure 4.3b**, while the SEM result showing the surface morphology Pd@SiO₂ is presented in **Appx. IV.1** (Supplementary Information). The EDS revealed the different energy spectrums of the specific elements present in the material. Palladium element displayed minimal energy spectra compared to other elements due to tiny Pd loading encapsulated on the support, which is 0.52 wt% as obtained from the ICP-OES analysis, while the carbon (C) shown is as a result of carbon coating that was performed before the analysis.

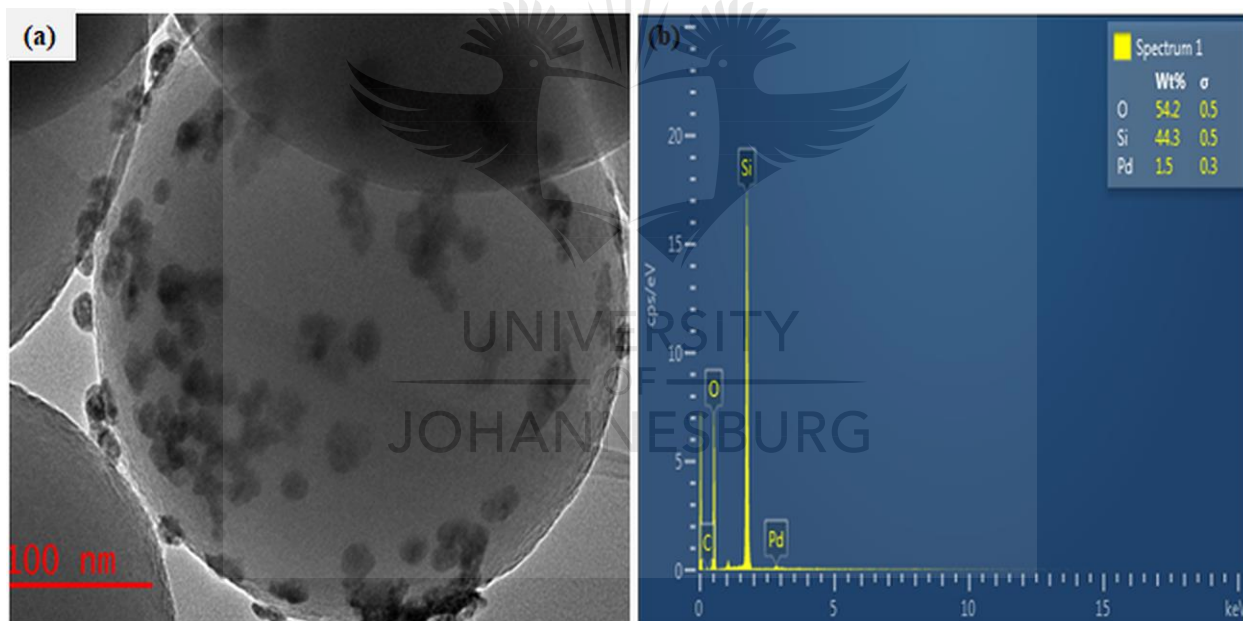


Figure 4.3: (a) TEM image obtained for Pd@SiO₂ and (b) is the EDS showing the composition of the Pd@SiO₂.

The H₂-TPR analysis result shown in **Figure 4.4a** was carried out to verify the reduction profile of Pd@SiO₂. The profile revealed Pd@SiO₂ exhibits only one reduction peak, which is mainly around 45 °C. This peak can be ascribed to the reduction peak of oxidized palladium species (PdO) present in Pd@SiO₂ [32,34].

The FTIR spectrum of Pd@SiO₂ in **Figure 4.4b** displayed both broad and sharp bands. The bands at 3342 and 1637 cm⁻¹ are associated with H-O-H asymmetric vibration due to the presence of moisture in the material [35]. The sharp peak that appeared at 1096.77 cm⁻¹ is ascribed to the asymmetric vibration of Si-O-Si [36].

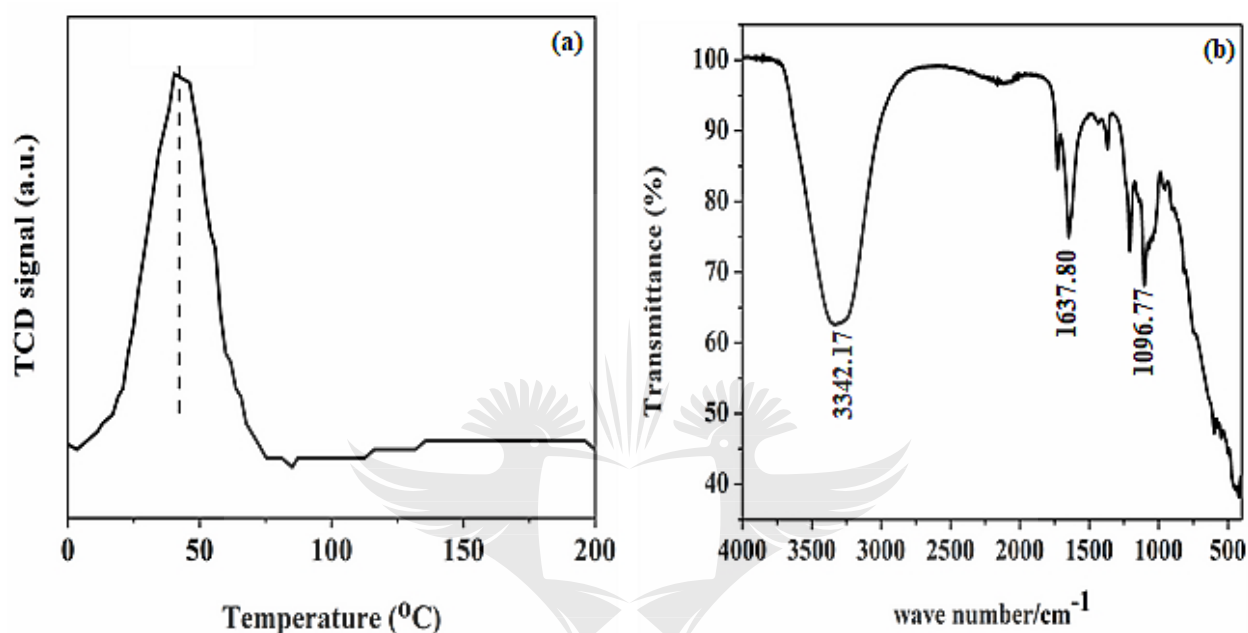


Figure 4.4: (a) H₂-Temperature program reduction analysis (b) FTIR profile of Pd@SiO₂.

4.3.2 Hydrogenation of ketone in HPMC solution

The mesoporous-based metal oxide catalysts were screened for the hydrogenation of acetophenone to select the best active catalyst for the reaction. The catalysts used are MnMMO, CoMMO, NiMMO, ZnMMO, ZrMMO, and FeMMO, but no reaction occurred (result not shown). However, the effect of BH₄⁻ on the substrate was observed, showing that the reaction is catalytically driven.

The catalytic reduction of acetophenone using Pd@SiO₂ formed 1-phenyl ethanol, a very useful intermediate in the food (flavor) and cosmetics (fragrance) industry. The conversion of 1-phenyl ethanol was processed by using **Eqn. (4.1)** supplementary, while the selectivity was computed with **Eqn. (4.2)**. The results obtained demonstrated that support material is a crucial tool in modifying the hydrophobicity of the surface character of the support [24].

Previously, it was reported that the influence of conversion in the chemoselectivity and catalytic activity depends not only on the solvent influence, metal particle, and the electronic properties but also on the metal-support material and their interaction [39,40]. As seen in the TGA and FTIR analysis, the presence of silanol with a peculiar feature of affinity for water enhanced a hydrophilic effect upon the catalyst's surface through adsorption of the hydroxyl group and other polar molecules [24], which enhanced the selectivity and the product yield. In addition, the more substantial contributing effect of HPMC at higher temperature through phase restructuring, miscibility, and interconnected viscosity brought an incredible transformation.

The ^1H NMR spectroscopy result shown in **Appx. 4.2a-2d** confirmed the molecular structure of our aromatic product. The spectra revealed a doublet at 1.47 ppm integrated for three protons, corresponding to methyl protons as expected since the methyl protons coupled to a proton at stereogenic carbon. In addition, the quartet multiplicity and integration of one proton on the stereogenic carbon at 4.86 ppm depicted the formation of 1-phenyl ethanol [41]. Also, no carbonyl carbon of the substrate was seen at 7.30 ppm of 1-phenyl ethanol. The UV-Vis spectra recorded on a Shimadzu UV-1800 in a 3 mL quartz cuvette for both products formed, and the substrate were performed within the range of 250 and 700 nm. As shown from the spectra (**Figure 4.5**), two different characteristic absorption bands are displayed for the substrate and the product. The spectrum of 1-phenyl ethanol revealed a strong absorption peak between 299 ~ 367 nm, which may be ascribed to the formation of 1-phenyl ethanol in the electronic region of $\pi \rightarrow \pi^*$ transition. The chromatogram of the identified product performed by the GC-MS equipment is also presented in **Appx. 4.3**.

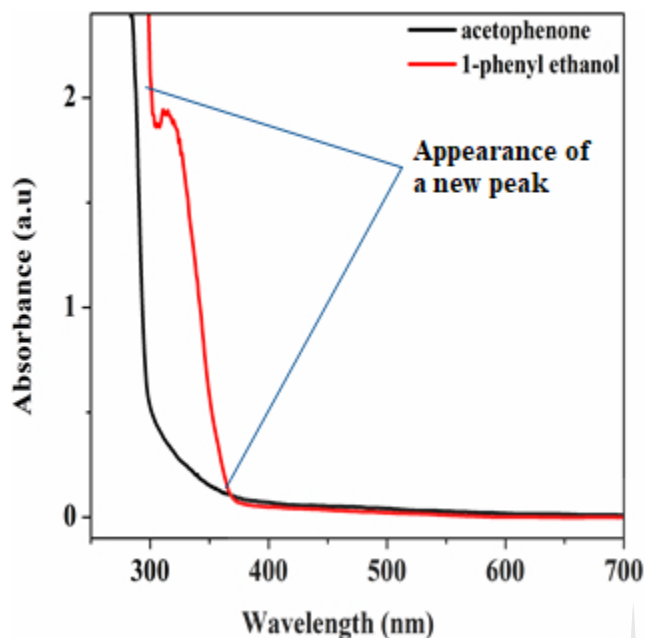


Figure 4.5: UV-Vis spectra of acetophenone substrate before catalysis, and after 1-phenyl ethanol product is formed.

4.3.3 Comparison test of HPMC solution with water

Comparison test reaction was performed with time to investigate the efficiency of HPMC solution and water while using the same parameters and reaction condition (0.22 g of Pd@SiO₂, 80 °C, 21.60 mmol of the substrate, 1.00 g of redox agent, 6.00 mL of solvent). The HPMC solution was prepared by dissolving 2% hydroxypropylmethyl in 100 mL of water. The result of the comparison is illustrated in **Figure 4.6**, and it shows that the conversion obtained in HPMC solution has a more significant influence upon acetophenone conversion to 1-phenyl ethanol. This more excellent performance is deduced to be due to increased intermolecular hydrogen bonding generated [42]. Although both mediums displayed a 100% total selectivity towards 1-phenyl ethanol, after 2 h, the highest conversion recorded in water was 55.32%, while 99.34% was observed for reaction in HPMC water. Therefore, HPMC solution was preferred above water to investigate other parameters.

At lower temperatures, HPMC displays liquid-like attributes that congeal upon an increase in temperature where it potentially controls the structural and rheological pattern of the mixture [43]. The hydroxypropyl group of the HPMC interacts with the molecule of water to form hydrogen

bonds, while around the hydrophobic region (methyl groups), an enclosure of orderly arranged water in the form of “cages” is formed at a lower temperature. When the temperature increases, the system gains energy, and the hydrogen bonds break free from their enclosure while the clusters of hydrophobic groups are likewise released. This resulted in the building up of an interconnected network of viscoelastic thermal gel, which enhances higher interaction and stability with the reaction medium. Viscosity has been reported to enhance stability within the colloidal dispersion by retarding the collapsibility of droplets and aggregation of particles [9]. Hence, this behavioral pattern in water makes HPMC a biopolymer of special interest for drug formulation release.

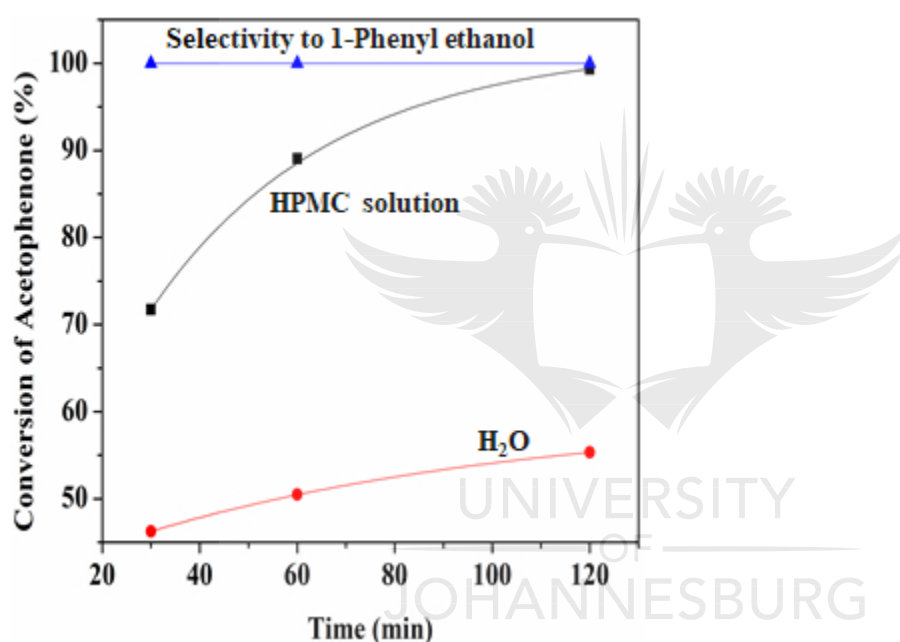


Figure 4.6: Percentage conversion comparison of HPMC modified water and unmodified water.

4.3.4 Effect of catalyst amount

One of the crucial parameters in catalytic transformation is the catalyst amount because it enhances substrate conversion, selectivity, and product yield or formation. The different catalyst variations were investigated using three variations from 0.12 to 0.33 g while other parameters remained constant. The percentage mole of each catalysts amount is 0.000623, 0.001144, and 0.001712 mol for 0.12, 0.22, and 0.33 g respectively. The result is shown in **Figure 4.7a**. All three variations depicted a progressive increase in the conversion as the time increases with a maximum conversion of 99.34% after 120 min at 80 °C. This result is due to the increase in the number of active sites of

the catalyst as the reaction is taking place on the catalyst's surface. From the turnover number (TON) obtained, which is number of mole of substrate consumed/ mole of catalyst [44]. It is noteworthy that 0.12 g of catalyst is the optimum catalyst loading as 75% conversion was obtained within 1h of the reaction period. The TON values ranges from 3679×10^3 , 2.009×10^3 , 1.335×10^3 mol for 0.12, 0.22, and 0.33 g respectively.

Initially, both BH_4^- and the substrate are adsorbed on the catalyst surface, and as the reaction proceeds, the carbonyl group of the acetophenone is activated by the catalyst to bond with the nucleophile of the BH_4^- . Then, the next step is the interaction of BH_4^- and the carbonyl carbon atom on the catalyst's surface, thereby enhancing its electrophilicity. Hence, the protons (H^+) or electrophile released from HPMC solution attacks the oxygen generated from the carbonyl group leading to the formation of 1-phenyl ethanol [36]. The process is completed by the product's desorption from the catalyst surface, where a weak covalent bond initially bonded it. Hence, the process continues in a repetitive pattern of substrate adsorption and product desorption. The hydrogenation process increases when the active sites are in abundance, while the reaction only ceases when the hydride ions produced by BH_4^- are used up [45]. The same conversion trend is seen in **Appx. 4.4a** and **4.5a** at different temperatures.

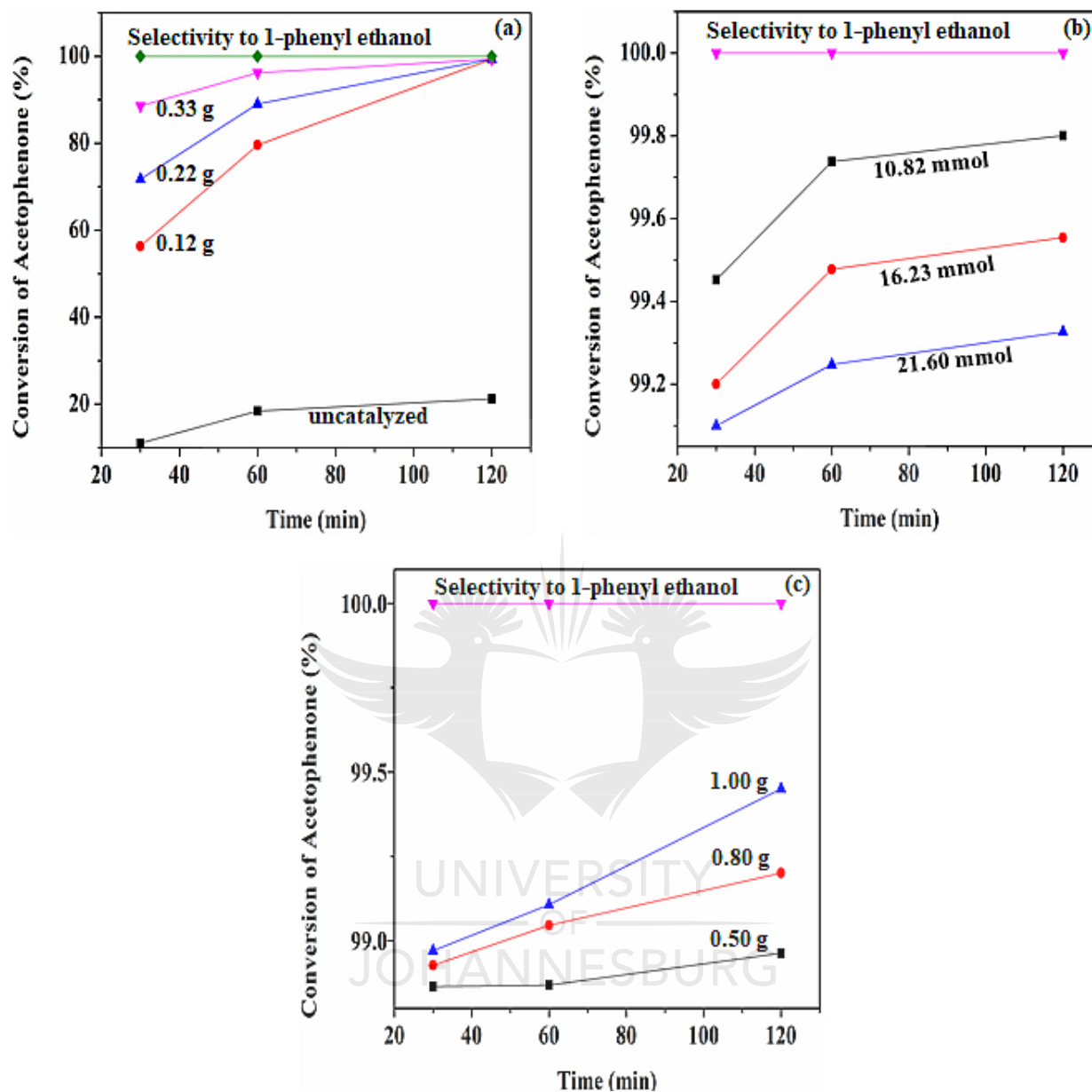


Figure 4.7: Different plots revealing the variations at 80 °C of (a) catalyst amount variation, (b) substrate variation, (c) Borohydride variation obtained.

However, an increase in the conversion as the catalyst increases was observed, and the result is present in **Table 4.1**. Moreover, to know the effect of hydrogen supply and the contribution of BH_4^- used in the reaction, the hydrogenation was carried out in the catalyst's absence. The result showed up to 21.21 % conversion of acetophenone at 80 °C while the reaction did not proceed in

the absence of both the catalyst and the supply of hydrogen. This indicates that the reaction is mainly a function of the catalyst.

Table 4.1:

Data obtained for the conversion of acetophenone at different catalyst amount.

Catalyst (g)	Conversion (%)		
	at 30 (min)	at 60 (min)	at 120 (min)
0.12	56.33	79.60	96.21
0.22	71.73	89.06	99.33
0.33	88.57	96.21	99.34

Condition: 80 °C, 21.60 mmol of the substrate, 1.00 g of redox agent, 6.00 mL of solvent.

4.3.5 Effect of substrate amount

The substrate variation was observed using three amount from 10.82, 16.23 mmol, to 21.60 mmol, and it is represented in **Figure 4.7b**. The result showed an increase in conversion trend as the time increases with the highest conversion of 99.80% recorded in 120 min at 80 °C. The conversion trends as the substrate concentration increased is > 99.80 > 99.55, and > 99.32% for 10.82, 16.23, and 21.60 mmol, respectively, after 120 min. It is worth noting that the increase in conversion with a decrease in substrate amount may be due to the higher solubility of the substrate obtained in HPMC solution at a minimum substrate amount. Organic substrate dissolution for reactivity to form product is enhanced in HPMC solution. In addition, these patterns could also result from the saturation of the substrate upon the catalyst surface. Other plots obtained from the data acquired for the substrate variation at different temperatures are shown in **Appx. 4.4b** and **4.5b**. Supplementary table (**ST.**) **4.1** also presented the data obtained for the different temperatures at the same catalyst and the substrate amount.

4.3.6 Effect of borohydride amount

The investigation carried out on the effect of BH_4^- was performed using three different parameters as well. As shown in **Figure 4.7c**, the result revealed an increase in the percentage conversion trend as the BH_4^- increases. This indicates an increase in the generation of the nucleophile, which is attacked by the electrophile from the water leading to an increase in the desorption of the product

formed from the surface of the catalysts. The pattern of increase in the conversion as the hydrogen donation increases was also acquired at other temperatures. This is illustrated in **Appx. 4.4c** and **4.5c**.

4.3.7 Effect of temperature

The investigation of the effect of temperature on chemo-selective hydrogenation of acetophenone was probed using three different temperatures of 30, 60, and 80 °C. The amount of catalyst used and other reactant parameters were kept constant while changing the temperature. The graphical plot is illustrated in **Figure 4.8a**. At each temperature variation, selectivity of 100% toward 1-phenyl ethanol was achieved with an overall highest percentage of 65.62, 96.22, and 99.80% at 30, 60, and 80 °C, respectively, using the minimum substrate amount (10.82 mmol). The increase in the catalytic conversion as the temperature increase may be due to a modulated enlargement in molecular diffusion at a higher temperature, leading to an improved conversion rate and enhanced productivity [46]. Moreover, increasing temperature creates a higher interacting environment for both the hydrophobic and hydroxyl (hydrophilic) counterparts in thermal gel such as HPMC.[43] This is also demonstrated in the observed rate constant k_{obs} computed: in the order of $0.16 \text{ min}^{-1} < 0.24 \text{ min}^{-1} < 0.29 \text{ min}^{-1}$ at 30, 60, and 80 °C respectively. The graph of k_{obs} against the temperature is revealed in **Appx.4.6**.

The observed activation energy for the Pd@SiO₂ catalyst was computed from the graph of $\ln k_{obs}$ against (1/T) as presented in **Figure 4.8b**. To the best of our knowledge, there are only a few reports on the activation energy for acetophenone hydrogenation. The estimated value obtained was discovered to be 19.05 kJ·mol⁻¹. This is an indication of a typical catalytically driven chemical reaction.

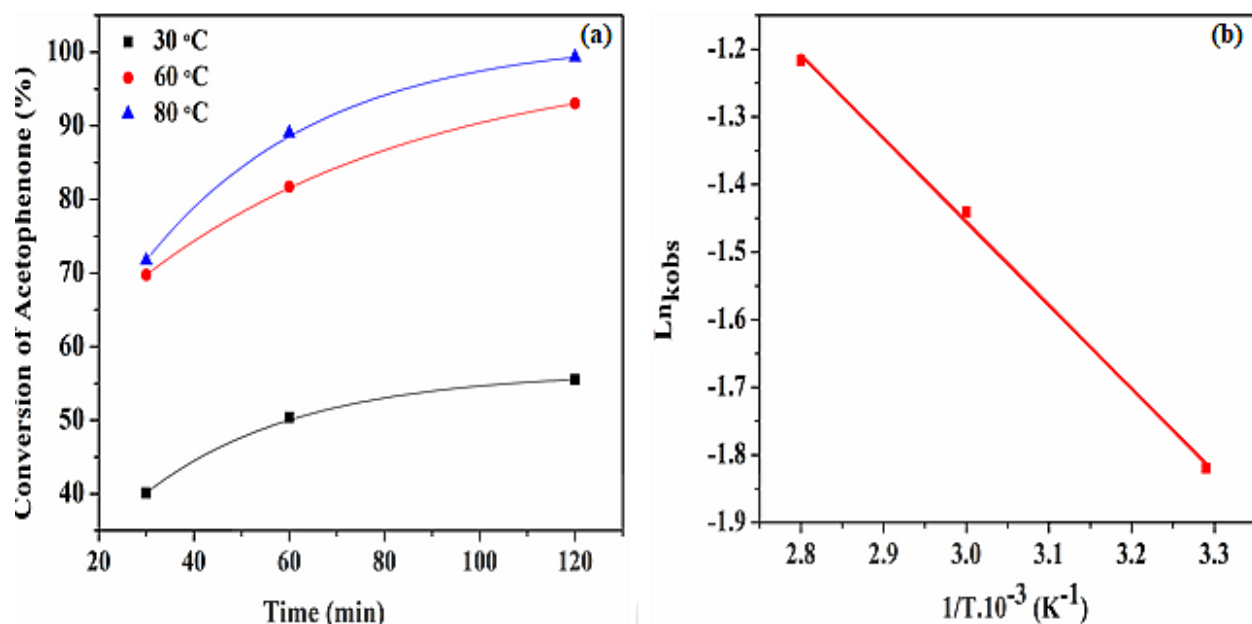


Figure 4.8: (a) Percentage conversion of acetophenone at different temperatures used, (b) The Arrhenius plot of $\ln k_{obs}$ against $1/T$ at various temperatures.

4.3.8 Turnover frequency of Pd@SiO₂ Catalyst

The catalyst's turnover frequency (TOF) is one of the crucial tools in estimating or probing the activity of a catalyst [44]. It is a valuable assessment for catalytic comparison of catalysts of the same characteristic domain [47]. The TOF can be expressed as the number of converted moles of acetophenone (substrate) divided by the number of loaded catalyst amounts and reaction time. **Table 4.2** presented the TOF calculated for the conversion of acetophenone at different temperatures. The result obtained showed a consistent increase in TOF as the temperature increases. We can say that increase in temperature significantly contributes to and influences the activity of the Pd@SiO₂ catalyst. In addition, product formation also improved at higher temperatures.

Table 4.2:

Data showing the increasing order of the TOF obtained at different temperatures.

Temperature (°C)	TOF (min ⁻¹)
30	368.31
60	585.57
80	625.29

4.3.9 Stability and recyclability test

Ultimately, a critical aspect of heterogeneity in catalysis is the ability to recover and reuse catalysts with an insignificant change in their activities. This attribute confirms their stability in the reaction media. Pd@SiO₂ catalyst's stability was investigated over a period of 3-cycles in the reaction medium, as displayed in **Figure 4.9**. The result showed that the catalyst had no significant deactivation or reduction in activity as the number of cycles increased. The selectivity toward 1-Phenyl ethanol remained at 100% for the 3-cycles, while the conversion obtained at the third cycle was 90%. This result represents a good characteristic of Pd@SiO₂ catalyst stability. Furthermore, ICP-OES measurements also revealed some negligible Pd (0.05 mg/L) was available within the reaction medium at the end.

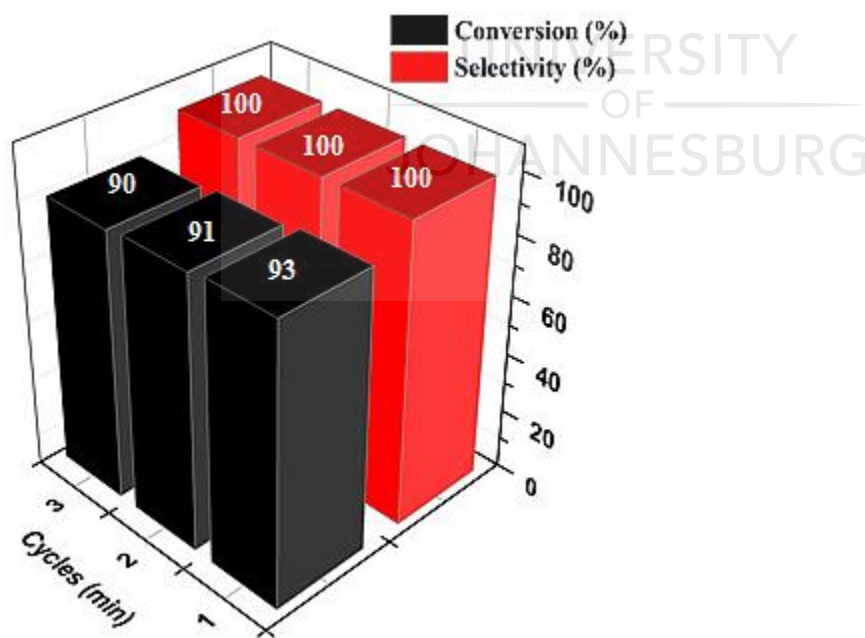


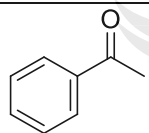
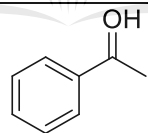
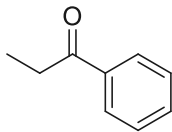
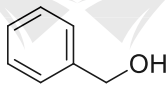
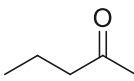
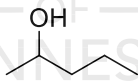
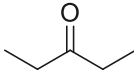
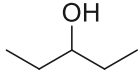
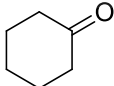
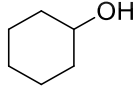
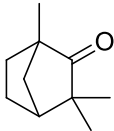
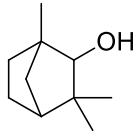
Figure 4.9. Recyclability plot of acetophenone conversion to 1-Phenyl ethanol (at 80 °C, 0.22 g catalyst, 21.60 mmol of acetophenone).

4.3.10 Hydrogenation with other Ketones

In addition, the hydrogenation reaction was carried out with five other varieties of ketone substrates which are propiophenone, 3-pentanone, 2-pentanone, cyclohexanone, and fenchone. An excellent quantitative conversion was achieved for all the substrates, as shown in **Table 4.3**, from entries 2 to 6. The NMR analysis obtained for the structural product identification is shown in **Appx. 4.7a, and b, Appx. 4.7a, and b, Appx. 4.11a, and b, Appx. 4.13a, and b, and Appx. 4.15a, and b**. Further products confirmation was carried out through GC-MS analysis, and it revealed the various products generated after the hydrogenation. The results obtained are shown in **Appx. 4.8, Appx. 4.10, Appx. 4.12, Appx. 4.14, and Appx. 4.16**.

Table 4.3:

Reduction of other ketone substrates by Pd@SiO₂

Entry	Substrate	Product	Time (min)	Conversion (%)
1			120	96.21
2			120	94.64
3			120	94.38
4			120	98.49
5			120	96.48
6			120	95.97

Condition: 21.60 mmol of substrate in HPMC solution; 80 °C.

4.3.11 Comparative study of Pd@SiO₂ with other Pd based Catalyst

A comparison of Pd@SiO₂ activity for the hydrogenation of acetophenone was made with the previous reports to quantify the effectiveness of the catalyst. This is summarized in **Table 4.4**. From the summary, the conversion and selectivity obtained for using Pd@SiO₂ catalysts are impressively comparable to the reported values in the table. Also, the time taken for the production of 1-phenyl ethanol depicted an impressive performance. The parameters obtained for TOF calculation also expressed the efficiency and capability of Pd@SiO₂ in the hydrogenation reaction with regards to other values in the literature. Moreover, the energy of activation obtained in this report which is lower than those in previous reports presented the needed energy that can substantially yield the production of 1-phenyl ethanol.



Table 4.4:Comparison of Pd@SiO₂ catalysts activity with Pd-based catalysts previous reports towards hydrogenation of ketone.

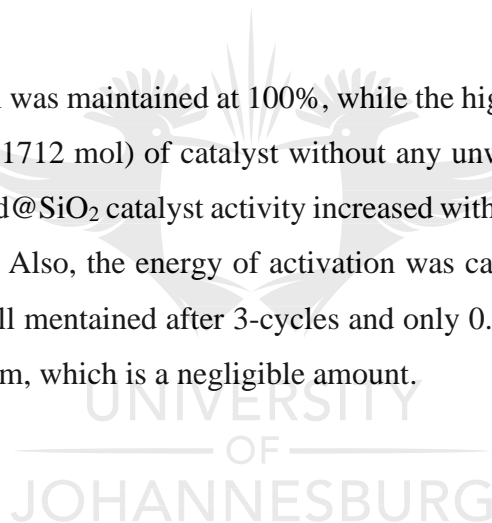
Catalyst	Hydrogen source	Conversion (%)	Selectivity (%)	Temp (°C)	Time (min)	E _a (kJ·mol ⁻¹)	Product	TOF (min ⁻¹)	Ref.
PdNPs	NaBH ₄	99.8	100	28.0	6	-	Isopropanol	-	[25]
Pd/SA	Pressurized H ₂	95	55	60.0	60	-	Ethylbenzene	-	[26]
Pd/C	Pressurized H ₂	96.0	96	39.9	180	-	1-Phenylethanol	-	[47]
Pd/N-VGCF ^c	ATM H ₂	77	31	70.0	300	-	(R)-1-Phenylethanol	116.7	[35]
Pd/N-VGCF ^b	ATM H ₂	76	33	70.0	300	-	(R)-1-Phenylethanol	83.3	[35]
Pd@Ph-POP	Pressurized H ₂	100	100	60.0	60	38.00	Ethylbenzene	5.42	[36]
Pd@Al ₂ O ₃	Pressurized H ₂	75	3	60.0	60	124.00	Ethylbenzene	3.80	[36]
Pd-RuEnCat	Pressurized H ₂	97	71	80.0	240	61.90	1-Phenylethanol	-	[21]
Pd@SiO ₂	NaBH ₄	99.8	100	80.0	30	19.05	1-Phenylethanol	625.29	TW

Temp = Temperature, Ref = Reference, TW = This work.

4.4 Conclusion

The Pd@SiO₂ catalyst was successfully synthesized, and the solvent used was an advantage for the effective reduction of acetophenone. This is due to silanol groups occupying the catalyst's surface, making the adsorption of acetophenone and hydrogen easy and quick. The catalytic reduction of acetophenone conducted in HPMC solution using BH₄⁻ as a hydrogen source demonstrated to be an attractive, efficient, effective, and eco-friendly alternative. The investigation revealed HPMC solution as a promising channel for the sustainable catalytic transformation of acetophenone. Moreover, an enabling reaction medium was generated through intermolecular interaction from the HPMC at a higher temperature. Also, the nucleophile generated through the BH₄⁻ effectively reacted with the oxygen present in the carbonyl group before interaction with the protons (H⁺), which resulted in the formation of 1-Phenyl ethanol.

The selectivity of 1-phenyl ethanol was maintained at 100%, while the highest conversion obtained was 99.80% at 80°C using 0.33g (0.001712 mol) of catalyst without any unwanted product or by-product. The TOF values recorded for the Pd@SiO₂ catalyst activity increased with increased temperature having the highest value of 625.29 min⁻¹. Also, the energy of activation was calculated to be 19.05 kJ·mol⁻¹. The activity of the catalyst was still maintained after 3-cycles and only 0.05 mg/L of Pd@SiO₂ catalyst were present in the reaction medium, which is a negligible amount.



4.5 References

- [1] M.B. Gawande, V.D.B. Bonifácio, R. Luque, P.S. Branco, R.S. Varma, Benign by design: Catalyst-free in-water, on-water green chemical methodologies in organic synthesis, *Chem. Soc. Rev.* 42 (2013) 5522–5551.
- [2] L. Fumagalli, A. Esfandiari, R. Fabregas, S. Hu, P. Ares, A. Janardanan, Q. Yang, B. Radha, T. Taniguchi, K. Watanabe, G. Gomila, K.S. Novoselov, A.K. Geim, Anomalously low dielectric constant of confined water, *Science* 360 (2018) 1339–1342.
- [3] S.M. Kim, H.S. Yoo, H. Hosono, J.W. Yang, S.W. Kim, Chemoselective reduction and oxidation of ketones in water through control of the electron transfer pathway, *Sci. Rep.* 5 (2015) 1–9.
- [4] M. Bihani, P.P. Bora, M. Nachtegaal, J.B. Jasinski, S. Plummer, F. Gallou, S. Handa, Microballs Containing Ni(0)Pd(0) Nanoparticles for Highly Selective Micellar Catalysis in Water, *ACS Catal.* 9 (2019) 7520–7526.
- [5] M. Billamboz, F. Mangin, N. Drillaud, C. Chevrin-Villette, E. Banaszak-Léonard, C. Len, Micellar catalysis using a photochromic surfactant: Application to the Pd-catalyzed Tsuji-Trost reaction in water, *J. Org. Chem.* 79 (2014) 493–500.
- [6] T. Kitanosono, K. Masuda, P. Xu, S. Kobayashi, Catalytic Organic Reactions in Water toward Sustainable Society, *Chem. Rev.* 118 (2018) 679–746.
- [7] S. Buda, M. Pasternak, J. Mlynarski, Aqueous Phase Asymmetric Catalysis. In *Enantioselective Homogeneous Supported Catalysis*, Royal Society of Chemistry, (2011) 206-236.
- [8] K. Deshmukh, M.B. Ahamed, R.R. Deshmukh, S.K.K. Pasha, P.R. Bhagat, K. Chidambaram, Biopolymer composites with high dielectric performance: interface engineering, in: *Biopolym. Compos. Electron.*, Elsevier, (2017) 27–128.
- [9] L.L. Tundisi, G.B. Mostaço, P.C. Carricondo, D.F.S. Petri, Hydroxypropyl methylcellulose: Physicochemical properties and ocular drug delivery formulations, *Eur. J. Pharm. Sci.* 159 (2021) 105736.
- [10] C. Allenspach, P. Timmins, S. Sharif, T. Minko, Characterization of a novel hydroxypropyl methylcellulose (HPMC) direct compression grade excipient for pharmaceutical tablets, *Int. J. Pharm.* 583 (2020) 119343.
- [11] W. Rhimi, A. Boulila, R. Gheribi, K. Khwaldia, Development, characterization and

- application of hydroxypropylmethylcellulose films enriched with cypress seed extract, *RSC Adv.* 8 (2018) 23615–23622.
- [12] T. Jayaramudu, K. Varaprasad, R.D. Pyarasani, K.K. Reddy, A. Akbari-Fakhabadi, V. Carrasco-Sánchez, J. Amalraj, Hydroxypropyl methylcellulose-copper nanoparticle and its nanocomposite hydrogel films for antibacterial application, *Carbohydr. Polym.* 254 (2021) 117302.
- [13] M.N. da Silva, J. de Matos Fonseca, H.K. Feldhaus, L.S. Soares, G.A. Valencia, C.E.M. de Campos, M. Di Luccio, A.R. Monteiro, Physical and morphological properties of hydroxypropyl methylcellulose films with curcumin polymorphs, *Food Hydrocoll.* 97 (2019) 105217.
- [14] R. Noyori, T. Ohkuma, Asymmetric catalysis by architectural and functional molecular engineering: Practical chemo- and stereoselective hydrogenation of ketones, *Angew. Chemie - Int. Ed.* 40 (2001) 40–73.
- [15] D. Petkova, N. Borlinghaus, S. Sharma, J. Kaschel, T. Lindner, J. Klee, A. Jolit, V. Haller, S. Heitz, K. Britze, J. Dietrich, W.M. Braje, S. Handa, Hydrophobic Pockets of HPMC Enable Extremely Short Reaction Times in Water, *ACS Sustain. Chem. Eng.* 8 (2020) 12612–12617.
- [16] N.C. Mamillapalli, G. Sekar, Metal free chemoselective reduction of α -keto amides using TBAF as catalyst, *RSC Adv.* 4 (2014) 61077–61085.
- [17] D. Wang, D. Astruc, The Golden Age of Transfer Hydrogenation, *Chem. Rev.* 115 (2015) 6621–6686.
- [18] N. Castellanos-Blanco, M. Flores-Alamo, J.J. García, Nickel-catalyzed reduction of ketones with water and triethylsilane, *Inorganica Chim. Acta.* 466 (2017) 324–332.
- [19] Y. Gou, X. Liang, B. Chen, Catalytic hydrogenation of acetophenone over shape controlled Pd catalysts supported on sheet-like NiO, *Catal. Today.* 216 (2013) 200–204.
- [20] N. Su, X. Chen, B. Yue, H. He, Preparation of free-standing mesoporous metal catalysts and their applications in heterogeneous enantioselective hydrogenations, *Catal. Sci. Technol.* 5 (2015) 638–649.
- [21] S.R. More, G.D. Yadav, Effect of supercritical CO₂ as reaction medium for selective hydrogenation of acetophenone to 1-phenylethanol, *ACS Omega.* 3 (2018) 7124–7132.
- [22] X.B. Zhang, W.N. Lu, J.L. Wang, B.H. Liao, Y.H. Qin, Y.J. Zhang, B. Zhang, S.A. Xin,

- Selective catalytic hydrogenation of acetophenone to 1-phenylethanol over Co/mordenite in water, *Catal. Commun.* 119 (2019) 124–128.
- [23] R.T. Kumah, N. Tsaulwayo, B.A. Xulu, S.O. Ojwach, Structural, kinetics and mechanistic studies of transfer hydrogenation of ketones catalyzed by chiral (pyridyl)imine nickel(ii) complexes, *Dalt. Trans.* 48 (2019) 13630–13640.
- [24] D.C. Costa, J.F. Bengoa, S.G. Marchetti, V. Vetere, Impact of the surface hydrophobicity/hydrophilicity ratio on the catalytic properties of Ni nanoparticles/MCM-41 system used in the hydrogenation of acetophenone, *Catal. Today.* 372 (2020) 20–26.
- [25] A. Balouch, A. Ali Umar, A.A. Shah, M. Mat Salleh, M. Oyama, Efficient heterogeneous catalytic hydrogenation of acetone to isopropanol on semihollow and porous palladium nanocatalyst, *ACS Appl. Mater. Interfaces.* 5 (2013) 9843–9849.
- [26] M. Chen, N. Maeda, A. Baiker, J. Huang, Hydrogenation of acetophenone on Pd/silica–alumina catalysts with tunable acidity: mechanistic insight by *in-situ* ATR-IR spectroscopy, *ACS Catal.* 8 (2018) 6594–6600.
- [27] S. Fujita, Y. Onodera, H. Yoshida, M. Arai, Selective hydrogenation of acetophenone with supported Pd and Rh catalysts in water, organic solvents, and CO₂-dissolved expanded liquids, *Green Chem.* 18 (2016) 4934–4940.
- [28] H. Yang, L. Fu, L. Wei, J. Liang, B.P. Binks, Compartmentalization of incompatible reagents within Pickering emulsion droplets for one-pot cascade reactions, *J. Am. Chem. Soc.* 137 (2015) 1362–1371.
- [29] M. Thommes, K. Kaneko, A. V Neimark, J.P. Olivier, F. Rodriguez-reinoso, J. Rouquerol, K.S.W. Sing, Physisorption of gases, with special reference to the evaluation of surface area and pore size distribution (IUPAC Technical Report), 87 (2015) 1051–1069.
- [30] Matshitse R. Brunauer-Emmett-Teller (BET) surface area analysis *Rhodes Univ. Natl. Res. Found.*, 384 2010.
- [31] O.R. Onisuru, C.O. Oseghale, R. Meijboom, *In-situ* replacement of Cu-DEN: an approach for preparing a more noble metal nanocatalyst for catalytic use, *New J. Chem.* 44 (2020) 20322–20333.
- [32] M.Y. Byun, D.-W. Park, M.S. Lee, Effect of Oxide Supports on the Activity of Pd Based Catalysts for Furfural Hydrogenation, *Catalysts.* 10 (2020) 837.

- [33] A. Heel, G. Kasper, Production and characterization of Pd/SiO₂ catalyst nanoparticles from a continuous MOCVS/MOCVD aerosol process at atmospheric pressure, *Aerosol Sci. Technol.* 39 (2005) 1027–1037.
- [34] Y.H. Ahmad, A.T. Mohamed, K.A. Mahmoud, A.S. Aljaber, S.Y. Al-Qaradawi, Natural clay-supported palladium catalysts for methane oxidation reaction: effect of alloying, *RSC Adv.* 9 (2019) 32928–32935.
- [35] J. Yang, Q. Liang, H. Hou, Thermal decomposition mechanism and kinetics of Pd/SiO₂ nanocomposites in air atmosphere, *J. Therm. Anal. Calorim.* 135 (2019) 2733–2745.
- [36] M.T. Shah, A. Balouch, K. Rajar, Sirajuddin, I.A. Brohi, A.A. Umar, Selective heterogeneous catalytic hydrogenation of ketone (C=O) to alcohol (OH) by magnetite nanoparticles following Langmuir-Hinshelwood kinetic approach, *ACS Appl. Mater. Interfaces.* 7 (2015) 6480–6489.
- [37] S. Sahin, P. Mäki-Arvela, J.-P. Tessonnier, A. Villa, S. Reiche, S. Wrabetz, D. Su, R. Schlögl, T. Salmi, D.Y. Murzin, Palladium catalysts supported on N-functionalized hollow vapor-grown carbon nanofibers: The effect of the basic support and catalyst reduction temperature, *Appl. Catal. A Gen.* 408 (2011) 137–147.
- [38] R. Paul, S.C. Shit, T. Fovanna, D. Ferri, B. Srinivasa Rao, G.T.K.K. Gunasooriya, D.Q. Dao, Q. Van Le, I. Shown, M.P. Sherburne, Realizing Catalytic Acetophenone Hydrodeoxygenation with Palladium-Equipped Porous Organic Polymers, *ACS Appl. Mater. Interfaces.* 12 (2020) 50550–50565.
- [39] T.N. Ye, J. Li, M. Kitano, M. Sasase, H. Hosono, Electronic interactions between a stable electrone and a nano-alloy control the chemoselective reduction reaction, *Chem. Sci.* 7 (2016) 5969–5975.
- [40] G. Vilé, D. Albani, N. Almora-Barrios, N. López, J. Pérez-Ramírez, Advances in the design of nanostructured catalysts for selective hydrogenation, *ChemCatChem.* 8 (2016) 21–33.
- [41] M. Li, B. Li, H.-F. Xia, D. Ye, J. Wu, Y. Shi, Mesoporous silica KIT-6 supported superparamagnetic CuFe₂O₄ nanoparticles for catalytic asymmetric hydrosilylation of ketones in air, *Green Chem.* 16 (2014) 2680–2688.
- [42] Y. Wang, L. Yu, F. Xie, S. Li, Q. Sun, H. Liu, L. Chen, On the investigation of thermal/cooling-gel biphasic systems based on hydroxypropyl methylcellulose and hydroxypropyl starch, *Ind. Crops Prod.* 124 (2018) 418–428.

- [43] Y. Wang, L. Yu, Q. Sun, F. Xie, Hydroxypropyl methylcellulose and hydroxypropyl starch: Rheological and gelation effects on the phase structure of their mixed hydrocolloid system, *Food Hydrocoll.* 115 (2021) 106598.
- [44] S. Kozuch, J.M.L. Martin, “Turning over” definitions in catalytic cycles, (2012) 2787–2794.
- [45] G. Guella, C. Zanchetta, B. Patton, A. Miotello, New insights on the mechanism of palladium-catalyzed hydrolysis of sodium borohydride from ^{11}B NMR measurements, *J. Phys. Chem. B.* 110 (2006) 17024–17033.
- [46] O.R. Onisuru, O.A. Alimi, K. Potgieter, R. Meijboom, Continuous-Flow Catalytic Degradation of Hexacyanoferrate Ion through Electron Transfer Induction in a 3D-Printed Flow Reactor, *J. Mater. Eng. Perform.* 30 (2021) 4891–4901.
- [47] M. Guo, J. He, Y. Li, S. Ma, X. Sun, One-step synthesis of hollow porous gold nanoparticles with tunable particle size for the reduction of 4-nitrophenol, *J. Hazard. Mater.* 310 (2016) 89–97.
- [48] N. Hiyoshi, O. Sato, A. Yamaguchi, M. Shirai, Acetophenone hydrogenation over a Pd catalyst in the presence of H_2O and CO_2 , *Chem. Commun.* 47 (2011) 115.

Chapter 5

Continuous Flow Catalytic Degradation of Hexacyanoferrate Ion through electron transfer induction in a 3D-Printed Flow Reactor

JMEPEG (2021) 30:4891–4901
<https://doi.org/10.1007/s11665-021-05527-4>

©ASM International
1059-9495/\$19.00



Continuous-Flow Catalytic Degradation of Hexacyanoferrate Ion through Electron Transfer Induction in a 3D-Printed Flow Reactor

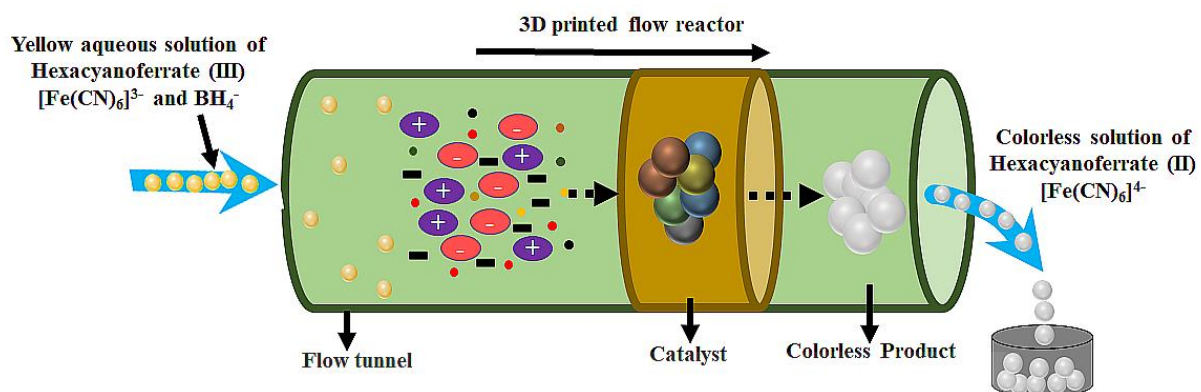
Oluwatayo Racheal Onisuru, Oyekunle Azeez Alimi, Kariska Potgieter, and Reinout Meijboom

Submitted: 3 November 2020 / Revised: 30 December 2020 / Accepted: 23 January 2021 / Published online: 16 February 2021

The benefits of 3D-printing technology in the manufacturing of laboratory equipment, in particular catalytic applications, have recently been brought to the limelight. In this paper, continuous-flow reaction devices consisting of syringe pumps and flow reactors were fabricated using a 3D-printing technique which aims at circumventing the high cost of procuring the convectional reactors for catalytic reactions. Mesoporous manganese metal oxide (MnMMO) and mesoporous cobalt metal oxide (CoMMO) catalysts were synthesized and fully characterized. The catalytic activity of the prepared nanocatalysts was evaluated in a continuous-flow operation using an in-house 3D-printed flow device for the reduction of hexacyanoferrate ion into a useful intermediate compound industrially. Different reaction parameters such as flow rates, temperature, and catalyst amount were investigated for the system's optimization. The result showed an impressive output with an outstanding conversion of 94.1% hexacyanoferrate ion in 6-minute reaction time. Also, the excellent stability of five-run reusability on hexacyanoferrate ion was performed in a safe, faster, and well-controlled microenvironment.

UNIVERSITY
OF
JOHANNESBURG

Graphical abstract



UNIVERSITY
OF
JOHANNESBURG

Abstract

The benefits of 3D-printing technology has lately been recognized in the fabrication of laboratory equipment, especially catalytic equipment. This work aims to design continuous flow reaction devices composed of syringe pumps and flow reactors using a 3D printing approach to avoid the high cost of buying convectional reactors for catalytic reactions. We synthesized mesoporous manganese metal oxide (MnMMO) and mesoporous cobalt metal oxide (CoMMO) catalysts and fully characterized them. The synthesized nanocatalysts were assessed for their catalytic activity in a continuous flow operation utilizing an in-house 3D-printed flow apparatus to ultimately reduce hexacyanoferrate ion to a valuable chemical intermediate (hexacyanoferrate (II) ion $[\text{Fe}(\text{CN})_6]^{4-}$) which is useful industrially. Various reaction parameters such as flow rates, temperature, and catalyst concentration were studied to optimize the reaction system. The result demonstrated an outstanding output of 94.1% conversion of hexacyanoferrate ion in a six-minute reaction period. Additionally, the catalyst showed remarkable stability of 5-run reusability on hexacyanoferrate ion transformation was established in a well-controlled, safe, quick microenvironment.

Keywords: 3D-Printing; Continuous flow reaction; Microfluidic reactor; Mesoporous metal oxide; Hexacyanoferrate.



5.1 Introduction

Significant progress has been made in developing continuous flow catalytic systems for application in chemical reactions and synthesis over the last two decades. This is because continuous flow systems adhere to the twelve principles of green chemistry and function more safely and efficiently than batch processing systems [1]. Compared to batch reactions, catalytic reactions in continuous flow systems demonstrate an outstanding performance [2]. Additionally, it is known to have advantages such as improved homogeneity and heat transmission, simplified scale-up, and the ability to perform multi-step reactions using several reactors in a single flow [2].

Furthermore, flow chemistry's advantages include a high surface area to volume ratio, increase in qualitative reaction parameters, compact equipment size, and adaptability of module layouts [3]. A microreactor is a functional unit of the continuous flow system typically used for small-scale reactions involving two or more chemicals that require mixing [4]. Compared to the batch system, the advantages of this method include a shorter reaction time, optimization, reduced cost, portability, and minimal reagent usage [4,5]. Thus, continuous flow microfluidic reactors have overcome the shortcomings of the batch system and enabled a rapid, safe, and convenient method of carrying out synthesis and catalysis [6,7]. The disadvantages of batch reactions include the lack of rapid and comprehensive high-throughput reactions, the inability to repeat experimental procedures reliably, and the inability to scale up good laboratory experiments, particularly those involving exothermic reactions [8].

Continuous flow microreactors are used in various scientific fields, including catalysis, nanoparticle production, polymerization, electrochemistry, and sensing [9]. While the benefits of flow chemistry are evident across all fields, designing and fabricating flow apparatus remains a significant issue. Interestingly, the coupling of flow chemistry and 3D printing has emerged as a novel and rapidly increasing area of research in recent years [10–17]. Not only does this lower production costs, but it also opens up new avenues for chemical synthesis [10,18]. The introduction of additive manufacturing (AM), which allows for the unlimited possibility of producing and assembling components in a single step, is a game-changing method with benefits across multiple industries [19]. Complex digital computer-generated models designed under AM procedures have mechanical properties similar to those of recognized manufacturing protocols [19]. Numerous

publications have been published on the use of microfluidic flow systems in the fabrication of nanoparticles (NPs) and chemical reactions [3,20–26]. To our full understanding and awareness, however, such systems have not been employed to catalyze the reduction of potassium hexacyanoferrate (III) $[\text{K}_3\text{Fe}(\text{CN})_6]$.

The heterogeneous catalytic reduction of hexacyanoferrate (III) $[\text{Fe}(\text{CN})_6]^{3-}$ by sodium borohydride has been described as a model electron transfer of an inorganic reaction under batch conditions [27–30]. However, there are few or no publications on hexacyanoferrate (III) redox transition in a microfluidic system. Mesoporous metal oxides (MMOs) are a promising class of heterogeneous catalysts that have been exploited in biological processes and large-scale chemical production [31]. This is because MMOs offer unique properties such as large interior surface areas, a wide range of pore sizes, and designable pore networking that can facilitate incorporating various active sites and supported catalyst species. Manganese and Co oxides have been shown to be catalytically effective in redox processes involving metal oxides [32]. Manganese oxide's exceptional structural variety accounts for its unique applications and functionalities as catalysts for thermally catalyzed processes and the breakdown of organic contaminants into less harmful compounds [33].

The production of the hexacyanoferrate (II) ion $[\text{Fe}(\text{CN})_6]^{4-}$ from $[\text{Fe}(\text{CN})_6]^{3-}$ is critical due to its industrial and medical applications. Hexacyanoferrate (II) ion has been reported as useful requirement for human and animal metabolism [34]. (For additional information on the potassium hexacyanoferrate (II) ion, see the supplementary material.) We catalyzed the degradation of $[\text{K}_3\text{Fe}(\text{CN})_6]$ to $[\text{K}_4\text{Fe}(\text{CN})_6]$ using sodium borohydride in a 3D-printed syringe pump under a continuous flow condition which is faster, safer, and cleaner than the standard batch approach.

5.2 Experimental section

5.2.1 Materials

Chemicals were obtained from a variety of commercial sources and were of analytical grade. Sigma-Aldrich supplied cobalt(II) nitrate hexahydrate $[\text{Co}(\text{NO}_3)_2 \cdot 6\text{H}_2\text{O}]$ (99%), 1-butanol (99.8%), F127, manganese(II) nitrate hexahydrate (99%), and potassium hexacyanoferrate $\text{K}_3[\text{Fe}(\text{CN})_6]$ (99.0 percent). Fluka supplied sodium borohydride (NaBH_4) at a concentration of

98.0 percent%. Nitric acid (HNO_3) (69-70%) was obtained from Rochelle Chemicals (RSA), while sodium carbonate (Na_2CO_3) (99.50%), sodium bicarbonate (NaHCO_3) (99.50%), and sodium hydroxide (NaOH) (99.9%) were procured from Promack chemicals. All solutions were made using Milli-Q water at a concentration of $18.2 \text{ M}\Omega\cdot\text{cm}$. A high-quality open-source fused deposition modeling 3D printer, the Prusa i3 MK3S, was purchased from Josef Prusa's website <https://prusa3d.com>. A 1.75 mm diameter 3D printing filament (Wanhao polylactic acid, PLA) was purchased at www.3dprintingstore.co.za.

5.2.2 Design of the reactor and experimental setup

The CAD design is exported as an STL file, and the resulting 3D-printed flow reactor is fabricated as depicted in **Figure 5.1a**. To achieve optical transparency, the reactor was constructed utilizing translucent polylactic acid (PLA) thermoplastic filament. **Figure 5.1a** depicts the fixed position of the catalyst within the flow reactor and the flow stream. The cylindrical U-shaped device measures 80 mm in length and 37 mm in width. It has a 4 mm internal diameter and a 9 mm exterior diameter. The reactor has a total volume of 1.7 mL. Additional parameters for 3D-printing are presented in the supplementary table (**S. Table 5.1**). To improve compact layer building, the edge effect was examined using an infill density of 80% and a flow rate of 95%, in addition to the other details in **S. Table 5.1**. The reaction apparatus was altered to fit inside a 100 mL beaker, as illustrated in **Figure 5.1a**. This enables the flow device to be handled and manipulated more efficiently throughout the catalytic process. The post-processing of 3D-printed items includes the removal of supports and smoothing.

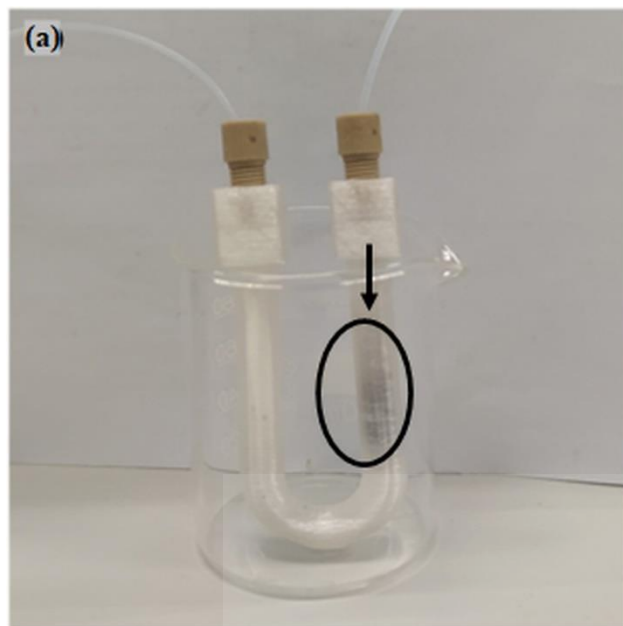


Figure 5.1: (a) Three-dimensional printing of a transparent U-shaped reactor using a thermoplastic polylactic acid filament.

5.2.3 Mesoporous manganese metal oxide fabrication (MnMMO)

Mesoporous manganese metal oxide was synthesized using a modified approach from the literature [31]. Typically, 15 mL of ethanol was used to dissolve the F127 (1.6 g) surfactant, and 2.5101 g of manganese (II) nitrate tetrahydrate (10 mmol) was added to the formulation. This was then agitated to ensure complete dissolution of the solids. Ethylene glycol (15 mL) was then added, and the mixture was stirred for another 2 h. Finally, after an overnight aging period at 80 °C, the catalyst was dried for 6 h at 150 °C and calcined for 4 h at 400 °C using a 2 °Cmin⁻¹ ramping temperature.

5.2.4 Mesoporous cobalt metal oxide fabrication (CoMMO)

Cobalt mesoporous metal oxide fabrication was synthesized following a recent publication [31]. To dissolve 1.6 g of F127 surfactant, 15 mL of ethanol was added. After this, cobalt (II) nitrate hexahydrate was added to the mixture (2.9103 g, 10 mmol). The mixture was then stirred until the solids were completely dissolved. While the mixture was still mixing, 15 mL of ethylene glycol was added and stirred for an additional about 2 h to ensure thorough mixing. It was kept overnight

at 80 °C before being dried for 6 h at 150 °C. Following that, it was calcined for 4 h at a 2 °Cmin⁻¹ ramp rate at a temperature of 400 °C.

5.2.5 Characterization of catalysts

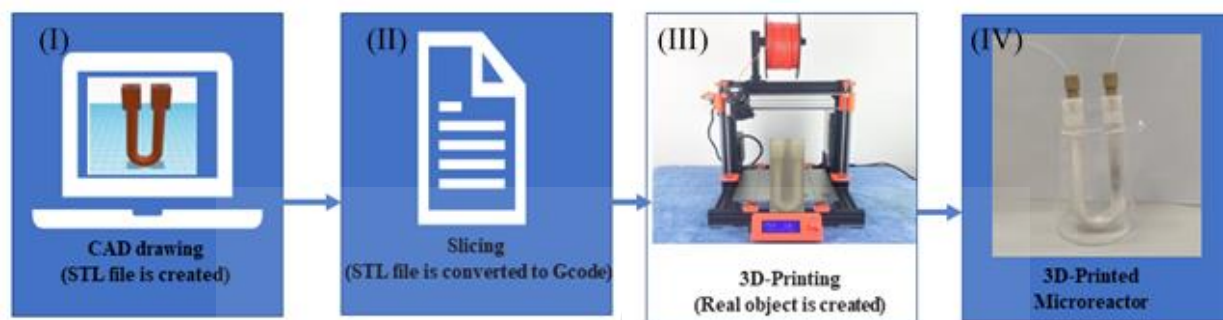
Nitrogen sorption with Brunauer-Emmett-Teller (BET) was used to measure the surface area, while the Barret-Joyner-Halenda (BJH) desorption isotherm was used to determine the distribution of pore size and volume after degassing the sample to an unvarying weight. Powder X-ray diffraction (p-XRD) patterns were obtained at room temperature using a Philips XPERT-PRO diffractometer system. It uses operating radiation of Cu K α 1, K α 2, and Ni K β (λ –1. 4406, 1. 44443, and 1.39225, respectively) at a wide-angle of 2 θ range of 10°–90° angle of diffraction patterns with 0.170° step. Before performing the High-Resolution Transmission Electron Microscopy (H-TEM), images were captured using a JEOL JEM-2100F electron microscope equipped with a 200 kV accelerating voltage. A small amount of the catalyst was dispersed in methanol, and a few drops were deposited on the carbon-coated grid. Hydrogen temperature-programmed reduction was performed using a Micromeritics Autochem II 2920 to determine the catalyst's reducibility by probing with 10% H₂/Ar at a flow rate of 50 mL min⁻¹ throughout a temperature range of 25 - 800 °C with a 10 °Cmin⁻¹ ramp rate. This was done after the catalyst surface was purified with argon flow for 1 h at a temperature of 200 °C. To determine the material's thermal stability, it was heated to a temperature range of 25 - 1000 °C at a rate of 10 °Cmin⁻¹ using a Perkin-Elmer STA 6000 TGA with a nitrogen flow rate of 100 mLmin⁻¹.

5.2.6 Fabrication of microfluidic systems

Microfluidic flow system design

A U-shaped reactor and syringe pump are what made the continuous flow system. Rossi *et al.* [35] classified the design and production of flow devices into four stages, as illustrated in **Scheme 5.1**. The computer-aided designs (CAD) from **Scheme 5.1**, stage I, were made using the Autodesk Tinkercad software tool [36]. The slicing procedure manages the printer's movement, printing process, and print quality by transforming the CAD file (stereolithographic file exported from stage I) to a computer numerical control program (g-code), a printer programming language. Stage II involves transferring the created g-code file to the printer through an SD (secure digital) card for printing (stage III). The last stage involves fabricating the three-dimensional object (the actual

object) and preparing it for use (stage IV). It is worth noting that the 3D-printed reactor is not only smaller, cheaper, and more efficient than conventional batch reactors, but it is also more versatile and can be built in the lab without the need for additional equipment. Additionally, the smaller size of the printed reactor optimizes heat transfer, mixing efficiency, and reagent consumption.



Scheme 5.1: The schematic depiction of the technique for 3D printing as described by Rossi et al. [35].

Flow reactor design

As seen in **Scheme 5.1** (IV), the reactor is a U-shaped cylindrical device with a single input/output channel through which the catalyst can be immobilized along the flow route. The reactor's entry and exit junctions are integrated with a screw to connect to conventional HPLC fittings. Compared to the straight channel reactor design used in our earlier work [37], the U-shaped convoluted design used in this study supports increased mixing and performs well compared to conventional batch reactors. In terms of fabrication, the U-shaped reactor has a significant advantage, particularly in the laboratory. Additionally, in terms of material quality, the polylactic acid thermoplastic material utilized to fabricate the reactor is inexpensive, biodegradable, and stable for all thermal conditions used for the reaction. It is worth noting that the 3D printing procedure imprinted the synthesized CoMMO catalyst into the flow reactor. The detailed procedure's description is in the supplementary information **5.1 (Appx. 5.1)**.

Before the catalytic reaction, the fidelity of the catalyst imprinted flow reactor was determined using a comprehensive characterization process termed fidelity testing. The fidelity tests aid in determining the flow reactor's and other microfluidic connections' maximum working conditions

before mechanical failure (leaking, clogging, or deformation) is noticed. The test was conducted according to the procedure previously reported by Alimi *et al* [8]. To summarize, the syringe pump was attached to the flow reactor, and distilled water was pumped at a variable flow rate. Visual inspection was used to detect leakage and determine the position of the imprinted catalyst within the reactor. The syringe pump system was used to capture flow data, and the fidelity test was used to find the optimal flow rate.

Syringe pump design

The syringe pump employed in this reaction is constructed according to the description of Alimi *et al.* [38], as seen in the figure supplementary (**Appx. V.2.**). The syringe pump, which is 150 mm wide, 47 mm deep, and 52 mm tall, is composed of two unique designs and files: (a) the stationary body; and (b) the moveable syringe carrier, also known as the plunger. The plunger is adjustable for usage with a wide variety of commercially available 1-20 mL syringes. The movable syringe carrier can slide 50 mm in both directions along the half length of a typical syringe. The 1.8-degree Nema 17 stepper motor was chosen for this syringe pump based on its withholding torque, as specified in the catalog [39], with a withholding torque of 5.5 kgcm⁻¹ to minimize backpressure. M3 screws and nuts were utilized to fasten the stepper motor to the 3D-printed component, and a screw was also used to connect the threaded rod to the stepper motor.

5.2.7 Hexacyanoferrate ion catalytic redox transformation in a 3D-printed U-shaped flow reactor

The reaction was conducted with the aid of a continuous flow device composed of a syringe pump fitted with a 3 mL syringe. This was coupled with an electric controller box, a catalyst bed reactor, and a Teflon tube for reactant and product inlet and outflow, respectively. Hexacyanoferrate [Fe(CN)₆]³⁻ has a maximum absorption wavelength of λ 420 nm when a carbonate buffer solution containing NaHCO₃ and Na₂CO₃ is added (0.025 M). With the aid of a 3 mL syringe, the reaction was performed using a 0.08 mM aqueous solution of K₃[Fe(CN)₆] prepared from a 10 mM stock solution. The 3 mL syringe was used to siphon a freshly prepared NaBH₄ (1 mM) from the stock solution (0.1 M) in 0.1 M NaOH and carbonate buffer. These were prepared to a maximum volume of 3 mL using deionized water. After inserting the syringe into the pump's plunger, the reactant was made to flow across the catalyst bed. This procedure was repeated for various flow rates (FR)

ranging from 6.0 mLmin⁻¹ to 0.5 mLmin⁻¹ with catalyst doses ranging from 1 mg to 3 mg. This was done to determine the optimal catalyst dosage and residence time required to complete the reaction. The changes in flow rates as a function of temperature change from 25 to 55 °C were also determined. The colorless solution recovered from the Teflon tube outlet was examined by a microplate reader functionalized with UV-vis spectroscopy at λ 420 nm, indicating hexacyanoferrate ion reduction from K₃[Fe(CN)₆] to K₄[Fe(CN)₆] [27]. This was likewise done and documented for various flow rates and temperatures. Eqn. (1) was used to obtain the various conversion profile.

$$\text{Conversion (\%)} = \left(1 - \frac{A_t}{A_0}\right) \times 100 \quad (5.1)$$

A₀ and A_t denote the initial and final absorbance values of hexacyanoferrate at 420 nm, respectively.

5.3 Result and discussion

5.3.1 Characterization techniques

The nitrogen adsorption-desorption features of the synthesized mesoporous metal oxides were explained using the IUPAC categorization system [40]. **Figure 5.2a.** illustrates the pore volume and porosity of MnMMO and CoMMO having a type IV adsorption isotherm with a typical H3 hysteresis loop between 0.6 - 1 P/P₀. This is a peculiar trait of a mesoporous structure that is organized [41]. MnMMO has a surface area of 28.46 m²g⁻¹, while CoMMO has a surface area of 28.25 m²g⁻¹, as determined by the Roquoerel plot. Manganese mesoporous metal oxides and CoMMO pore volumes were determined as illustrated in **Figure 5.2b** were computed to be 0.120 cm³g⁻¹ and 0.148 cm³g⁻¹, respectively, using the Barrett-Joyner-Halenda (BJH) formula.

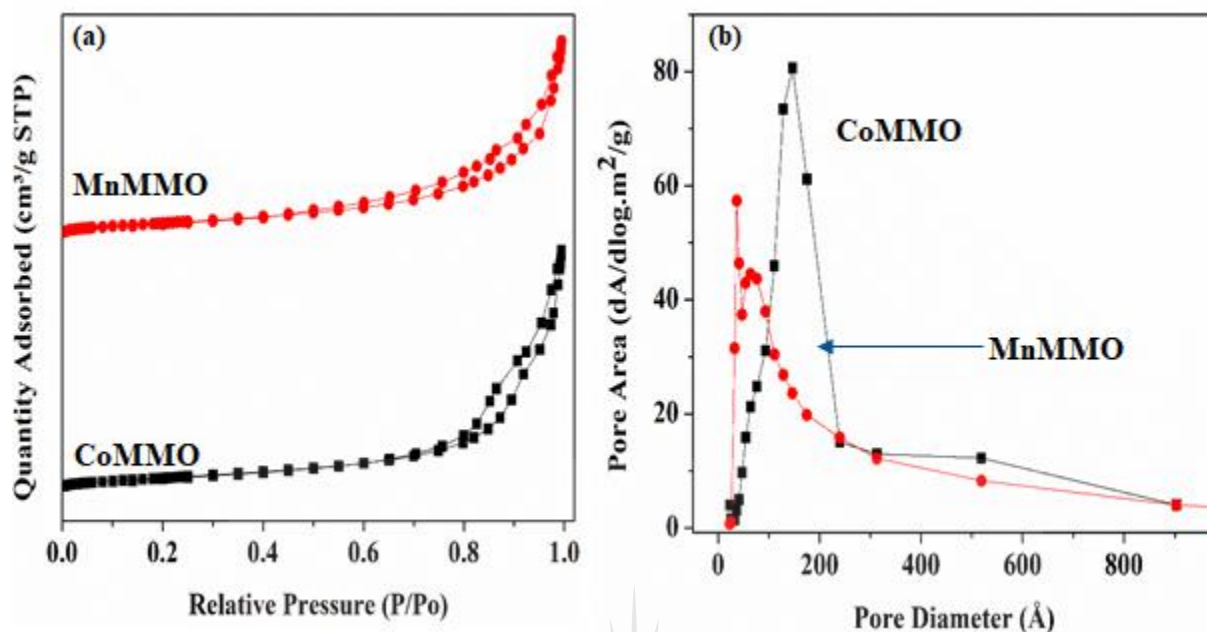


Figure 5.2: (a) Measurement of N₂ adsorption-desorption for MnMMO and CoMMO. (b) Pore volume pattern for MnMMO and CoMMO.

The H₂-TPR profiles of MnMMO and CoMMO are depicted in **Figure 5.3a**, and they revealed the temperature-dependent reducibility peaks associated with the materials. Two peaks at 438 °C and 240 °C were observed for the MnMMO catalyst, and these peaks are consistent with literature reports [42,43]. The lower temperature peak is attributable to Mn²⁺ reduction, whereas the second temperature peak is related to complete MnO reduction. Likewise, CoMMO demonstrated a single broad peak of intensity at 375 °C. This peak is also observed in the previous results [42,44], indicating that Co²⁺ is reduced from Co³⁺.

The p-XRD analysis revealed both the crystallinity and mesoporosity of MnMMO and CoMMO. **Figure 5.3b** illustrates the measurement of the materials' wide-angle patterns ($2\theta = 10^\circ$ - 80°). A complicated diffractogram was observed for manganese mesoporous metal oxide. The strong peaks at 32° and 36° align to the crystal structure of Mn₃O₄ as described in JCPDS 80-0382. The presence of MnO₂ and Mn₂O₃ were indicated by additional diffraction peaks [43]. The distinctive peaks of CoMMO have been proven to be similar to those of Co₃O₄ (JCPDS 74-1657) in a cubical phase [43].

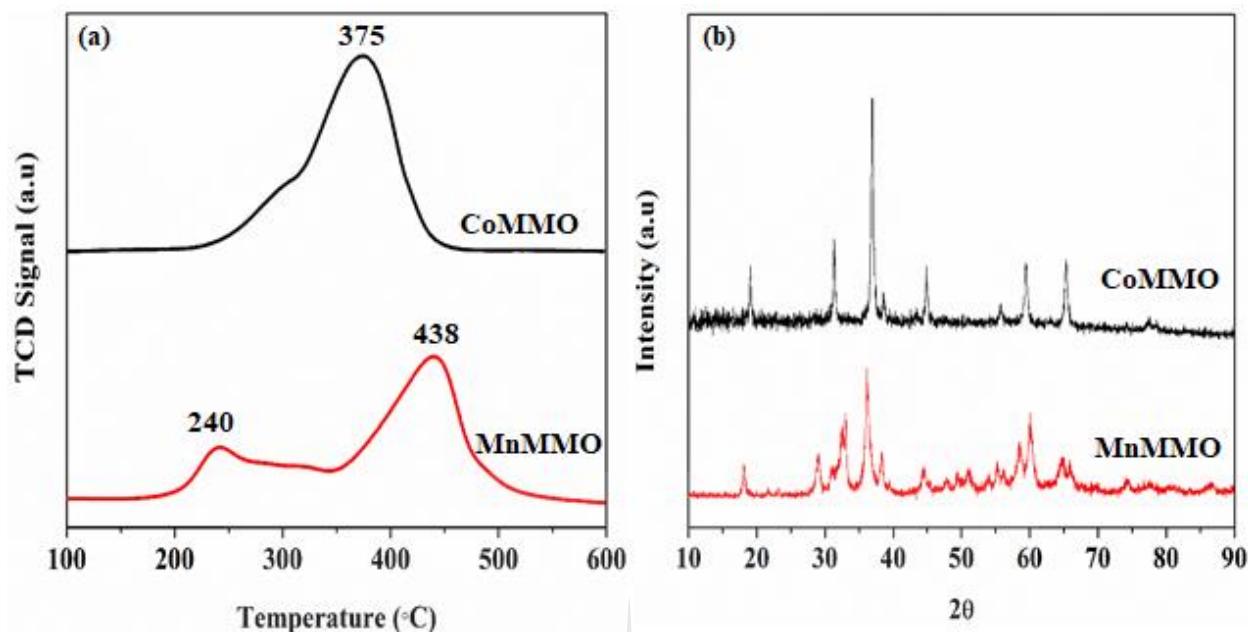


Figure 5.3: (a) H₂-TPR profiles of MnMMO and CoMMO (b) p-XRD analysis graphs of MnMMO and CoMMO.

The TEM micrographs displaying the crystallinity of structured nanoparticles are shown in **Figure 5.4a** and **5.4b**. The images were obtained at two different magnifications, 100 nm and 50 nm. The materials' varied crystallite forms were disclosed at a higher resolution, while the meso-order frameworks were shown at a lesser magnification. These are comparable to those previously reported [45,46]. The mesoporosity was supported by the earlier description of N₂ adsorption-desorption measurement.

The thermogravimetric analyses and CoMMO (TG/TGA) are shown in **Figure 5. 4a** and **5. 4b**, respectively. Weight loss was seen in the disintegration of MnMMO from ambient temperature to 729 °C, and the TGA also demonstrated a multi-step decomposition. This is due to the changes in the oxidation state of Mn ions when the metal oxide decomposes. At 730 °C, the entire breakdown stage was attained. The thermal investigation of CoMMO confirmed that the formative phase of CoO commenced around 820 °C, with the majority of the combustion occurring between 710 and 819 °C were as a result of oxygen loss from Co₃O₄.

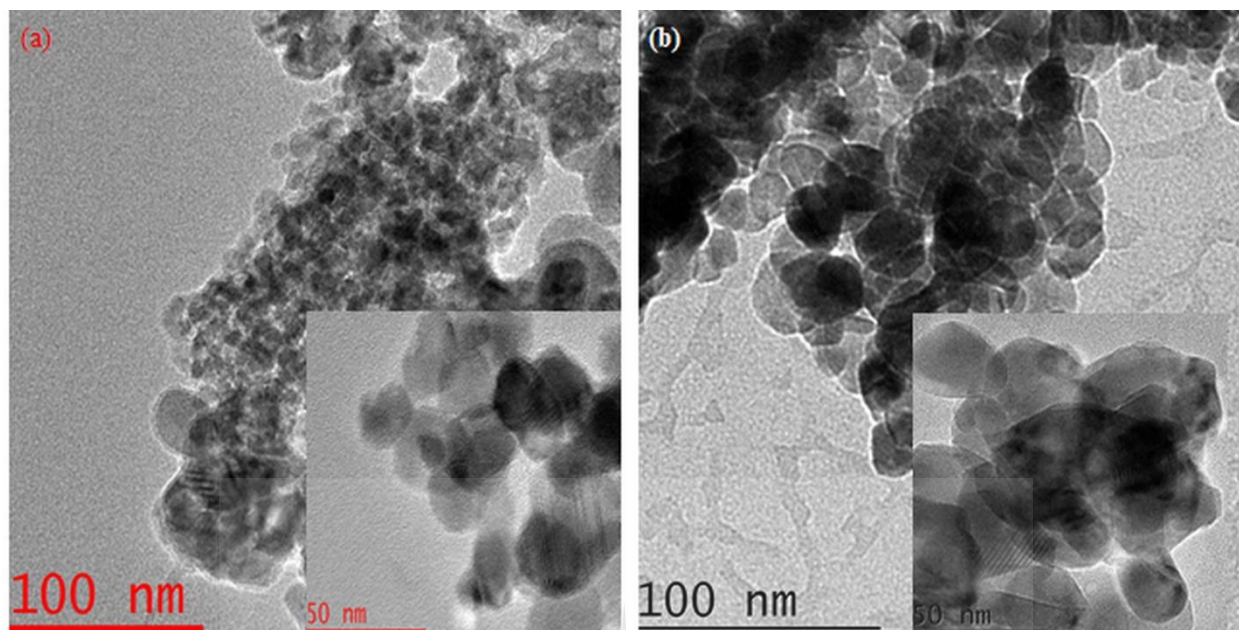


Figure 5.4: Transmission Electron Micrograph of (a) MnMMO and (b) CoMMO.

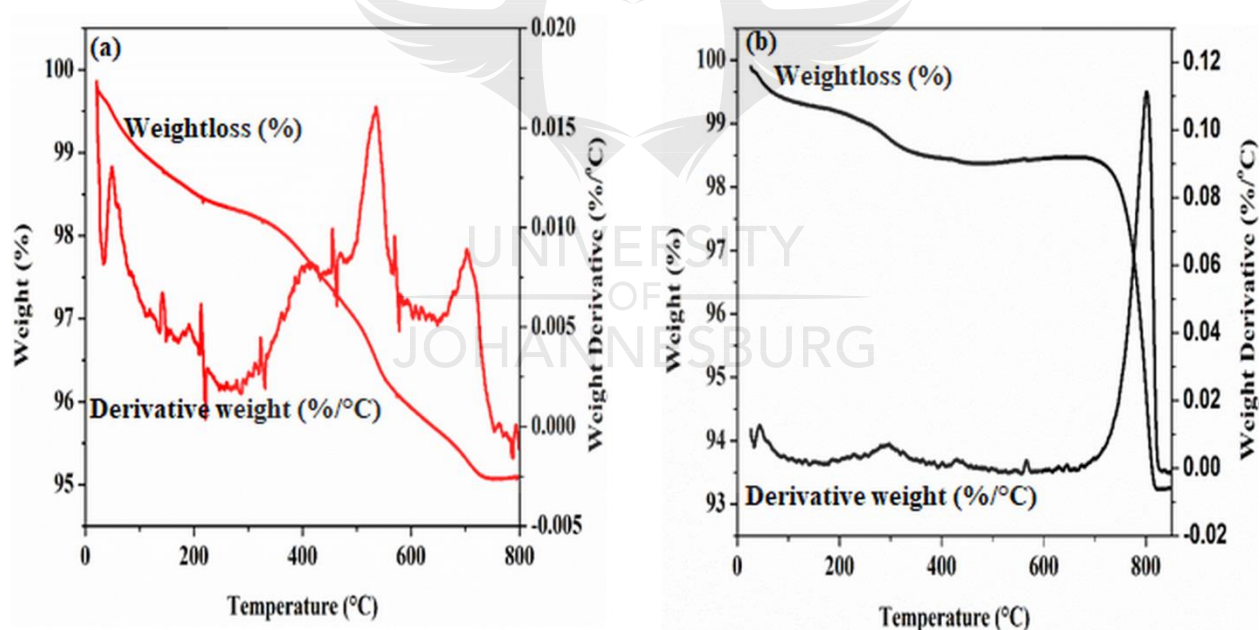


Figure 5.5: Thermal analysis of (a) MnMMO and (b) CoMMO.

5.3.2 Catalytic transformation in the microfluidic reactor

Over the years, the catalytic reduction of potassium hexacyanoferrate (III) as a model reaction under batch protocol has attracted considerable interest [28,47–50]. To our knowledge, however, the redox transformation of $[\text{Fe}(\text{CN})_6]^{3-}$ in a microfluidic flow reactor has not been documented.

These aqueous $[\text{Fe}(\text{CN})_6]^{3-}$ transformations were carried out in a microfluidic reactor with a variety of operating conditions to achieve the highest possible conversion from $[\text{Fe}(\text{CN})_6]^{3-}$ to $[\text{Fe}(\text{CN})_6]^{4-}$. This is because enhanced and faster catalytic reaction times are one of the microreactor advantages [51].

The effect of flow rate

Flow rate is a critical and highly strategic component in continuous flow operating efficiency [52]. Reducing the flow rate increases the residence time (RT) and vice versa. The residence time is the amount of time the reactant spends in contact and effectively interacts with the catalyst before exiting the microreactor. It is proportionate to the amount of reactant converted and the amount of product formed. Consideration of reaction time is frequently not a critical parameter in continuous flow operating procedures, as it is with typical vessel-based operations. Therefore, RT is taken into account [53]. This is represented in the **Eqn. (5.1)** supplementary [38].

Interestingly, the conversion rate increases as the substrate flow rate into the flow reactor are reduced. This is because decreasing the flow rate increases the residence period of the ferrocyanide ion within the reactor, resulting in improved interaction between the ferrocyanide ion and the catalyst. The reactant's transition was delayed, resulting in an extended contact period between the reactants and the catalyst. Increased reactant conversion has been proposed due to the reduced FR, which allows for a longer contact time between the catalyst and the reagents [54]. **Figure 5.6a** substantiates this conclusion. The reduction spectrum revealed a considerable decrease in ferrocyanide reduction at a very high flow rate of 6.0 mLmin^{-1} and a short residence time with an isosbestic point, indicating the synthesis of hexacyanoferrate (II). These actions resulted in the conversion of $[\text{Fe}(\text{CN})_6]^{3-}$ and a progressive decrease in the flow rate, as shown in **Table 5.1**. Other flow rate absorption dependent spectra produced at 25, 35, 45, and 55 °C are shown in **Appx. 5.3, Appx. 5.4, Appx. 5. 4, and Appx. 5.6**, respectively, demonstrating the gradual decrease in absorbance of $[\text{Fe}(\text{CN})_6]^{3-}$ ions at λ 420 nm.

Table 5.1:

Data showing the results for the impact of flow rate at 45°C on the reaction and the conversion obtained using 3 mg of MnMMO.

Flow rate (mL·min ⁻¹)	Conversion (%)
6.0	57.4
3.0	60.0
1.5	62.4
1.3	60.0
1.0	73.7
0.5	88.0

Effect of catalyst dose on hexacyanoferrate

The catalyst amount is critical in reaction optimization since reactant conversion and formation of the product are dependent not only on RT, FR, and temperature but also on the catalyst amount. The effect of catalyst dosage was investigated by increasing the catalyst concentration from 1, 2, to 3 mg at room temperature while maintaining the FR at 6.0, 3.0, 1.5, 1.3, 1.0, and 0.5 mLmin⁻¹. At 45 °C, **Figure 5.6c** demonstrated that increasing the catalyst dosage significantly reduced [Fe(CN)₆]³⁻ with a rising conversion trend from 78.6, 81.8, to the highest conversion of 88.0%. Additionally, the efficiency of the catalysts was demonstrated by performing the reaction in the absence of catalysts and establishing that the reaction did not occur [34]. This indicates that the reaction is catalytic-dependent. It is critical to highlight that, despite the low catalyst dosages utilized in this reaction, the activity was outstanding, and the conversions obtained were quantitative. This efficiency, however, can be increased by increasing either the catalyst concentration or the residence time.

Additionally, we compared the catalytic activity of MnMMO and CoMMO printed inside the reactors. As illustrated in **Figure 5.6b**, MnMMO has a superior and more reducibility effect on the [Fe(CN)₆]³⁻ compared to CoMMO. The enhanced catalytic performance could be attributed to a greater oxygen vacancy density in MnMMO [32]. It has been shown that the chemical environment has a significant effect on the catalytic features and efficiency of metal oxide catalysts [32,42]. As a result, the MnMMO was chosen for subsequent reactions.

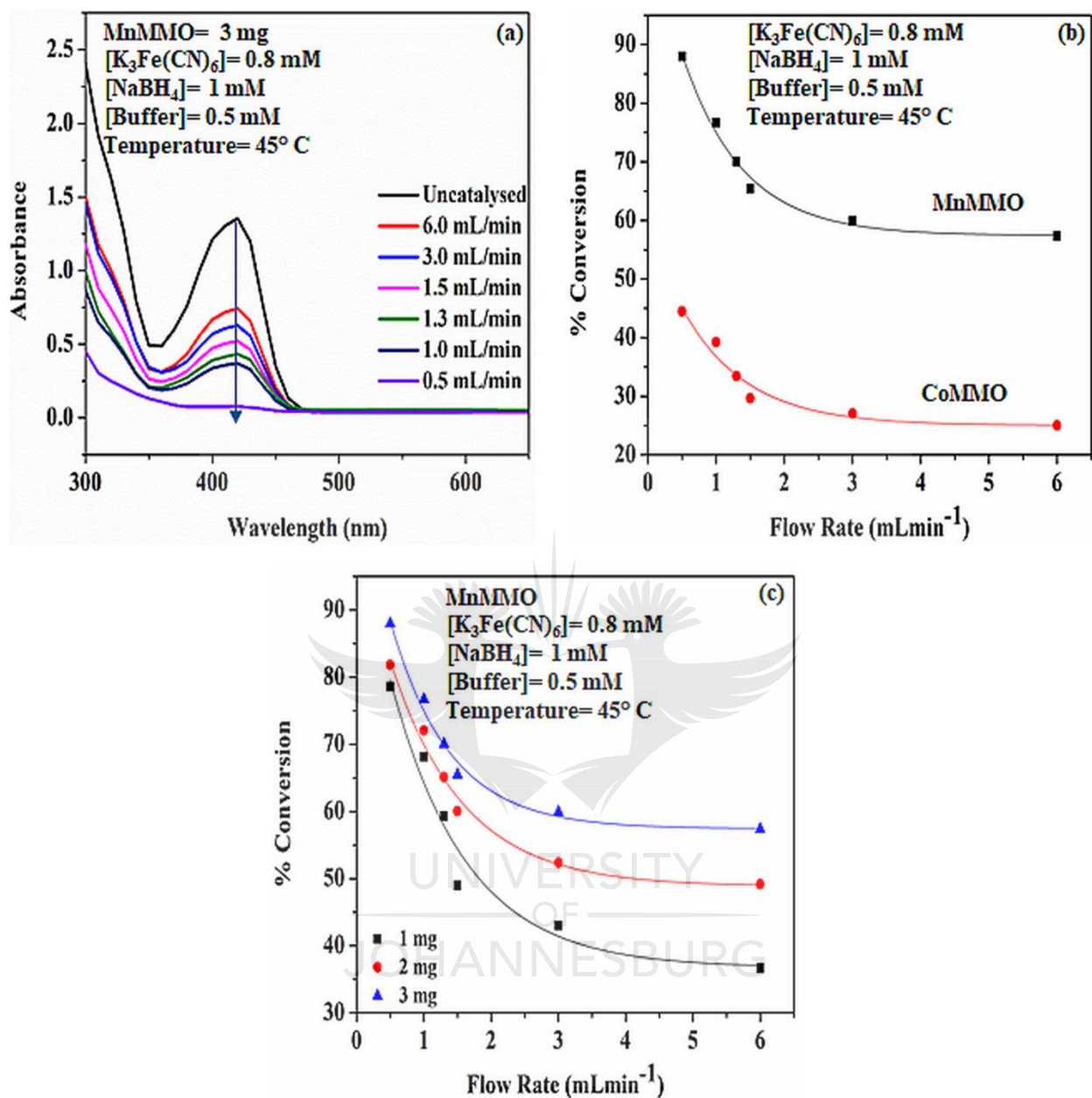


Figure 5.6: (a) Shows flow rate absorption spectrum as a function of ferrocyanide reduction. (b) Comparison of MnMMO and CoMMO conversion (percentage) (c) percentage conversion of ferrocyanide at various catalyst concentrations.

Temperature effects at different flow rates

To evaluate the effect of temperature on reaction performance, the reactants were thermostated for 4 min in a water bath to obtain the temperature required. The effect of FR at various temperatures, including 35, 45, and 55 °C, was investigated in the microreactor. This was accomplished by

maintaining a constant catalyst concentration (3 mg) and all other reactant parameters constant while maintaining the same FR ranges at various temperatures. The data acquired results are given in **Table 5.2**.

Table 5.2:

Data showing the conversion of $[\text{Fe}(\text{CN})_6]^{3-}$ obtained at different temperatures, at the minimum flow rate, and maximum flow rate using 3 mg of MnMMO.

Temperature (°C)	Conversion (%)	
	at 0.5(mL·min ⁻¹)	at 6.0 (mL·min ⁻¹)
25	69.2	44.7
35	78.9	49.4
45	88.0	57.4
55	96.1	64.0

At the lowest FR of 0.5 mLmin⁻¹, the percentage conversion increased noticeably from 69.2 to 96.1% as the temperature increased. Similarly, as the temperature increased from 25 to 55 °C, the same pattern of increasing conversion was found at the optimum flow rate of 6 mLmin⁻¹. **Figure 5.7a** illustrates these. These increases can be attributable to the enhancement of $[\text{Fe}(\text{CN})_6]^{3-}$ molecular diffusion at elevated temperatures [54]. Increased reaction temperatures resulted in increased activity, resulting in increased conversion and productivity [55].

The apparent rate constant was determined using a non-linear plot of the experimental data [56], which was created using TgK Scientific Limited's kinetic studio 2010 software (www.tgkscientific.com). This was accomplished by **Eqn (5.2)**.

$$\ln\left(\frac{C_t}{C_0}\right) = \ln\left(\frac{A_t}{A_0}\right) = -k_{app}/t \quad (5.2)$$

Where C_t and C_0 denote the concentrations of $[\text{Fe}(\text{CN})_6]^{3-}$ at t (min) and 0 (min), respectively. A_t and A_0 denotes the absorbance of the product (A_t) and the reactants (A_t and A_0 , respectively (A_0)). \ln is the natural logarithm expression, whereas k or k_{app} is the apparent rate constant.

As shown in **Figure 5.7b**, the apparent rate constants derived from kinetic fitting were 0.48 ± 0.0094 , 0.69 ± 0.0104 , 0.78 ± 0.0082 , and $0.84 \pm 0.0103 \text{ min}^{-1}$ at 25, 35, 45, and 55 °C, respectively. It was found that when the temperature rises, the rate constant increases. This demonstrated that as the reaction temperature was increased, the rate of ferrocyanide reduction increased as well. The obtained rate constants are equivalent to those reported previously [30].

Activation parameters determination

Using the Arrhenius equation, **Eqn (5.3)**, the activation parameters for the flow reaction were determined by varying temperatures [57].

$$\ln k = \ln A - \frac{E_a}{RT} \quad (5.3)$$

Where A denotes the Arrhenius constant and E_a represents the activation energy determined by plotting $\ln k$ against $1/T$. Moreover, R signifies the ideal gas constant, while T indicates the temperature (Kelvin).

The Arrhenius equation illustrates the relationship between activation energy and kinetic rate constant. E_a is a critical parameter in reaction kinetics because it relates the temperature dependence of the apparent rate constant to the apparent rate constant [58], as illustrated in **Figure 5.7c**. The reported E_a (5.17 kJmol^{-1}) was calculated and found to be significantly less than the values in earlier investigations [29,47]. The reaction's low activation energy indicates that only a little amount of energy is required to activate the reduction process [59]. As a result, the $[\text{Fe}(\text{CN})_6]^{3-}$ transition state requires minimal energy.

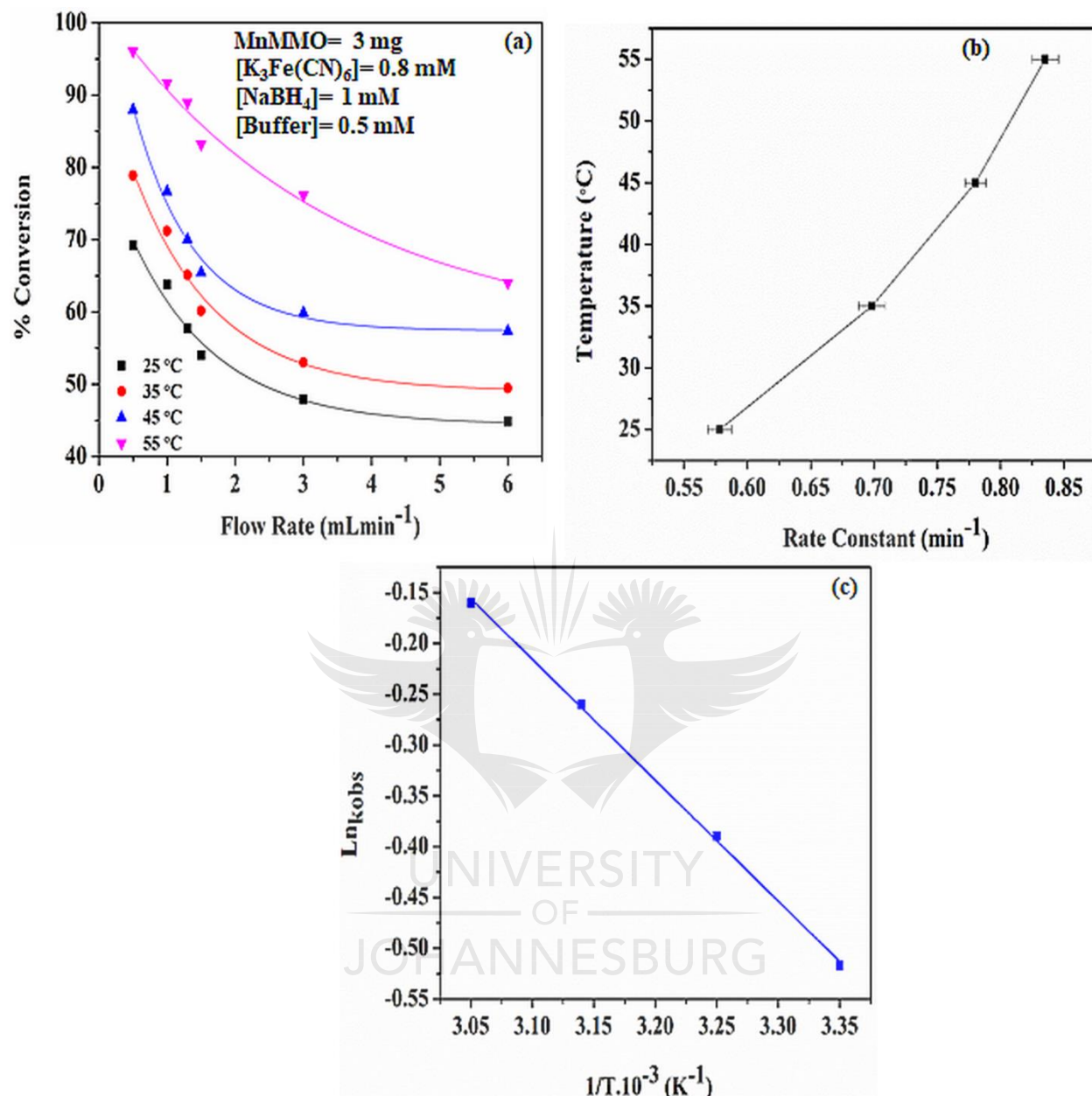


Figure 5.7: (a) Percentage conversion of ferrocyanide at various temperatures, (b) plot demonstrating the rate constant's temperature dependence, and (c) thermodynamic plot of $\ln k_{\text{obs}}$ versus $1/T$ at various temperatures.

5.3.3 Catalyst turnover frequency

The calculation of the turnover frequency (TOF) is a critical measurement in determining catalytic performance [59]. TOF is defined as the molecular weight of the substrate $[\text{Fe}(\text{CN})_6]^{3-}$ transformed to product divided by the molecular weight of the metal oxide (MnMMO) per minute of reaction.

The TOF computed for the conversion of $[\text{Fe}(\text{CN})_6]^{3-}$ at various temperatures is presented in **Table.5 3**.

Table 5.3:

Data showing the increasing order of the TOF obtained at different temperatures.

Temperature (°C)	TOF (min ⁻¹)
25	4.56
35	5.20
45	5.80
55	6.33

The increase in the TOF number as the temperature is raised revealed that the catalytic performance is being enhanced by heat. In addition, the finding indicates that MnMMO has a high catalytic activity for the transformation of $[\text{Fe}(\text{CN})_6]^{3-}$.

5.3.4 Stability and recyclability of catalysts

The recoverability and recyclability of catalysts are critical economic factors that are unique to heterogeneity in catalysis. Because heterogeneous catalysts may be recovered and reused, they have an advantage over homogeneous catalysts. However, in flow reactors, catalyst recoverability is not an issue because the catalysts are already separated by being embedded inside the catalytic beds. The effect of recycling MnMMO on $[\text{Fe}(\text{CN})_6]^{3-}$ reduction was studied five times in succession, and the measured rate constant (k_{obs}) for each catalytic run was determined. The result acquired is depicted in **Figure 5.8**. As the number of cycles increased, the plot of relative absorbance against residence time in **Figure 5.8a** revealed a gradual drop in catalytic activity. This is also demonstrated in the histogram chart of the k_{obs} vs the catalytic run (**Figure 5.8b**), which was generated from each linear fit for all five cycles. The significant drop seen is attributed to catalytic system deactivation. The linear fits of each cycle are depicted in **Appx. 5.7** using **Eqn (5.4)**.

$$-\text{Ln}\left[1 - \frac{(A_0 - A_t)}{A_0}\right] = k_{obs} \times t \quad (5.4)$$

Where A_0 denotes the initial absorbance and A_t denotes the absorbance at the time of residence t (min).

For the first, second, third, fourth, and fifth runs, the k_{obs} are 0.23 ± 0.0326 , 0.22 ± 0.0339 , 0.21 ± 0.0293 , 0.19 ± 0.0293 , and $0.17 \pm 0.0294 \text{ min}^{-1}$, respectively. The rate constant demonstrated that the catalyst activity was maintained during the recycling period following the original run.

However, as the number of cycles increases, the catalyst activity decreases; a minimum quantitative conversion of 64.5% was observed in the fifth run (**Appx. 5.8**). This is a typical demonstration of the stability of a catalyst. Further, a maximum conversion rate of 72.1% was attained in the initial run. This value was more significant than the value realized during the original room temperature catalytic run. The increase in conversion may be attributed to the elimination of moisture trapped within the pores of the catalyst after putting it in the vacuum oven following the reactor's initial experimental run. Initially, the catalyst reactor was used as it was obtained from the 3D-printing machine. We assumed that moisture had been trapped within the catalyst pore due to the printer's fan when the reactor was being printed.

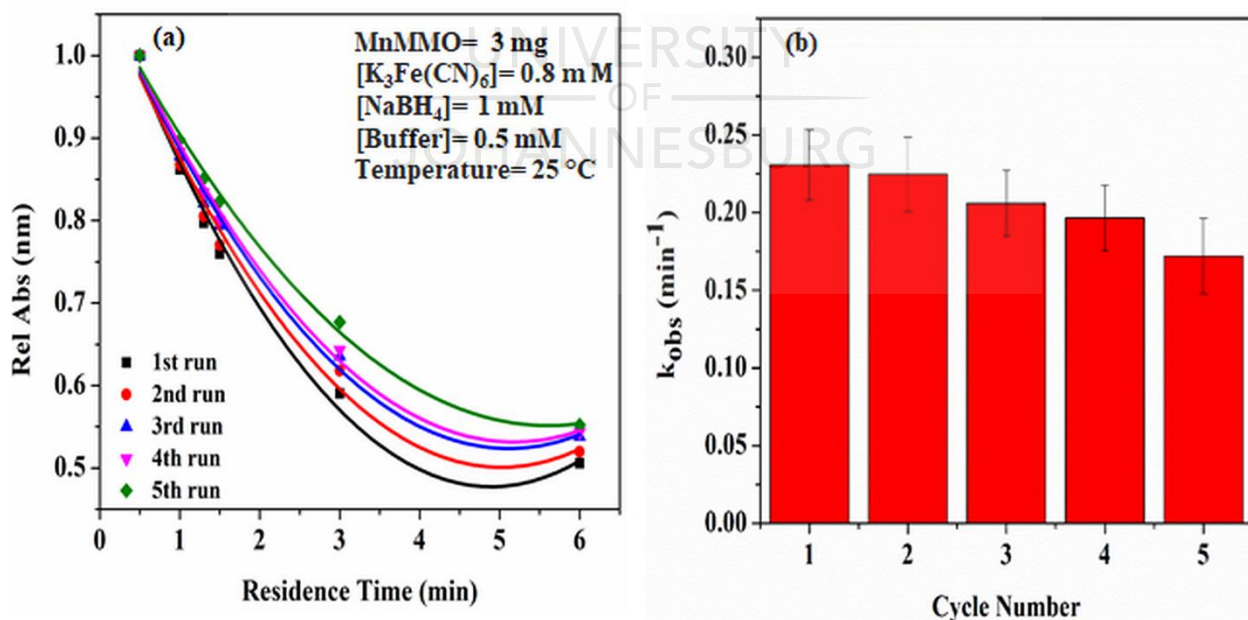


Figure 5.8: (a) The plot of relative absorbance against residence time (b) Catalyst recycling bar graph.

5.3.4 Comparative analysis

A comparative analysis with earlier findings confirmed MnMMO's excellent catalytic performance. This is indicated in **Table 5.4** by the rate constant, E_a , and the percentage conversion. The rate constant, which is more significant than those reported in most previous studies, indicated a well-favored catalytic reduction. The low activation energy obtained indicates that $[\text{Fe}(\text{CN})_6]^{3-}$ can be obtained at a lower energy level. Moreover, this small E_a value accounted for the high rate constant observed, indicating that MnMMO had a significant role in accelerating the degradation of $[\text{Fe}(\text{CN})_6]^{3-}$. The percentage conversion reported after a few min of reaction time is impressively comparable to other conversions. Moreover, the TOF values computed depicted the catalyst system's activity as active material in comparison to other values.



Table 5.4:

Comparison of $\text{Fe}(\text{CN})_6^{3-}$ reduction by other catalysts under batch system reported with this work (TW), continuous flow system.

Catalyst	Conversion (%)	Condition	Time (min)	E_a (kJ·mol ⁻¹)	Rate constant (min ⁻¹)	TOF(min ⁻¹)	Ref.
Ni(P ₄ MO ₆ O ₃₁) ₂	29.11	Batch	180	84.11	6.35×10^{-3}	4.15×10^{-5}	[61]
Cd(P ₄ MO ₆ O ₃₁) ₂	41.93	Batch	150	25.35	13.16×10^{-3}	5.87×10^{-5}	[61]
AuNPs	-	Batch	1	15.60 ± 1.1	1.537×10^{-3}	-	[47]
PEGDMA@AuNPs	-	Batch	20	-	8.370×10^{-2}	0.03×10^2	[30]
AuNPs	-	Batch	18	30.98 ± 1.34	2.4×10^{-1}	7.2×10^{-1}	[29]
NiWO ₄ NPs	-	Batch	240	-	6.4×10^{-3}	9.4×10^{-4}	[62]
Pt NNs	-	Batch	60	26.0	$9.1 \times 10^{-3} \pm 0.7$	1.0×10^{-2}	[63]
Pt NBs	-	Batch	60	6.40	$1.690 \times 10^{-1} \pm 0.6$	1.0×10^{-2}	[63]
Mn-phosphomolybdate	60.70	Batch	150	-	1.5×10^{-3}	7.5×10^{-3}	[64]
Au@citrate	-	Batch	120	-	5.34×10^{-2}	-	[48]
MnMMO	94.1	Flow	6	5.17	5.800×10^{-1}	0.046×10^2	TW

TW = This work.

5.4 Conclusion

The 3D-printed microreactors used in this continuous flow catalytic reaction were designed to accommodate a wide range of temperatures without compromising the reaction, enabling a faster, more environmentally friendly, less expensive, and more energy-efficient reduction hexacyanoferrate (III) to hexacyanoferrate (II). The printed reactor can be compared well with commercially available batch reactors. In terms of manufacture, the U-shaped reactor has a significant advantage, particularly in the laboratory. Additionally, in terms of material quality, the polylactic acid thermoplastic material used to fabricate the reactor is inexpensive, biodegradable, and stable at most reaction temperatures. The percentage conversion of Fe^{III} to Fe^{II} (94.1%) was achieved in six minutes at 55 °C, and the activation energy was computed to be 5.17 kJmol⁻¹. With over five reaction runs, the stability of Mn mesoporous metal oxide demonstrated a remarkable and effective catalytic activity. Also, the catalyst showed great turnover frequency, with a minimum of 55 min⁻¹ value recorded.



5.5 References

- [1] M.R. Chapman, M.H.T. Kwan, G. King, K.E. Jolley, M. Hussain, S. Hussain, I.E. Salama, C. Gonza, L.A. Thompson, M.E. Bayana, A.D. Clayton, B.N. Nguyen, N.J. Turner, N. Kapur, A.J. Blacker, Simple and Versatile Laboratory Scale CSTR for Multiphase Continuous-Flow Chemistry and Long Residence Times, *Org. Process Res. Dev.* 21 (2017) 1294–1301.
- [2] J.M. Neumaier, A. Madani, T. Klein, T. Ziegler, Low-budget 3D-printed equipment for continuous flow reactions, *Beilstein J. Org. Chem.* 15 (2019) 448–466.
- [3] K. Maresz, A. Ciemięga, J. Mrowiec-Białoń, Selective Reduction of Ketones and Aldehydes in Continuous-Flow Microreactor—Kinetic Studies, *Catalysts.* 8 (2018) 221.
- [4] S. Zeibi Shirejini, A. Mohammadi, Halogen–lithium exchange reaction using an integrated glass microfluidic device: an optimized synthetic approach, *Org. Process Res. Dev.* 21 (2017) 292–303.
- [5] C. De Risi, O. Bortolini, A. Brandolese, G. Di Carmine, D. Ragno, A. Massi, Recent advances in continuous-flow organocatalysis for process intensification, *React. Chem. Eng.* (2020).
- [6] X. Liu, B. Ünal, K.F. Jensen, Heterogeneous catalysis with continuous flow microreactors, *Catal. Sci. Technol.* 2 (2012) 2134–2138.
- [7] R. Ricciardi, R. Munirathinam, J. Huskens, W. Verboom, Improved Catalytic Activity and Stability Using Mixed Sulfonic Acid- and Hydroxy-Bearing Polymer Brushes in Microreactors, *ACS Appl. Mater. Interfaces.* 6 (2014) 9386–9392.
- [8] O.A. Alimi, N. Bingwa, R. Meijboom, Chemical Engineering Research and Design Homemade 3-D printed flow reactors for heterogeneous catalysis, *Chem. Eng. Res. Des.* 150 (2019) 116–129.
- [9] A. Tanimu, S. Jaenicke, K. Alhooshani, Heterogeneous catalysis in continuous flow microreactors : A review of methods and applications, *Chem. Eng. J.* 327 (2017) 792–821.
- [10] M.R. Penny, S.T. Hilton, Design and development of 3D printed catalytically-active stirrers for chemical synthesis, *React. Chem. Eng.* 5 (2020) 853–858.
- [11] S. Rossi, A. Puglisi, M. Benaglia, Additive Manufacturing Technologies : 3D Printing in Organic Synthesis, *ChemCatChem.* 10 (2018) 1–15.

- [12] D. Ko, K. Gyak, D. Kim, Emerging Microreaction Systems Based on 3D Printing Techniques and Separation Technologies, *J. Flow Chem.* 7 (2017) 72–81.
- [13] C. Parra-cabrera, C. Achille, S. Kuhn, R. Ameloot, C. Parra-cabrera, 3D printing in chemical engineering and catalytic technology: structured catalysts, mixers and reactors, *Chem Soc Rev.* 47 (2017) 209–230.
- [14] A.K. Au, W. Huynh, L.F. Horowitz, A. Folch, 3D-Printed Microfluidics, *Angew. Chem. Int. Ed.* 55 (2016) 3862–3881.
- [15] P.J. Kitson, S. Glatzel, W. Chen, C. Lin, Y. Song, L. Cronin, 3D printing of versatile reactionware for chemical synthesis, *Nat. Protoc.* 11 (2016) 920–936.
- [16] S.K. and A.F. Nirveek Bhattacharjee, Arturo Urrios, The upcoming 3D-printing revolution in microfluidics, *Lab Chip.* 16 (2016) 1720–1742.
- [17] A.J. Capel, S. Edmondson, S.D.R. Chistie, R.D. Goodridge, R.J. Bibb, M. Thurstans, Design and additive manufacture for flow chemistry, *R. Soc. Chem.* 13 (2013) 4583–4590.
- [18] L.P. Bressan, J. Robles-Najar, C.B. Adamo, R.F. Quero, B.M.C. Costa, D.P. de Jesus, J.A.F. da Silva, 3D-printed microfluidic device for the synthesis of silver and gold nanoparticles, *Microchem. J.* 146 (2019) 1083–1089.
- [19] M.S. Hossain, H. Taheri, *In-Situ* Process Monitoring for Additive Manufacturing Though Acoustic Techniques, *J. Mater. Eng. Perform.* (2020) 1–14.
- [20] M. V Bandulasena, G.T. Vladislavljević, O.G. Odunmbaku, B. Benyahia, Continuous synthesis of PVP stabilized biocompatible gold nanoparticles with a controlled size using a 3D glass capillary microfluidic device, *Chem. Eng. Sci.* 171 (2017) 233–243.
- [21] L. Xu, J. Peng, M. Yan, D. Zhang, A.Q. Shen, Chemical Engineering and Processing : Process Intensification Droplet synthesis of silver nanoparticles by a micro fluidic device, *Chem. Eng. Process. Process Intensif.* 102 (2016) 186–193.
- [22] R. Karnik, F. Gu, P. Basto, C. Cannizzaro, L. Dean, W. Kyei-manu, R. Langer, O.C. Farokhzad, Microfluidic Platform for Controlled Synthesis of Polymeric Nanoparticles, *Nano Lett.* 8 (2008) 2906–2912.
- [23] L. Uson, M. Arruebo, V. Sebastian, J. Santamaria, Single phase microreactor for the continuous, high-temperature synthesis of < 4 nm superparamagnetic iron oxide nanoparticles, *Chem. Eng. J.* 340 (2018) 66–72.
- [24] L.L. Lazarus, C.T. Riche, B.C. Marin, M. Gupta, N. Malmstadt, R.L. Brutchey, Two-

- Phase Micro fluidic Droplet Flows of Ionic Liquids for the Synthesis of Gold and Silver Nanoparticles, (2012).
- [25] C. Rosso, S. Gisbertz, J.D. Williams, H.P.L. Gemoets, W. Debrouwer, B. Pieber, C.O. Kappe, An oscillatory plug flow photoreactor facilitates semi-heterogeneous dual nickel/carbon nitride photocatalytic C-N couplings, *React. Chem. Eng.* 5 (2020) 597–604.
- [26] H.P.L. Gemoets, Y. Su, M. Shang, V. Hessel, R. Luque, T. Noël, Liquid phase oxidation chemistry in continuous-flow microreactors, *Chem. Soc. Rev.* 44 (2016) 83–117.
- [27] T. Ge, Z. Hua, X. He, Y. Zhu, W. Ren, L. Chen, L. Zhang, H. Chen, C. Lin, H. Yao, J. Shi, One-pot synthesis of hierarchically structured ZSM-4 zeolites using single micropore-template, *Chinese J. Catal.* 36 (2015) 866–873.
- [28] P. Hervés, M. Pérez-lorenzo, L.M. Liz-marzán, J. Dzubiella, Y. Lu, M. Ballauff, P. Herve, J. Dzubiella, Y. Lu, M. Ballauff, Chem Soc Rev Catalysis by metallic nanoparticles in aqueous solution : model reactions w, *Chem. Soc. Rev.* 41 (2012) 5577–5587.
- [29] A.G. Assefa, A.A. Mesfin, M.L. Akele, A.K. Alemu, B.R. Gangapuram, V. Guttena, M. Alle, Microwave-assisted green synthesis of gold nanoparticles using Olibanum gum (*Boswellia serrate*) and its catalytic reduction of 4-nitrophenol and hexacyanoferrate (III) by sodium borohydride, *J. Clust. Sci.* 28 (2017) 917–935.
- [30] J. Chen, F. Chen, Y. Wang, M. Wang, Q. Wu, X. Zhou, X. Ge, One-step synthesis of poly (ethyleneglycol dimethacrylate)-microspheres-supported nano-Au catalyst in methanol–water solution under γ -ray radiation, *RSC Adv.* 6 (2016) 55878–55883.
- [31] X. Liu, Y. Shen, R. Yang, S. Zou, X. Ji, L. Shi, Y. Zhang, D. Liu, L. Xiao, X. Zheng, S. Li, J. Fan, G.D. Stucky, Inkjet printing assisted synthesis of multicomponent mesoporous metal oxides for ultrafast catalyst exploration, *Nano Lett.* 12 (2012) 4733–4739.
- [32] Y. Du, Q. Meng, J. Wang, J. Yan, H. Fan, Y. Liu, H. Dai, Three-dimensional mesoporous manganese oxides and cobalt oxides: High-efficiency catalysts for the removal of toluene and carbon monoxide, *Microporous Mesoporous Mater.* 162 (2012) 199–206.
- [33] S.K. Ghosh, H. Rahaman, Noble Metal–Manganese Oxide Hybrid Nanocatalysts,

Elsevier Inc., 2019.

- [34] P. Veerakumar, K. Salamalai, P. Thanasekaran, K.C. Lin, Simple Preparation of Porous Carbon-Supported Ruthenium: Propitious Catalytic Activity in the Reduction of Ferrocyanate(III) and a Cationic Dye, *ACS Omega*. 3 (2018) 12609–12621.
- [35] S. Rossi, R. Porta, D. Brenna, A. Puglisi, M. Benaglia, Stereoselective Catalytic Synthesis of Active Pharmaceutical Ingredients in Homemade 3D-Printed Mesoreactors, *Angew. Chemie*. 129 (2017) 4354–4358.
- [36] M. Hibben, S. Holmes, *TINKERING WITH TINKERCAD A Beginner's Guide to Creating 3D Printer Designs With Presenters : Tinkering ! With ! Tinkercad !*, n.d.
- [37] O.A. Alimi, C.A. Akinnawo, O.R. Onisuru, R. Meijboom, 3-D printed microreactor for continuous flow oxidation of a flavonoid, *J. Flow Chem.* (2020).
- [38] O.A. Alimi, T.B. Ncongwane, R. Meijboom, Design and fabrication of a monolith catalyst for continuous flow epoxidation of styrene in polypropylene printed flow reactor, *Chem. Eng. Res. Des.* (2020) 395–409.
- [39] G. 2016 C.S.M. Phytron, *CATALOGUE STEPPER MOTORS Precision for challenging applications*, (2016).
- [40] M. Thommes, K. Kaneko, A. V Neimark, J.P. Olivier, F. Rodriguez-Reinoso, J. Rouquerol, K.S.W. Sing, Physisorption of gases, with special reference to the evaluation of surface area and pore size distribution (IUPAC Technical Report), *Pure Appl. Chem.* 87 (2015) 1051–1069.
- [41] N. Masunga, G.S. Tito, R. Meijboom, *Applied Catalysis A, General Catalytic evaluation of mesoporous metal oxides for liquid phase oxidation of styrene*, *Appl. Catal. A, Gen.* 552 (2018) 154–167.
- [42] A. Jha, T. Chandole, R. Pandya, H.S. Roh, C. V. Rode, Solvothermal synthesis of mesoporous manganese oxide with enhanced catalytic activity for veratryl alcohol oxidation, *RSC Adv.* 4 (2014) 19440–19455.
- [43] K. Stangeland, D.Y. Kalai, Y. Ding, Z. Yu, Mesoporous manganese-cobalt oxide spinel catalysts for CO₂ hydrogenation to methanol, *J. CO₂ Util.* 32 (2019) 146–154.
- [44] M. Qiu, S. Zhan, H. Yu, D. Zhu, S. Wang, Facile preparation of ordered mesoporous MnCo₂O₄ for low-temperature selective catalytic reduction of NO with NH₃, *Nanoscale*. 7 (201 4) 2568–2577.
- [45] A.K. Ilunga, I.R. Legodi, S. Gumbi, R. Meijboom, Isothermic adsorption of morin onto

- the reducible mesoporous manganese oxide materials surface, *Appl. Catal. B Environ.* 224 (2018) 928–939.
- [46] B.M. Mogudi, P. Ncube, R. Meijboom, Catalytic activity of mesoporous cobalt oxides with controlled porosity and crystallite sizes: evaluation using the reduction of 4-nitrophenol, *Appl. Catal. B Environ.* 198 (2016) 74–82.
- [47] S. Carregal-romero, P. Jorge, P. Herv, L.M. Liz-marz, P. Mulvaney, Colloidal Gold-Catalyzed Reduction of Ferrocyanate (III) by Borohydride Ions : A Model System for Redox Catalysis, 26 (2010) 1271–1277.
- [48] I. Sarhid, I. Lampre, D. Drago, P. Beaunier, B. Palpant, H. Remita, Hexacyano ferrate (III) reduction by electron transfer induced by plasmonic catalysis on gold nanoparticles, *Materials (Basel)*. 12 (2019) 3012.
- [49] Q. Xia, D. Su, X. Yang, F. Chai, C. Wang, J. Jiang, One pot synthesis of gold hollow nanospheres with efficient and reusable catalysis, *RSC Adv.* 4 (2014) 58522–58527.
- [50] R. Kanwar, R. Bhar, S.K. Mehta, Designed Meso-macroporous Silica Framework Impregnated with Copper Oxide Nanoparticles for Enhanced Catalytic Performance, *ChemCatChem*. 10 (2018) 2087–2095.
- [51] Y. Liu, X. Jiang, Why microfluidics? Merits and trends in chemical synthesis, *Lab Chip*. 17 (2017) 3960–3978.
- [52] G. Liu, X. Ma, X. Sun, Y. Jia, T. Wang, Controllable synthesis of silver nanoparticles using three-phase flow pulsating mixing microfluidic chip, *Adv. Mater. Sci. Eng.* 2018 (2018).
- [53] I.M. Mándity, S.B. Ötvös, F. Fülöp, Strategic Application of Residence-Time Control in Continuous-Flow Reactors, *ChemistryOpen*. 4 (2014) 212–223.
- [54] X. Pu, Y. Su, Heterogeneous catalysis in microreactors with nanofluids for fine chemicals syntheses: Benzylolation of toluene with benzyl chloride over silica-immobilized FeCl₃ catalyst, *Chem. Eng. Sci.* 184 (2018) 200–208.
- [55] C.P. Haas, T. Müllner, R. Kohns, D. Enke, U. Tallarek, High-performance monoliths in heterogeneous catalysis with single-phase liquid flow, *React. Chem. Eng.* 2 (2017) 498–411.
- [56] G. Lente, Facts and alternative facts in chemical kinetics: remarks about the kinetic use of activities, termolecular processes, and linearization techniques, *Curr. Opin. Chem. Eng.* 21 (2018) 76–83.

- [57] S.R. Thawarkar, B. Thombare, B.S. Munde, N.D. Khupse, Kinetic investigation for the catalytic reduction of nitrophenol using ionic liquid stabilized gold nanoparticles, *RSC Adv.* 8 (2018) 38384–38390.
- [58] Z. Mohammadi, M.H. Entezari, Sono-synthesis approach in uniform loading of ultrafine Ag nanoparticles on reduced graphene oxide nanosheets: An efficient catalyst for the reduction of 4-Nitrophenol, *Ultrason. Sonochem.* 44 (2018) 1–13.
- [59] C. Xiao, Q. Wu, A. Chang, Y. Peng, W. Xu, W. Wu, Responsive Au@ polymer hybrid microgels for the simultaneous modulation and monitoring of Au-catalyzed chemical reaction, *J. Mater. Chem. A.* 2 (2014) 9514–9523.
- [60] K. Hareesh, R.P. Joshi, D. V Sunitha, V.N. Bhoraskar, S.D. Dhole, Anchoring of Ag-Au alloy nanoparticles on reduced graphene oxide sheets for the reduction of 4-nitrophenol, *Appl. Surf. Sci.* 389 (2016) 1050–1055.
- [61] W. Wang, Z. Han, X. Wang, C. Zhao, H. Yu, Polyanionic clusters [M (P4Mo6) 2](M= Ni, Cd) as effective molecular catalysts for the electron-transfer reaction of ferricyanide to ferrocyanide, *Inorg. Chem.* 55 (2016) 6435–6442.
- [62] U. Nithiyantham, S.R. Ede, S. Anantharaj, S. Kundu, Self-assembled NiWO₄ nanoparticles into chain-like aggregates on DNA scaffold with pronounced catalytic and supercapacitor activities, *Cryst. Growth Des.* 15 (2015) 673–686.
- [63] A.M. Kalekar, K.K.K. Sharma, A. Lehoux, F. Audonnet, H. Remita, A. Saha, G.K. Sharma, Investigation into the catalytic activity of porous platinum nanostructures, *Langmuir.* 29 (2013) 11431–11439.
- [64] K. Gong, Y. Liu, Z. Han, Manganese-phosphomolybdate molecular catalysts for the electron transfer reaction of ferricyanide to ferrocyanide, *RSC Adv.* 5 (2015) 47004–47009.

Chapter 6

Conclusions and recommendations

6.1 Conclusions

6.1.1 Catalytic activities

The synthesis of Au, Pd, and bimetallic AuPd-PVP NPs was performed by adapting a polyol synthesis method, and the NPs formation was confirmed with a UV-vis spectroscopy technique. Kinetic investigation of orange II acid reduction in the presence of NaBH₄ was then carried out to access the catalytic activity of the catalysts. The reduction absorbance was monitored in a microplate reader at λ 480 (25, 35, and 45, °C), and the data acquired was modeled after the Langmuir-Hinshelwood mechanism.

All the three catalysts investigated followed the Langmuir-Hinshelwood model, and the reaction occurred spontaneously upon the catalyst's surfaces. The reduction processes possessed an endothermic reaction type, and AuPd-PVP NPs exhibited the highest catalytic performance compared to the other catalysts. Although, the catalysts were effective, but recyclability of the catalysts from the reaction medium was a major limitation. Therefore, generation 4 amine-terminated PAMAM dendrimers were used as templates in the initial synthesis of silica framework mesoporous support for CuDENS to form Cu_n@SiO₂ NPs. After that, a galvanic displacement methodology with Au³⁺ was carried out on Cu_n@SiO₂ to generate Au_n@SiO₂ NPs upon an *in-situ* exchange to form an heterogeneous catalyst.

The activities of the catalysts were tested by the initial reduction of 4-nitrophenol, where Au_n@SiO₂ NPs appeared as the highest performing catalyst. Thereafter, with Au_n@SiO₂ NPs, oxidation of Rh B and styrene was investigated in the presence of H₂O₂ and TBHP, respectively. The catalyst demonstrated to be effective, and its stability was confirmed by quantitative product yield obtained after three consecutive runs following the initial investigation. As confirmed by the ICP-OES analysis, the leaching test revealed there was little or no leaching of the metal into the reaction medium (0.03 mg/L).

Moreover, a sol-gel method was adapted to synthesize silica support of Pd@SiO₂, while Pd metal was immobilized onto the silica support by a wet impregnation method. The catalyst's activity was investigated in chemoselective hydrogenation of acetophenone using HPMC solution, while NaBH₄ was used as a hydrogen source. The catalyst displayed an effective and efficient activity that generated a percentage conversion of 99.334% with an optimum 100% selectivity towards 1-phenyl ethanol with no unwanted product.

Conclusively, because continuous flow procedure is an easier, safer, and faster method for catalytic transformation, catalytic application of MnMMO and CoMMO was carried out using a continuous flow protocol and the combined possibilities of 3D-printing techniques. A U-shaped, easy-to-handle flow device was printed with the catalysts inside. With the aid of a 3D-printed syringe pump, the degradation process of hexacyanoferrate was investigated with respect to parameters such as effect of flow rate, catalyst dose, and effect of temperature. The color change that accompanied the degradation process at each variation was consistently monitored in a microplate reader at 420 nm.

Manganese mesoporous metal oxides showed the highest percentage conversion of 94.1% in just 6 min, and the activation energy was computed to be 5.17 kJ·mol⁻¹. The recyclability study of MnMMO proved the stability of the catalyst after five catalytic cycles.

6.2 Recommendations

The kinetics of the catalytic degradation in chapter 2 could be investigated in respect of diffusion rate to differentiate which catalyst is diffusion-limited. The synthetic procedure of galvanic displacement in chapter 3 can also be exploited more by using less expensive metals such as nickel or iron. Moreover, the eco-friendly hydrogenation of acetophenone over Pd@SiO₂ catalyst in chapter 4 could also be employed in a continuous flow procedure for optimization. Biodegradable and ecofriendly HPMC could be employed in the synthesis of other biocompatible catalysts for industrial application.

Finally, CoMMO in chapter 5 can be optimized by increasing the catalyst amount to enhance the percentage conversion of hexacyanoferrate. Also, the 3D-printing application could be used

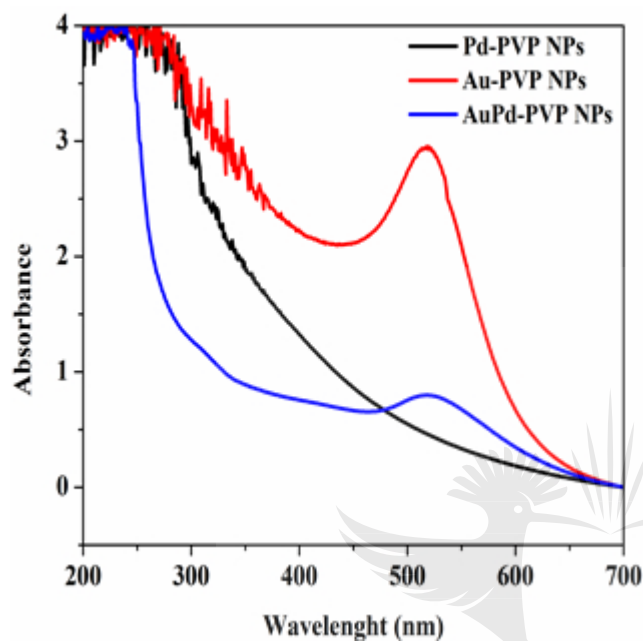
as a tool for fabricating other reaction wares for chemical synthesis and reaction to save cost, promote safety, and enhance productivity.



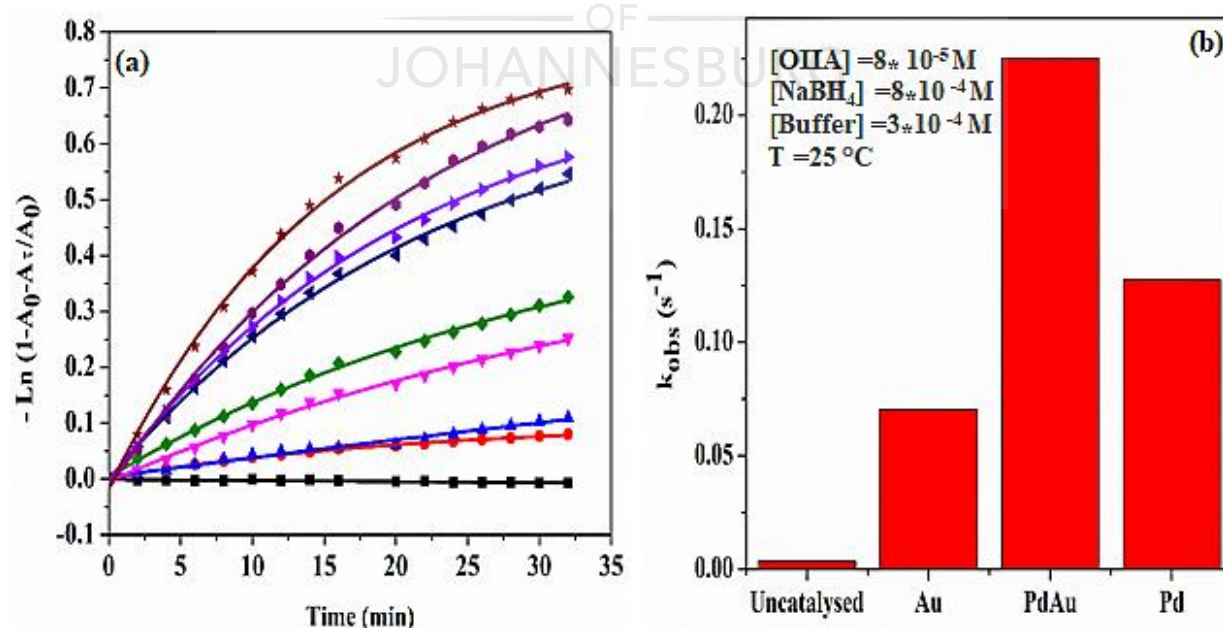
Appendix

Supplementary information

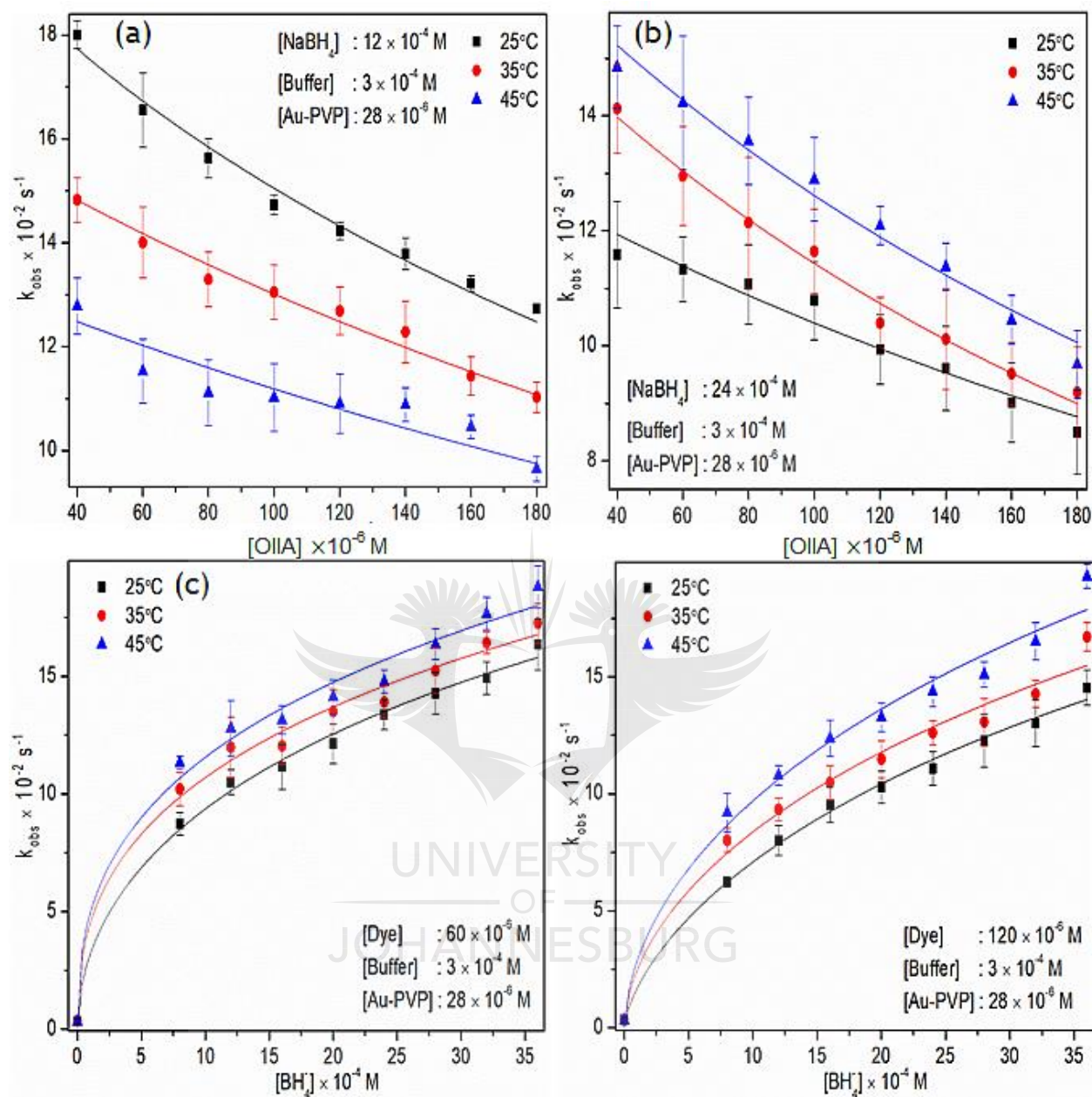
Chapter 2



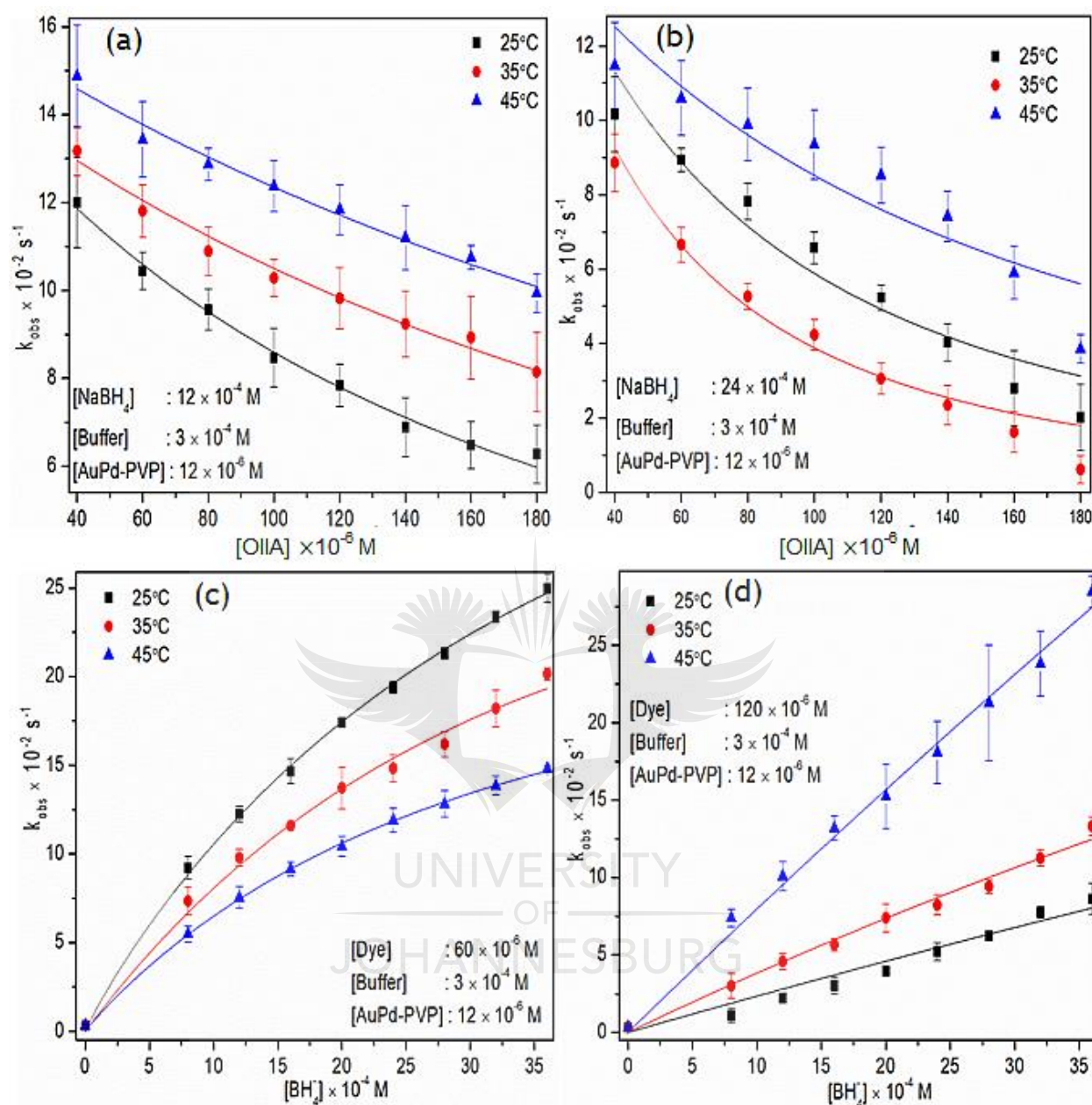
Appx. 2.1: UV-vis Spectrum of (a) Pd-PVP NPs, (b) Au-PVP NPs, and (c) PdAu-PVP bimetallic NPs



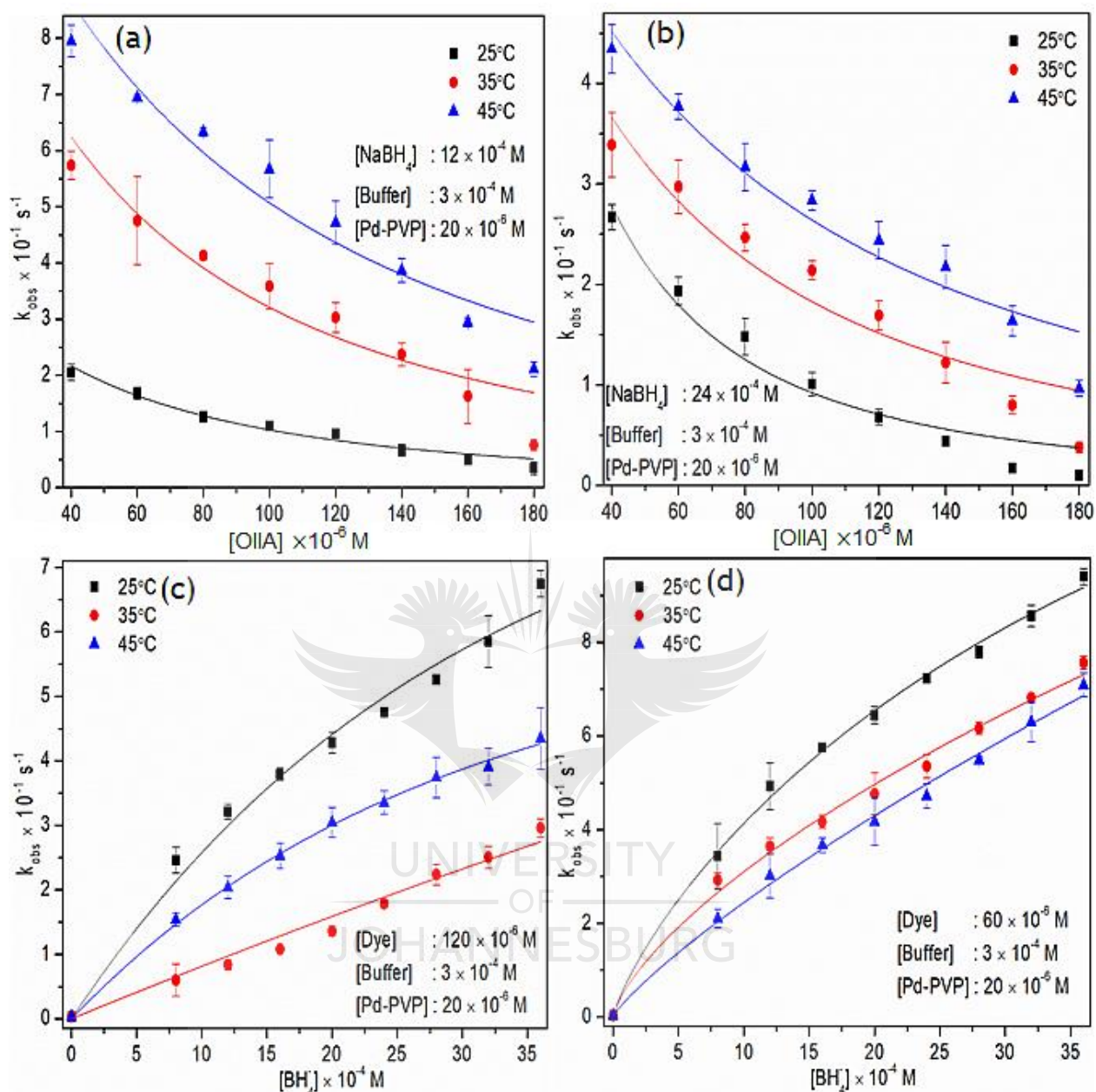
Appx. 2.2: (a) data fits *pseudo*-first-order (b) Histogram comparison of the observed rate constant of the different catalysts.



Appx. 2.3: The plot of observed rate constant dependence on the OII concentration while maintaining a constant $[\text{NaBH}_4]$ (in a, and b), and on NaBH_4 concentration while keeping $[\text{OII}]$ (in c, and d) constant using Langmuir-Hinshelwood approach for Au-PVP catalyzed reaction.

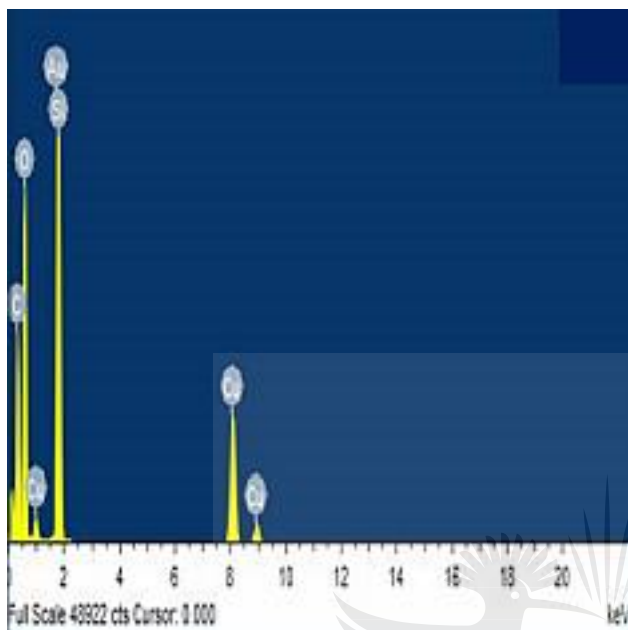


Appx. 2.4: The plot of observed rate constant dependence on the OII concentration while maintaining a constant $[\text{NaBH}_4]$ (in a, and b), and on NaBH_4 concentration while keeping $[\text{OII}]$ (in c, and d) constant using Langmuir-Hinshelwood approach for AuPd-PVP catalyzed reaction.

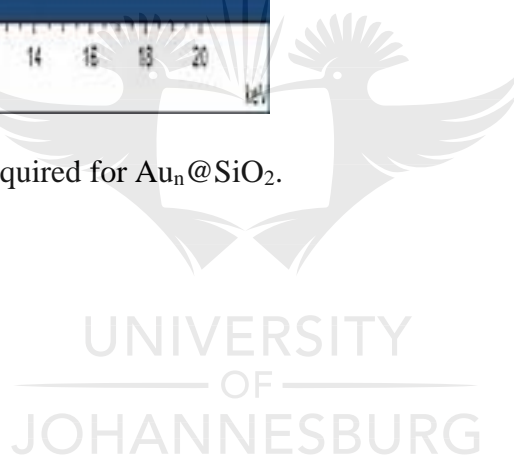


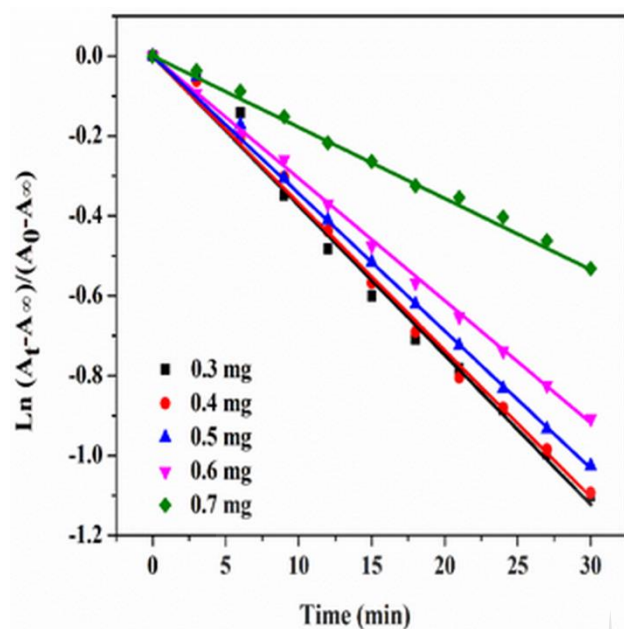
Appx. 2.4: The plot of observed rate constant dependence on the OII concentration while maintaining a constant $[\text{NaBH}_4]$ (in a, and in b), and on NaBH_4 concentration while keeping $[\text{OII}]$ (in c, and d) constant using Langmuir-Hinshelwood approach for Pd-PVP catalyzed reaction.

Chapter 3

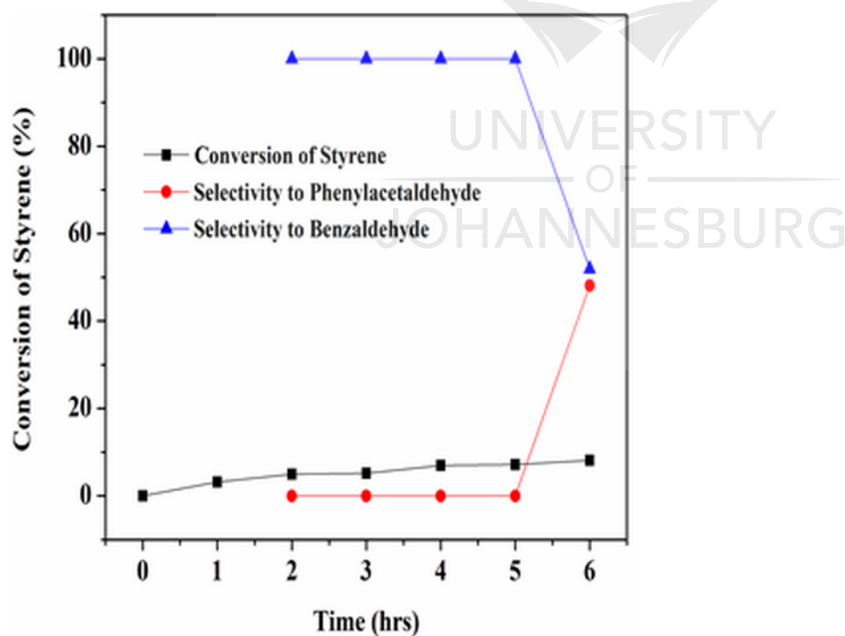


Appx.3.1: EDX analysis acquired for Au_n@SiO₂.



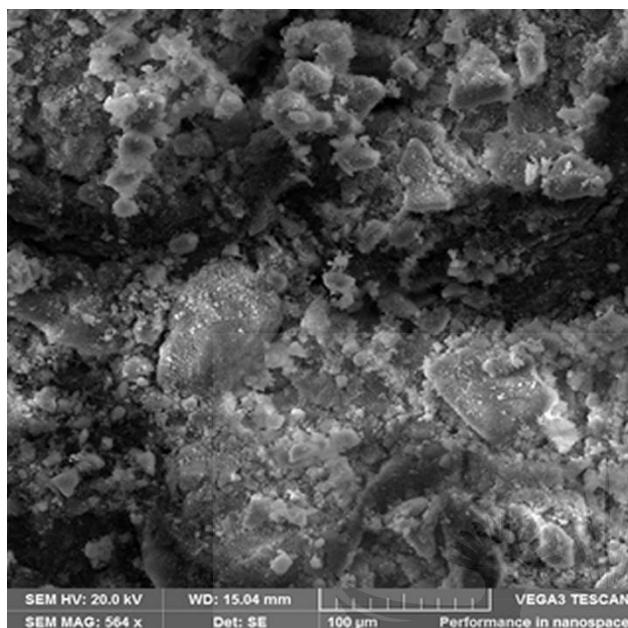


Appx. 3.2: A linear pseudo-first order data fit revealing obtained RhB oxidation of using $Au_n@SiO_2$.



Appx. 3.3: The graph obtained for the oxidant (TBHP) effect styrene.

Chapter 4

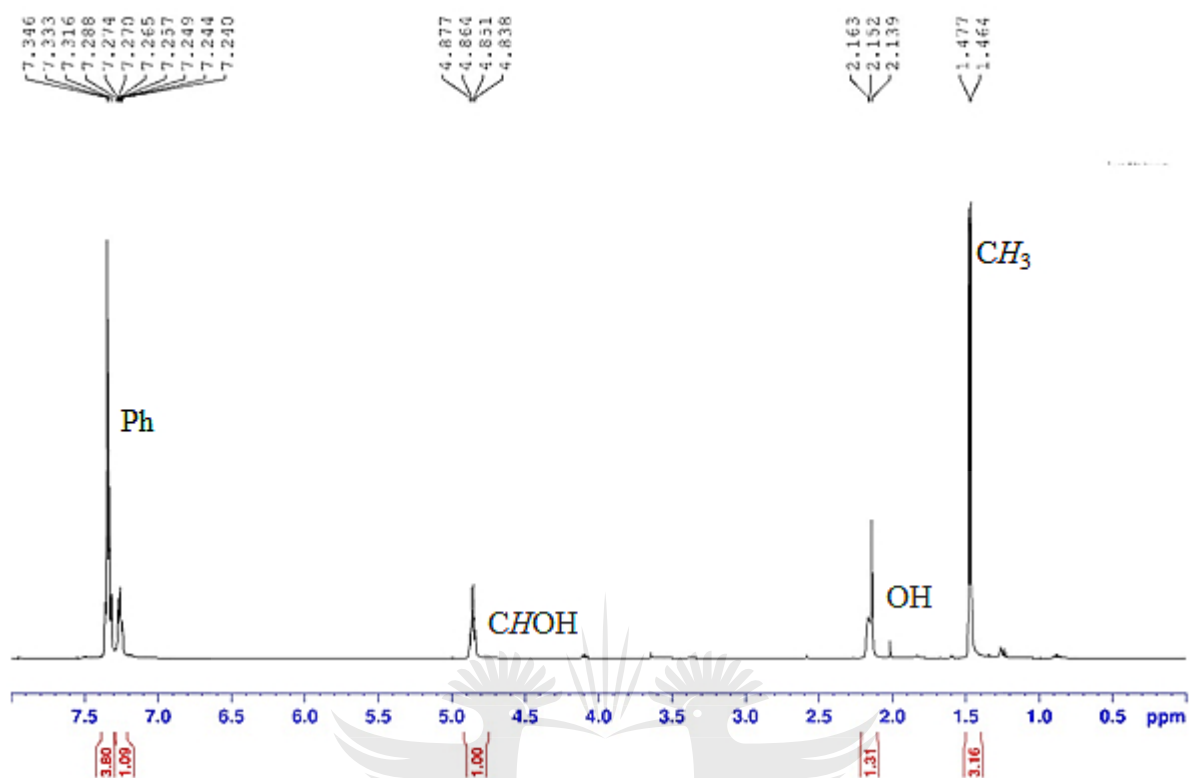


Appx. 4.1: Image of SEM obtained for Pd@SiO₂

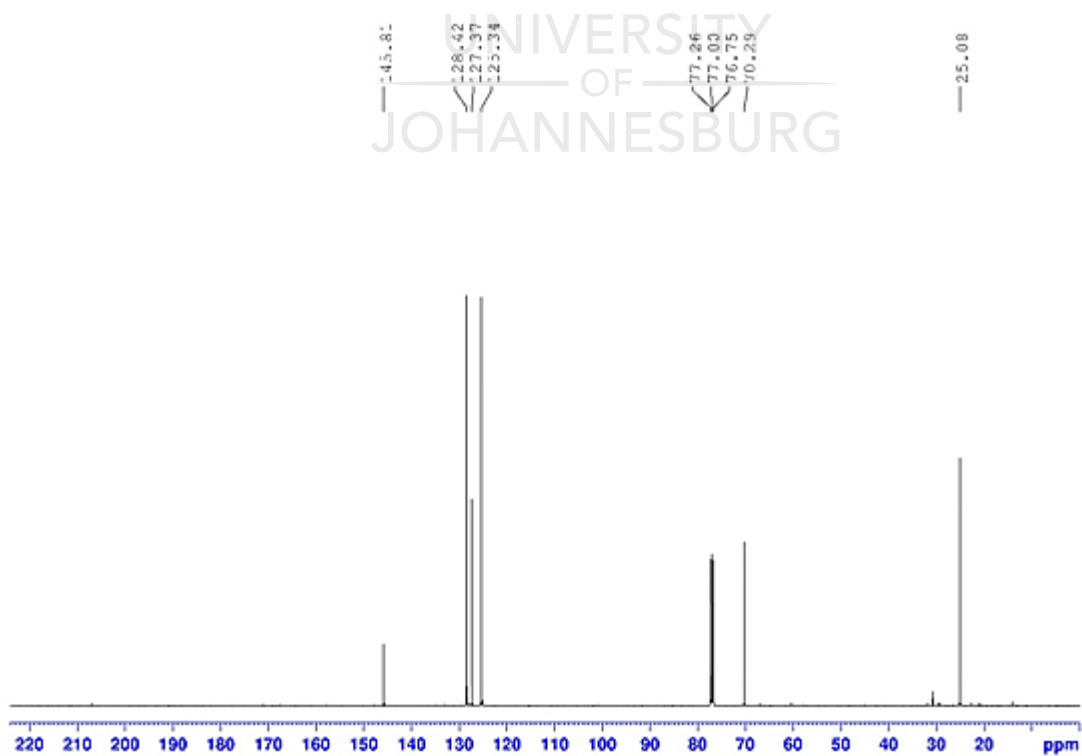
$$\text{Conversion (\%)} = \frac{(\text{Substrate}_0 - \text{Substrate}_t) \times 100}{\text{Substrate}_0} \quad (4.S1)$$

$$\text{Selectivity (\%)} = \left(\frac{\text{moles of product}}{\text{moles of substrate}_0} \right) \times 100 \quad (4.S2)$$

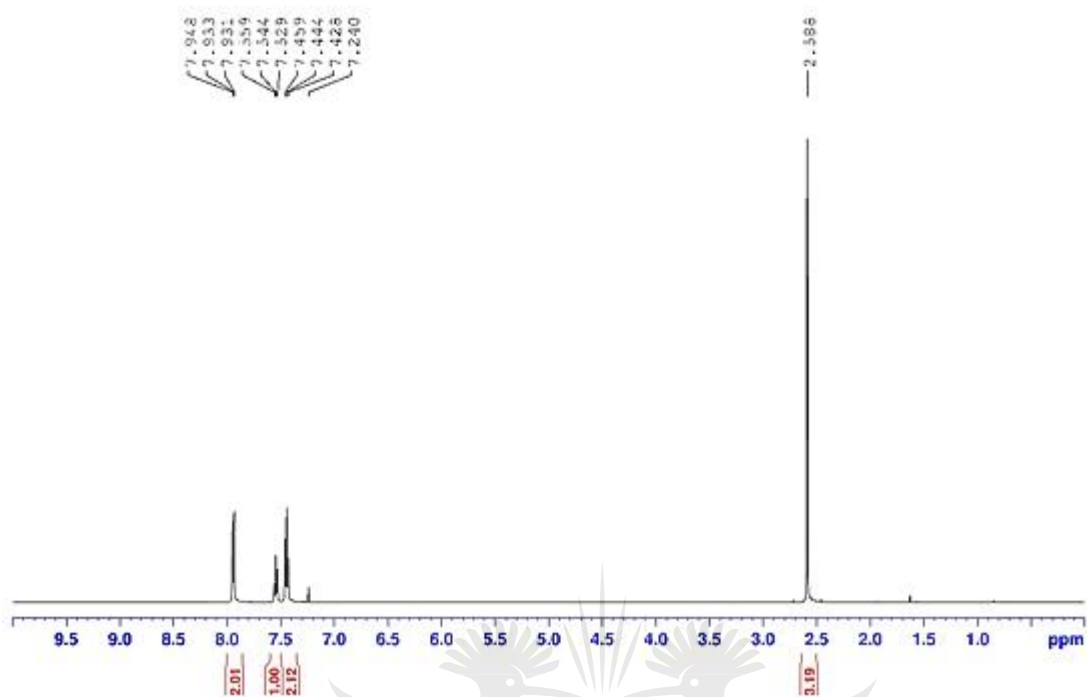
Substrate₀ represents the initial mole of the substrate, and substrate_t is the present mole of the substrate at the time t.



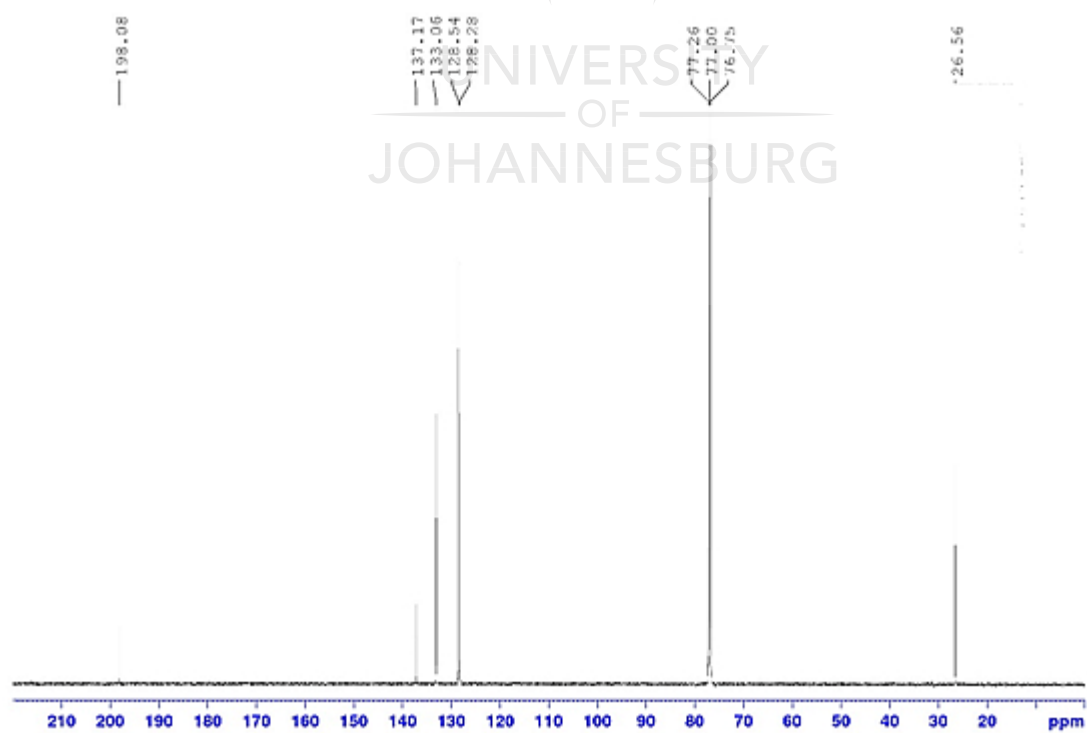
Appx. 4.2a: NMR Spectra of the produced 1-Phenyl ethanol using Pd@SiO₂.



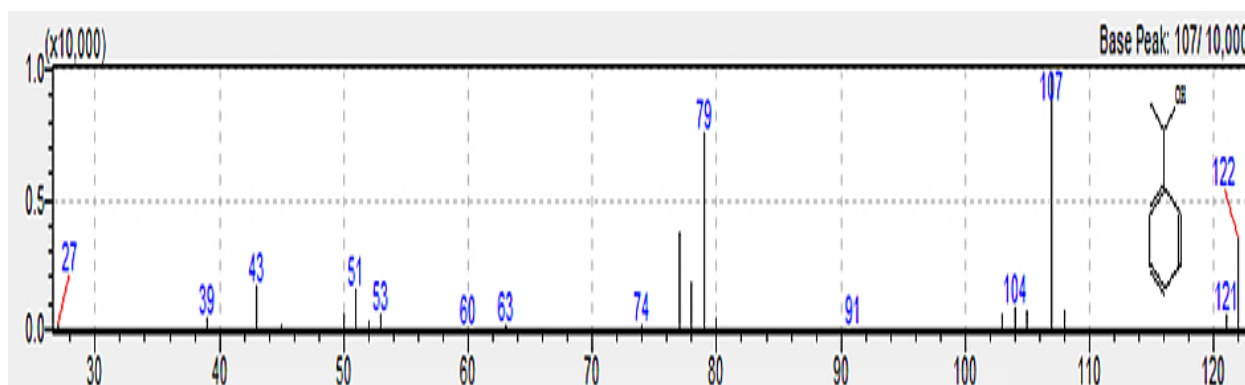
Appx. 4.2b: NMR Spectra of the produced 1-Phenyl ethanol using Pd@SiO₂.



Appx. 4.2c: NMR Spectra of the produced 1-Phenyl ethanol using Pd@SiO₂.

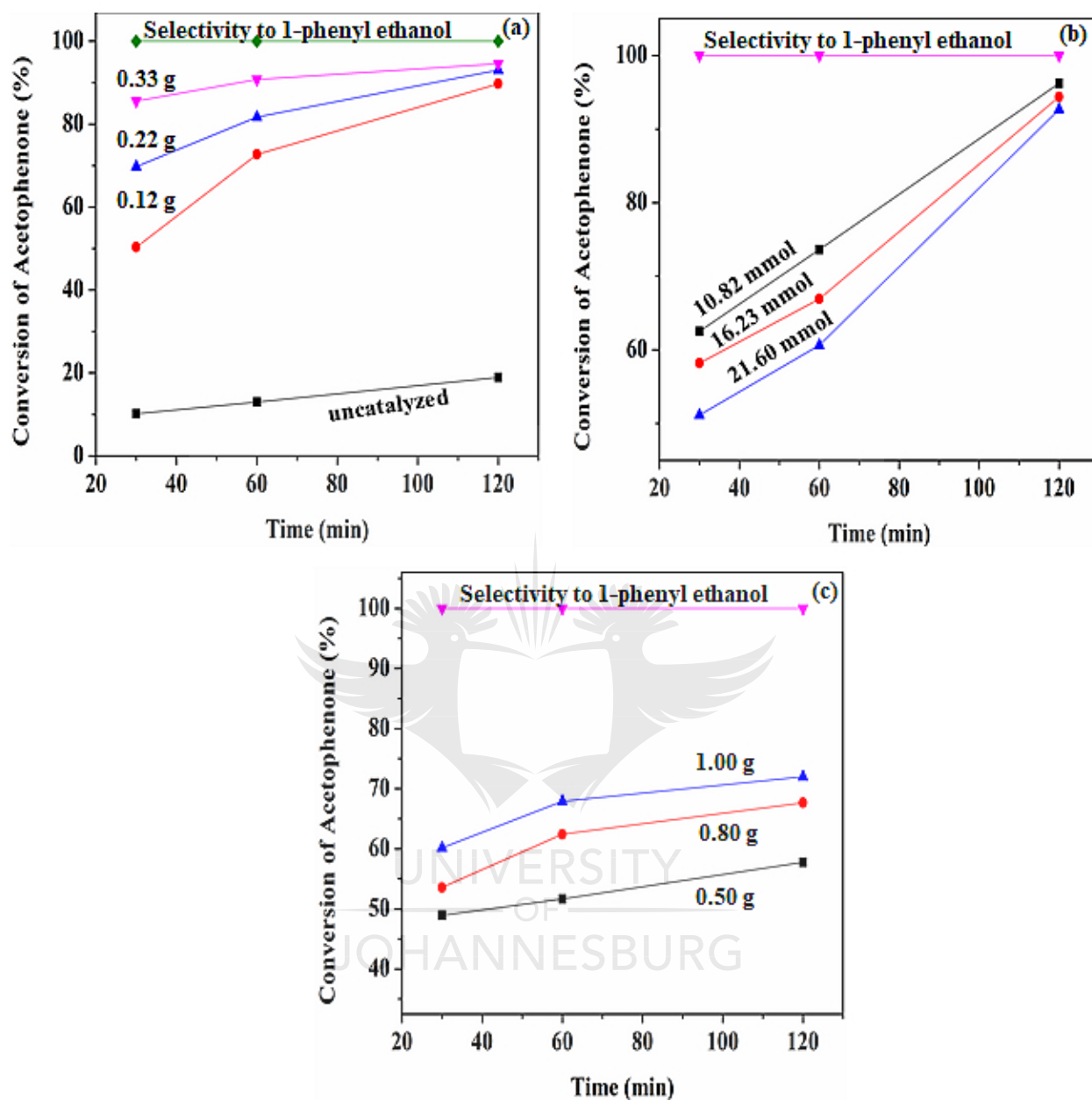


Appx. 4.2d: NMR Spectra of the produced 1-Phenyl ethanol using Pd@SiO₂.

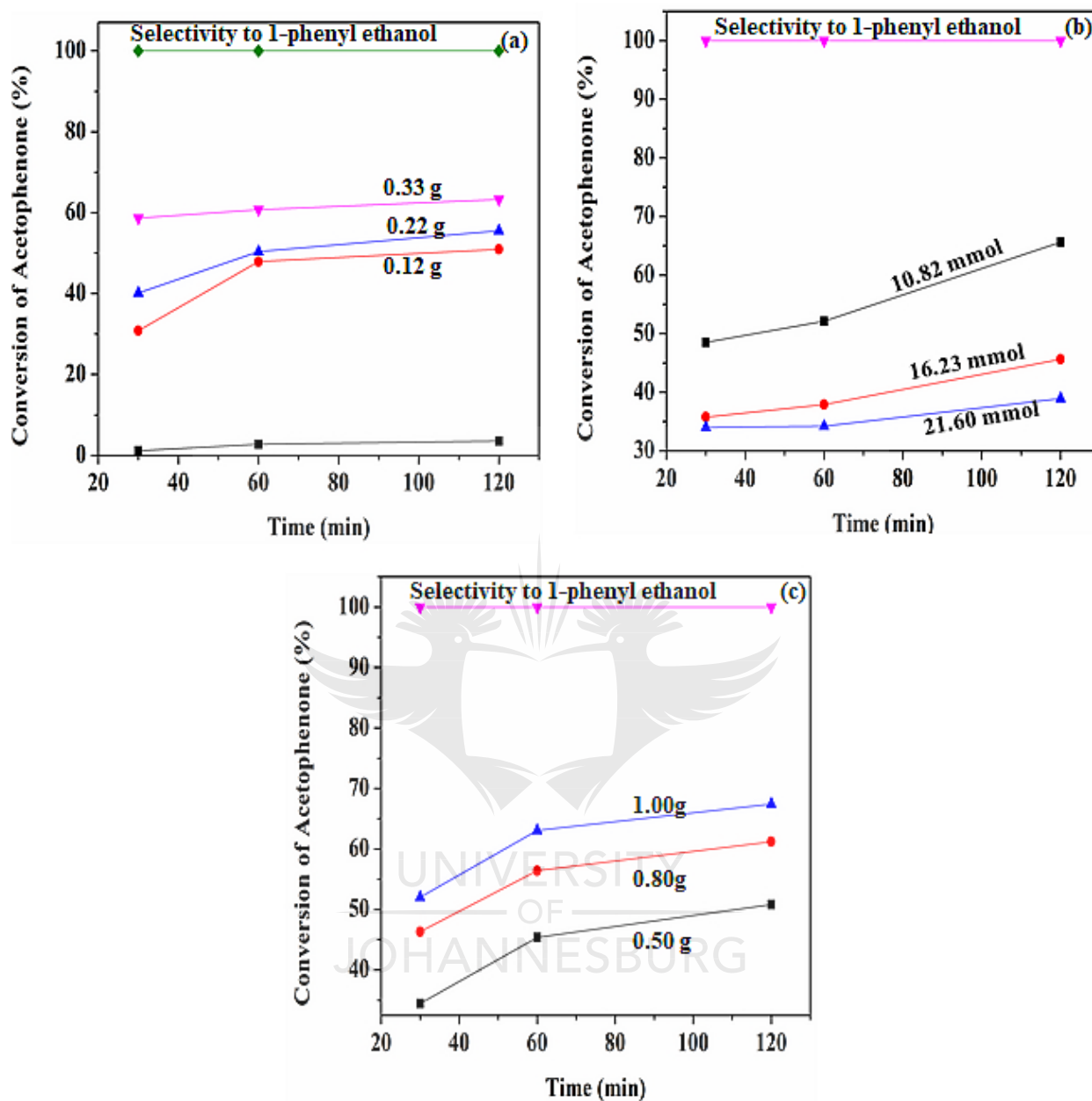


Appx. 4.3: Product chromatogram of the GC-MS analysis obtained for the hydrogenation of acetophenone at 80 °C after 30 min.





Appx. 4.4: Different plots revealing the variations at 60 °C of (a) catalyst amount variation, (b) substrate variation, (c) Borohydride variation obtained.



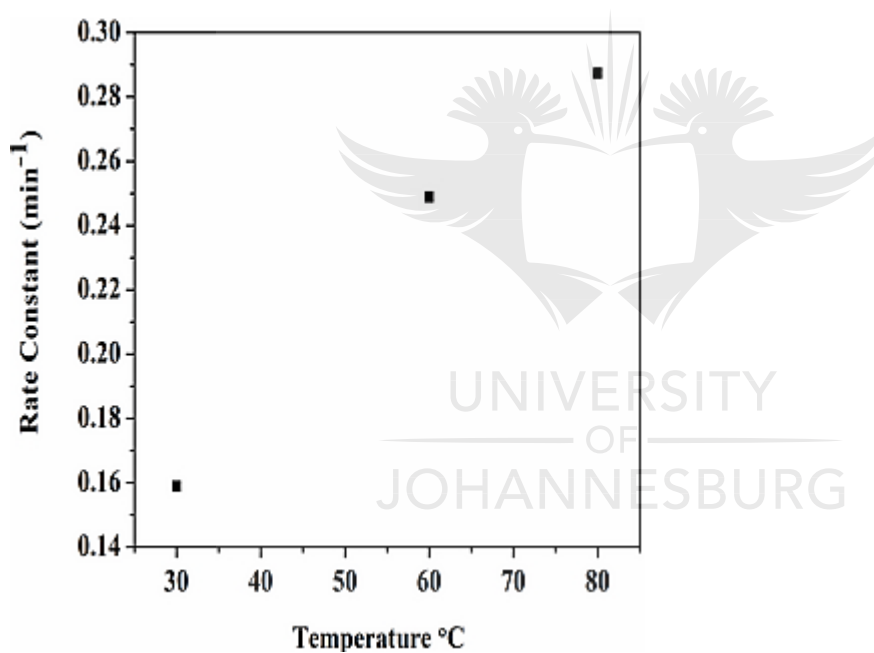
Appx. 4. 4: Different plots revealing the variations at 30 °C of (a) catalyst amount variation, (b) substrate variation, (c) Borohydride variation obtained.

Supplementary Table (ST) 4.1:

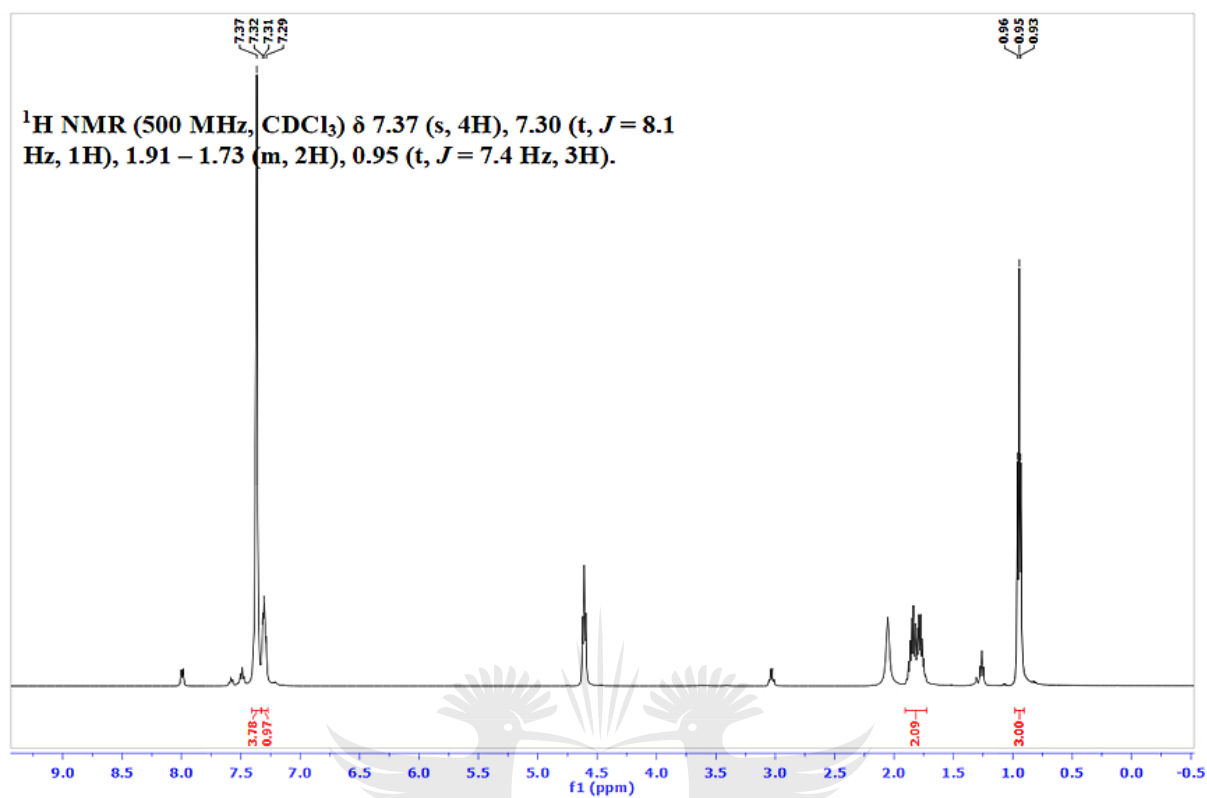
Data obtained for the conversion of acetophenone at different temperatures using the same amount of catalyst and the substrate.

Temperature (°C)	Conversion (%)		
	at 30 (min)	at 60 (min)	at 120 (min)
30	33.99	34.21	38.93
60	51.15	60.63	92.67
80	99.09	99.25	99.33

Condition: 21.60 mmol of the substrate, 1.0 g of redox agent, 0.22 g of Pd@SiO₂, 6 mL of solvent.

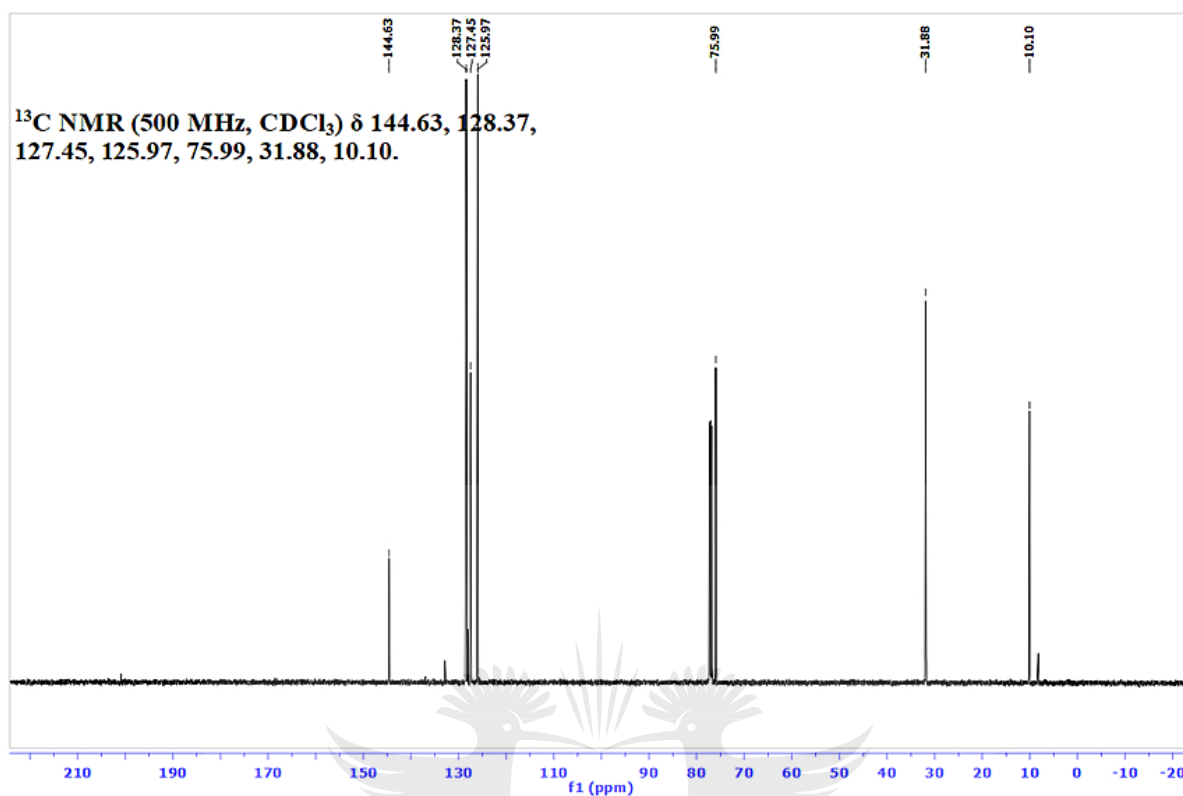


Appx. 4.6: Plot showing the dependence of the rate constant on the temperature.

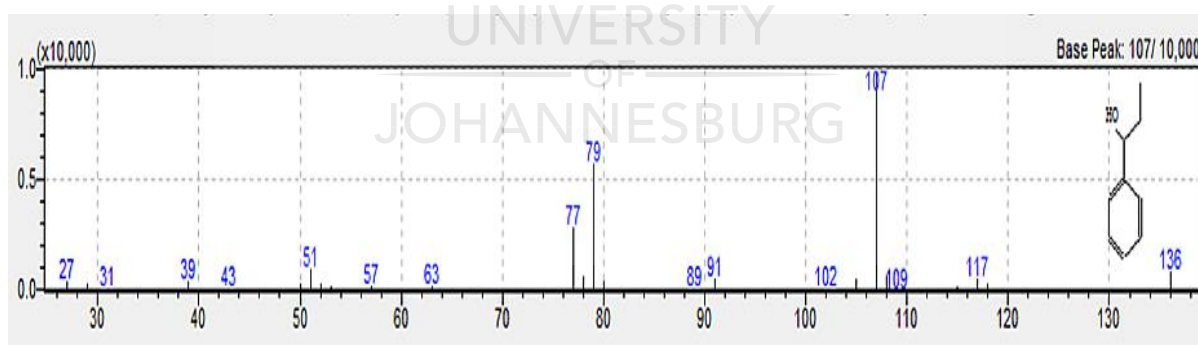


Appx. 7a. ^1H NMR Spectrum of the generated benzene methanol using Pd@SiO_2 .

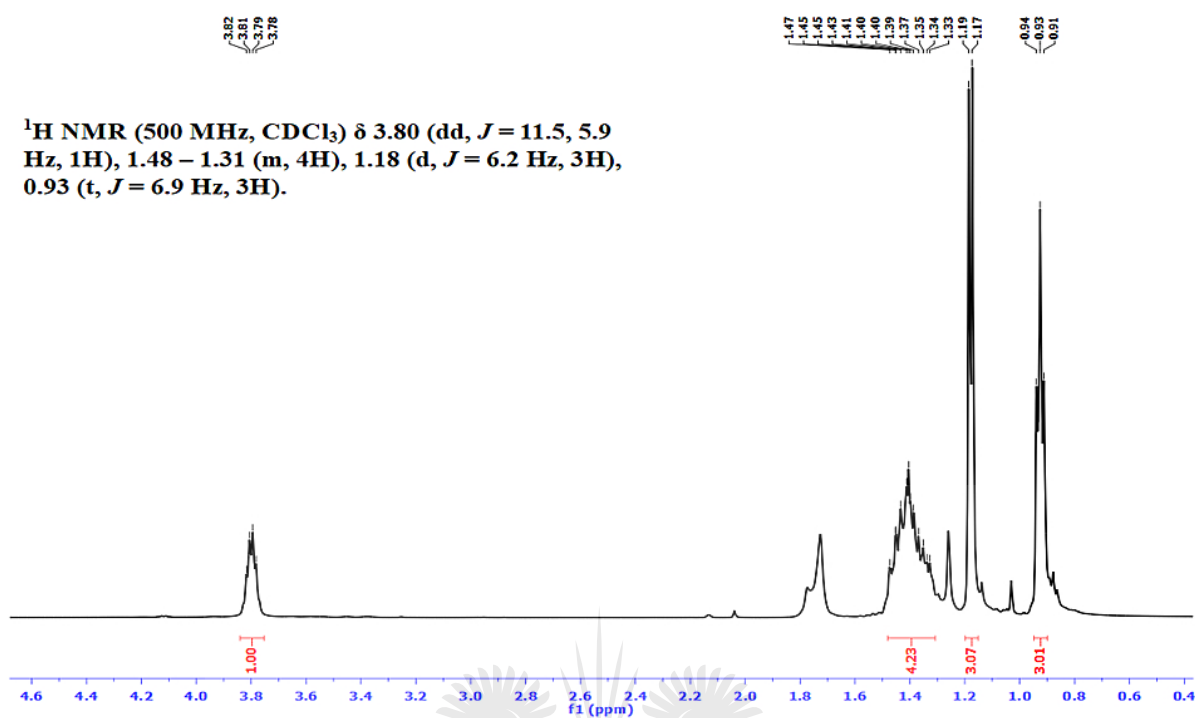
UNIVERSITY
OF
JOHANNESBURG



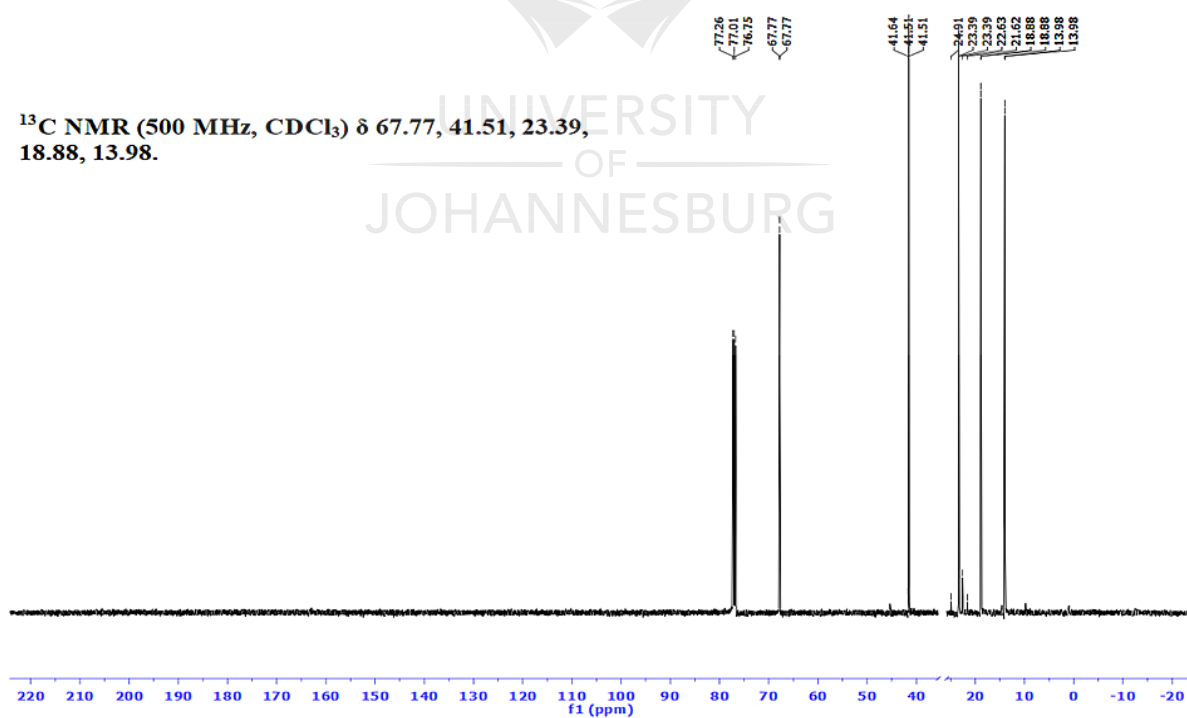
Appx. 7b. ^{13}C NMR Spectrum of the generated benzene methanol using $\text{Pd}@\text{SiO}_2$.



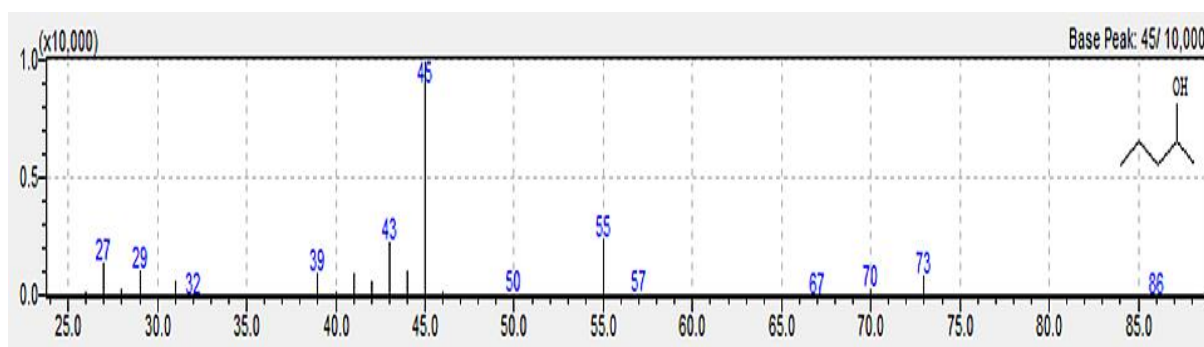
Appx. 8. Product chromatogram of the GC-MS analysis obtained for the hydrogenation of propiophenone at $80\text{ }^\circ\text{C}$.



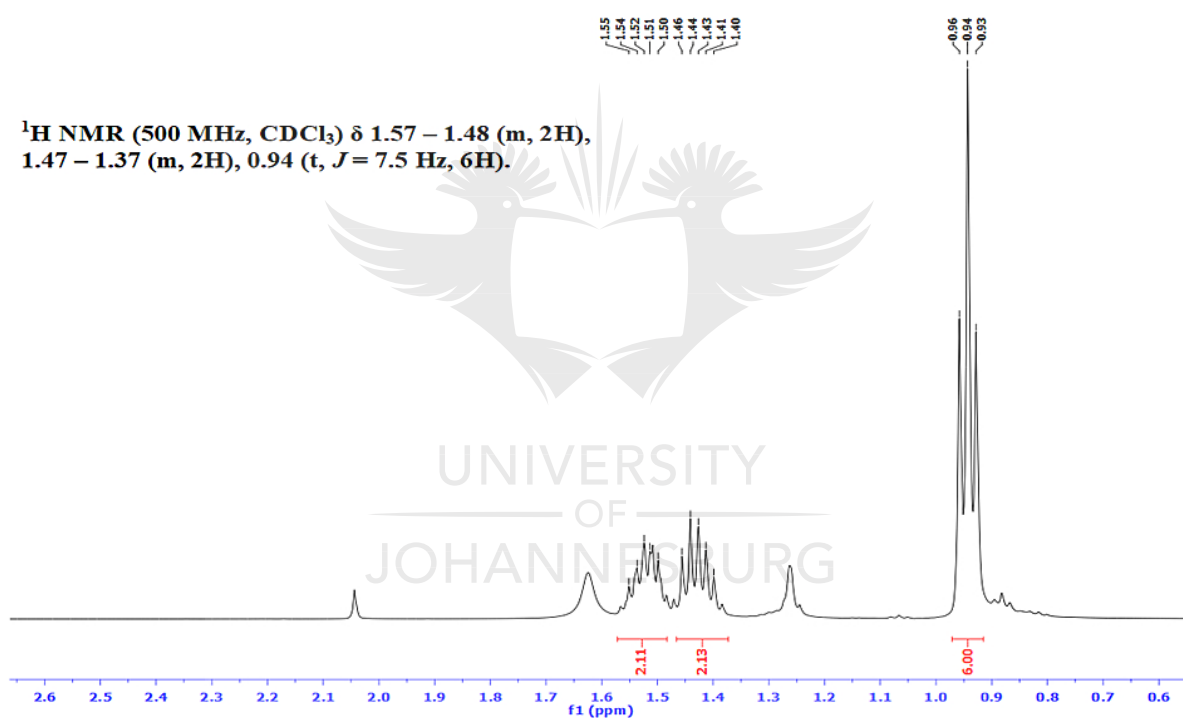
Appx. 9a. ¹H NMR Spectrum of the generated 2-Pentanol using Pd@SiO₂.



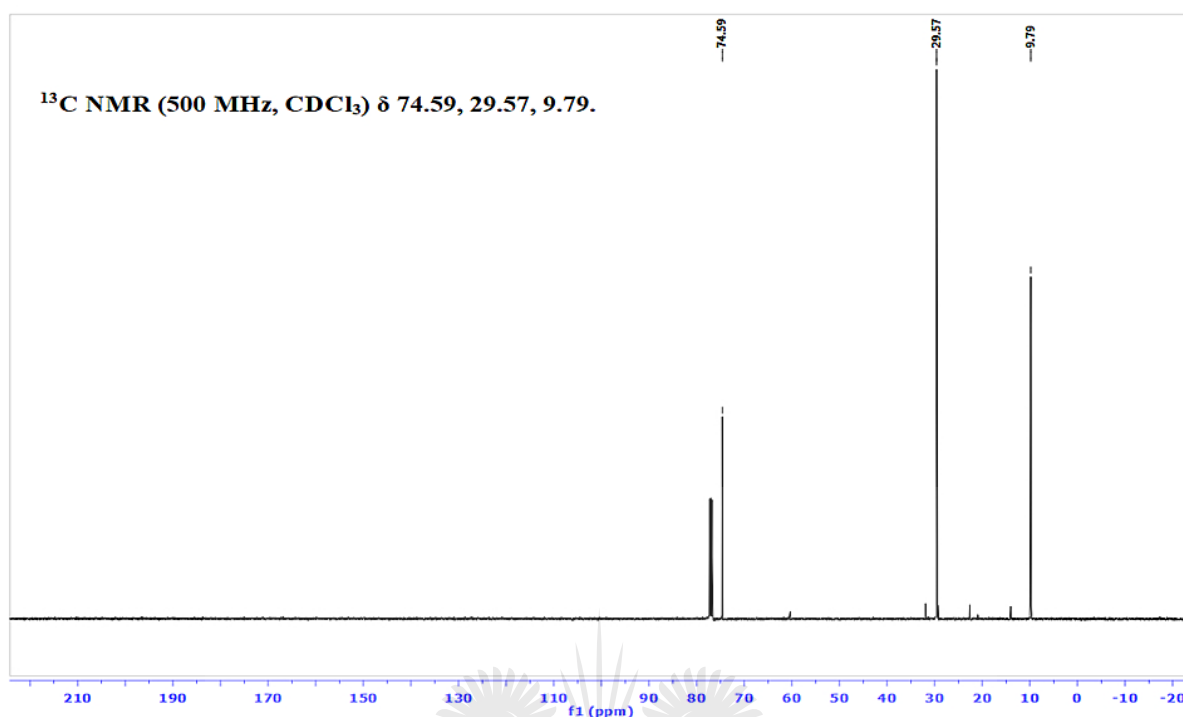
Appx. 9b. ¹³C NMR Spectrum of the 2-Pentanol using Pd@SiO₂.



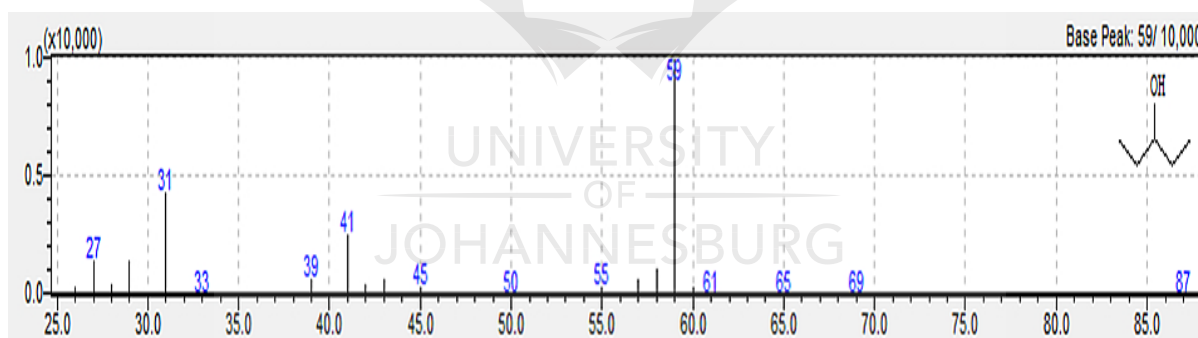
Appx. 10. Product chromatogram of the GC-MS analysis obtained for the hydrogenation of 2-Pentanone at 80 °C.



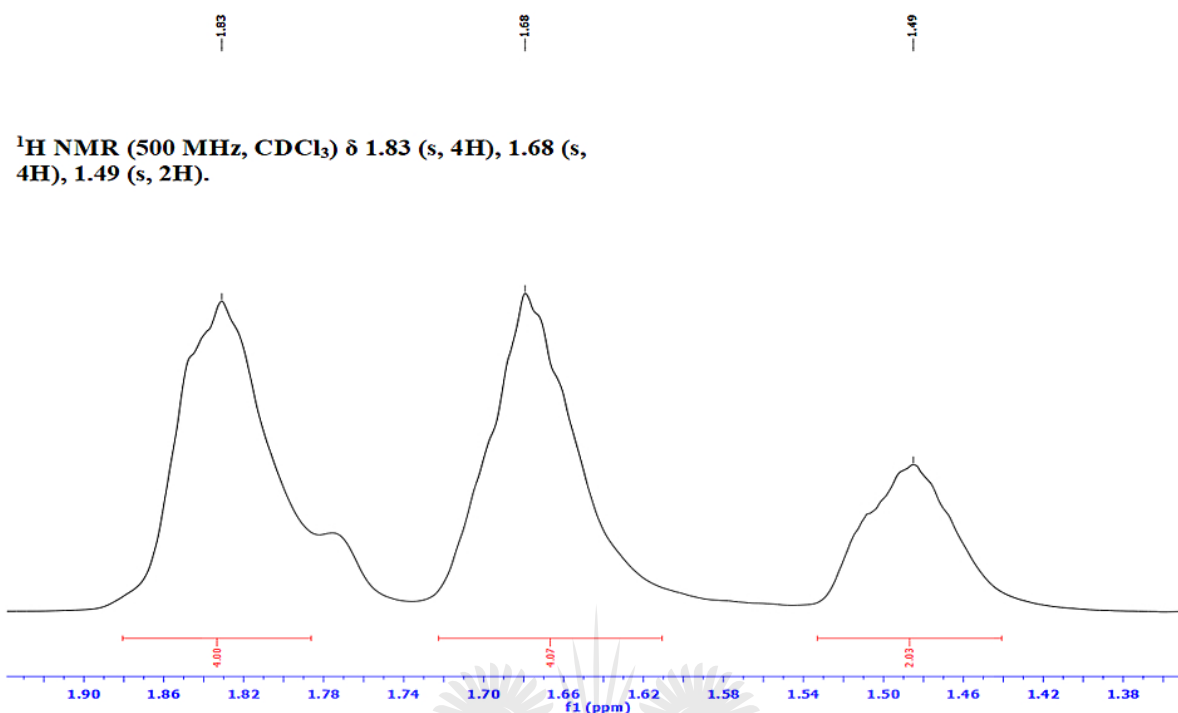
Appx. 11a. ¹H NMR Spectrum of the generated 3-Pentanol using Pd@SiO₂.



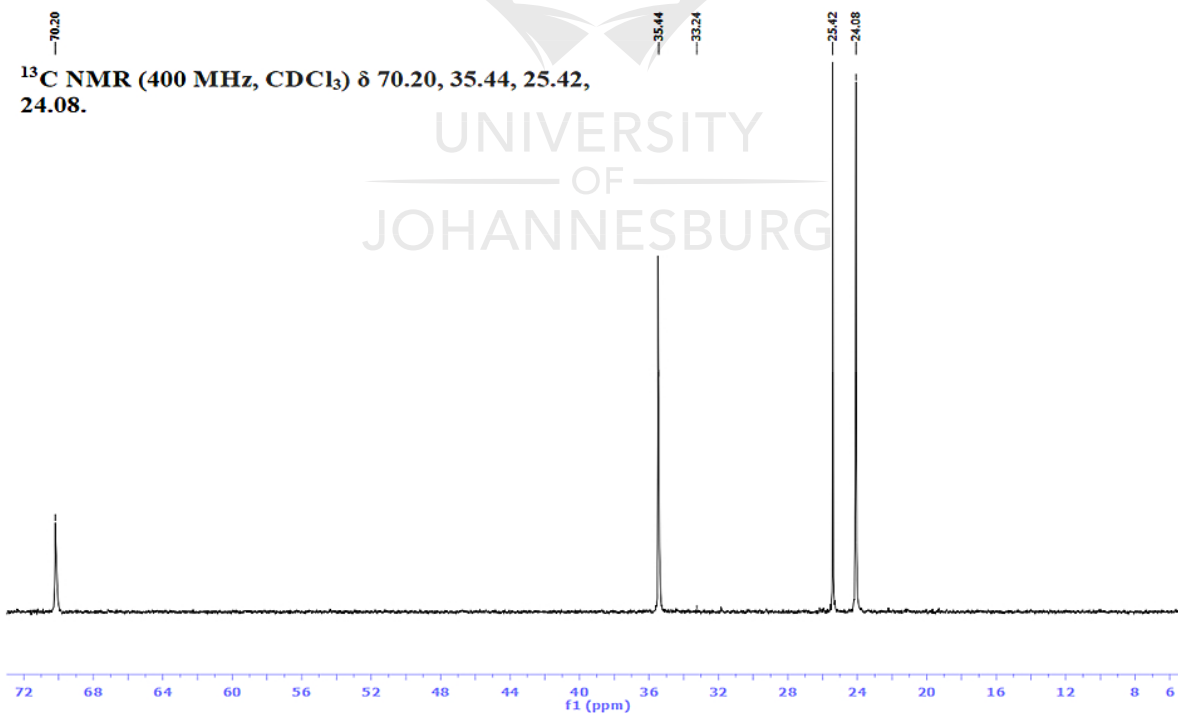
Appx. 11b. ^{13}C NMR Spectrum of the 3-Pentanol using Pd@SiO_2 .



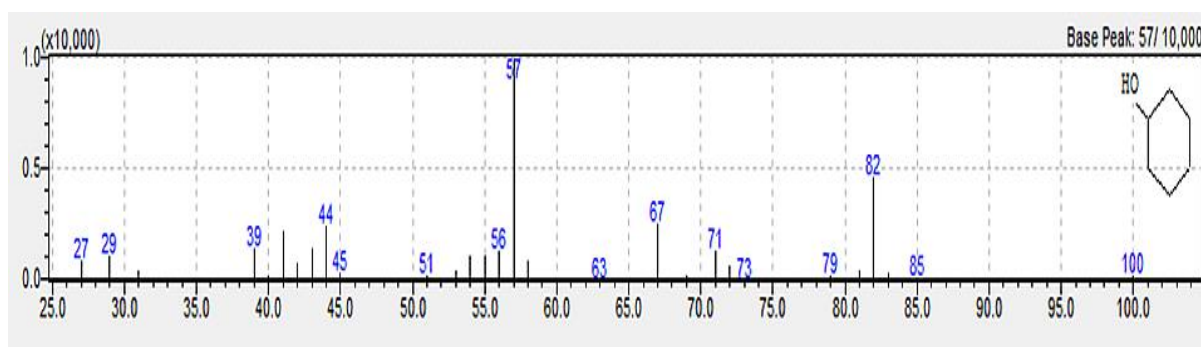
Appx. 12. Product chromatogram of the GC-MS analysis obtained for the hydrogenation of 3-Pentanone at 80 $^{\circ}\text{C}$.



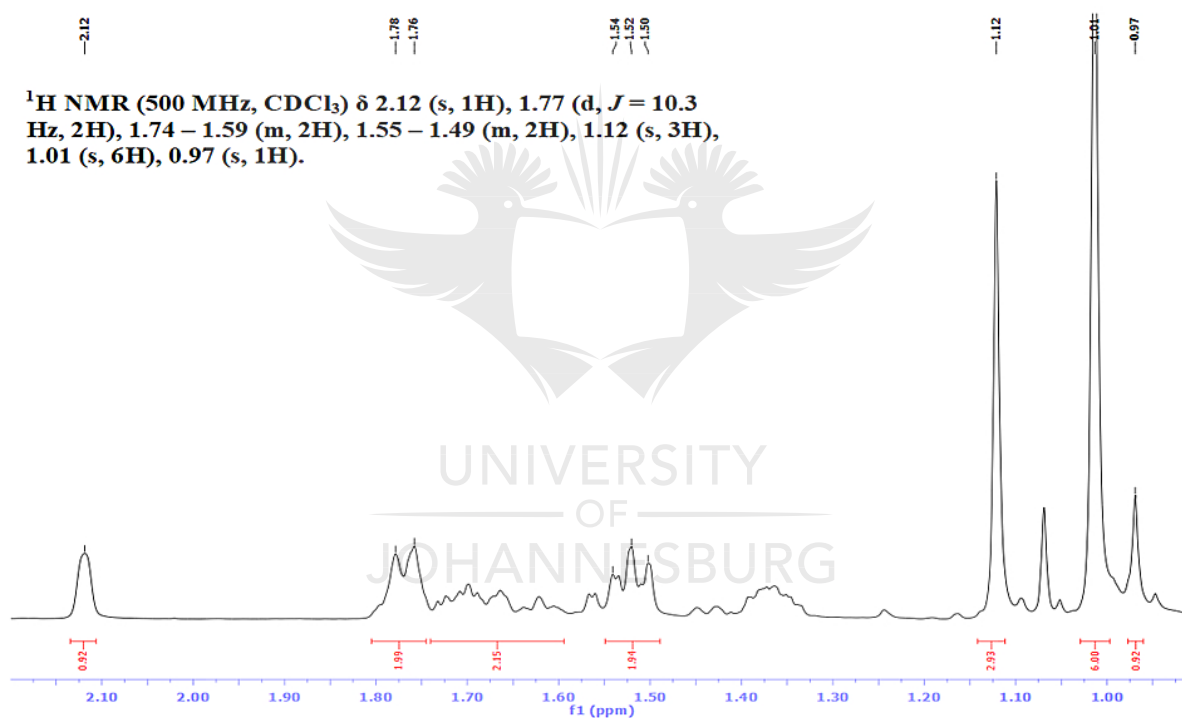
Appx. 13a. ^1H NMR Spectrum of the generated cyclohexanol using Pd@SiO_2 .



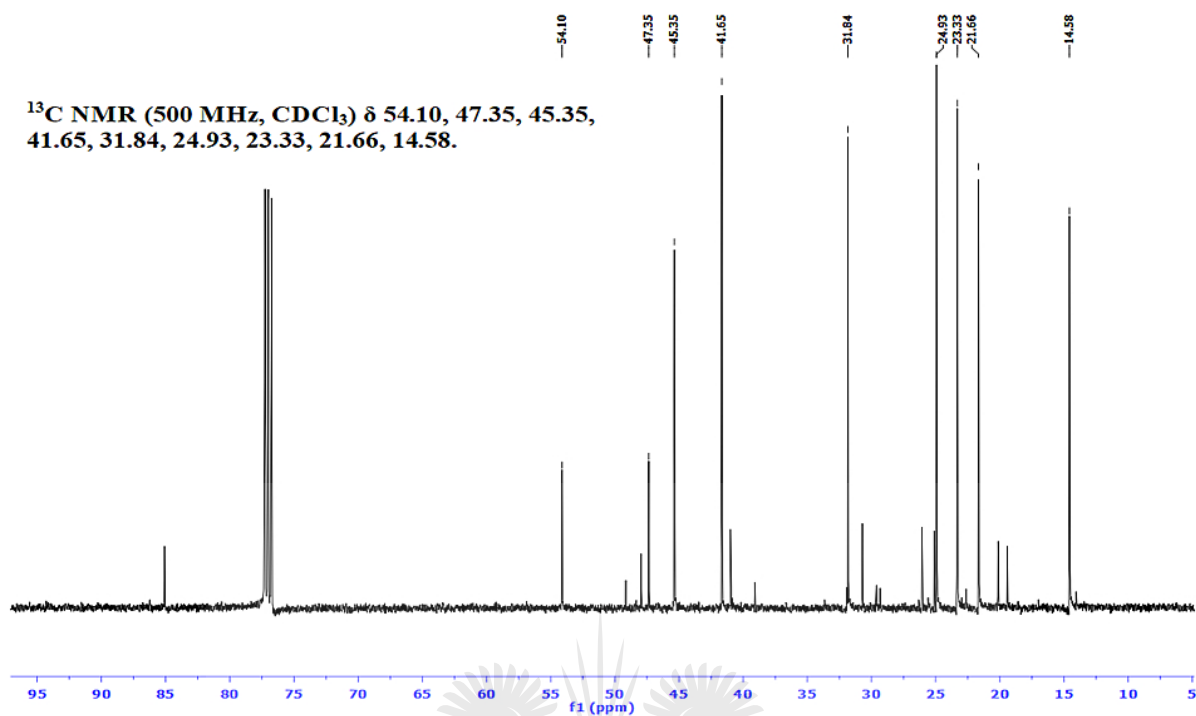
Appx. 13b. ^{13}C NMR Spectrum of the generated cyclohexanol using Pd@SiO_2 .



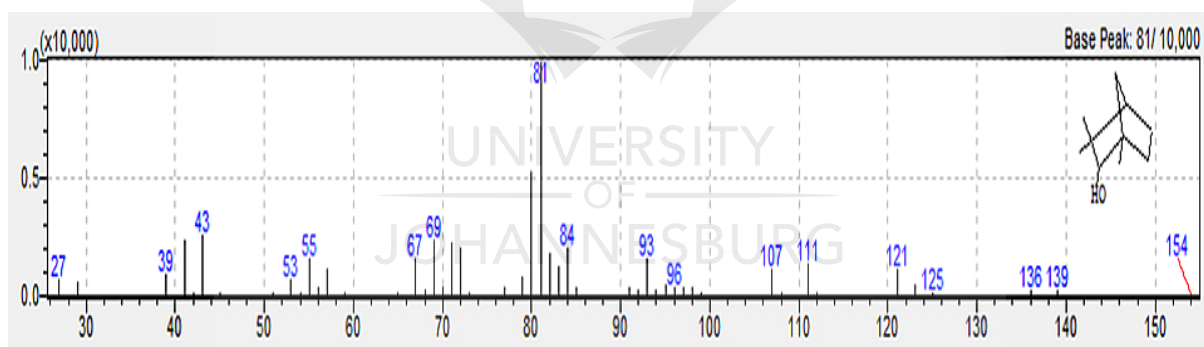
Appx. 14. Product chromatogram of the GC-MS analysis obtained for the hydrogenation of 3-cyclohexanone at 80 °C.



Appx. 15a. ¹H NMR Spectrum of the generated fenchol using Pd@SiO₂.



Appx. 15b. ^{13}C NMR Spectrum of the generated fenchol using Pd@SiO_2 .



Appx. 16. Product chromatogram of the GC-MS analysis obtained for the hydrogenation of 3-Fenchone at 80 °C.

Chapter 5

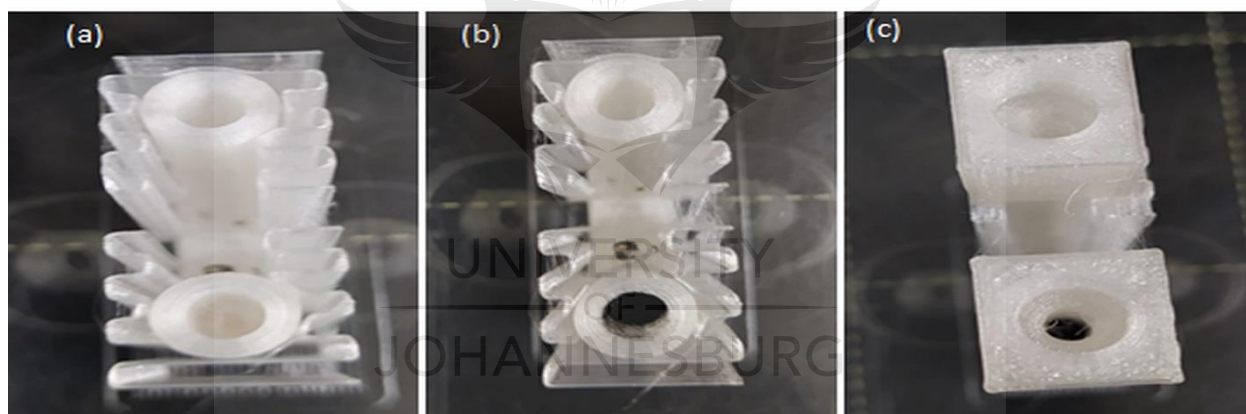
5. S1 Potassium hexacyanoferrate (III)

Potassium hexacyanoferrate (III) is one of the most pervasive toxic contaminants in the air, water, and soil [1]. It has been established that it is mutagenic and carcinogenic and that it is acutely harmful when accumulated in people, aquatic species, and other living organisms across numerous food chains [2]. Even when found in trace concentrations, it influences the ecosystem, resulting in environmental morbidity [1]. This is consistent with the fact that most cyanide complexes are highly harmful to the environment and severely toxic to humans and aquatic life [3].

Numerous catalytic methods have been developed to treat $[K_3Fe(CN)_6]$ pollution in the environment. These include Carregal Romero's group's [4,5] use of gold nanoparticles (AuNPs) for the reduction of $[K_3Fe(CN)_6]$ in an aqueous phase. Their findings were encouraging. However, the catalyst exhibited low stability, and they encountered difficulties extracting it from the reaction media. Additionally, Chen, Chen, Wang, Wang, Wu, Zhou, and Ge 2016 created sub-micron poly(ethyleneglycol dimethacrylate) microspheres supported by nano-Au (PEGDMA@AuNPs) for catalyzing the reduction of $[K_3Fe(CN)_6]$ in an aqueous solution using $NaBH_4$ [6]. Although the catalysts demonstrated intense activity and a low-rate constant, their stability was not noted. Similarly, in Gong, Liu, and Han 2015, the authors employed Mn-Phosphomolybdate to reduce $[K_3Fe(CN)_6]$ in aqueous conditions, and while conversion greater than 50% was obtained, the conversion time was quite long [7]. Additionally, Wang, Han, Wang, Zhao, and Yu 2016 reduced aqueous $[K_3Fe(CN)_6]$ with $Ni(P_4MO_6O_{31})_2$, applying sodium thiosulphate ($Na_2S_2O_2$) as the reductant, and found low conversions over a longer reaction duration [8]. Sahid, Lampre, Dragoë, Beaunier, Palpant, and Remita 2019 produced spherical Au-NPs@citrate with a diameter of 15 nm and catalyzed the reduction of $[K_3Fe(CN)_6]$ in the presence of $Na_2S_2O_2$ [9]. Regardless of how active the catalyst was, the reaction took well over 30 minutes. Therefore, it is critical to demonstrate an enhanced catalytic reduction reaction employing a solid and effective catalytic system.

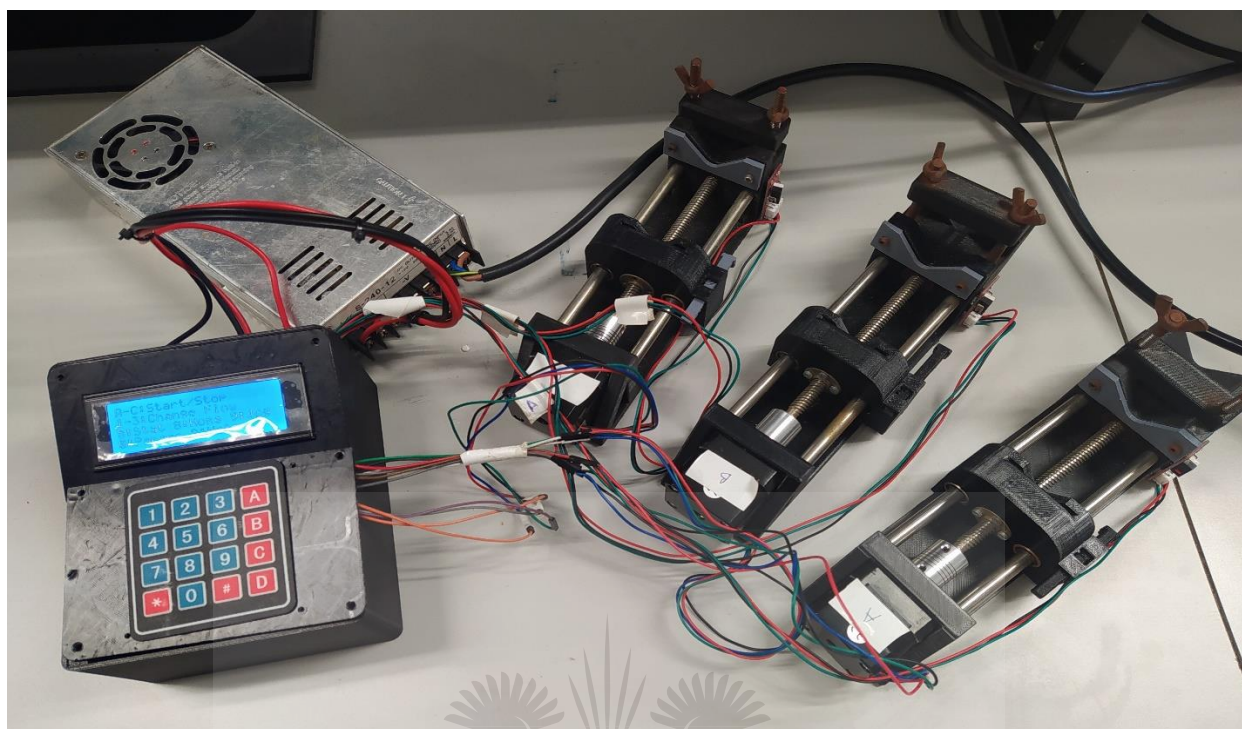
Supplementary Table 5.1:**Data showing the 3D printing parameter details**

Print parameters	PLA filament
Brim	Yes
Print speed	100 %
Filament flow	95 %
Nozzle temp	198 °C
Bed temperature	55°C
Layer height	0.2 mm
Bed surface	Covered with PEI
Support structures	Yes
Infill	80 %



Appx. 5.1: The loading of the catalyst into the catalyst bed is demonstrated experimentally.

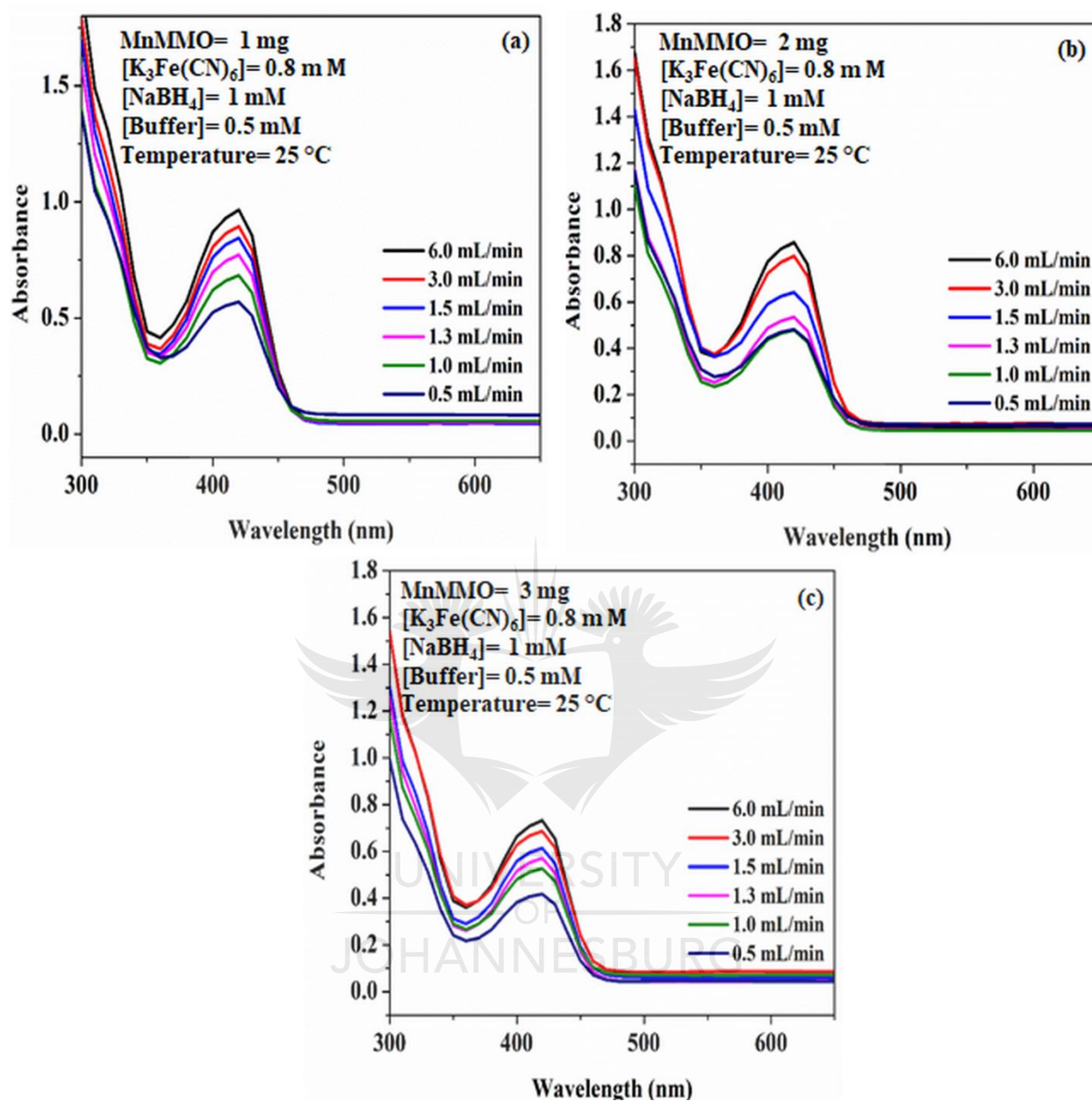
(a) The reactor was printed (b) Printing was suspended temporarily, the reactor was packed with gauze wool, and the catalyst was introduced (c) Printing was resumed, and the catalyst was inprinted.



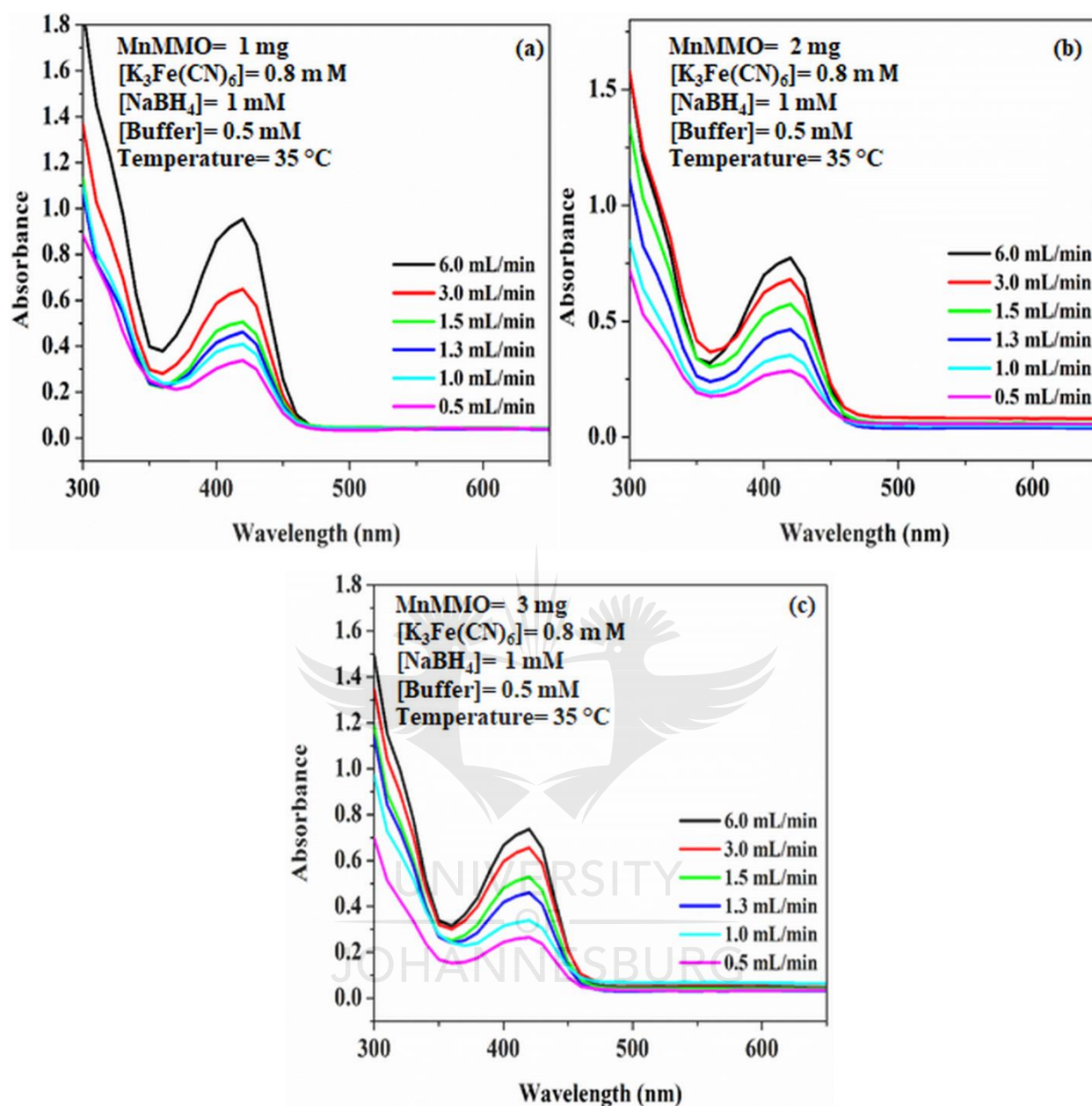
Appx. 5.2: 3D printed syringe pumps

$$RT \text{ (min)} = \frac{\text{Reaction Volume}}{\text{Total Flow Rate (mL/min)}} \quad (1)$$

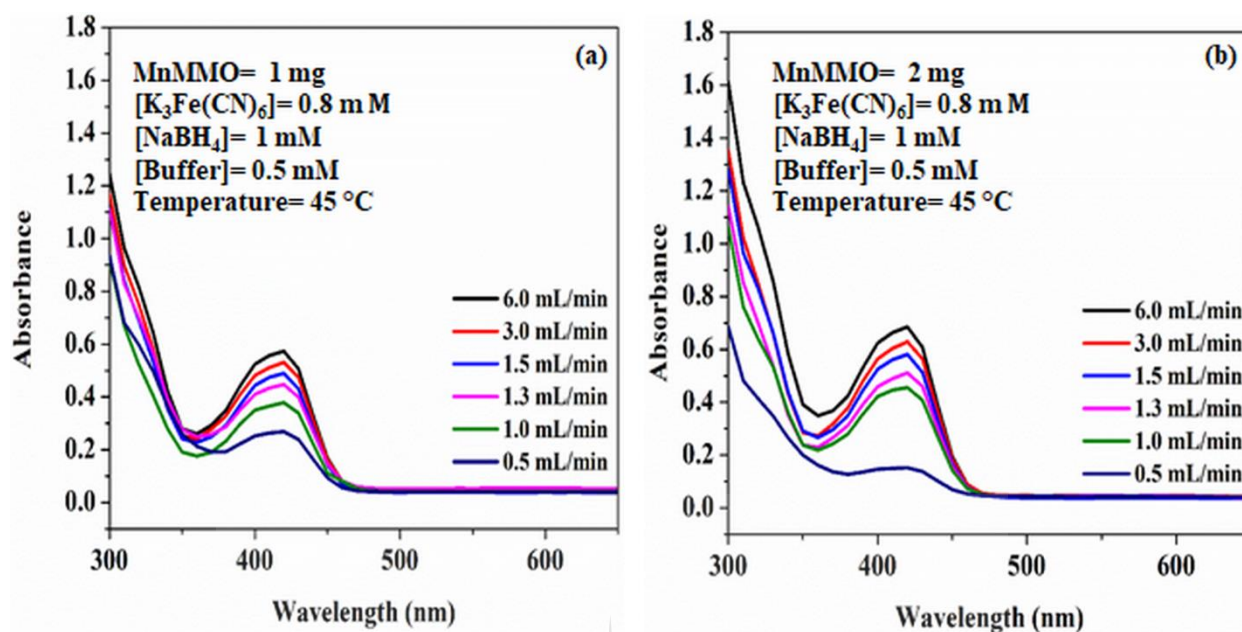
UNIVERSITY
OF
JOHANNESBURG



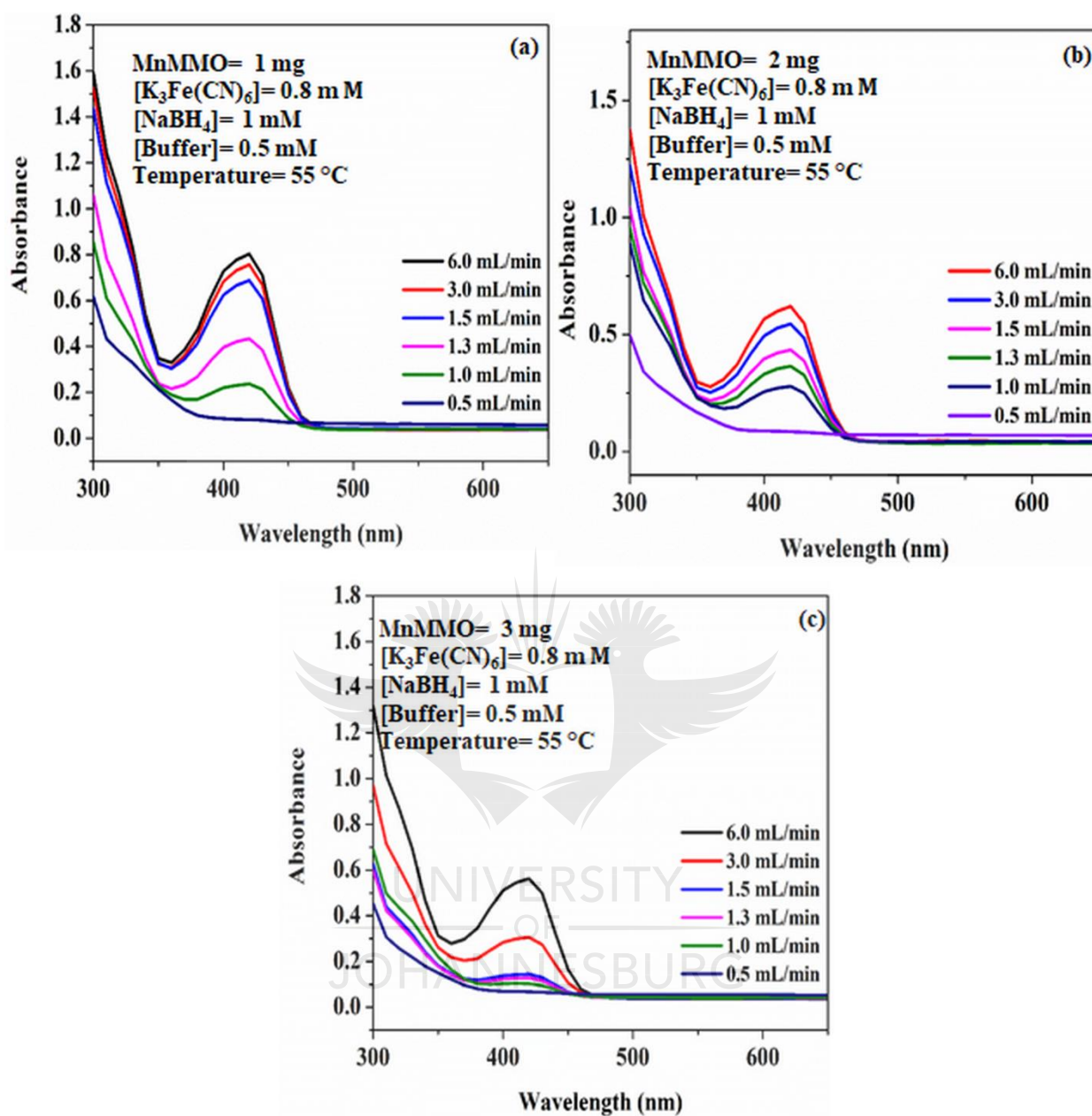
Appx. 5.3: The absorption spectra of flow rate dependence of ferrocyanide reduction at 25 °C with (a) 1 mg, (b) 2 mg, and (c) 3 mg MnMMO using the plate reader.



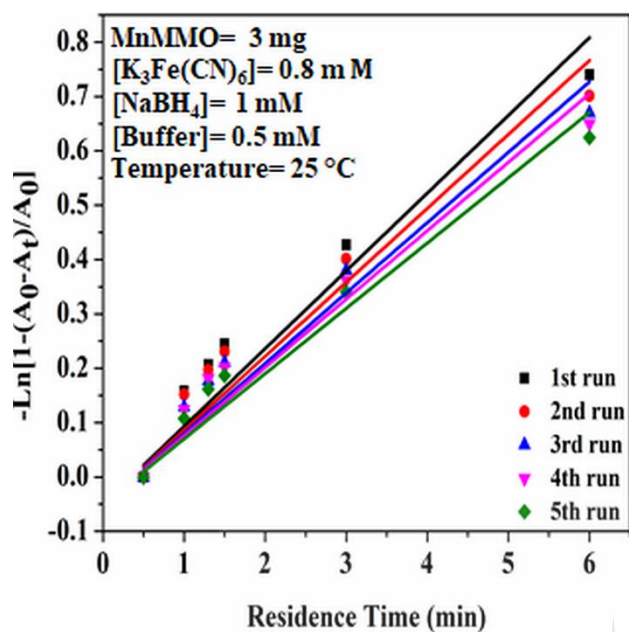
Appx. 5.4: The absorption spectra of flow rate dependence ferrocyanide reduction at 35 °C with (a) 1 mg, (b) 2 mg, and (c) 3 mg MnMMO using the plate reader.



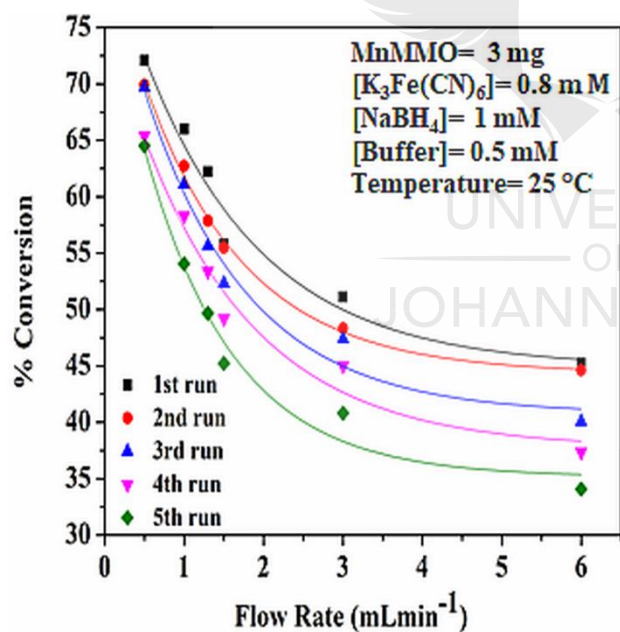
Appx. 5. 4: The absorption spectra of flow rate dependence ferrocyanide reduction at 45 °C with (a) 1 mg and (b) 2 mg MnMMO using the plate reader.



Appx. 5.6: The absorption spectra of flow rate dependence ferrocyanide reduction at 55 °C with (a) 1 mg, (b) 2 mg, and (c) 3 mg MnMMO using the plate reader.



Appx. 5.7: Linear fits plot of each catalytic run.



Appx. 5.8: Graph revealing the catalyst's stability by plotting conversion against the residence time.

5. S2 References

- [1] P. Veerakumar, K. Salamalai, P. Thanasekaran, K.C. Lin, Simple Preparation of Porous Carbon-Supported Ruthenium: Propitious Catalytic Activity in the Reduction of Ferrocyanate(III) and a Cationic Dye, *ACS Omega*. 3 (2018) 12609–12621.
- [2] Q. Xia, S. Fu, G. Ren, F. Chai, J. Jiang, F. Qu, Fabrication of Fe₃O₄@ Au hollow spheres with recyclable and efficient catalytic properties, *New J. Chem.* 40 (2016) 818–824.
- [3] N. Deihimi, M. Irannajad, B. Rezai, Equilibrium and kinetic studies of ferricyanide adsorption from aqueous solution by activated red mud, *J. Environ. Manage.* 227 (2018) 277–285.
- [4] S. Carregal-romero, P. Jorge, P. Herv, L.M. Liz-marz, P. Mulvaney, Colloidal Gold-Catalyzed Reduction of Ferrocyanate (III) by Borohydride Ions : A Model System for Redox Catalysis, 26 (2010) 1271–1277.
- [5] S. Carregal-Romero, N.J. Buurma, J. Pérez-Juste, L.M. Liz-Marzán, P. Hervés, Catalysis by Au@ pNIPAM nanocomposites: effect of the cross-linking density, *Chem. Mater.* 22 (2010) 3051–3059.
- [6] J. Chen, F. Chen, Y. Wang, M. Wang, Q. Wu, X. Zhou, X. Ge, One-step synthesis of poly (ethyleneglycol dimethacrylate)-microspheres-supported nano-Au catalyst in methanol–water solution under γ -ray radiation, *RSC Adv.* 6 (2016) 55878– 55883.
- [7] K. Gong, Y. Liu, Z. Han, Manganese-phosphomolybdate molecular catalysts for the electron transfer reaction of ferricyanide to ferrocyanide, *RSC Adv.* 4 (201 4) 47004–47009.
- [8] W. Wang, Z. Han, X. Wang, C. Zhao, H. Yu, Polyanionic clusters [M (P₄Mo₆)₂](M= Ni, Cd) as effective molecular catalysts for the electron-transfer reaction of ferricyanide to ferrocyanide, *Inorg. Chem.* 4 4 (2016) 6435–6442.
- [9] I. Sarhid, I. Lampre, D. Drago, P. Beaunier, B. Palpant, H. Remita, Hexacyano ferrate (III) reduction by electron transfer induced by plasmonic catalysis on gold nanoparticles, *Materials (Basel)*. 12 (2019) 3012.

Issue 46, 2020 Previous Article | Next Article

From the journal: **New Journal of Chemistry**

In situ replacement of Cu-DEN: an approach for preparing a more noble metal nanocatalyst for catalytic use† Check for updates

Oluwatayo Racheal Onisuru,^a Charles O. Oseghale^a and Reinout Meijboom^b

Abstract

The advantage of dendritic monodisperse macromolecules' dual templating ability was useful in the formation of silica-supported copper nanoparticles Cu₂₀@SiO₂NPs. This was acquired by the initial synthesis of a silica framework (G4-PAMAM-NH₂-SiO₂) as a mesoporous support using amine-terminated generation 4 PAMAM dendrimers (G4-PAMAM-NH₂). The encapsulated Cu₂₀@SiO₂ NPs, calcined at 500 °C, were made to undergo a displacement reaction with Au³⁺ generated from the equivalent molar addition of HAuCl₄. This resulted in

About Cited by | Related

In situ replacement of Cu-DEN: an approach for preparing a more noble metal nanocatalyst for catalytic use

O. R. Onisuru, C. O. Oseghale and R. Meijboom, *New J. Chem.*, 2020, **44**, 20322 DOI: 10.1039/D0NJ04381H

To request permission to reproduce material from this article, please go to the [Copyright Clearance Center request page](#).

If you are an **author contributing to an RSC publication**, you do not need to request permission provided correct acknowledgement is given.

If you are the **author of this article**, you do not need to request permission to reproduce figures and diagrams provided correct acknowledgement is given. If you want to reproduce the whole article in a third-party publication (excluding your thesis/dissertation for which permission is not required) please go to the [Copyright Clearance Center request page](#).

CCC | RightsLink[®] Home | Help | Live Chat | Oluwatayo Onisuru

Continuous-Flow Catalytic Degradation of Hexacyanoferrate Ion through Electron Transfer Induction in a 3D-Printed Flow Reactor

Author: Oluwatayo Racheal Onisuru et al
 Publication: Journal of Materials Engineering and Performance
 Publisher: Springer Nature
 Date: Feb 16, 2021
Copyright © 2021, ASM International

Review Order

Please review the order details and the associated terms and conditions.

No royalties will be charged for this reuse request although you are required to obtain a license and comply with the license terms and conditions. To obtain the license, click the Accept button below.

Licensed Content		Order Details	
Licensed Content Publisher	Springer Nature	Type of Use	Thesis/Dissertation
Licensed Content Publication	Journal of Materials Engineering and Performance	Requestor type	academic/university or research institute
Licensed Content Title	Continuous-Flow Catalytic Degradation of Hexacyanoferrate Ion through Electron Transfer Induction in a 3D-Printed Flow Reactor	Format	print and electronic
		Portion	full article/chapter
		Will you be translating?	no
		Circulation/distribution	1 - 29

SPRINGER NATURE LICENSE
TERMS AND CONDITIONS

Oct 06, 2021

This Agreement between Mrs. Oluwatayo Onisuru ("You") and Springer Nature ("Springer Nature") consists of your license details and the terms and conditions provided by Springer Nature and Copyright Clearance Center.

License Number 5162960763567

License date Oct 06, 2021

Licensed Content
Publisher Springer Nature

Licensed Content
Publication Journal of Materials Engineering and Performance

Licensed Content Title Continuous-Flow Catalytic Degradation of Hexacyanoferrate Ion through Electron Transfer Induction in a 3D-Printed Flow Reactor

Licensed Content
Author Oluwatayo Racheal Onisuru et al

Licensed Content Date Feb 16, 2021

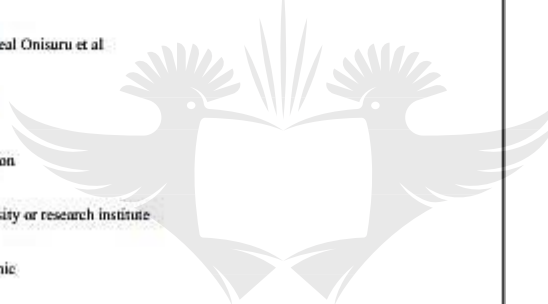
Type of Use Thesis/Dissertation

Requestor type academic/university or research institute

Format print and electronic

Portion full article/chapter

Will you be no



UNIVERSITY
OF
JOHANNESBURG